

ABSTRACT

Title of Document: A MULTISCALE APPROACH TO
PARAMETERIZATION OF BURNING
MODELS FOR POLYMERIC MATERIALS.

Jing Li, Ph.D. , 2014

Directed By: Assistant Professor, Stanislav I. Stoliarov, and
Department of Fire Protection Engineering

A quantitative understanding of the processes that occur in the condensed phase of burning materials is critical for the prediction of ignition and growth of fires. A number of models have been developed to simulate these condensed phase processes. The main issue that remains to be resolved is the determination of parameters to be input into these models, which are formulated in terms of fundamental physical and chemical properties.

This work is focused on developing and applying a systematic methodology for the characterization of polymeric materials based on milligram-scale and bench-

scale tests to isolate specific chemical and/or physical processes in each scale level. The entire study is divided into two parts corresponding to two different scale tests and analysis. The first part is concentrated on the measurement of kinetics and thermodynamics of the thermal degradation of polymeric materials at milligram-scale. It employs a simultaneous thermal analysis instrument capable of thermogravimetric analysis (TGA) and differential scanning calorimetry (DSC). A numerical model is utilized to fit TGA data and obtain thermal degradation kinetics to a continuum pyrolysis model. This model is subsequently employed to analyze DSC heat flow and extract sensible, melting and degradation reaction heats. The extracted set of kinetic and thermodynamic parameters is shown to simultaneously reproduce TGA and DSC curves for a set of 15 widely used commercial polymers.

Then the first part of this study was extended to bench-scale gasification experiments that were carried out in a controlled atmosphere pyrolysis apparatus (CAPA) which has been recently developed in our group. The CAPA is used to measure material gravimetric and thermal changes during thermal decomposition in an anaerobic atmosphere with a capability of analyzing material thermal transport properties. These properties, combined with material kinetics and thermodynamics from the first part of this study, were used as inputs for a pyrolysis model to simulate one-dimensional polymer gasification under wide range of external heat fluxes. The predictive power of this model and validity of its parameters are verified against the results of gasification experiments. 7 out of 15 polymers were validated in bench-scale and the parameterized simulations are in reasonable agreement with experimental data under wide range of conditions.

A MULTISCALE APPROACH TO PARAMETERIZATION OF BURNING
MODELS FOR POLYMERIC MATERIALS.

By

Jing Li

Dissertation submitted to the Faculty of the Graduate School of the
University of Maryland, College Park, in partial fulfillment
of the requirements for the degree of
Doctor of philosophy
2014

Advisory Committee:

Professor Stanislav I. Stoliarov, Chair

Professor James G. Quintiere

Professor Michael R. Zachariah, Dean's representative

Professor Peter B. Sunderland

Dr. Kevin B. McGrattan

© Copyright by
Jing Li
2014

Dedication

To my parents

Jibang Li (李继榜), Huiling Liu (刘慧玲)

and my dear Li Dabao (李骞)

Acknowledgements

Firstly, I would like to thank my family in China for their unwavering supports, endless encouragements during my last 27 years. Every time I came back to my hometown -- Xi'an, China no matter where I had been from, I can feel the warmest love from them. This dissertation cannot be done without my love Li Dabao either. Her presence, patience and encouragements have always been essential flavorings during the most important period of my PhD training.

I am indebted to my advisor, Professor Stoliarov, for leading me into a beautiful and exciting field and providing the opportunity to conduct this research and enrich my experience. His wealth of knowledge in the fields of polymeric material, chemistry and fire science have educated me to overcome many obstacles that I experienced in the last three years. He is also a good friend who provides me meticulous guidance, countless hours of discussion, and sustained encouragement.

I thank my advisory committees, Professor James Quintiere, Professor Peter Sunderland, Professor Michael Zachariah, Professor Chunsheng Wang, Professor Bao Yang and Dr. Kevin B. McGrattan for their time, input, and help in reading and my proposal, dissertation and providing valuable comments. This work was supported by the National Institute of Standards and Technology (NIST) Grant #60NANB10D022. Special thanks go to this project grant monitor, Dr. Kevin B. McGrattan from NIST, for his important assistance and support over the years.

I also want to thank all my group members for their helps, comments and discussions that make my work in real and enjoyable. My study and research have

greatly benefited from discussions with many fellow graduate students from different departments in University of Maryland. Particularly I want to thank Xuan Liu, Xi Ding, Mark McKinnon, Isaac Leventon, Mollie Semmes, Ryan Fisher, Fernando Raffan, Kevin Korver from my group. And Dr. Guoqiang Jian, Yijing Liu, Jingyu Feng, Yihang Liu from chemistry and chemical engineering department for their useful discussions. I also want to thank my college classmate from USTC, Dr. Junhui Gong, who helped me a lot performing gasification experiments during his one-year guest visit in our group. I have to admit that my work could be delayed for at least a couple of months without his help. Last but not least, I want to thank Ms. Olga Zeller and Ms. Mary L. Holt for ordering all the parts that essential to finish my research and study.

Jing Li (李劲)

Table of Contents

LIST OF TABLES	IX
LIST OF FIGURES	XI
CHAPTER 1 : INTRODUCTION.....	1
SECTION 1.1 POLYMER FLAMMABILITY	1
SECTION 1.2 MECHANISM OF POLYMER COMBUSTION	2
SECTION 1.3 NON-CHARRING AND CHARRING POLYMERS	4
CHAPTER 2 : LITERATURE REVIEW	6
SECTION 2.1 MATERIAL FLAMMABILITY TESTS	6
SECTION 2.2 MATERIAL PYROLYSIS PROCESSES	16
SECTION 2.3 RESEARCH MOTIVATION AND OVERVIEW	23
CHAPTER 3 EXPERIMENTAL	29
SECTION 3.1 MATERIALS AND SAMPLE PREPARATION	29
SECTION 3.2 MILLIGRAM-SCALE TESTING	31
Section 3.2.1 Milligram-scale testing on non-charring polymers	31
Section 3.2.2 Milligram-scale testing on charring polymers.....	34
Section 3.2.3 Instrument calibration and data collection for milligram-scale testing	34
Section 3.2.4 Scanning Electron Microscopy (SEM).....	38
SECTION 3.3 BENCH-SCALE TESTING.....	38
Section 3.3.1 Measurement of absorption coefficients.....	38

Section 3.3.2 Gasification experiments part I	40
Section 3.3.3 Gasification experiments part II	45
CHAPTER 4 : MODELING.....	52
SECTION 4.1 THERMAKIN FRAMEWORK.....	52
SECTION 4.2 MILLIGRAM-SCALE MODELING	54
SECTION 4.3 BENCH-SCALE MODELING	55
Section 4.3.1 Modeling for gasification experiments part I	58
Section 4.3.2 Gasification experiments part II	59
CHAPTER 5 : RESULTS- KINETICS AND THERMODYNAMICS FOR NON- CHARRING POLYMERS.....	60
SECTION 5.1 TGA OF POM.....	60
SECTION 5.2 DSC OF POM	64
SECTION 5.3 TGA OF PMMA, HIPS, PA 66, PP, PLA AND ABS	70
SECTION 5.4 DSC OF PMMA, HIPS, PA 66, PP, PLA AND ABS.....	74
CHAPTER 6 : RESULTS- KINETICS AND THERMODYNAMICS FOR CHARRING POLYMERS.....	80
SECTION 6.1 TGA OF KYDEX.....	80
SECTION 6.2 DSC OF KYDEX.....	82
SECTION 6.3 TGA OF DGEBA, PET, KEVLAR, BACY, PPS, PEI AND PEEK.....	87
SECTION 6.4 DSC OF DGEBA, PET, KEVLAR, BACY, PPS, PEI AND PEEK	91
SECTION 6.5 SEM OF CHARS	98

**CHAPTER 7 : RESULTS-HEAT TRANSFER PARAMETERIZATION AND
PYROLYSIS MODEL VALIDATION FOR NON-CHARRING POLYMERS**

..... **101**

SECTION 7.1 ABSORPTION COEFFICIENTS. 101

SECTION 7.2 PMMA GASIFICATION EXPERIMENT AND VALIDATION PART I. 101

 Section 7.2.1 PMMA pyrolysis model parameterization 101

 Section 7.2.2 Prediction of burning rate for PMMA with insulation on bottom.
 103

SECTION 7.3 GASIFICATION EXPERIMENT AND VALIDATION PART II FOR NON-
CHARRING POLYMERS..... 106

 Section 7.3.1 Uniformity of thermometry for non-charring polymers 106

 Section 7.3.2 Thermal conductivity calibration and validation for non-charring
 polymers 108

 Section 7.3.4 Prediction of burning rate for non-charring polymers..... 115

**CHAPTER 8 : RESULTS-HEAT TRANSFER PARAMETERIZATION AND
PYROLYSIS MODEL VALIDATION FOR CHARRING POLYMERS 120**

SECTION 8.1 ABSORPTION COEFFICIENTS. 121

SECTION 8.2 EXPERIMENTAL OBSERVATION..... 121

 Section 8.2.1 ABS and PET 121

 Section 8.2.2 Kydex and PEI..... 125

SECTION 8.3 MODELING..... 131

 Section 8.3.1 ABS and PET 131

 Section 8.3.2 Kydex and PEI..... 132

SECTION 8.4 THERMAL CONDUCTIVITY CALIBRATION.....	135
Section 8.4.1 ABS and PET	135
Section 8.4.2 Kydex and PEI.....	140
SECTION 8.5 SAMPLE HEIGHT AND BURNING RATE PREDICTION	147
Section 8.5.1 ABS and PET	147
Section 8.5.2 Kydex and PEI.....	151
SECTION 8.6 HRR CALCULATION.....	157
CHAPTER 9 : CONCLUDING REMARKS	159
APPENDIX A FDS SIMULATION FOR NON-CHARRING POLYMERS....	162
APPENDIX B PARAMETERIZED MODELS FOR CHARRING POLYMERS	
.....	170
BIBLIOGRAPHY	176

List of Tables

Table 2-1 Selective ASTM standards that relevant to solid material fire safety in different scenarios	7
Table 3-1 Source of materials analyzed in this study.	30
Table 5-1 Rules used to guide TGA curve fitting	62
Table 5-2 Kinetic parameters describing decomposition reactions for POM.....	63
Table 5-3 Heat capacities of material components for POM.....	66
Table 5-4 Kinetic parameters describing decomposition reactions and melting (E_m and A_m) for all non-charring polymers.....	71
Table 5-5 Heat capacities of material components for non-charring polymers.....	75
Table 5-6 Heats of melting and decomposition for non-charring polymers.....	75
Table 5-7 Heats of gasification for non-charring polymers.....	79
Table 6-1 Kinetic parameters describing decomposition reactions for Kydex.....	81
Table 6-2 Heat capacities of material components for Kydex.....	84
Table 6-3 Kinetic parameters describing decomposition reactions and melting for charring polymers.	88
Table 6-4 Heat capacities of material components for charring polymers.....	92
Table 6-5 Heats of decomposition reactions and melting (endo is positive) for charring polymers.	93
Table 6-6 Heats of gasification for charring polymers.	98
Table 7-1 Absorption coefficients for non-charring polymers	101
Table 7-2. Thermal conductivities for HIPS and POM.	112
Table 8-1 Absorption coefficients for ABS and charring polymers	121

Table 8-2 Thermal transport properties for ABS.....	137
Table 8-3 Thermal transport properties for PET.....	139
Table 8-4 Thermal transport properties for Kydex.....	142
Table 8-5 Thermal transport properties for PEI.....	145
Table A. 1 FDS Input Parameters for PMMA.....	163
Table A. 2 FDS Input Parameters for POM.....	165
Table A. 3 FDS Input Parameters for HIPS.....	168
Table B. 1 Parameters for ABS.....	170
Table B. 2 Parameters for PET.....	171
Table B. 3 Parameters for Kydex.....	172
Table B. 4 Parameters for PEI.....	174

List of Figures

Figure 2.1 Experimental set-up for a cone calorimeter measurement [31].....	9
Figure 2.2 Fire Propagation Apparatus (FPA) [33].	10
Figure 2.3 Schematic illustration of the gasification apparatus [37].	12
Figure 2.4 Illustration for pyrolysis-combustion flow calorimeter [47].	14
Figure 2.5 The schematic diagram of FCC [48].	15
Figure 3.1 Sketch of heating furnace and sample carrier.....	32
Figure 3.2 Heat capacity of sapphire.	37
Figure 3.3 Heat capacity of sapphire in the presence of degrading PMMA.....	38
Figure 3.4 Radiation absorption coefficient measurement setup.....	39
Figure 3.5 Heat flux result from ABS absorption coefficient measurement experiment.	40
Figure 3.6. Schematic of the CAPA.....	42
Figure 3.7 Top surface background temperature at different level of heat fluxes under cone heater.	43
Figure 3.8 Copper plate temperature measurements in CAPA and model simulation at external heat flux of 40 kW m^{-2}	45
Figure 3.9 Schematic of modified controlled atmosphere pyrolysis apparatus.	46
Figure 3.10 Comparison of temperature measurements using thermocouples and IR camera for blackened copper plate at radiative heat flux of 40 kW m^{-2}	47
Figure 3.11 Comparison of temperature measurements using thermocouples and IR camera for HIPS with blackened aluminum foil on its bottom at radiative heat flux of 30 kW m^{-2}	48

Figure 3.12 Copper plate bottom surface temperature measurements in CAPA using IR camera and model prediction at external heat flux of 20, 40 and 60 kW m ⁻²	49
Figure 3.13 Heat flux at various level of locations.	51
Figure 4.1 Schematic of virgin polymer sample defined in the model of bench-scale experiments when insulation is present.	58
Figure 4.2 Schematic of virgin polymer sample defined in the model of bench-scale experiments part II.	59
Figure 5.1 TGA of POM at 10 K min ⁻¹	60
Figure 5.2 Experimental and simulated TGA of POM at 10 K min ⁻¹	63
Figure 5.3 Experimental and simulated TGA of POM at 30 K min ⁻¹	64
Figure 5.4 DSC of POM at 10 K min ⁻¹	65
Figure 5.5 DSC of POM normalized by instantaneous heating rate. Linear fits represent heat capacities of the condensed phase at various stages of heating.	66
Figure 5.6 Determination of melting and decomposition contributions to the POM DSC signal.	67
Figure 5.7 Experimental and simulated DSC of POM at 10 K min ⁻¹	69
Figure 5.8 Time integral of 10 K min ⁻¹ DSC of POM.	70
Figure 5.9 Experimental and simulated TGA of PMMA, HIPS and PA 66 at 10 K min ⁻¹ and 30 K min ⁻¹	72
Figure 5.10 Experimental and simulated TGA of PP, PLA and ABS at 10 K min ⁻¹ and 30 K min ⁻¹	73
Figure 5.11 Experimental and simulated DSC of PMMA, HIPS and PA 66 at 10 K min ⁻¹	76

Figure 5.12 Experimental and simulated DSC of PP, PLA and ABS at 10K min ⁻¹ ...	77
Figure 6.1 TGA of Kydex at 10 K min ⁻¹	80
Figure 6.2 Experimental and simulated TGA of Kydex at 10 K min ⁻¹	81
Figure 6.3 Experimental and simulated TGA of Kydex at 30 K min ⁻¹	82
Figure 6.4 DSC of Kydex at 10 K min ⁻¹	83
Figure 6.5 DSC of Kydex (left) and Kydex decomposition residue (right) normalized by instantaneous heating rate.	84
Figure 6.6 Determination of decomposition reaction contributions to the Kydex DSC signal.	85
Figure 6.7 Experimental and simulated DSC heat flow (left) and heat flow integral (right) for Kydex at 10 K min ⁻¹	86
Figure 6.8 Experimental and simulated TGA of DGEBA, PET and Kevlar at 10 and 30 K min ⁻¹	89
Figure 6.9 Experimental and simulated TGA of BACY, PEI and PEEK at 10 and 30 K min ⁻¹	90
Figure 6.10 Experimental and simulated TGA of PPS at 10 K min ⁻¹	91
Figure 6.11 Experimental and simulated DSC of DGEBA, Kevlar and PET at 10 K min ⁻¹	95
Figure 6.12 Experimental and simulated DSC of BACY, PEI and PEEK at 10 K min ⁻¹	96
Figure 6.13 Experimental and simulated DSC of PPS at 10 K min ⁻¹	97
Figure 6.14 SEM images of chars produced as a result of anaerobic thermal degradation of Kydex, DGEBA, PET and Kevlar.	99

Figure 6.15 SEM images of chars produced as a result of anaerobic thermal degradation of BACY, PPS, PEI and PEEK.....	100
Figure 7.1 Back temperature measurement using thermocouple and model prediction of anaerobic pyrolysis for PMMA at 20 and 60 kW m ⁻² (the error bars for both heat fluxes are not significantly shown because the temperature measurement differences from two thermocouples are small).	103
Figure 7.2 MLR measurements using CAPA and model prediction of PMMA anaerobic pyrolysis with insulation at 20 kW m ⁻²	104
Figure 7.3 MLR measurements using CAPA and model prediction of PMMA anaerobic pyrolysis with insulation at 40 kW m ⁻²	105
Figure 7.4 MLR measurements using CAPA and model prediction of PMMA anaerobic pyrolysis with insulation at 60 kW m ⁻²	105
Figure 7.5 Infrared images of bottom surfaces of the non-charring samples undergoing gasification.....	107
Figure 7.6 Spatial variation in bottom surface temperature histories.	108
Figure 7.7 Experimental and simulated bottom surface temperature histories obtained for PMMA at 20 kW m ⁻²	109
Figure 7.8 Experimental and simulated bottom surface temperature histories obtained for PMMA at 40 and 60 kW m ⁻²	110
Figure 7.9 Experimental and simulated bottom surface temperature histories obtained for HIPS at 30 kW m ⁻²	111
Figure 7.10 Experimental and simulated bottom surface temperature histories obtained for HIPS at 50 and 70 kW m ⁻²	111

Figure 7.11 Experimental and simulated bottom surface temperature histories obtained for POM at 30 kW m ⁻²	112
Figure 7.12 Experimental and simulated bottom surface temperature histories obtained for POM at 50 and 70 kW m ⁻²	112
Figure 7.13 Thermal conductivity for PMMA	113
Figure 7.14 Thermal conductivity for HIPS.	114
Figure 7.15 Thermal conductivity for POM.	115
Figure 7.16 Experimental and simulated burning rate histories obtained for PMMA at 20-60 kW m ⁻²	117
Figure 7.17 Experimental and simulated burning rate histories obtained for HIPS at 30-70 kW m ⁻²	118
Figure 7.18 Experimental and simulated burning rate histories obtained for POM at 30-70 kW m ⁻²	119
Figure 8.1 Char residues after gasification experiments for ABS at 50 kW m ⁻²	122
Figure 8.2 Infrared images of bottom surfaces of the ABS sample undergoing gasification at 50 kW m ⁻²	123
Figure 8.3 Char residues after gasification experiments for PET at 50 kW m ⁻²	124
Figure 8.4 Infrared images of bottom surfaces of the PET sample undergoing gasification at 50 kW m ⁻²	125
Figure 8.5 Char residues after gasification experiments for Kydex at 50 kW m ⁻² ..	126
Figure 8.6 Side views and Infrared images of bottom surfaces of the Kydex sample undergoing gasification at 50 kW m ⁻²	127
Figure 8.7 Char residues after gasification experiments for PEI at 50 kW m ⁻²	129

Figure 8.8 Side views and Infrared images of bottom surfaces of the PEI sample undergoing gasification at 50 kW m^{-2}	130
Figure 8.9 Experimental measurements and linear fits for the height to sample bottom vs time for Kydex and PEI at various heat fluxes.....	134
Figure 8.10 Relation of incident radiative heat flux on top surface and time.....	135
Figure 8.11 Experimental and simulated bottom surface temperature histories obtained for ABS at 30 kW m^{-2}	136
Figure 8.12 Experimental and simulated bottom surface temperature histories obtained for ABS at 50 kW m^{-2}	137
Figure 8.13 Experimental and simulated bottom surface temperature histories obtained for ABS at 70 kW m^{-2}	138
Figure 8.14 Experimental and simulated bottom surface temperature histories obtained for PET at 50 kW m^{-2}	139
Figure 8.15 Experimental and simulated bottom surface temperature histories obtained for PET at 70 kW m^{-2}	140
Figure 8.16 Experimental and simulated bottom surface temperature histories obtained for Kydex at 30 kW m^{-2} (fitted range).....	141
Figure 8.17 Experimental and simulated bottom surface temperature histories obtained for Kydex at 30 kW m^{-2}	141
Figure 8.18 Experimental and simulated bottom surface temperature histories obtained for Kydex at 50 kW m^{-2}	142
Figure 8.19 Experimental and simulated bottom surface temperature histories obtained for Kydex at 70 kW m^{-2}	143

Figure 8.20 Experimental and simulated bottom surface temperature histories obtained for PEI at 50 kW m ⁻² (fitted range).....	144
Figure 8.21 Experimental and simulated bottom surface temperature histories obtained for PEI at 50 kW m ⁻²	144
Figure 8.22 Experimental and simulated bottom surface temperature histories obtained for PEI at 70 kW m ⁻²	146
Figure 8.23 Experimental and simulated bottom surface temperature histories obtained for PEI at 90 kW m ⁻²	146
Figure 8.24 Side view snapshots of PET at 50-90 kW m ⁻²	147
Figure 8.25 Experimental and simulated thickness histories obtained for ABS at 50 kW m ⁻²	148
Figure 8.26 Experimental and simulated burning rate histories obtained for ABS at 30-70 kW m ⁻²	149
Figure 8.27 Experimental and simulated thickness histories obtained for PET at 50 kW m ⁻²	150
Figure 8.28 Experimental and simulated burning rate histories obtained for PET at 50 and 70 kW m ⁻²	151
Figure 8.29 Experimental and simulated thickness histories obtained for Kydex at 50 kW m ⁻²	152
Figure 8.30 Experimental and simulated burning rate histories obtained for Kydex at 30 and 70 kW m ⁻²	153
Figure 8.31 Experimental and simulated thickness histories obtained for PEI at 50 kW m ⁻²	154

Figure 8.32 Experimental and simulated burning rate histories obtained for PEI at 50 and 90 kW m ⁻²	156
Figure 8.33 Maximum heat release rate verse heat flux for polymers (These maximum heat release rates were calculated by multiplying the maximum gasification experiment burning rate and effective HOC values obtained from this study).	158
Figure A. 1 Comparison of predicted and measured mass loss rates for PMMA.....	165
Figure A. 2 Comparison of predicted and measured mass loss rates for POM.	167
Figure A. 3 Comparison of predicted and measured mass loss rates for HIPS.	169

Nomenclature

Abbreviation

ABS	poly(acrylonitrile butadiene styrene)
ASTM	American Society for Testing Materials
BACY	polymerized bisphenol A cyanate ester
CAPA	Controlled Atmosphere pyrolysis Apparatus
DGEBA	polymerized diglycidylether of bisphenol A
DSC	differential scanning calorimetry
FAA	Federal Aviation Administration
FPA	Fire Propagation Apparatus
HIPS	high impact polystyrene
Kevlar	poly(paraphenylene terephthalamide)
HOC	heat of combustion
Kydex	poly(methyl methacrylate)-poly(vinyl chloride) alloy
MCC	Microscale Combustion Calorimetry
MLR	mass loss rate
MPC	Mass Pyrolysis Calorimetry
NFPA	National Fire Protection Association
NIST	National Institute of Standard Technology
PA 66	polyamide 6,6
PCFC	Pyrolysis Combustion Flow Calorimetry
PE	polyethylene
PEEK	poly(ether ether ketone)
PEI	polyetherimide
PET	poly(ethylene terephthalate)
PFCC or FCC	Pyrolysis Flaming Combustion Calorimetry
PLA	poly(lactic acid)
PMMA	poly(methyl methacrylate)
POM	poly(oxymethylene)
PP	polypropylene
PPS	poly(phenylene sulfide)
SEM	Scanning Electron Microscopy
TGA	thermogravimetric analysis
UL	Underwriter's Laboratories

Equation symbols

A	Arrhenius pre-exponential factor
α	radiation absorption coefficients
c	heat capacity
D	cylindrical coordinates
E	Arrhenius activation energy
e	base of the natural logarithm
f	reflectivity
h	heat of reaction
I	radiation heat flux
J	mass flux
k	thermal conductivity
λ	gas transfer coefficients
m	mass
q	stoichiometric coefficient
ρ	density
r	reaction rate
R	gas constant
σ	Stefan-Boltzmann constant
t	time
T	temperature
x	cartesian coordinate
ξ	concentration
<i>Subscript</i>	
<i>0 or init</i>	initial stage
<i>base</i>	baseline
<i>d</i>	decomposition
<i>e</i>	final simulation
<i>ex</i>	external
<i>g</i>	gasification
<i>j,k,l</i>	component
<i>max</i>	maximum stage
Melt or <i>m</i>	molten polymer
Res1	residue of polymer decomposition stage 1
Res2	residue of polymer decomposition stage 2
<i>v</i>	vaporization

Chapter 1 : Introduction

Section 1.1 Polymer flammability

Polymeric materials or plastics are generally defined as materials that contain essential ingredients such as polymers. Polymers are organic substances with extremely high molecular mass. Most of this class of materials is synthesized or semi-synthesized from petrochemicals with other substances for special purpose. Polymers are ubiquitous in both high technology and routine household applications. Thousands of polymers were created and widely used in the last century and endless types of new polymers are continually being produced around the world. An attractive combination of customizable mechanical properties, low weight, and easy processability makes them an irreplaceable part of today's modern society [1].

One of the main disadvantages associated with a widespread use of these materials is their inherent flammability [2] because of a large fraction of carbon and hydrogen atoms in these organic substances that make their compositions very similar to that of fossil fuels. Combustion can occur easily under sufficiently heat and oxygen for some polymers. For example, most early credit cards and Ping-Pong balls were made of highly flammable and hazardous celluloid plastic. Therefore most polymer-containing end products (i.e. electrical cables, furniture and home or office decorating materials and carpets) that exist everywhere in our daily lives must pass certain fire safety requirements (for example, UL 94) to assure personal and public safety [3].

Researchers are examining and exploring hundreds of ways to reduce the polymer flammability in application, transportation and storage while keeping their other advantages. The burning of solid polymeric material is a complex process that

involves multiple chemical and physical phenomena such as pyrolysis at the condensed phases including phase transitions, chemical reactions, heat transfer, mass diffusion and flame or flameless combustion that occurs at the gaseous phase [4]. It is important to quantitatively understand the fundamental principles behind polymer ignition and burning. From this aspect, chemists and material scientists can understand how to best modify existing polymers to reduce their flammability in order to pass such tests without significantly increasing the cost of end products.

Section 1.2 Mechanism of polymer combustion

When most polymers or solid materials burn in presence of a flame, they burn similarly to other liquids and gaseous fuels. The flame is usually termed a diffusion flame. In diffusion flame, combustion occurs at the interface where the oxidizer meets the combustible gaseous fuel which is generated from the thermal degradation of the condensed phase fuel and the gaseous fuel is transported by diffusion and controls convection. Gas phase combustion provides the continual sources of heat, which can be categorized into two groups: radiative and convective, over the boundaries of condensed phase thermal degradation. The gas phase combustion phenomena, including chemical reactions, turbulence, soot generation and oxidization, species concentration distribution etc. were intensively studied for years and are reasonably well understood. For example, scientists in the last century have been able to understand the combustion of gaseous fuels and chemical processes, in terms of elementary chemical reactions with defined chemical kinetic parameters [5]. Commercial computational software, such as CHEMKIN [6], is available in the market for basic chemical kinetic simulations.

The condensed phase thermal degradation reaction mechanisms, which dominate the overall burning rate play an important role in the delivery of gaseous combustibles for the gas phase combustion [3]. There are several kinds of chemical and physical processes that occur in the condensed phase and some of them are key factors that affect overall material flammability and combustion. The mechanisms of how these phenomena interact and give rise to gaseous fuel generation that defines material flammability [3] have been studied by many researchers [7-13] for various types of polymers. For example, thermal degradation dynamics of polymers were studied for various of polymers (Polyethylene(PE) [14], Polypropylene (PP) [15], poly(methyl methacrylate) (PMMA) [16], and poly(isobutylene) (PIB) [17]) at an atomistic and molecular level to find the factors that governs the overall thermal degradation kinetics.

However, the process that governs the polymer combustion at the condensed phase is not only governed only at the molecular level, though it can affect ignitability and overall combustion process. When polymers thermally degrade and burn, a number of physical and chemical processes occur simultaneously and it is hard to separate them individually. Previous evidence and studies lead to the conclusion that without clearing an understanding of macro-scale morphology and heat transfer within condensed phase, especially for some charring polymers, no quantitative connection can be made between molecular-level phenomena and polymer flammability performance. Therefore in this study, special attention has been focused on thermal degradation process at milligram scale and bench scale of polymeric materials at the condensed phase.

Section 1.3 Non-charring and charring polymers

In most cases, solid polymer long chains break down into a number of smaller fragments, which can either be monomers or groups of chemical species, under thermal decomposition. Some polymers break down completely in the condensed phase leaving no significant amount of residue. Those polymers that usually remain within 5 wt.% of the initial mass are categorized into non-charring polymers. However, some polymer chains break in a different manner. Those heavier molecule fragments crosslink, and instead of further chain scission, they remain in the condensed phase and forms as carbonaceous residues. Those polymers are named charring polymers. The charring processes for polymer thermal degradation in the condensed phase are complicated and they can be affected by many factors such as naturally chemical composition, incorporation of flame retardants [18] and surface treatment (i.e intumescent coating). Other than the polymeric materials themselves, ambient conditions are also important factors to lead the charring processes. For example, Martel's research [19] in late 1980s disclosed that oxygen has a decisive effect on the charring process for some polymers without containing aromatic rings in their main chain. There is no standard criterion to regularize the minimum amount of residue for charring polymer. In this work, we choose 10 wt.% as the minimum value to determine this group of polymers by studying their thermal degradation residues upon heating up to 1223 K from room temperature in a thermally thin condition at purely inert condition.

It was found that charring polymers during bench-scale burning have lower ignitability [1] and lower heat release rate than non-charring polymer because of the following reasons: lower amount of volatile fuel is produced by burning charring

polymer and a formation of insulation layer which reduce heat and mass transfer at the condensed phase. However, production cost of charring polymer is usually more expensive than cost of non-charring polymer. Therefore in the engineering market, one of the ways for chemists and material scientists to reduce the polymer flammability in order to pass material fire safety tests is by adding the flame retardant additives [20, 21]. A conventional solution to the problem is to use halogenated flame-retardant additives. However, with more and more concerns on the use of halogenated flame-retardant additives for its tendency to bioaccumulate and potential toxicity [22], researchers are seeking halogen-free fire additives for inducing char formation. The current state of the art approaches [23] to improve polymer flame retardancy are blending with some charring polymers to non-charring polymers, using of nontraditional charring agent, using of nanoparticles and improving intumescence. The polymer nanocomposite [24-26] is one of the most promising improvements to replace the conventional formulations in the area of flame retardancy. For instance, Zanetti *et al.* [27] reported that the use of nanoclays in the polymer nanocomposites can led to the reduction of oxygen permeability to improve its thermo-oxidative stability and thermal stability in some cases [28]. Kashiwagi *et al.*[29] found that nanoparticle fillers such as carbon nanotubes can surpass nanoclays to simultaneously improve both mechanical and flammability properties. Intumescent materials are called “Intumescent” because their surfaces begin to swell and then expand when heated to critical temperature. As a result, a foamed cellular layer is formed and shields the unpyrolyzed material from the action of the heat flux or the flame [30].

Chapter 2 : Literature review

This chapter focuses on providing an overview of previous studies that address material flammability and in particular polymeric material flammability. Other similar solid materials are also discussed, such as wood - a natural composite polymer made of cellulose, hemicelluloses and lignin. Cellulose (≈ 42 wt.% in wood) and lignin (≈ 28 wt.%) are organic compounds and corresponding approximately to the formula $(C_6H_{10}O_5)_n$ and $(C_{31}H_{34}O_{11})_n$ respectively. The physical and chemical processes that occur at the condense phase, and which control the material flammability and ignitability and are discussed in detail here. In addition, key parameters that dominate the overall burning of material are discussed and research works of the measurement for these parameters are reviewed. Pyrolysis numerical pyrolysis models that are capable of simulating the process of thermal degradation, material ignition and combustion are also reviewed and existing impediments and challenges to accurate model prediction are addressed. Last but not least, the motivation and primary contribution of this dissertation is emphasized.

Section 2.1 Material flammability tests

As mentioned in the chapter 1, material flammability especially for polymeric material is generally a big concern for fire protection for material manufactures. The way to judge whether a particular polymer is more flammable than the other one really depends on the scenarios in which the polymers are placed. Therefore, the fire behavior when polymeric materials are exposed to fire is generally evaluated as a quantitative measurement through a number of flammability tests that resemble certain types of fire scenarios. There are numbers of organizations around the world

which proposes such standard tests such as American Society for Testing Materials (ASTM), which is mostly adopted in the United State, and Underwriter’s Laboratories (UL), National Fire Protection Association (NFPA) and International Conference of Building officials (ICBO). Most of the material flammability testing standards are similar despite that they are issued and adopted in different areas. Table 2-1 lists selective ASTM standards that are relevant to solid material fire safety in different scenarios.

Table 2-1 Selective ASTM standards that relevant to solid material fire safety in different scenarios

Standard number	Standard description
ASTM C209	Insulating board
ASTM D568	Plastics, vertical
ASTM D635	Plastics, horizontal
ASTM D757	Plastics, horizontal, incandescence, Globar
ASTM D1433	Plastics, 45 degree angle
ASTM D1692	Cellular plastics, horizontal
ASTM D1929	Plastics, ignition, Setchkin furnace
ASTM D2863	Measuring the Minimum Oxygen Concentration to Support Candle-Like Combustion of Plastics
ASTM D3014	Cellular plastics, vertical , Butler chimney
ASTM D3713	Plastics, ignition, small flame
ASTM D4100	Plastics, smoke, gravimetric, Arapahoe chamber
ASTM D4151	Blankets, flammability
ASTM D4205	Rubber, flammability and combustion
ASTM D4986	Cellular polymers, horizontal, similar to ASTM D1692
ASTM D7309	Determining Flammability Characteristics of Plastics Using Microscale Combustion Calorimetry
ASTM E84	Building materials, surface burning, 25-foot tunnel

ASTM E119	Standard fire tests
ASTM E136	Combustibility
ASTM E162	Surface flammability, radiant panel
ASTM E286	Surface flammability, 8-foot tunnel
ASTM E1354	Heat and Visible Smoke Release Rates for Materials Using an Oxygen Consumption Calorimeter
ASTM E2058	Standard Test Methods for Measurement of Material Flammability Using a Fire Propagation Apparatus
ASTM E2254	Room Fire Test of Wall and Ceiling Materials
ASTM E2257	Room Fire Test of Wall and Ceiling Materials
ASTM F501	Aerospace material, vertical

All these testing standards aim to resemble real fire scenarios, and are either primarily research tests or primarily acceptance tests, from micro scale to room scale. The complexity and costs for the fire tests increase dramatically as the scale increasing. Full scale tests are usually too expensive to afford for most users. However, larger scale of fire tests resembles the real fire scenarios closer. Therefore, one of the most widely used testing standards named ASTM 1354 in the United States is carried out at a bench scale, which places in the middle range among those scales. The instrument used in this type of test is named cone calorimeter, which is widely and effectively used in the field of fire safety engineering. It usually measures heat release rate of the solid materials which is difficult to perform in the full-scale tests. It was initially developed by National Institute of Standard Technology (NIST) researchers [31] about 30 years ago and relied on an empirical observation that releasing energy from burning material is directly proportional to the quantity of consumed oxygen [32]. There are several standard tests that are carried under this instrument, such as ASTM D 6113, ASTM E1474, ASTM E1740 and ASTM F1550.

As shown in Figure 2.1, a testing sample is heated underneath a conical radiant electrical heater, which delivers a uniform one-dimensional external radiative heat flux that simulates the burning surroundings in a room fire. The exhaust gases after combustion are collected from a hood with centrifugal fan on top and are then analyzed by a gas analyzer. Concentrations of O₂, CO and CO₂ are measured in the gas analyzer. Other key parameters (i.e., heat release rate, mass loss rate, smoke production, etc.) of material under external heat flux measuring up to 100 kW m⁻² can be calculated. In addition, from these types of tests, the time to ignition, combustion time and total smoke released are also characterized.

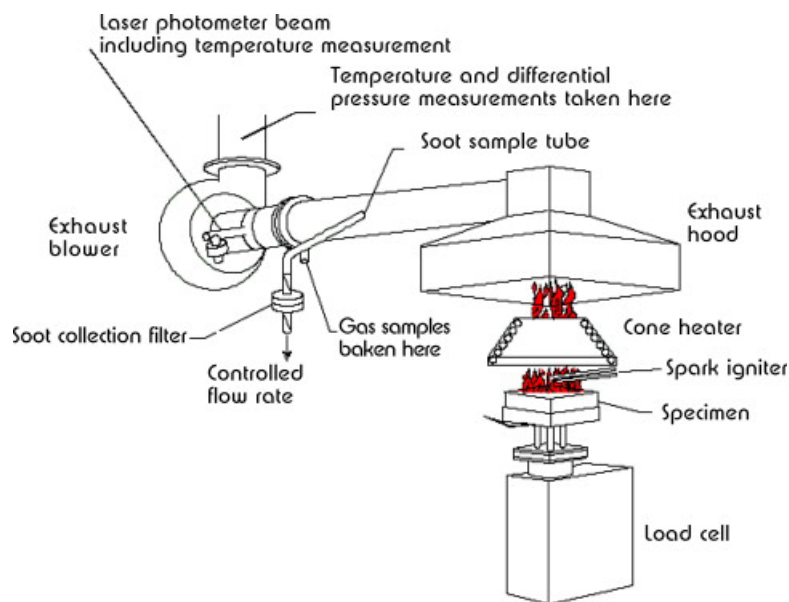


Figure 2.1 Experimental set-up for a cone calorimeter measurement [31].

Although cone calorimeter measures the heat release rate well for many materials, one of the major issues, which has existed for years, is the measurements that are taken near ambient air under well-controlled environments. Usually, this is not the same case that occurs at the real fire scenarios, especially in some compartment fires when the ventilations are limited. Therefore, researchers from FM

Global developed an apparatus that can control the testing environment by purging gases flow uniformly into an infrared-grade quartz tube, which shields the sample and gasification products from the ambient air. As shown in Figure 2.2, instead of using a conical radiant electrical heater, four high-power high-density infrared tungsten halogen heaters are used to generate a uniform external heat flux of up to 120 kW m^{-2} . The exhaust system, which is similar to a cone calorimeter, is used to analyze the combustion production gas. Many important parameters are related to material flammability, such as critical heat flux for ignition, thermal response parameter, effective heat of combustion and smoke yield are then recorded.

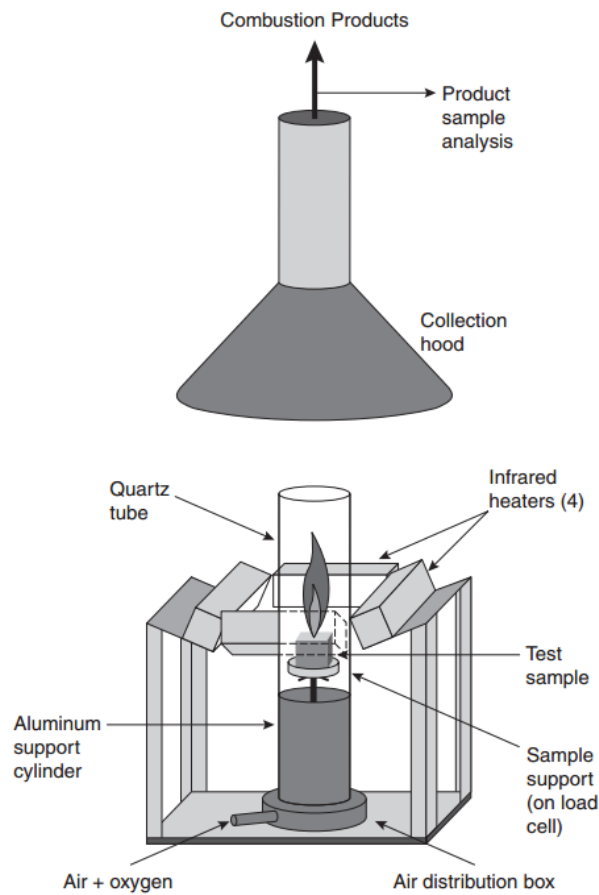


Figure 2.2 Fire Propagation Apparatus (FPA) [33].

Because of its significant characteristics, FPA is designed and used to evaluate existing standards for fire propagation along cables and the flammability of clean room materials. However, one of the main issues related to this apparatus that limits its use is the spectral radiance from the radiative lamps. There are more than one evidences that disclose the fact that the radiative spectrum from the lamps used in FPA does not cover the entire range of radiative wavelengths is observed in the real fire scenario. There is a clear shift to the time to ignition using cone calorimeter and FPA for PMMA [34], especially for high heat flux [35]. In this case, experimental results directly from FPA need extra work to amend by applying the integration of entire radiative wavelength [36].

For a gasification test on a bench-scale, where flame is completely removed from the burning sample, FPA can produce good results except for a couple of issues. Besides the radiative spectral from lamps, the hot quartz during the gasification affects the boundary conditions that need to be well controlled. Kashiwagi *et al.* [37] from NIST built a well-controlled gasification apparatus that is somewhat similar in design to a cone calorimeter. The primary difference between their apparatus and cone calorimeter is that the sample is placed inside a sealed cylindrical chamber in which nitrogen is continuously purged at a prescribed rate rather than in the open air, as in the case of a cone calorimeter. As shown in Figure 2.3, the cylindrical chamber, which is made of stainless-steel and painted black internally, is designed to remain a constant temperature at 25°C by water cooling and minimize background radiation. Incident flux (20 kW m^{-2} to 70 kW m^{-2}) is delivered by a cone heater on top of the testing samples. Mass loss rate, rather than calorimetry, is recorded during material

gasification. Visual observation and video are available to provide excellent documentation of the pyrolysis process. In general, this apparatus provides a well-controlled gasification condition to study the material, mainly polymers, and pyrolysis under uniform heat fluxes and it has been used extensively after its invention [29, 38-46]. However, this apparatus has two main drawbacks that limit its use in gasification experiments: cost and limited diagnostics. During the tests, this instrument require significant power from the heater and exhaust system and extremely large amounts of nitrogen flow (approximately 1200 SLPM). Besides mass loss rate, only video data is taken from the top side view during the gasification. No other diagnostics are applied in the test, such as temperature measurement.

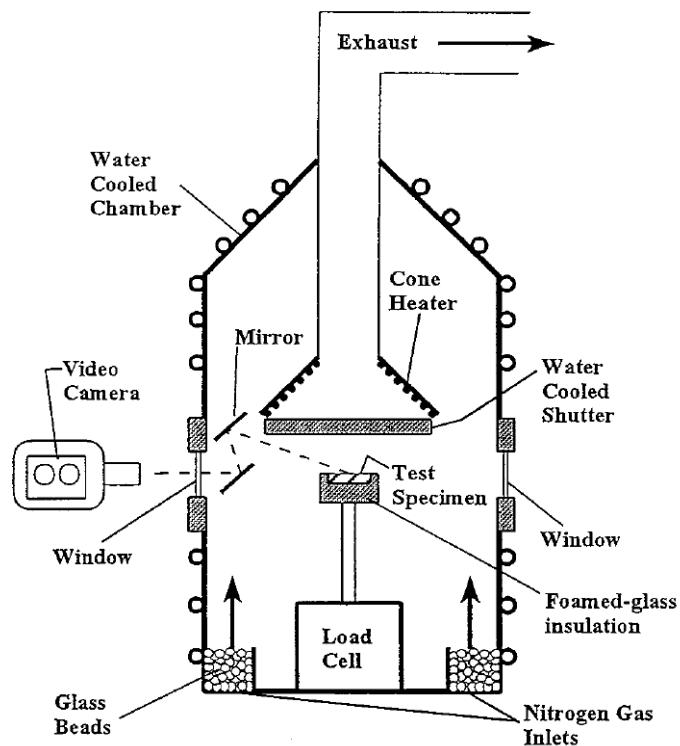


Figure 2.3 Schematic illustration of the gasification apparatus [37].

All these tests require a gram-scale of the samples to examine the material flammability which is fairly expensive, especially for manufacturers that design and make new polymeric materials with flame retardants. Therefore, a number of researchers have made considerable efforts in developing laboratory instruments to measure the heat release rate of milligram-scale samples.

One of the successful inventions in recent years for material flammability study on the milligram-scale is the Microscale Combustion Calorimetry (MCC), which was initially developed by Lyon *et al.* [47] from the Federal Aviation Administration (FAA). MCC, also is named Pyrolysis Combustion Flow Calorimetry (PCFC), which measures the complete combustion of the given material in milligram scale. According to ASTM D7309, MCC is used to screen research materials at the milligram level for a fireproof aircraft cabin. The principle of MCC is shown in Figure 2.4. The milligram sample is placed inside the pyrolyzer at a prescribed heating rate. The gaseous volatiles meet with oxidizer (typically O₂) inside the combustor. This combustor is preheated to 900°C for complete combustion and oxygen consumption is recorded in real time by an oxygen analyzer that sits close to a mass flow meter. The heat release rate is then calculated, similarly to cone calorimeter and FPA, using oxygen depletion technique [32].

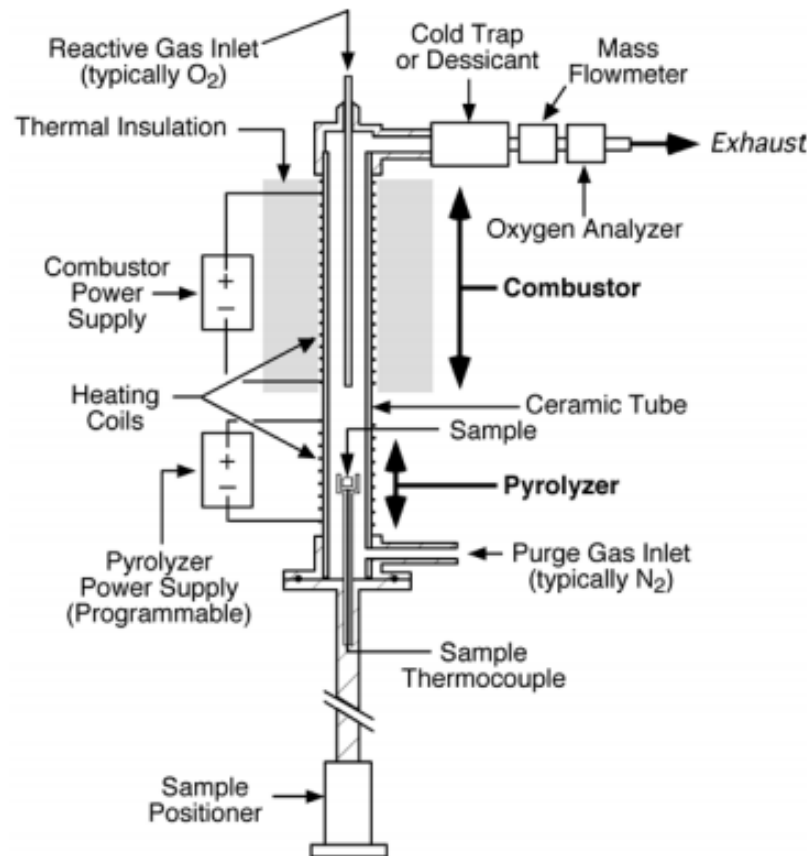


Figure 2.4 Illustration for pyrolysis-combustion flow calorimeter [47].

Although ASTM D7309 or MCC is widely used by chemists and material scientists to screen new material at the milligram level and measure the complete combustion of polymer. However, the major concerns raised by fire protection engineers in the past, is the comparison of combustion efficiency with the real material burning, like the flaming and soot generation observed in the cone calorimeter or FPA. A new instrument that aims at measuring the flaming combustion at the milligram scale, which shares the advantages between MCC and the cone calorimeter named Pyrolysis Flaming Combustion Calorimetry (PFCC or FCC), is recently developed by Stoliarov *et. al* [48]. The schematic diagram for FCC is shown in Figure 2.5. In this figure, the FCC in essence consisted of four parts: the pyrolyzer,

the base, the combustion chamber and the gas analyzing system. In FCC, a sample of approximately 30 mg was being heated in the pyrolyzer. Instead of forcing pyrolysis volatiles in the combustor in MCC, FCC has an igniter to generate flaming combustion at the gas phase where oxygen consumption is recorded similarly with MCC and heat release rate is calculated using oxygen depletion technique [32]. The actual flaming combustion took place in the combustion chamber which was made of quartz tube that had extremely low thermal expansion coefficient. The flame height, combustion time, time to ignition information can also be measured since quartz tube is transparent.

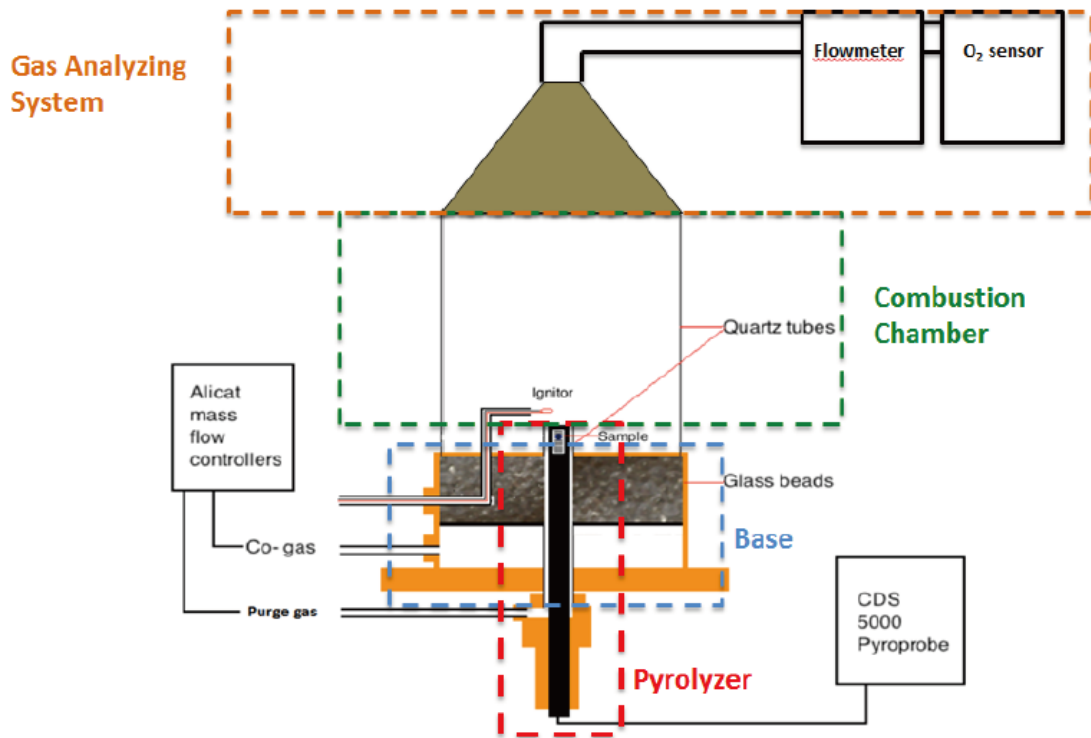


Figure 2.5 The schematic diagram of FCC [48].

All these laboratory scale testing methods hold their own advantages and represent in well-controlled behavior in different levels of scale. However, each of the

above method has its own disadvantages, obviously. Besides the drawback of being expensive, the bench-scale cone calorimeter test is a complex process and it is hard to separate the effect of gas-phase combustion and condensed-phase pyrolysis. Although MCC is capable of separating the aforementioned effect, it fails to capture gas phase effects because of forced combustion. FCC decoupled the gas-phase combustion and condensed phase pyrolysis and measures the effective heat of combustion in a reasonable manner with combustion efficiency result within the cone calorimeter results. However, the FCC was not fully capturing the effect that bromine acts as gas phase combustion inhibitor to the extent that cone calorimeter was capturing [48].

Section 2.2 Material pyrolysis processes

From the material flammability aspect, there are two processes that dominate the polymeric material burning rate under condensed phase: thermal and chemical processes.

The thermal process always occurs at the initial state when polymeric materials are subjected to external heat, such as from visible flame or fires. Researchers were using Fourier's law to represent the heat conduction inside the solid phase. One of the early examples was a research paper by Tinney [49] who modeled the pyrolysis of one small wooden dowel under external heat using a one-dimensional assumption, before polymer flammability issue draws public attention widely. He described the conduction equation in cylindrical coordinates in Equation 2.1 to describe the temperature distribution in the solid state $T(D, t)$. T , D , t represent temperature of the wood, radial distance from the center of the wooden dowel and

time respectively. A number of researchers focused on different geometries [9, 50-56] following the methodology of Tinney [49].

$$\rho C_p \frac{\partial T}{\partial t} = k \left(\frac{\partial^2 T}{\partial D^2} + \frac{1}{D} \frac{\partial T}{\partial D} \right) \quad (2.1)$$

Where k represents the thermal conductivity of material, which is the key parameter of this equation. k is assumed temperature-independent for simplicity. ρ is the density of wood. C_p denotes the wood heat capacity. A solution of Equation 2.1 can be obtained either numerically or by analytically providing an initial condition and two boundary conditions are specified. There are a number of scientific papers that have stepped into the study of inclusion of char formation [8, 57-61] and used temperature-dependent properties during solid material combustion and pyrolysis, which makes the problems more realistic. Properties other than thermal conductivity such as specific heat capacity, emissivity, surface absorptivity and density were obtained accurately from experiments and coupled into modeling [62-68]. Other terms affecting heat transfer such as convection and radiation were also considered and added into the thermal model to calculate the temperature distribution in the later models [9, 56, 64, 65, 68]. The physical process also involves a series of phase transformations such as glass-liquid transition for some amorphous materials (or in amorphous regions within semicrystalline materials) and melting.

The chemical process of material pyrolysis includes chemical decomposition and volatilization. For most solid polymeric material, the decomposition process to produce a gaseous fuel can be idealized by an Arrhenius type of reaction. As

described in a thermal analysis handbook [69], the reaction rate of thermally activated process can be described:

$$\frac{d\alpha}{dt} = Ae^{\frac{-E_a}{RT}} f(\alpha) \quad (2.2)$$

where α is the extent of conversion and can be defined as

$$\alpha = \frac{m_i - m_T}{m_i - m_f} \quad (2.3)$$

Where m_T is the mass at temperature T and m_i and m_f are respectively the initial and final masses for a given step of mass change. Pre-exponential factor (A) and activation energy (E) are two Arrhenius parameters. T is the temperature and t is the time. The reaction model is defined as

$$f(\alpha) = (1 - \alpha)^n \quad (2.4)$$

n is the reaction order. Many researchers frequently found that the first order reaction assumption in their models predicts the experiments well for most of common solid materials such as wood [58, 66, 70], non-charring polymers [71-77] and charring polymers [76, 78, 79]. The other two key parameters, A and E , are intensively studied almost by every material flammability scientist for different types of solid materials for decades. The determination of kinetic characteristics and parameters including Arrhenius parameters and reaction model can be obtained from experiments in several methods. Isothermal and non-isothermal methods are two frequently used methods. In isothermal method, yield-time measurements are made while the reactant is maintained at a constant known temperature, while in nonisothermal method, the sample is subjected to a controlled rising temperature.

Many researchers used the isothermal [70, 73, 80, 81] method to calculate these kinetic parameters while some chose the non-isothermal method [82, 83]. One of the great advantages of the isothermal method is that changes in the apparent order of the reaction and the apparent activation energy in the reaction mechanisms are easily detectable [84]. In practice, a sample requires some time to reach experimental set temperature which experiences non-isothermal heating period. During this period, the sample undergoes unknown transformations that are likely affecting the final results. Non-isothermal method mitigates this problem that restricts the use of isothermal method at high temperature. The main drawback for non-isothermal conditions, as described in the literature for various analysis methods, such as differential ones ($\frac{d\alpha}{dt}$ values need conveniently obtain data of Derivative Thermogravimetric Analysis) [85], integral (equation 2.2 is integrated without an analytical solution to handle TGA data) [86], the kinetic parameters were found to be slightly different from method to method for the same polymer under the same conditions [87].

A model-free approach based on the principle of reaction rate at a constant extent of conversion is only a function of temperature is called isoconversional methods. It requires multiple experiments conducted at different heating rates [88, 89]. From this method, if the reaction rate is not too high, activation energy, which obviously corresponds to a given extent of conversion can be estimated model-independently by assuming that the extent of conversion does not vary during the temperature jump. These are multiple issues using isoconversional methods and one of those, as Agrawal [90] pointed, is no identical effective conversion value could be estimated due to the fact that no unique overall conversion for the individual reactions

exists in some complex multi-step reactions at various of heating rates. In fact, it was called “model-free” because E could be estimated independent of the reaction order. However, to get the complete set of Arrhenius parameters, A cannot be estimated if no value is assigned for the reaction order. Therefore, Arrhenius parameters cannot thus be used for elucidation of the reaction mechanism, nor for predicting the thermal behaviour of the polymer in both isothermic and other non-isothermic conditions [91, 92].

When polymers undergo thermal decomposition, it also involves obvious energy absorption or release in addition to gaseous volatiles generation. The total energy that gasifies the solid material per unit mass from room temperature is quantified by a value termed as heat of gasification (h_g). h_g can be defined:

$$h_g = \int_{T_0}^{T_p} c(T)dT + \Delta h_m + \Delta h_d + \Delta h_v \quad (2.5)$$

The four terms on the right-hand side of Equation 2.5 represent the four thermal and chemical processes that occur for a solid material gasification as the temperature rises: sensible enthalpy changes [$c(T)$ is temperature-dependent heat capacity], heat of melting for material that melts at T_{melting} ($T_0 < T_{\text{melting}} < T_p$), heat of decomposition and heat of vaporization. Usually for most polymeric materials, Δh_d accounts for the energy that is required by the polymer molecule to break into smaller fragments during thermal decomposition process and equals to the chemical bonds dissociation energy. Δh_v is the amount of heat required to subsequently vaporize the decomposition products from the condensed phase to the gas phase. For material flammability research, h_g is an important parameter that affects the material burning

rate and it has been measured and tabulated for a number of materials [33, 93]. More than one reasons have been found that the h_g for the same material is not technically constant from many researchers' measurements. The first parameter that affects the h_g calculation is T_p , the pyrolysis temperature where the volatilization occurs. Most solid materials do not instantaneously volatilize completely at a fixed T_p , but are finite temperature ranges near T_p . In principle, the heating rate does affect the h_g because the temperature range at which the degradation takes place shifts to higher values with an increasing rate of heating. As a consequence, the solid (or molten) polymer is heated to a higher temperature before it degrades. The details discussed for the heating rate effect can be found in Chapter 5.

Besides A , E and c_p , there is a list of parameters that affect the material flammability and heat and mass transfer, such as density, emissivity, absorption coefficient and thermal conductivity. Usually measurements for those properties are carried out and the values are tabulated at room temperature [94]. Most of these properties are temperature-dependent properties but the knowledge of the data from the room temperature to the material pyrolysis temperature is limited. With the development of science and technology in polymer research, researchers are able to measure these temperature-dependent properties for polymers. For example, most polymer properties handbooks such as the one recently updated [1] list the volumetric changes during heating, and this value can be up to 20 % from room temperature and ignition temperature. Temperature-dependent values for polymer specific heat capacities were also studied by a number of researchers [71, 95-99]. For example,

Henderson [99] measured specific heat of virgin and decomposed polymer composites between temperatures of 333 to 1003 K.

Thermal conductivities for polymers were measured by groups of researchers but they are still scattered throughout the literature and little to no information is available for various polymers at different temperatures. Most studies were focused on PMMA measurements at room temperature [100-102] and seldom go beyond 300 K and up to 600 K [71, 77, 103]. Zhang and his coworkers [104, 105] made careful thermal conductivity measurements for a number of common polymers such as PE, Polystyrene (PS), PP and PC (Polycarbonate). Due to the lack of experimental data and difficulties associated with accurate measurements of polymer thermal conductivity at higher temperatures when melting or decomposition in present, crude approximations were often used in the past for many polymers that including composites.

Changes in above parameters will affect the material heat release rate or burning rate curve, which is an important output of the fire models that used in the research and engineering applications. While the fundamental physical and chemical processes can be well explained and calculated by the mass and energy conservation equations in the state of art fire modeling tools, for instance NIST Fire Dynamics Simulator (FDS), accurate prediction of the heat release rate or mass lose rate requires good input data with physical-meaningful parameters. It is hard to measure or obtain all the properties precisely; however, knowing which parameters dominate the overall process of solid material burning is the key to improve prediction. Researchers in the past few years examined the effect of variations in the polymer properties on the

polymer burning behaviors [106-109] to gain better knowledge about the importance of each property. The key finding from these sensitivity analysis studies leads the conclusion that the knowledge of the kinetics (defined by the Arrhenius pre-exponential factor and activation energy to resemble the rate of decomposition), heat of decomposition and char yield is crucial for predicting the peak and average heat release rate. Other properties such as density, heat capacity, thermal conductivity and optical properties are less important and can be estimated from the mean of various literature.

Section 2.3 Research motivation and overview

To better understand how chemical and physical phenomena such as phase transitions, chemical reactions, heat transfer and mass diffusion interact to give rise to gaseous fuel generation, a number of numerical pyrolysis models have been developed. The solid phase submodel in the FDS [65], ThermaKin [110], Gpyro [68] and Pyropolis [67] are pyrolysis modeling computer codes that were developed during the last few years. These models require property values that describe the aforementioned chemical and physical phenomena as input and compute the rates of gaseous fuel generation by solid material objects exposed to external heat.

While some progress has been made in the development of experimental procedures for the measurement of these properties [11, 39, 40, 71, 98, 111-114], the accuracy, generality and robustness of these procedures clearly require further refinement. For example, several approaches to the property determination have been developed. Lautenberger and Fernandez-Pello [115] proposed using data from bench-scale fire tests as a target for property value optimization. They employed a genetic

algorithm to solve a multi-parameter optimization problem. Subsequently, Chaos and co-authors [116] advanced this methodology by using controlled pyrolysis experiments in a fire propagation apparatus [117] and performed property calculation using a more efficient, shuffled complex evolution optimization algorithm.

One of the main advantages of the optimization-based property evaluation is that a complete set of properties can be obtained from a relatively small number of standard bench-scale tests. The main drawback, according to Ghorbani et al. [118], is that the derived values may not represent true material properties. As a consequence, the parameterized model does not provide reliable predictions outside the range of conditions realized in the calibration experiments. Bal and Rein [119] argued that maintaining a consistent level of complexity for all modeled processes is highly important for minimization of uncertainties arising in the parameterization process.

Besides estimating these properties from the experiments with parameter optimization algorithms, an alternate way to access these fundamental properties is measuring the individual parameters with separate experimental devices and it was performed by a number of researchers [71, 111, 120-124]. The fact that many of the newly synthetic polymer fundamental properties are frequently unknown, it prevent us from using these models in fire safety applications. Besides, most of these material properties measurement methods dissimilated for a wide range of polymeric materials. The purpose of this work was to develop a systematic experimental procedure for the measurement and validation of the core subset of these properties including mass loss kinetics parameters, heat capacities, heats of melting, heats of decomposition reactions and heat transfer properties. This procedure is based on milligram-scale and

bench-scale approaches to isolate specific chemical and/or physical processes in each test so that each property can be systematically measured or calculated from the data analysis and interpretation. The wide range of scales and conditions in the modeling are validated against pyrolysis experiments to ensure that the property values reflect the fundamental aspects of material behavior. While inverse modeling is still employed for some property evaluations, the resulting optimization problems are always well-defined and the optimum values can be obtained in a few iterations.

To obtain polymer kinetics and thermodynamics at the milligram scale, thermogravimetric analysis (TGA) and differential scanning calorimetry (DSC) are among the most frequently used techniques employed for these types of measurements. The main advantage of these techniques is associated with the use of small material samples (3-10 mg) and relatively slow and steady heating rates (3-30 K min⁻¹) [125]. These heating conditions minimize the effects of heat and mass transport inside the sample on mass loss (in the case of TGA) and heat flow (in the case of DSC), which makes it possible to exclude the transport from data analysis and interpretation. In this study, both of these techniques were utilized to determine the aforementioned properties.

TGA experiments performed in an inert atmosphere were used to develop a reaction mechanism describing material volatilization upon heating. The mass loss data analysis was based on the assumption that a polymer degrades through consecutive first-order reactions. The parameters of these reactions were obtained by fitting a TGA curve with a numerical model capable of solving kinetic equations for an arbitrary user-defined reaction mechanism under linear heating conditions. This

approach differs significantly from that traditionally employed in the field of thermal analysis. In the traditional approach, as described in the section 2.2.2, solid degradation is described by a single n -th order reaction, whose activation energy may depend on the degree of conversion [126].

DSC is used routinely to measure heat capacities and heats of melting of polymeric solids [125]. In this dissertation, this technique was extended to anaerobic thermal degradation reactions for non-charring and charring polymers. Measurement of the heats of degradation is a challenging task because of instrumental baseline instabilities caused by volatile products [98] and the fact that both sensible and reaction heats contribute to the heat flow as the material's temperature is raised through degradation. Several research groups have attempted to perform these measurements with some degree of success [98, 114, 127]. The main distinguishing features of the current approach are that it employs a simultaneous thermal analysis (STA) instrument calibrated using the melting of organic and inorganic compounds (the advantages of this instrument and its calibration procedure are discussed below) and a unique DSC data analysis methodology. This methodology utilizes a TGA-derived kinetic mechanism to generate a sensible heat baseline for the reaction region of the DSC curve and yields a complete thermo-kinetic model (including heat capacity of the condensed-phase constituents, heat of melting and heats of decomposition) that reproduces both TGA and DSC experiments.

Then our approach is extended to a larger (bench) scale to measure material gravimetric and thermal changes during thermal decomposition in an anaerobic atmosphere with a capability of analyzing material thermal transport properties. In

this work, standard cone calorimetry tests [128] (without the part of analyzing exhaust gas) were modified to enable inert atmosphere, radiation-driven gasification under thoroughly controlled, near-one-dimensional heating conditions similar to those realized in a fire propagation apparatus [117] or a NIST gasification device [37]. Heat transfer through a solid was monitored in two different methods: placing thermocouples and focusing an infrared camera on the bottom surface of a horizontally-mounted sample, of which the top surface faced the cone heater. The advantage of using the non-contact nature of infrared camera measurement made it possible to collect both sample mass and temperature data simultaneously, which reduced the number of bench-scale experiments by a factor of two. Spatial resolution of the temperature data (collected only using the infrared camera) made it possible to assess the validity of the one-dimensional thermal transport assumption always invoked during analysis of this type of experiments. Therefore, the thermal transport properties of materials can be calculated. These properties, combining with material kinetics and thermodynamics obtained from the milligram scale, serve as inputs for the parameterized model with simulating one-dimensional pyrolysis. The resulting models were employed to predict the gasification burning rate histories at 20-90 kW m⁻² of external radiant heat flux, which almost cover the most frequently conditions that are used in the general room fire modeling. The simulation results are then validated against the experimental burning rate histories at various levels of heat fluxes.

This overall parameterization methodology is expected to minimize possible compensation errors and extend the scope of the model validity; however as a trade-

off, it requires a notably larger number and broader range of experimental measurements with respect to other standalone tests such as NIST gasification and FPA tests.

This main achievement for dissertation is the development of a systematic methodology for parameterization of continuum pyrolysis models for polymeric material at multi-scale levels. The accurate measurements of material kinetics, thermodynamics and thermal transfer properties at wide range of scales and conditions ensure that the property values reflect the fundamental aspects of material behavior. Validation work was also performed against other numerical modeling solvers to guarantee the measurements are not model-specific either. This methodology covers the most promising (from the fire safety prospective) and most complex class of combustible materials—charring and intumescent polymers and even potentially for composites materials in the market.

Chapter 3 Experimental

Section 3.1 Materials and sample preparation

The polymers examined in this study are seven representative non-charring materials: poly(oxymethylene) (POM), poly(methyl methacrylate) (PMMA), high-impact polystyrene (HIPS), polyamide 6,6 (PA 66), polypropylene (PP), poly(lactic acid) (PLA), and poly(acrylonitrile butadiene styrene) (ABS) and eight charring polymeric materials which produce a significant amount of carbon rich residues during their thermal degradation process: poly(methyl methacrylate)-poly(vinyl chloride) alloy (Kydex), polymerized diglycidylether of bisphenol A (DGEBA), poly(ethylene terephthalate) (PET), poly(paraphenylene terephthalamide) (Kevlar), polymerized bisphenol A cyanate ester (BACY), poly(phenylene sulfide) (PPS), polyetherimide (PEI) and poly(ether ether ketone) (PEEK). The materials were classified as non-charring because the residual mass obtained as a result of heating milligram-sized samples from room temperature to 873 K in an anaerobic environment was found to be below 10 wt.%. The char yield produced by charring polymers anaerobic pyrolysis heated from room temperature to 1223 K varied between 11 and 51 wt.%.

With the exception of PLA, all non-charring polymers were supplied in the form of large (approximately 1220×610 mm), extruded sheets, which were about 6 mm thick. PLA sheets were 0.7 mm thick. Detailed information on the material origins is summarized in Table 3-1. For charring polymers, Kydex, PET, PPS, PEI and PEEK were purchased in large, extruded sheets (approximately 1220×610×6.4 mm in size). Kevlar was purchased in the form of woven fabric

samples (150×100×0.2 mm). DGEBA and BACY were prepared in our laboratory by curing manufacturer supplied resins in a square mold (80×80×6.4 mm). 1-2 wt.% of 2-ethyl-4-methylimidazole was added to DGEBA resin to promote curing. No curing agent was used for BACY. DGEBA and BACY specimens were cured in a convection oven. In the case of DGEBA, the oven temperature was increased from 293 to 393 K in 50 K increments and was held constant for 4 hours after each increase. In the case of BACY, the oven temperature was increased from 293 to 523 K using the same incremental approach. Detailed information on the source of purchased materials is provided in Table 3-1.

Table 3-1 Source of materials analyzed in this study.

Polymer	Manufacturer	Trade Name	Distributor
Poly(oxymethylene) (POM)	Ensinger	Acetal	Curbell Plastics, Inc.
Poly(methyl methacrylate) (PMMA)	CYRO Industries	Acrylic	Evonik Industries
High Impact Polystyrene (HIPS)	Spartech Plastics	HIPS	Professional Plastics
Polyamide 6,6 (PA 66)	Quadrant EPP	Nylon 101	Modern Plastics
Polypropylene (PP)	Compression Polymers Corp.	Protec HPP	U.S. Plastic Corp.
Poly(lactic acid) (PLA)	NatureWorks	PLA Rejuven8 Plus	Spartech
Poly(acrylonitrile butadiene styrene) (ABS)	Westlake Plastics	Absylux	Modern Plastics
Poly(methyl methacrylate)-poly(vinyl chloride) alloy (Kydex)	Kydex, LLC	Kydex [®] T	Professional Plastics
Diglycidylether of bisphenol A	Sigma	Bisphenol A diglycidyl ether	Sigma-Aldrich

Poly(ethylene terephthalate) (PET)	Ensinger	PET	Curbell Plastics
Poly(paraphenylene terephthalamide) (Kevlar)	DuPont	Kevlar [®] Plain Weave Fabric	Fibre Glast Developments
Bisphenol A cyanate ester	Lonza	Primaset Cyanate Esters	Lonza
Poly(phenylene sulfide) (PPS)	Ensinger	PPS	Curbell Plastics
Polyetherimide (PEI)	GE Plastics	Ultem 1000	Curbell Plastics
Poly(ether ether ketone) (PEEK)	Victrex plc	PEEK grade 450G	Victrex plc

Thermal analysis samples for milligram-scale test were prepared by cutting polymer specimens into thin, flat squares, less than 0.5 mm in thickness and 4 to 7 mg in mass. Bench-scale samples were prepared by cutting squares (80×80 mm) (the thickness and density for different polymers varies, and they were measured using a caliper and a balance at the room temperature the details are discussed in the Chapter 7 and Chapter 8) from the supplied sheets. The sample mass is about 40 to 60 g for a single square. These samples were conditioned in a desiccator in the presence of Drierite for a minimum of 48 hours prior to testing to minimize their moisture.

Section 3.2 Milligram-scale testing

Section 3.2.1 Milligram-scale testing on non-charring polymers

A Netzsch F3 Jupiter STA was employed in this study. This apparatus combines a TGA instrument equipped with 1 µg-resolution microbalance and a heat flux DSC implemented using a Netzsch TGA-DSC sample carrier. Stoliarov's [98] previous DSC-based decomposition heat measurements indicated that significant heat flow errors may result from a relatively low temperature of the enclosure containing

sample and reference containers (due to deposition of volatiles on the cold walls and consequent changes in the heat transfer characteristics of the enclosure). In the current apparatus, which was selected to mitigate this problem, the containers were positioned in the middle of a long (26 cm), vertical, uniformly heated furnace (as shown in Figure 3.1), which wall temperature exceeded that of the containers throughout the heating process. More information on the design of the F3 Jupiter STA can be found elsewhere [129].

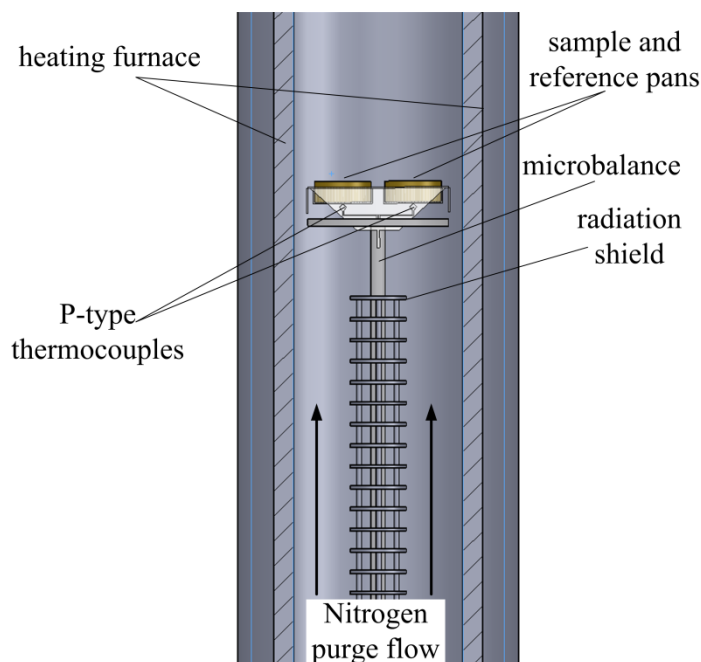


Figure 3.1 Sketch of heating furnace and sample carrier.

An anaerobic environment was created inside the furnace by continuously purging it with nitrogen at a rate of $50 \text{ cm}^3 \text{ min}^{-1}$. Most TGA and DSC experiments were conducted using the same heating program. A sample was first heated to 313 K and maintained at this temperature for 25 min. This period was included to ensure that the system is initially in thermal equilibrium and free of oxygen. Subsequently, the sample was heated to 873 K at a heating rate of 10 K min^{-1} . The mass and heat

flow data were collected only during the second, linear heating phase of the test. The selection of the heating rate was based on a recent theoretical analysis [130] that indicated that using 10 K min^{-1} for $<10 \text{ mg}$ samples insures a uniform temperature inside the sample even when the heat associated with decomposition processes is significant. The experiments carried on this heating rate were repeated 7 times and averaged prior to analysis (details are explained in the section 3.2.3). Additional TGA experiments were performed at 30 K min^{-1} . These experiments were used to evaluate how well the kinetic model developed using 10 K min^{-1} data performs at higher heating rates. The high (30 K min^{-1}) heating rate TGA experiments were only repeated 3 times (and averaged prior to analysis).

Each material test was preceded by a baseline test, where empty sample and reference containers were subjected to the same heating program. The baseline mass (in the case of TGA) or heat flow history (in the case of DSC) was subtracted from the corresponding data obtained from the sample test. All TGA and DSC data presented below have been baseline corrected.

While the instrument used in this study is capable of simultaneous TGA and DSC, these experiments were conducted separately only for non-charring polymers. It was initially assumed that accurate TGA readings require a well-ventilated sample container. Therefore, all TGA tests for non-charring polymers were performed using open ceramic pans. DSC tests were performed using Platinum-Rhodium pans with lids. The lids had small (0.25mm in diameter) orifice for ventilation. This container configuration was used to maximize the thermal contact between a degrading sample and heat flow sensing thermocouple located underneath the container. Subsequent

comparison of the mass loss data collected with both configurations showed that the presence of a lid had no significant impact on the mass loss.

Section 3.2.2 Milligram-scale testing on charring polymers

Same anaerobic environment was created inside the furnace by continuously purging it with nitrogen at a rate of $50 \text{ cm}^3 \text{ min}^{-1}$ as stated in non-charring polymer milligram-scale testing. TGA and DSC experiments were conducted simultaneously using a somewhat different heating program compared to the program used for the non-charring polymer. One significant difference of the thermal treatment to the non-charring polymer is the sample was heated to higher temperature up to 1223 K at the same heating rate. Additional TGA experiments were also performed at 30 K min^{-1} .

All thermal analysis experiments for charring polymers were performed using Platinum-Rhodium crucibles with lids. TGA and DSC experiments on PPS were conducted only at 10 K min^{-1} and only 3 times because the gases evolved during the decomposition were found to be damaging to the STA's sample carrier. Additional DSC experiments were performed on char residue produced in the polymer thermal analysis experiments. These experiments were performed on 3-5 mg samples at 10 K min^{-1} and were repeated 3 times for char produced from each material. The char was compacted in the crucible prior to DSC to ensure a good thermal contact with crucible bottom.

Section 3.2.3 Instrument calibration and data collection for milligram-scale testing

The STA apparatus requires two types of calibration: temperature and sensitivity. The temperature calibration provides a relation between measured and

actual sample temperature. The sensitivity calibration provides a conversion between the difference in voltage generated by sample and reference thermocouples (P-type thermocouples were employed in this study, see Figure 3.1) and sample heat flow. For open ceramic pans (used in TGA experiments), temperature calibration was performed using known melting points of pure metals including indium, tin, bismuth, zinc and aluminum. These melting points span the temperature range between 430 K and 933 K. No sensitivity calibration was performed for these sample containers. For Platinum-Rhodium pans with lids (used in DSC experiments), temperature and sensitivity calibrations were performed using a set of organic and inorganic compounds with known melting points and heats of melting. This set included biphenyl, benzoic acid, RbNO_3 , KClO_4 , CsCl , AgSO_4 , K_2CrO_4 and BaCO_3 . The melting points of these compounds span the temperature range between 343 K and 1081 K. The calibrations were carried out following the STA manual recommendations [131, 132]. All calibration materials were supplied by Netzsch. 10 K min^{-1} heating rate and $50 \text{ cm}^3 \text{ min}^{-1}$ nitrogen purge flow were used in all calibration runs. The temperature and sensitivity calibrations were checked (by collecting data on 2-3 calibration substances) once a month. The instrument was completely recalibrated every six months.

The rationale behind choosing heat-of-melting-based sensitivity calibration was that the heat flow profile produced by the melting processes (a peak in time or temperature coordinate) was similar in shape to that of polymer decomposition. It was unclear, however, whether such calibration could be used to measure sensible heat (associated with heat capacity of a given polymer). To examine the ability of the

calibrated instrument to measure heat capacity, three DSC tests were performed on a disk (6 mm in diameter and 0.25 mm in thickness) of sapphire, which has a well-known heat capacity temperature dependence [133]. These measurements were carried out within 313-1000 K temperature range, where sapphire does not experience any physical or chemical transitions. The heat capacity was computed by dividing measured heat flow (in W) by sapphire mass (in g) and instantaneous heating rate (in K s^{-1}). The instantaneous heating rate was used instead of nominal (or set point) because it had a tendency to deviate notably from the set point (10 K min^{-1}) during the first 100 K of heating.

The resulting heat capacities are compared with the literature data [133] in Figure 3.2. The individual measurements show notable deviations. However, these deviations are not systematic. Averaging these measurements produces a heat capacity temperature dependence (also shown in Figure 3.2) that closely follows the literature curve (within 350-1000 K temperature range, the difference never exceeds 8%). From this analysis, it was concluded that it is possible to measure heat capacity using the current approach. However, multiple experiments were needed to obtain reliable information on sensible heat flow. Therefore, each material (except for PPS) heat flow curve analyzed below was obtained by averaging 7 DSC experiments. The same methodology was applied to mass loss data. In addition to improving accuracy, multiple experiments provided the data necessary for the calculation of uncertainties in the extracted properties.

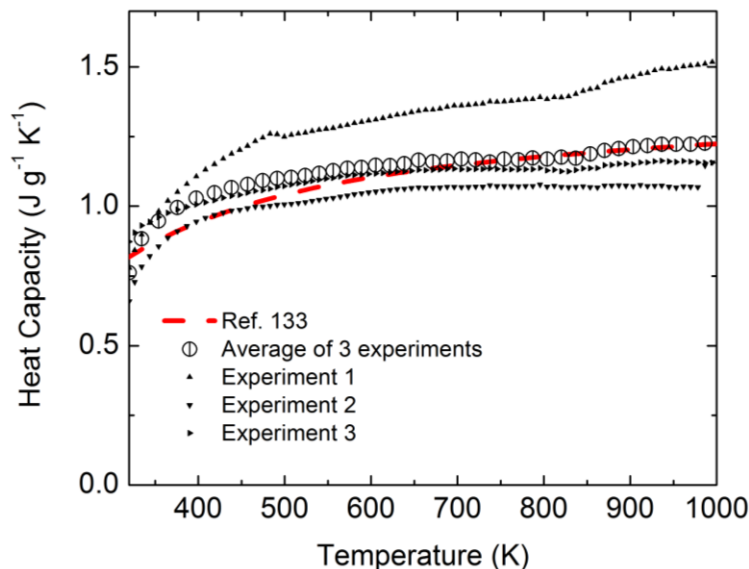


Figure 3.2 Heat capacity of sapphire.

Another important question related to calibration is whether the sensitivity remains stable in the presence of volatiles produced during decomposition. To examine this issue, three sapphire heat capacity measurements were performed in the presence of degrading PMMA. Each measurement consisted of two DSC tests. In the first test, a sample of PMMA was placed in the sample pan, while a sapphire disk was placed in the reference pan. In the second test, PMMA was placed in the sample pan, while the reference pan was kept empty. The heat flow obtained in the first test was normalized by the initial mass of PMMA and subtracted from the heat flow observed in the second test, which was also normalized by PMMA mass. The resulting difference was re-normalized by the mass of sapphire and divided by the nominal heating rate (10 K min^{-1}) to compute heat capacity. A comparison of the experimental results and literature data is shown in Figure 3.3. The heat capacity data obtained within PMMA degradation temperature range, 580-720 K, do show significant fluctuations. However, these fluctuations appear to be caused by instabilities in the

heating rate (no instantaneous heating rate normalization was performed for this data). On average, the sapphire heat capacity measured in the PMMA decomposition region falls within 3% of the literature data, which clearly indicates that the sensitivity calibration was not affected by the volatile decomposition products.

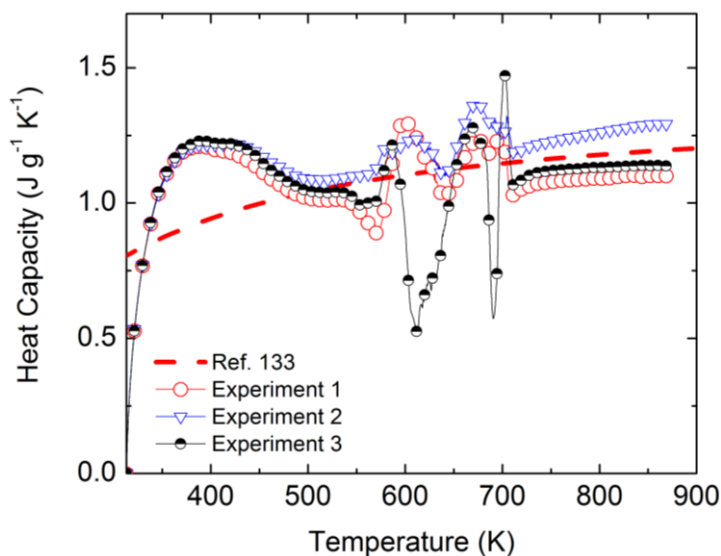


Figure 3.3 Heat capacity of sapphire in the presence of degrading PMMA.

Section 3.2.4 Scanning Electron Microscopy (SEM)

Char samples produced in the thermal analysis experiments were further examined with a Hitachi S3400 scanning electron microscope. The imaging was performed using 3 and 10 kV electrons. The purpose of this exercise was to determine whether there exist significant differences in the microscale topology of chars produced from different charring polymers.

Section 3.3 Bench-scale testing

Section 3.3.1 Measurement of absorption coefficients

A schematic of the experimental setup employed to estimate polymer broadband radiation absorption coefficients is shown in Figure 3.4. The experimental

procedure was similar to that outlined by Linteris *et al.* [134]. A slab of Kaowool PM with a cylindrical opening was used to collimate the radiation from the cone heater. The collimated radiation was sent through a polymer sample, which was milled locally down to thin polymer film. The thickness of the film is chosen 2 mm for non-charring polymers, while 1.5 mm for charring polymers. A water-cooled Schmidt-Boelter heat flux gauge located below the sample was used to detect the transmitted radiation. The film was exposed to about 35 kW m^{-2} of incident radiant heat. The data on transmitted radiation were collected for the first 20 s (for non-charring polymers) and 5 s (for charring polymers) after the beginning of exposure (to avoid contributions associated with conduction through the sample). Subsequently, the polymer sample was quickly removed after about 30 s of exposure and then the exact incident radiation was measured. An example of the heat flux measurement for this type of experiments is demonstrated in Figure 3.5.

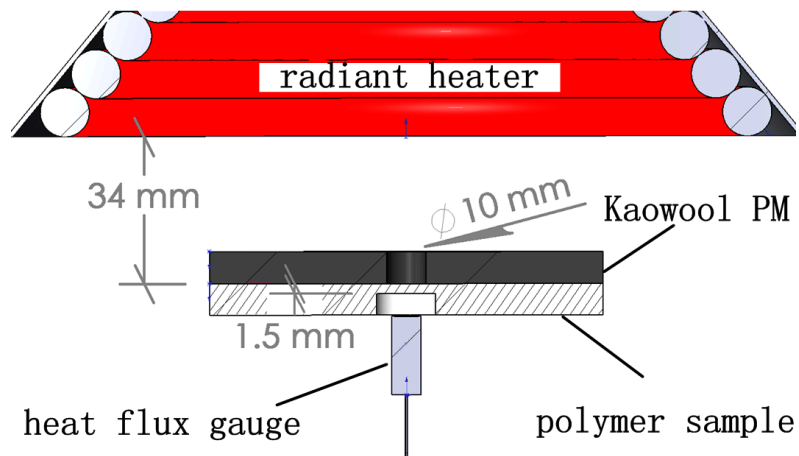


Figure 3.4 Radiation absorption coefficient measurement setup.

The radiative transport was assumed to be one-dimensional and insensitive to the variation in the spectral characteristics of the cone heater with heat flux. A Beer-Lambert-law-based expression (as shown in equation 3.1) taking into account

radiation reflection at the polymer-air interfaces, which was previously utilized by Tsilingiris [135], was used to compute the absorption coefficients. Where l is the polymer film thickness, f is reflection loss coefficient, and τ is spectral normal transmission. Broadband surface reflectivity of all polymers was estimated to be 0.05. The reflectivity value was computed from the index of refraction, which shows little variation among thermoplastics [134]. Only one transmission measurement for non-charring polymers and two transmission measurements for each charring materials were performed and the results were presented in Chapters 7 and 8.

$$\alpha = \frac{2\ln(1-f) - \ln \tau}{l} \quad (3.1)$$

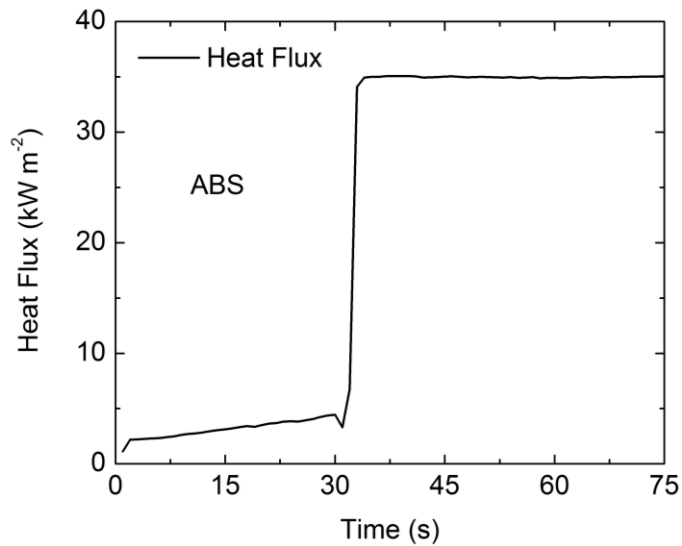


Figure 3.5 Heat flux result from ABS absorption coefficient measurement experiment.

Section 3.3.2 Gasification experiments part I

The goal of this section is aim to measure PMMA sample (80×80×6 mm) back surface temperature under gasification experiments using traditional method-thermocouple. The sample was gasified using controlled radiant heating. These

experiments were performed in a Govmark CC-1 cone calorimeter [136] equipped with the Controlled Atmosphere pyrolysis Apparatus (CAPA) [137] that was newly designed in our group. The cone calorimeter radiant heater was used to deliver a uniform and steady heat flux to the top surface of a horizontally mounted sample, while the calorimeter's precision balance system monitored sample mass loss. The CAPA (Figure 3.6) was used to provide a controlled gaseous environment in the immediate vicinity of the sample. The functionality of CAPA and NIST Gasification Device is comparable [37] but the size of CAPA is much smaller. As shown in this figure, CAPA consists of two concentric square metal ducts connected at the bottom and sits on top of the calorimeter's precision balance. Gas is introduced into the space between the ducts from the gas inlets in each of the four sides. The space above the gas inlets between the two ducts is filled with small (4.5 mm diameter) glass beads to ensure a uniform gas velocity. The upper edge of the inner duct is 10 mm below the top surface of the sample; the upper edge of the outer duct is 10 mm above the surface. The interior volume of the inner duct and sample holder each has a square cross section with sides measured 120 mm and 115 mm, respectively. The gap between these two is blocked by a lip installed on the sample holder (see Figure 3.6). The lip is located 1 mm above the upper edge of the inner duct, ensuring that the sample holder is suspended on the balance and does not make contact with the CAPA ducts to prevent mass measurement interference.

PMMA sample was mounted on a 25.4 mm thick layer of Kaowool PM thermal insulation, which has well-known thermophysical properties [138]. A 0.03 mm thick layer of aluminum foil was used to separate the bottom of the sample from

the insulation. The sample perimeter was wrapped with a 0.1 mm thick paper tape and thermally insulated with a 5 mm wide strip of Kaowool PM. This sample mounting procedure was found to maximize horizontal uniformity of the heating process while preserving the sample shape throughout gasification.

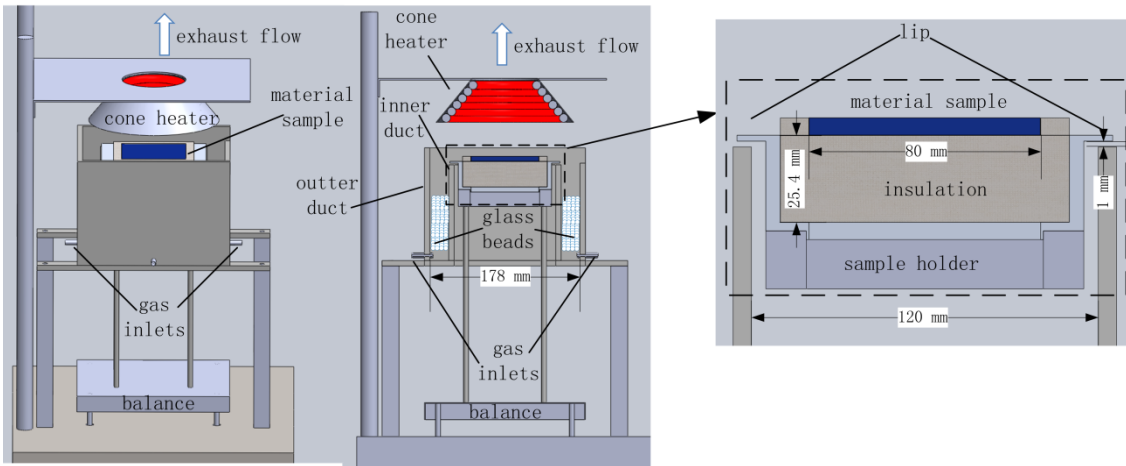


Figure 3.6. Schematic of the CAPA.

Mass loss rate measurements were repeated 3 times for each (20, 40, and 60 kW m^{-2}) radiant heat flux setting. In separate experiments, back surface temperature histories were measured three times each with samples exposed to 20 and 60 kW m^{-2} of radiant heat flux. Temperature measured at heat flux of 20 kW m^{-2} was used as a calibration target for PMMA thermal conductivity and temperature measured at heat flux of 60 kW m^{-2} was a reference for model validation. The temperature measurements were taken at three positions: at the sample's center and 28 mm diagonally inwards from two opposite corners. These measurements were performed using 0.25 mm diameter shielded type K thermocouples, which were placed beneath the aluminum foil and bonded to the foil with the Omega high temperature cement. Please note that, for this form of setup, only PMMA samples were tested.

In the experiments, the CAPA was operated at 225 L min^{-1} of nitrogen (measured at the standard ambient pressure of 100 kPa and temperature of 298 K) using ALICAT MCR series mass flow controller. The cone calorimeter exhaust flow rate was maintained at 1440 L min^{-1} . Under these conditions, oxygen concentration, measured 1 mm above the top sample surface using a Servomex 4100 gas analyzer, was found to hold steady at $2.2 \pm 0.4 \text{ vol.}\%$. Thus an effectively anaerobic environment was used in both thermal analysis and gasification experiments to simulate the pyrolysis conditions experienced by PMMA covered by a continuous diffusion flame.

The top surface background gas temperature was measured as an average of temperatures at four locations that near the level of sample top surface in the middle between the ducts by using a thin (0.13 mm diameter) type K thermocouple. The background gas temperature was found to be changed linearly from 330 to 390 K as the radiant heat flux under the cone heater increased from 20 to 80 kW m^{-2} , as shown in Figure 3.7 (x is the heat flux value in kW m^{-2}).

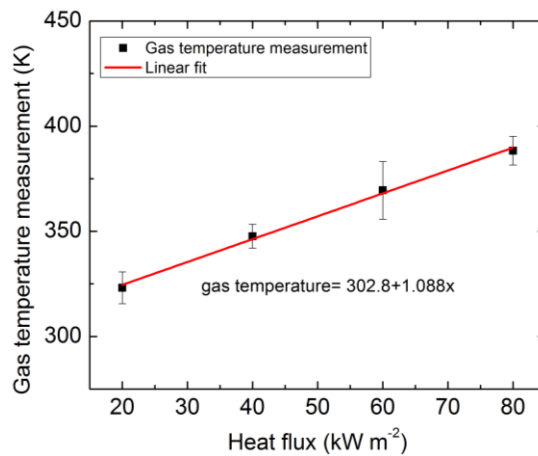


Figure 3.7 Top surface background temperature at different level of heat fluxes under cone heater.

The radiant heat flux was set using a water-cooled Schmidt-Boelter heat flux gauge, which was positioned at a location corresponding to the geometric center of the top sample surface. The variation of the heat flux across the surface was examined in an earlier study [139] and found to be within 3% of the center set point for the overwhelming majority of the surface area with the exception of the corners, which were within 10%. To quantify convective heat losses from the sample top surface in the CAPA, a 3 mm thick blackened (emissivity ≈ 0.95) copper plate of same sample dimensions was placed into CAPA instead of a sample. The plate was equipped with two imbedded type K thermocouples (0.25 mm in diameter). Insulation (80×80×25.4mm) was placed underneath the copper plate to provide same boundary conditions that applied to the PMMA gasification tests. Temperature measurements of the copper plate were conducted at incident radiant heat flux of 40 kW m^{-2} and the mean of the two thermocouples' readings is shown in Figure 3.8. A one dimensional pyrolysis model named ThermaKin (details can be found in Chapter 4) was utilized for reverse modeling to determine the convection coefficient, which was the only unclear parameter in this simulation. The convection coefficient on the top boundary was varied until the temperature of copper in the simulation result fits the experimental result. As the results shown in Figure 3.8, it was found that by setting a convection coefficient of $5 \text{ W m}^{-2} \text{ K}^{-1}$ the model fits the experimental results well. It was expected that the copper temperature model prediction is slight above experimental results. Because the copper top surface black paint was observed starting decomposing at high temperature ($> 600 \text{ K}$) and then the copper plate surface emissivity is likely below 0.95, while this value keeps constant in the simulation.

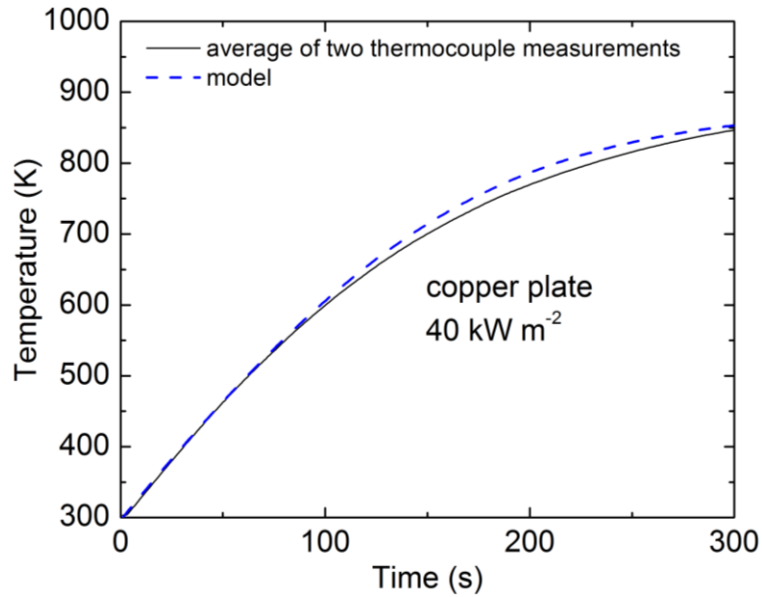


Figure 3.8 Copper plate temperature measurements in CAPA and model simulation at external heat flux of 40 kW m^{-2} .

Section 3.3.3 Gasification experiments part II

The CAPA sample holder, which detailed description is given in the earlier section 3.3.2, was modified to make it possible to focus an infrared camera on the bottom sample surface. A schematic of the modified CAPA is shown in Figure 3.9. The sample was placed on a 0.03 mm thick sheet of aluminum foil supported by a 0.8 mm thick aluminum mesh. The aluminum foil and mesh were coated with a high emissivity (≈ 0.95) paint.

A gold-coated, flat mirror (0.97 reflectivity in 0.8-10 μm range) was mounted about 10 cm below the sample to provide optical access for an infrared camera. The camera, FLIR E40, was mounted outside of the CAPA and focused on the aluminum foil supporting the sample bottom. The temperature readings were taken through the spacing in the aluminum mesh, which covered about 20% of the bottom sample surface. The camera was set for the paint emissivity. This novel solution to measure

the sample bottom temperature is aim to provide non-contact, spatially-resolved thermometry. The advantages of this solution combined with CAPA in polymer gasification experiments are the followings. As mentioned in the section 3.3.2, bottom temperature using thermocouples and mass loss rate are taken separately because of the sensitivity of the balance is greatly affectedly by the thermocouple wires. In the modified setup, this issue is solved because of using non-contact measurement by IR camera which reduced the number of bench-scale experiments by a factor two. In the meanwhile, since material gravimetric and thermal changes during gasification were recorded simultaneously, this type of experimental setup provides more reliable data because two types of measurements (temperature and mass) are obtained from exactly same experiments.

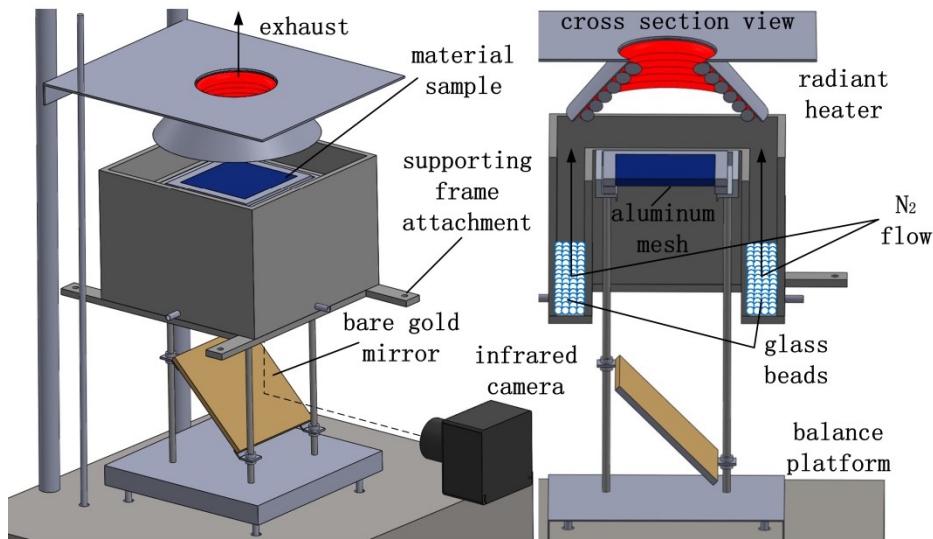


Figure 3.9 Schematic of modified controlled atmosphere pyrolysis apparatus.

To ensure that the camera provides accurate measurements, two steps of validation experiments were conducted. Firstly, a sample was replaced with a 3.0 mm thick copper plate coated with the high emissivity paint and equipped with 2 type K thermocouple probes (0.25 mm in diameter), which were embedded into the plate.

The plate was placed on the aluminum mesh and subjected to 40 kW m^{-2} of radiant heat flux. As shown in Figure 3.10, the IR camera temperatures were found to be within 5 K of those measured by the thermocouples up to the point where the plate temperature rose to 650 K. Above 650 K, a larger systematic difference of about 10 K was observed. This difference was attributed to a reduction in the emissivity of the paint (due to its partial degradation). In the second step, this experiment was repeated at 30 kW m^{-2} and the copper plate was replaced by a HIPS sample ($80 \times 80 \times 6.0 \text{ mm}$) which bottom surface was wrapped with the blackened aluminum foil. Two 0.25 mm diameter shielded type K thermocouples (0.13 mm in diameter), which were placed between the aluminum foil and HIPS bottom surface (at the sample's center and 28 mm diagonally inwards from one arbitrary corner) bonded to the foil with the Omega high temperature cement. The comparison of temperature measurements results using these two different methods shown on Figure 3.11 suggests that this experimental setup produces essentially identical results to the method using thermocouples.

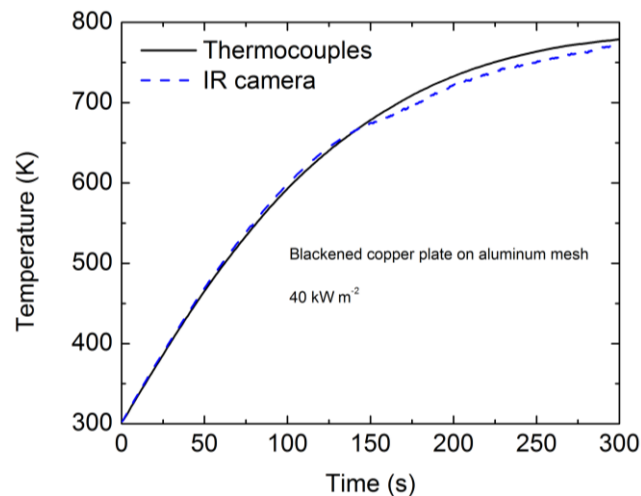


Figure 3.10 Comparison of temperature measurements using thermocouples and IR camera for blackened copper plate at radiative heat flux of 40 kW m^{-2} .

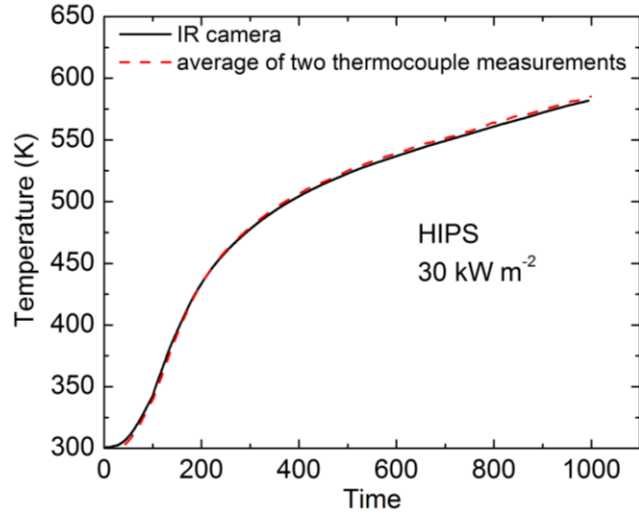


Figure 3.11 Comparison of temperature measurements using thermocouples and IR camera for HIPS with blackened aluminum foil on its bottom at radiative heat flux of 30kW m^{-2} .

As described in the section 3.3.2, convective heat losses from the top sample surface corresponding to the current flow conditions were determined using an inverse modeling of copper plate heating experiments. These losses were found to be well represented by a convection coefficient of $5\text{ W m}^{-2}\text{ K}^{-1}$ and background gas temperature that changed linearly from 330 to 390 K as the radiant heat flux increased from 20 to 80 kW m^{-2} . Convective loss from the bottom surface was characterized using a similar procedure as described in the section 3.3.2. One major change to the previous procedure is that, instead of using thermocouple to measure the copper plate temperature, IR camera was utilized to provide non-contact measurements. Both top and bottom surfaces of the copper plate were painted black with an emissivity of 0.95. Background temperature for the sample bottom surface was measured by a type K thermocouple (0.13 mm in diameter) at four locations near the bottom part of the CAPA inner duct wall and the mean value was found to be kept constant at 310 K at

various levels of heat fluxes. This background temperature is considered to provide approximate additional 0.5 kW m^{-2} radiation toward the bottom surface radiation at background temperature of 310 K. Provided the top surface convective loss is well defined in the section 3.3.2, the only unknown parameter is the bottom surface convection coefficient. The copper temperature measurements were performed under 20, 40 and 60 kW m^{-2} of incident radiant heat flux and the experimental and modeling results were shown in Figure 3.12. In all the simulations shown in Figure 3.12, the convective loss was found to be well represented by a convection coefficient of $4 \text{ W m}^{-2} \text{ K}^{-1}$.

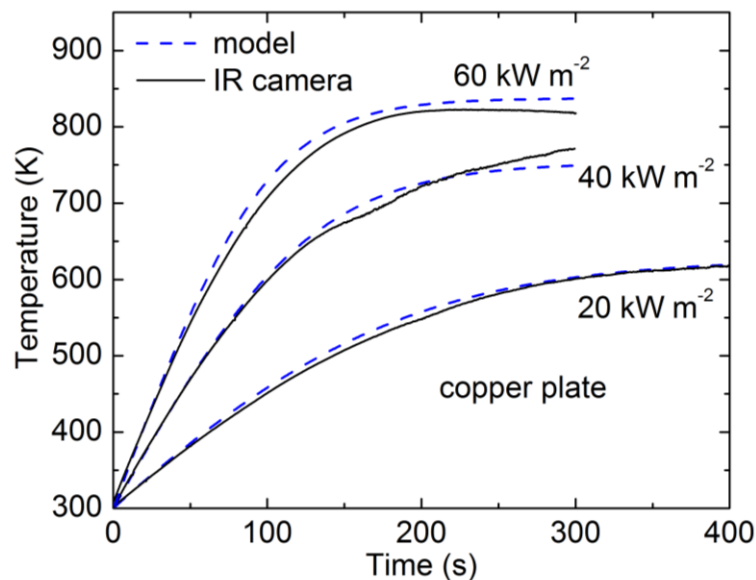


Figure 3.12 Copper plate bottom surface temperature measurements in CAPA using IR camera and model prediction at external heat flux of 20, 40 and 60 kW m^{-2} .

7 out of 15 non-charring and charring polymers were studied at this bench-level experiment. They are PMMA, POM, HIPS, ABS, PET, Kydex and PEI. Only for Kydex and PEI, since no dripping and melting occur, blackened aluminum foil was not used. However, the back of the samples were paint black (emissivity ≈ 0.95)

to obtain correct temperature measurements from IR camera. Most polymer gasification experiments were performed either at radiant heat fluxes of 20, 40, and 60 kW m⁻² or 30, 50 and 70 kW m⁻² (for PET, radiant heat fluxes were set to 50 and 70 kW m⁻²; for PEI, radiant heat fluxes were set to 50, 70 and 90 kW m⁻²). Each experiment was repeated 3 times to accumulate statistics.

As mentioned earlier in the Chapter 1, besides thermal decomposition, some charring solid polymers experience morphological changes including formation of residue layer (char), bubbles and fissures and melt flow that affect the thermal transport during polymer burning. Sometimes, the charred layer generated during thermal decomposition formed into mushroom-like intumescent structure. This intumescent structure was only observed obviously for Kydex and PEI in this study which needs analyzing specially. A video camera that intends to record the morphological visible change during the polymer gasification through a 6 mm thick quartz plate is placed at one side of the CAPA. The overall thicknesses of ABS, PET, Kydex and PEI samples at 50 kW m⁻² were measured from the video data by comparing an inert reference. The overall thicknesses for those polymers were determined from the top surface maximum level to their bottom.

For additional information, the incident radiative heat fluxes at various level of locations above the sample top surface were measured using a water-cooled Schmidt-Boelter heat flux gauge. The heat fluxes at the locations where sample top surface locates in the CAPA were initially set from 30 to 90 kW m⁻², and then the heat flux gauge was used to measure the heat flux at the elevated levels to resemble the phenomenon that the polymers' (such as Kydex and PEI) top surfaces were

observed swelling and expanding during gasification experiments. Five locations were randomly selected to cover the entire area size of 80×80 mm in each horizontal level. The mean value (dot) from this measurement against the distance (height) from the elevated location to the bottom of the sample surface is plotted in Figure 3.13. In this figure, linear fits (lines) for all conditions are also provided. The overall thickness changes of the polymers were recorded in time and the heat flux changes on top of the sample surface in time could be estimated by using the results in Figure 3.13.

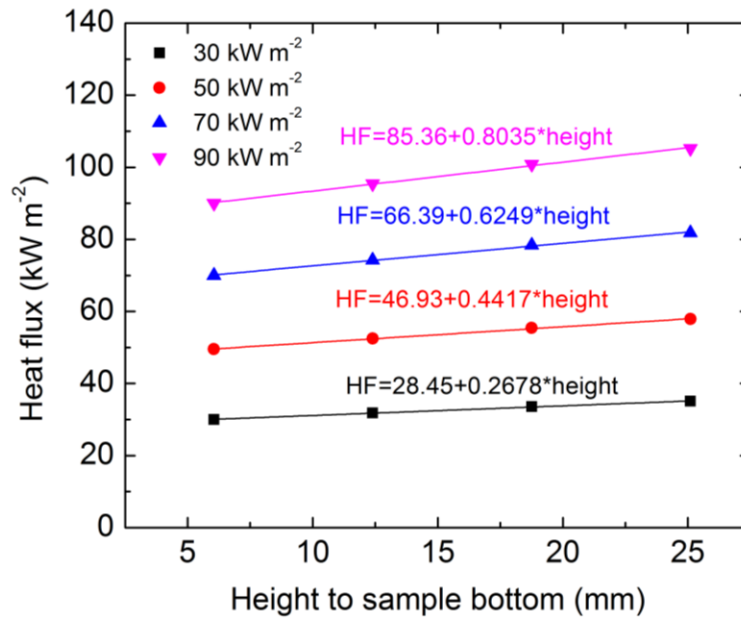


Figure 3.13 Heat flux at various level of locations.

Chapter 4 : Modeling

This chapter aims to provide a brief introduction for a flexible computational numerical solver named ThermaKin which is utilized in this study for the data analysis, interpretation and validation. ThermaKin computes the transient rate of gaseous fuel production from a pyrolyzing solid subjected to external (convective and/or radiative) heat. ThermaKin is capable to handle one- or two- dimensional object but in this study, only one one-dimensional mode was used. In this model, materials or computational objects are physically defined as a homogenous object or composites which consisting of layers of varying thickness. The material of the object is represented by a mixture of components, which may interact chemically and physically. The components are assigned individual temperature-dependent properties and categorized as solids or gases. The reaction mechanism in ThermaKin can be defined as in parallel or series of up to 30 zeroth to second order reactions. The model framework and model setup are also explained in this chapter. The detail description of ThermaKin can be found in FAA technical note [110]. ThermaKin has been validated by a number of researchers at various levels of scales in the last few years including myself [39, 71, 77, 79, 107, 109, 111, 140, 141].

Section 4.1 ThermaKin framework

In this study, ThermaKin (thermally thin mode) was employed to analyze TGA and DSC experiments and obtain a parametric description of the kinetics and thermodynamics of polymer degradation. Besides, ThermaKin (thermally thick mode) was also used to validate the final parameterized model against the gasification experiments. The key governing equations are summarized as follows:

$$\frac{\partial \xi_j}{\partial t} = \sum_{i=1}^{N_r} \theta_i^j r_i - \frac{\partial J_j}{\partial x} + \frac{\partial}{\partial x} \left(\xi_j \int_0^x \frac{1}{\rho} \frac{\partial \rho}{\partial t} dx \right) \quad (4.1)$$

$$\sum_{j=1}^N \xi_j c_j \frac{\partial T}{\partial t} = - \sum_{i=1}^{N_r} h_i r_i - \frac{\partial q}{\partial x} - \frac{\partial I_{ex}}{\partial x} + \frac{\partial I_{rr}}{\partial x} - \sum_{g=1}^{N_g} c_g J_g \frac{\partial T}{\partial x} + c \rho \frac{\partial T}{\partial x} \int_0^x \frac{1}{\rho} \frac{\partial \rho}{\partial t} dx \quad (4.2)$$

$$r_i = A_i \exp\left(-\frac{E_i}{RT}\right) \xi_k \xi_l \quad (4.3)$$

$$J_g = -\rho_g \lambda \frac{\partial (\xi_g / \rho_g)}{\partial x} \quad (4.4)$$

$$q = -k \frac{\partial T}{\partial x} \quad (4.5)$$

$$\frac{\partial I_{ex}}{\partial x} = -I_{ex} \sum_{j=1}^N \alpha_j \xi_j \quad (4.6)$$

$$\frac{\partial I_{rr}}{\partial x} = \frac{\sigma T^4}{I_{ex}^0} \frac{\partial I_{ex}}{\partial x} \quad (4.7)$$

Equation 4.1 is component j mass conservation statement formulated in terms of this component's concentration, ξ_j . This statement accounts for component consumption/production in chemical reactions, the rate of which is defined by Equation 4.3, gas flow within the solid, the flux of which is defined by Equation 4.4 (only gaseous components are considered to be mobile), and mass transfer associated with contraction/expansion of the material object (the last term in Equation 4.1). Equation 4.2 is the energy balance formulated in terms of temperature, T . This balance includes heat produced in chemical reactions, heat transfer due to conduction, the flux of which is given by Equation 4.5, radiative heat from an external source, the absorption of which is defined by Equation 4.6, re-radiation of energy to the environment defined by Equation 4.7, and convection associated with gaseous

component flow (the fifth right-hand-side term in Equation 4.2) and overall material expansion/contraction (the last term in Equation 4.2).

The symbols in Equations 4.1-4.7 are defined as follows. t is time; θ is a stoichiometric coefficient, which is negative when the corresponding component is a reactant and positive when it is a product; x is the Cartesian coordinate. ρ and c are density and heat capacity. h is the heat of reaction; A and E are the Arrhenius parameters; and R is the molar gas constant. λ , k and α are gas transfer, thermal conductivity, and radiation absorption coefficients. σ is the Stefan-Boltzmann constant; and I_{ex}^0 is the external radiation incident onto the object boundary. Properties without a subscript indicate the property of mixture (rather than that of an individual component). The density of mixture is defined as one over the sum of component mass fractions divided by the corresponding component densities. The volumetric contribution of gaseous components can be scaled by a user defined factor related to the local composition. A detailed description of ThermaKin can be found elsewhere [64, 110]

Section 4.2 Milligram-scale modeling

To model TGA and DSC experiments, one boundary of the one-dimensional object (representing a sample) was prescribed as external temperature history mimicking the experimental temperature program. The heat flux into the object was defined by the product of the convection coefficient and the difference between external and object surface temperatures. The value of the convection coefficient was set sufficiently high ($1 \times 10^5 \text{ W m}^{-2} \text{ K}^{-1}$) for the object surface to follow the external

temperature closely (within ≈ 0.1 K). The other boundary was defined to be impenetrable to heat flow. All polymers and its condensed-phase decomposition products were assumed to have the same density of 1 g cm^{-3} and thermal conductivity of $0.3 \text{ W m}^{-1} \text{ K}^{-1}$. This setup was used only in the milligram scale modeling to allow ThermaKin calculating the physical and chemical equations functionally (with no strange outputs) and minimize the temperature gradient inside the condensed phase object. The initial thickness of the object was selected to be 0.01 mm (thermally thin mode). This thickness selection insured that, throughout the heating process, the object temperature was uniform and defined by the external temperature program. Gaseous decomposition products were specified to leave the condensed phase upon formation. In essence, this model was set up to represent idealized TGA and DSC experiments where heat and mass transport were infinitely fast.

For simplicity, all considered reaction mechanisms were limited to a series of consecutive first order reactions (the concentration of the second, l 's, component in Equation 4.3 was always set to unity). All calculations for milligram-scale were performed using 0.001 mm element size and 0.005 s time step. Increasing or reducing these integration parameters by a factor of 2 did not produce significant changes in the results.

Section 4.3 Bench-scale modeling

The models of bench-scale tests included transient heat transfer inside the material. Heat was transferred to the material with a radiation boundary condition set to the external heat flux of the cone calorimeter tests. The gas transfer coefficient λ was set sufficiently high, $2 \times 10^{-5} \text{ m}^2 \text{ s}^{-1}$, for all material components and all

simulations to ensure that the fluxes of gases out of a material object were always equal to the rates of their production inside the object. This value corresponds to a reasonable upper bound, the average diffusivities of CO₂ and H₂O into air at 25°C [142]. In other words, the mass transport was assumed to be infinite fast and the gaseous decomposition products were specified to leave the condensed phase upon formation. All calculations on bench-scale were performed using 0.025 mm spatial discretization and 0.005 s time step. It was also examined that increasing or decreasing these integration parameters by a factor of 2 did not produce any significant changes in the results of the simulations indicating convergence of the numerical solutions.

Literature data [143] indicate that the densities of the thermoplastics have a weak temperature dependence. Densities and emissivities of all condensed-phase components (include intermediates and char) are assumed to be temperature-independent. For all the materials, those condensed-phase components properties were assumed to be equal to the corresponding polymer properties that measured at room temperature except for the intermediate components of PET, Kydex and PEI, residue of ABS, PET, Kydex and PEI. PET intermediate density is assumed to be the mean density value of the virgin material and its char residue. For Kydex and PEI, which produce significant amount of residues, their intermediate components densities for those two polymers are assigned to be equal to the corresponding polymer residues' densities. The densities calculation for those residues was explained in Chapter 8. Emissivity for those 4 polymers residues is estimated as 0.86, which is the value of the emissivity of graphite in the same temperature range when

char is formed [144], based on apparent high carbon content of degraded residues. All other condensed-phase components are assigned value of 0.95 from a recent work [134] that shows the little variation of reflectivity were found among thermoplastics. The reflectivity value was computed from the index of refraction [134] and assigned value of 0.05 for all the polymers in this dissertation for simplify.

Absorption coefficient (assumed temperature-independent also in m^{-1}) for of all condensed-phase components are assumed to be the same as it was measured in the experiment (section 3.3.1) to the corresponding virgin polymer properties except for the PEI and residue of HIPS, ABS , PET and Kydex. All the condensed-phase components in PEI pyrolysis were assumed to be optical opaque and non-transparent because from the experimental observation, PEI top blackened due to chemical decomposition and it varies by radiation intensity. For HIPS's residue, it is considered optical opaque too and absorption coefficient is defined infinitely high. For the other polymers that also produce char during bench-scale gasification experiments such as ABS, PET, Kydex and PEI, their char absorption coefficients are optimized with the char thermal conductivity during the inverse modeling process and summarized in Chapter 8. In general, less information on char absorption can be found, however, from the visual observation (details in Chapter 8), char is a semitransparent black pours object within absorption coefficient assumed to be in a range of 2500 to 10000 m^{-1} because of following reasons: for a normal semitransparent polymeric material, its absorption coefficient is usually around 2500 m^{-1} . If the value of absorption coefficient for an object is near 10000 m^{-1} , it is considered to be purely non-transparent. All these coefficients are expected to carry significant uncertainty (at

least 30%) and are dependent on the thickness of a sample used in the measurement [134]. However, as long as the measured values indicate that most of the radiation is absorbed within a relatively small (≈ 1 mm) thickness, as is the case here, the impact of these uncertainties on the overall heat transfer is negligible.

The heat capacity of all gaseous decomposition products was assumed to be equal to $1.8 \text{ kJ kg}^{-1} \text{ K}^{-1}$, which was the mean heat capacity of a series of C1-C8 hydrocarbons at 400-500 K [145]. The value of heat capacity had a minor impact on the simulation results because of the fast transport assumption implemented in the model.

Section 4.3.1 Modeling for gasification experiments part I

This part of experiment was simulated in transient heat transfer through PMMA samples with object dimensions defined as per Figure 4.1 and external boundary conditions matching those observed experimentally as discussed in section 3.3.2.

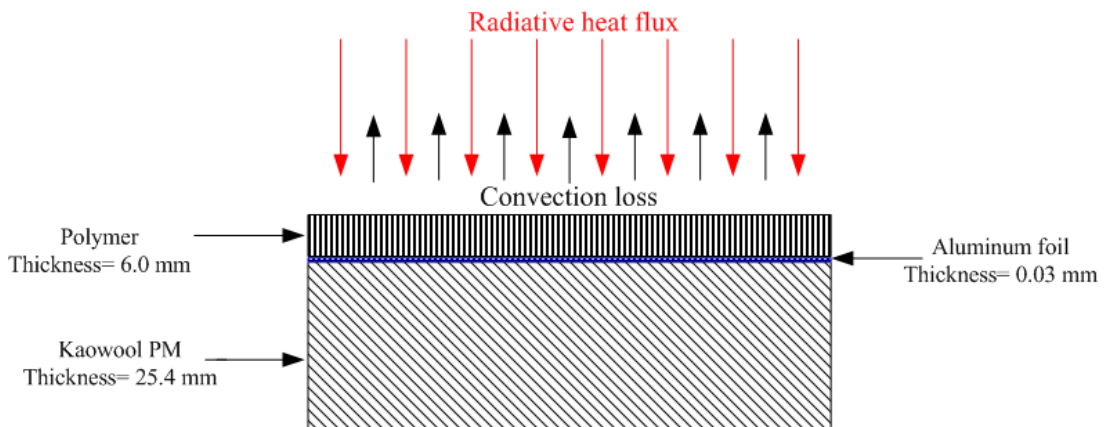


Figure 4.1 Schematic of virgin polymer sample defined in the model of bench-scale experiments when insulation is present.

The thermophysical properties for Kaowool and aluminum foil are well reported [146, 147] and summarized in Chapter 7.

Section 4.3.2 Gasification experiments part II

As explained in the section 3.3.3, gasification experiments part II has employed the IR camera to measure the sample bottom temperature instead of using thermocouples. Here the object schematic diagram dimensions and heat transfer used in the modeling is different from that used in the gasification experiments part I and is shown in Figure 4.2. The external top and bottom boundary conditions are set equal to which have been characterized in the section 3.3.3.

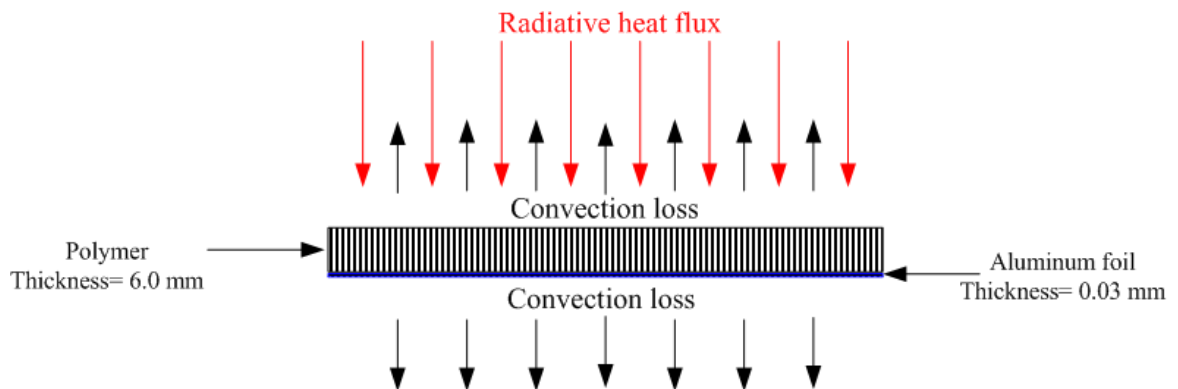
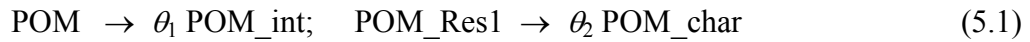


Figure 4.2 Schematic of virgin polymer sample defined in the model of bench-scale experiments part II.

Chapter 5 : Results- kinetics and thermodynamics for non-charring polymers

Section 5.1 TGA of POM

The results of 10 K min^{-1} TGA experiments performed on POM are shown in Figure 5.1. In this figure, sample mass (m) and mass loss rate (MLR) normalized by the initial mass (m_0) are plotted with respect to sample temperature. The MLR curve contains two major peaks indicating that at least two reactions,



are required to capture this polymer's decomposition behavior. POM_int and POM_char denote condensed-phase decomposition products. Gas-phase products are not shown because, as stated in Chapter 4, they are assumed to leave the condensed phase and sample container instantaneously. Note that these reactions describe a semi-global decomposition mechanism formulated to capture key features of the polymer mass loss dynamics. Each reaction corresponds to tens or, perhaps, hundreds of elementary chemical processes occurring in the corresponding temperature range.

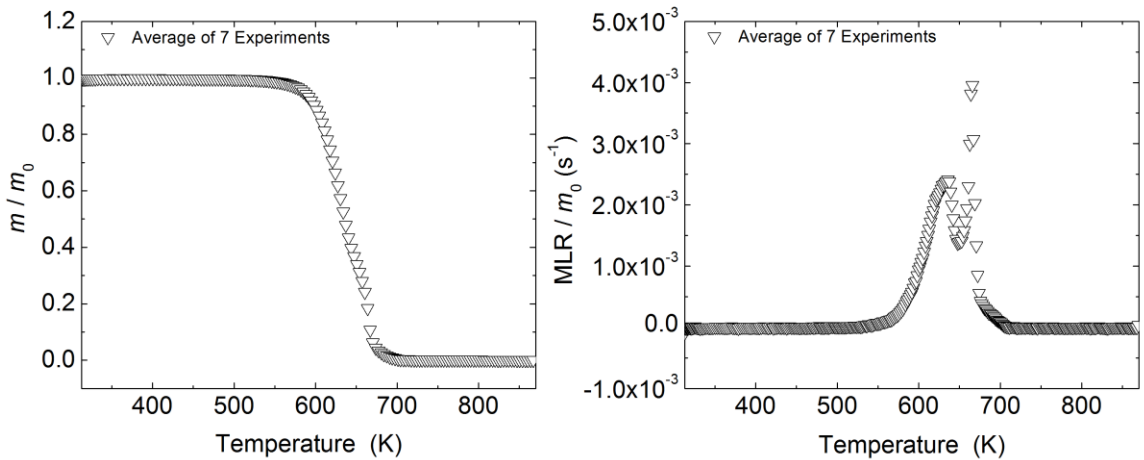


Figure 5.1 TGA of POM at 10 K min^{-1} .

The kinetic parameters describing these reactions were obtained as follows. The values of stoichiometric coefficients (or condensed-phase product yields) were determined directly from the TGA data. θ_1 was set to m/m_0 at the temperature of the MLR minimum located between the two peaks. θ_2 was set to $m/(\theta_1*m_0)$ at the end of the mass loss process (at $T \approx 750$ K). An initial guess for the Arrhenius parameters of each reaction was computed using an approximate solution for the first order decomposition under linear heating conditions [148]:

$$E = \frac{eRT_{max}^2 \frac{MLR_{max}}{m_{init}}}{(1-\theta) \frac{dT}{dt}} \quad (5.2)$$

$$A = \frac{e MLR_{max}}{m_{init}} e^{\frac{E}{RT_{max}}} \quad (5.3)$$

Here, the subscript *max* designates the values taken at the maximum of the corresponding MLR peak. m_{init} is the initial reactant mass (for the first reaction, $m_{init} = m_0$; for the second reaction, $m_{init} = \theta_1 m_0$). e is the base of the natural logarithm.

Subsequent refinement of the Arrhenius parameters was performed using ThermaKin. A and E of each reaction were changed in small increments; the results of the simulations were compared with the experimental TGA curves. The changes that lead to an improvement in the quality of the agreement were retained. The fitting process continued until the coefficient of determination of the model for the experimental MLR exceeded 0.9 (note this valued is different for charring polymers; details can be found in Chapter 6). Desired changes in the temperature or height of

each MLR peak were accomplished by augmenting the corresponding Arrhenius parameters in accordance with the rules summarized in Table 5-1.

Table 5-1 Rules used to guide TGA curve fitting.

Desired change in MLR peak	Procedure
Shift peak to higher temperature	Increase T_{max} and re-compute A and E using Equations 5.2 and 5.3 and mass, MLR and heating rate information from the corresponding experiment
Shift peak to lower temperature	Decrease T_{max} and re-compute A and E using Equations 5.2 and 5.3 and mass, MLR and heating rate information from the corresponding experiment
Increase peak height	Increase E and re-compute A using Equation 5.3 and mass and MLR information from the corresponding experiment
Decrease peak height	Decrease E and re-compute A using Equation 5.3 and mass and MLR information from the corresponding experiment

The results of this process are shown in Figure 5.2. The optimized kinetic parameters are given in Table 5-2. The model captures both POM mass and MLR behaviors accurately. To assess uncertainties in the fitted Arrhenius parameters, the simulations were compared with the TGA data obtained from individual experiments (Figure 5.1 and Figure 5.2 display only the average of seven experimental runs to avoid congestion). The Arrhenius parameters were varied, one at a time. The maximum variation in each parameter that corresponded to a shift in the simulation results that was still within the scatter of the experimental data was used to define this parameter's uncertainty. The computed uncertainty values are listed in Table 5-2.

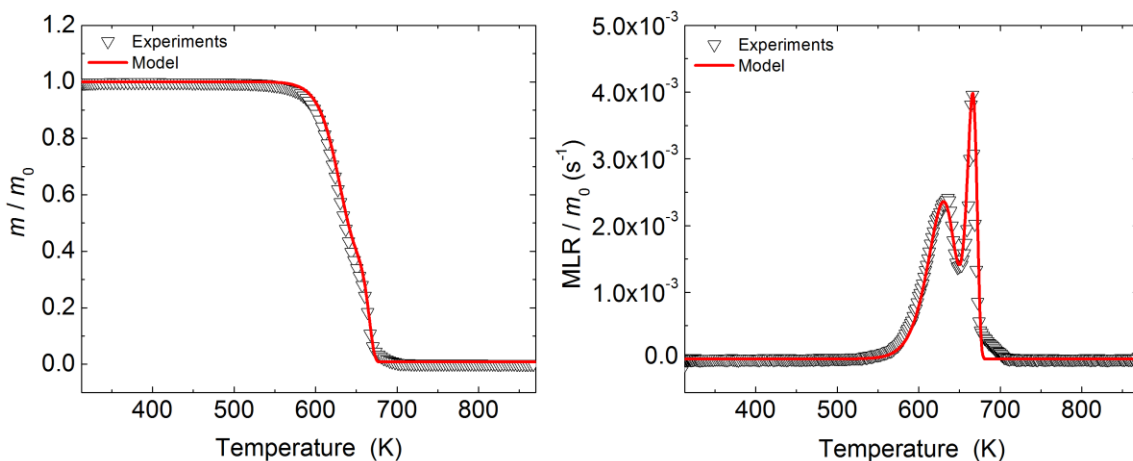


Figure 5.2 Experimental and simulated TGA of POM at 10 K min⁻¹.

Table 5-2 Kinetic parameters describing decomposition reactions for POM.

Polymer	A_1 (s ⁻¹)	E_1 (kJ mol ⁻¹)	θ_1	A_2 (s ⁻¹)	E_2 (kJ mol ⁻¹)	θ_2
POM	$3.84 \times 10^{14} \pm 50\%$	$200 \pm 5\%$	0.400	$4.76 \times 10^{44} \pm 20\%$	$590 \pm 2\%$	0.018

As a final test, the parameterized kinetic models' ability to reproduce experimental data at a higher heating rate was examined. A comparison of 30 K min⁻¹ experiments with a simulation (performed at the same heating rate) is shown in Figure 5.3. The agreement is reasonable, although not perfect. There is a clear shift toward higher temperature in the experimental data. Deviations of similar nature were observed for all non-charring polymers analyzed in this work (these results are discussed in the section 5.3). However, POM's 30 K min⁻¹ model and experiment disagreement was found to be by far the largest. This disagreement was attributed to inability of the sample to keep up with the set heating rate during the experiments. This inability is most pronounced in the case of POM because, as shown below, this polymer was found to have the highest heat of endothermic decomposition (see details in the section 5.4). A recent theoretical analysis [130] indicates that a

temperature gradient within a TGA sample caused by fast heating manifests itself as a high temperature shift of the MLR peak and that the magnitude of this shift increases with increasing decomposition endothermicity.

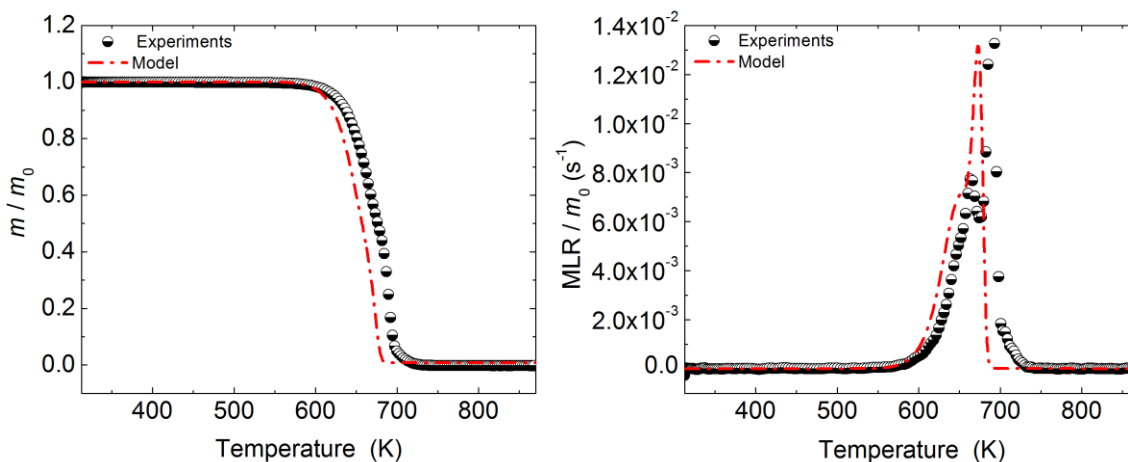


Figure 5.3 Experimental and simulated TGA of POM at 30 K min^{-1} .

Section 5.2 DSC of POM

Figure 5.4 shows the result of DSC experiments performed on POM. The heat flow normalized by the initial mass is plotted as a function of sample temperature. There are three distinct peaks in this heat flow curve. The lowest temperature peak, at about 455 K, is not accompanied by mass loss (according to the TGA data in Figure 5.1) and is assumed to correspond to melting process. The positions of the other two peaks approximately match the mass loss peaks and, therefore, are associated with the decomposition reactions.

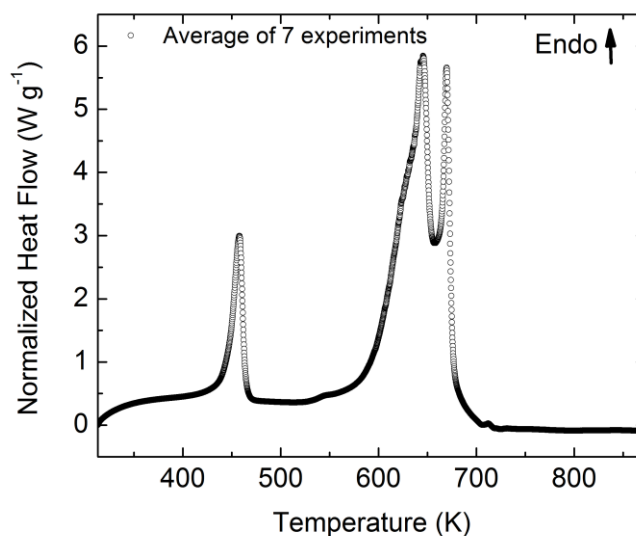


Figure 5.4 DSC of POM at 10 K min⁻¹.

At the first stage of analysis, the DSC curve was normalized by instantaneous heating rate. The parts of this curve that do not contain melting or decomposition peaks were fit with straight lines. The results of this process are shown in Figure 5.5. These linear temperature dependencies were associated with the heat capacities of solid POM (designated as POM) and molten POM (designated as POM_melt). These heat capacities are reported in Table 5-3. The amount of POM_char produced during the decomposition was too small (< 1% of the initial mass) to resolve its heat capacity. Therefore, it was assumed to be equal to 1 J g⁻¹ K⁻¹ (note that, due to a small yield, this assumption has little impact on the decomposition thermodynamics). The heat capacity POM_int also could not be resolved because of the overlap between two reaction peaks. Therefore, POM_int heat capacity was assumed to be equal to that of POM_melt. The uncertainties in the heat capacities reported in Table 5-3 were obtained from individual heat flow curves (only the average of seven experiments is

shown in Figure 5.5) by calculating two standard deviations of the mean at several temperatures within the fitted temperature range and averaging these uncertainty values.

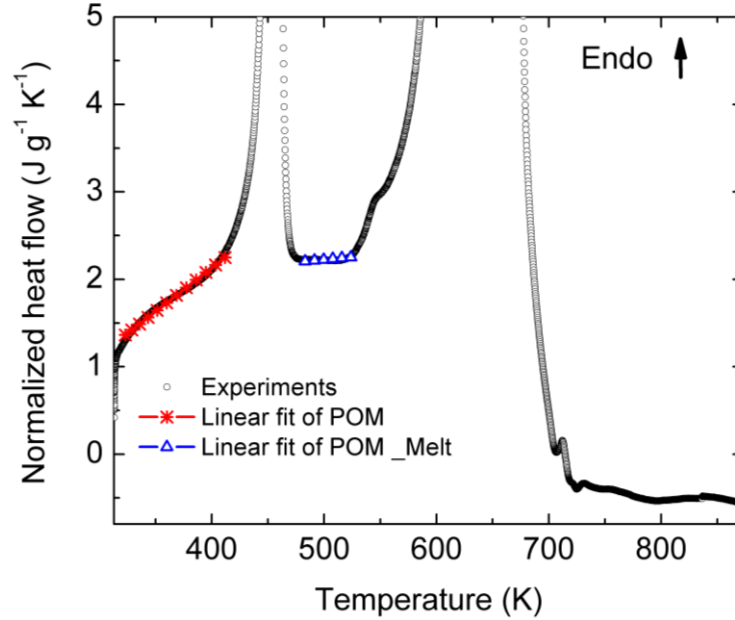


Figure 5.5 DSC of POM normalized by instantaneous heating rate. Linear fits represent heat capacities of the condensed phase at various stages of heating.

Table 5-3 Heat capacities of material components for POM.

Component	c ($\text{J g}^{-1} \text{K}^{-1}$)
POM	$(-1.86+0.0099T) \pm 14\%$
POM_melt	$(1.65+0.0012T) \pm 40\%$

At the second stage of analysis, the heat capacities were used to compute a sensible heat flow baseline. This baseline (H_{base} , measured in W g^{-1}) was calculated as follows:

$$H_{base}(t) = \frac{1}{m_0} \frac{dT}{dt} \sum_{j=1}^N c_j(T) m_j(t) \quad (5.4)$$

Here the temperature derivative versus time is the instantaneous heating rate. The summation is performed over all condensed-phase components (POM, POM_melt, POM_int, and POM_char). The baseline is resolved in terms of time. The temperature history comes directly from the experiments (average of seven experimental temperature histories was used in the calculations). Component masses were computed by assuming that POM converts to POM_melt instantaneously at the melting temperature, which was assumed to correspond to the maximum of the melting peak. In the decomposition region, component masses were resolved using the results of numerical modeling of TGA experiments (described in the section 5.1).

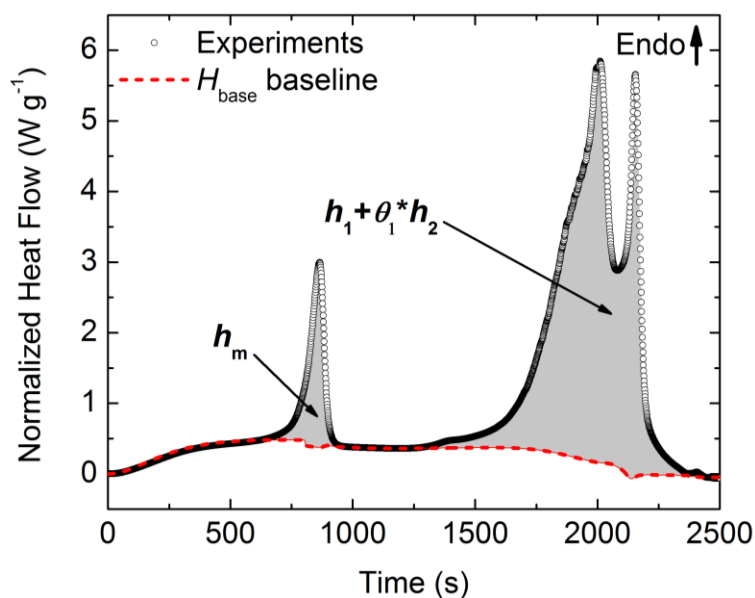


Figure 5.6 Determination of melting and decomposition contributions to the POM DSC signal.

This baseline is plotted together with the total DSC heat flow in Figure 5.6. Note that both data are presented as a function of time. Subtraction of this baseline from the total heat flow and subsequent integration of the difference in the melting region produced the value for the heat of melting (h_m) which is $192 \pm 6\%$ J g⁻¹. The

difference integration in the decomposition region produced the value of the total heat of decomposition, $h_1 + \theta_1 * h_2$ (the h value subscripts indicate references to the corresponding reactions, which kinetic parameters are reported in Table 5-2). This integration process is illustrated in Figure 5.6. The heat values for h_1 and h_2 were calculated to be $1192 \pm 5\%$ and $1352 \pm 5\% \text{ J g}^{-1}$ respectively. Only in the cases of POM and Kydex (details can be found in Chapter 6), the heats of individual reactions (h_1 and h_2) were obtained directly from the integration of experimental heat flow. For other polymers analyzed in this study, the reaction heat flow peaks were not clearly separated in time. Therefore, the last stage of analysis was also utilized to distribute the total heat of decomposition ($h_1 + \theta_1 * h_2$) obtained from the integration among individual reactions through fitting of the heat flow history in the reaction region.

These uncertainties for values of h_m , h_1 and h_2 were calculated as two standard deviations of the mean by performing this procedure for individual experiments (using the same average baseline) produced a set of h_m and total decomposition heats that were used to compute uncertainties.

It should be noted that what is referred to here as the heat of decomposition reaction is actually a sum of heats of two processes: chemical decomposition process, which involves breaking and formation of covalent chemical bonds and vaporization of the decomposition products, which involves breaking of the Van der Waals bonds. Both of these processes change the system's enthalpy and cannot be separated within the framework of the current experiments.

At the last stage of analysis, the heat capacities and heats of melting and decomposition were added to the ThermaKin model of POM. This model was used to simulate DSC. The reaction mechanism was augmented to include melting:



The heat of reaction representing melting was set to be equal to h_m . The reaction rate was defined by activation energy, E_m , and pre-exponential factor, A_m . The values of E_m (382 kJ mol^{-1}) and A_m ($2.7 \times 10^{42} \text{ s}^{-1}$) were fitted to reproduce the shape of the melting peak observed in the experiments. The heat flow profile matching was also used to distribute the total heat of decomposition ($h_1 + \theta_1 * h_2$) among the two reactions.

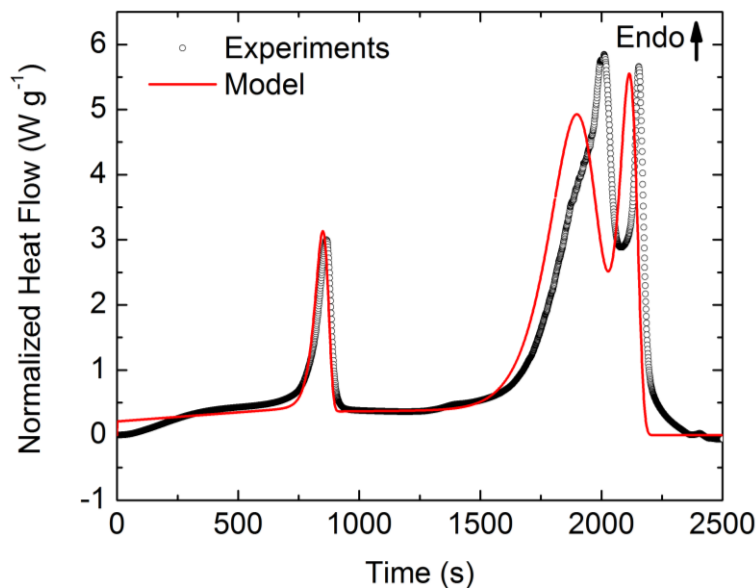


Figure 5.7 Experimental and simulated DSC of POM at 10 K min^{-1} .

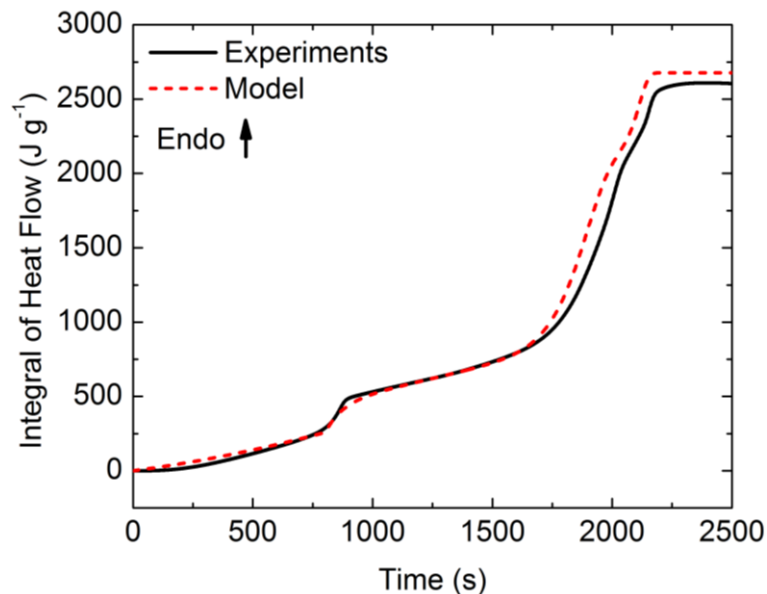


Figure 5.8 Time integral of 10 K min^{-1} DSC of POM.

A comparison of the resulting POM model with the experimental DSC heat flow history is shown in Figure 5.7. The agreement is good; however, it is not perfect. The small differences are primarily due to the fact that the instant experimental heating rate deviates somewhat from its set value (while in the simulation, no deviations take place). A comparison of the experimental and simulated integral DSC heat flows shown in Figure 5.8 further illustrates how well the model reproduces the experiment. At the end of the decomposition process ($t \approx 2250 \text{ s}$), the experimental and simulated integral heats converge within 3% of each other.

Section 5.3 TGA of PMMA, HIPS, PA 66, PP, PLA and ABS

The experimental and simulated TGA results obtained for the rest of the studied materials are shown in Figure 5.9 and Figure 5.10. For each polymer, the normalized mass (left plot) and MLR (right plot) measured at 10 and 30 K min^{-1} are compared with the corresponding modeling outcomes. The model parameters were

derived from 10 K min^{-1} experiments by following the procedure described in the section 5.1. These parameters for all non-charring polymers are summarized in Table 5-4. PLA was the only material mentioned in this chapter, in addition to POM, that required two reactions to reproduce experimental mass loss. Decomposition of the rest of the polymers was represented by a single reaction. All models capture 10 K min^{-1} experiments accurately. These models also reproduce 30 K min^{-1} data. The worst agreement is observed for PLA at 30 K min^{-1} . Similar to POM (see discussion in the section 5.1), this disagreement was attributed to inability of the sample to keep up with the set heating rate during experiments.

Table 5-4 Kinetic parameters describing decomposition reactions and melting (E_m and A_m) for all non-charring polymers.

Polymer	A_1 (s^{-1})	E_1 (kJ mol^{-1})	θ_1	A_2 (s^{-1})	E_2 (kJ mol^{-1})	θ_2	A_m (s^{-1})	E_m (kJ mol^{-1})
POM	$3.84 \times 10^{14} \pm 50\%$	$200 \pm 5\%$	0.400	$4.76 \times 10^{44} \pm 20\%$	$590 \pm 2\%$	0.018	2.7×10^{42}	382
PMMA	$8.60 \times 10^{12} \pm 40\%$	$188 \pm 2\%$	0.015	N/A	N/A	N/A	N/A	N/A
HIPS	$1.70 \times 10^{20} \pm 40\%$	$301 \pm 5\%$	0.043	N/A	N/A	N/A	N/A	N/A
PA 66	$3.86 \times 10^{12} \pm 50\%$	$200 \pm 2\%$	0.026	N/A	N/A	N/A	2.0×10^{39}	420
PP	$9.60 \times 10^{22} \pm 50\%$	$350 \pm 2\%$	0.018	N/A	N/A	N/A	2.5×10^{35}	308
PLA	$1.68 \times 10^{18} \pm 50\%$	$245 \pm 3\%$	0.100	$4.58 \times 10^6 \pm 30\%$	$126 \pm 5\%$	0.400	6.0×10^{40}	355
ABS	$1.00 \times 10^{14} \pm 40\%$	$219 \pm 2\%$	0.023	N/A	N/A	N/A	N/A	N/A

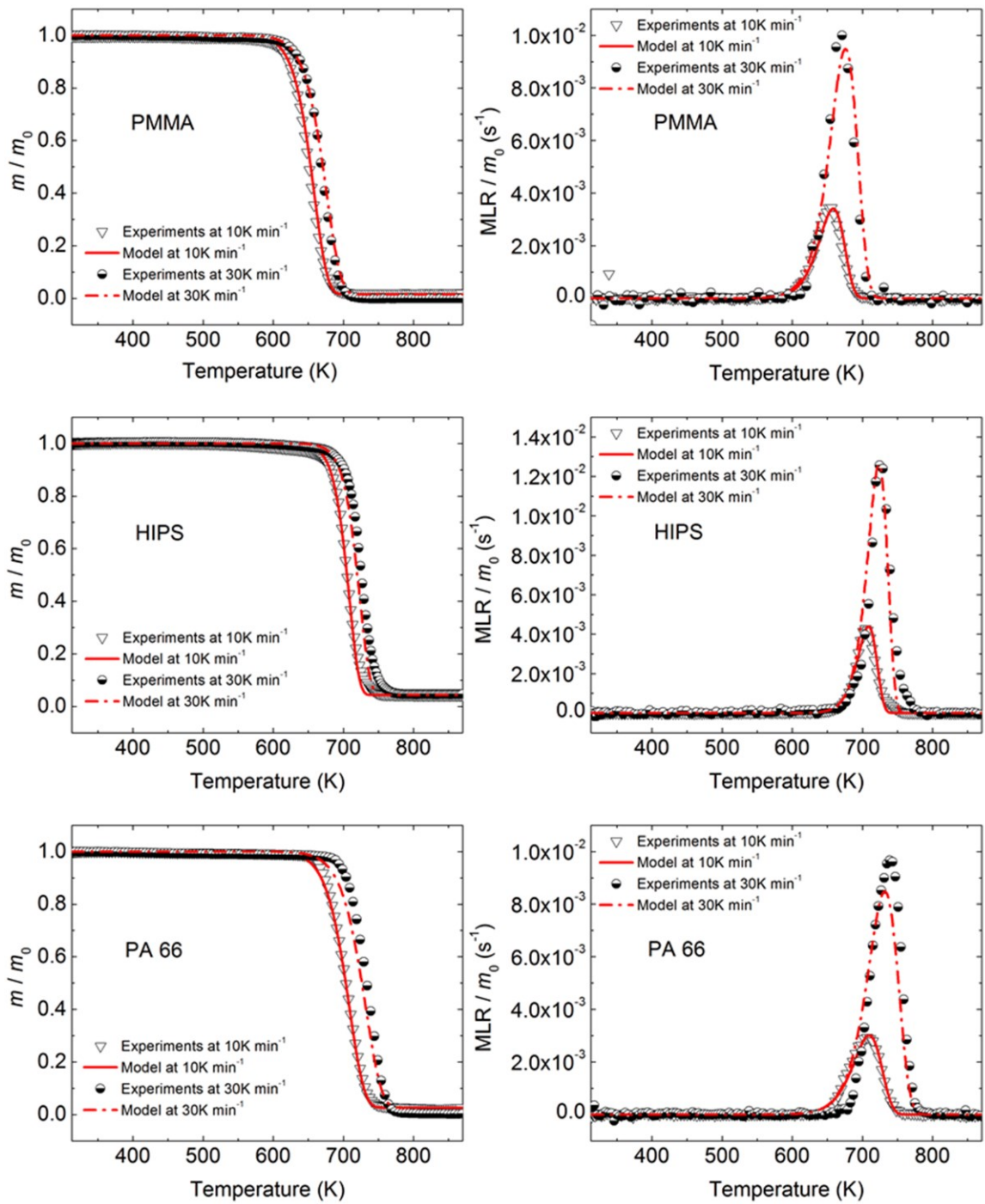


Figure 5.9 Experimental and simulated TGA of PMMA, HIPS and PA 66 at 10 K min⁻¹ and 30 K min⁻¹.

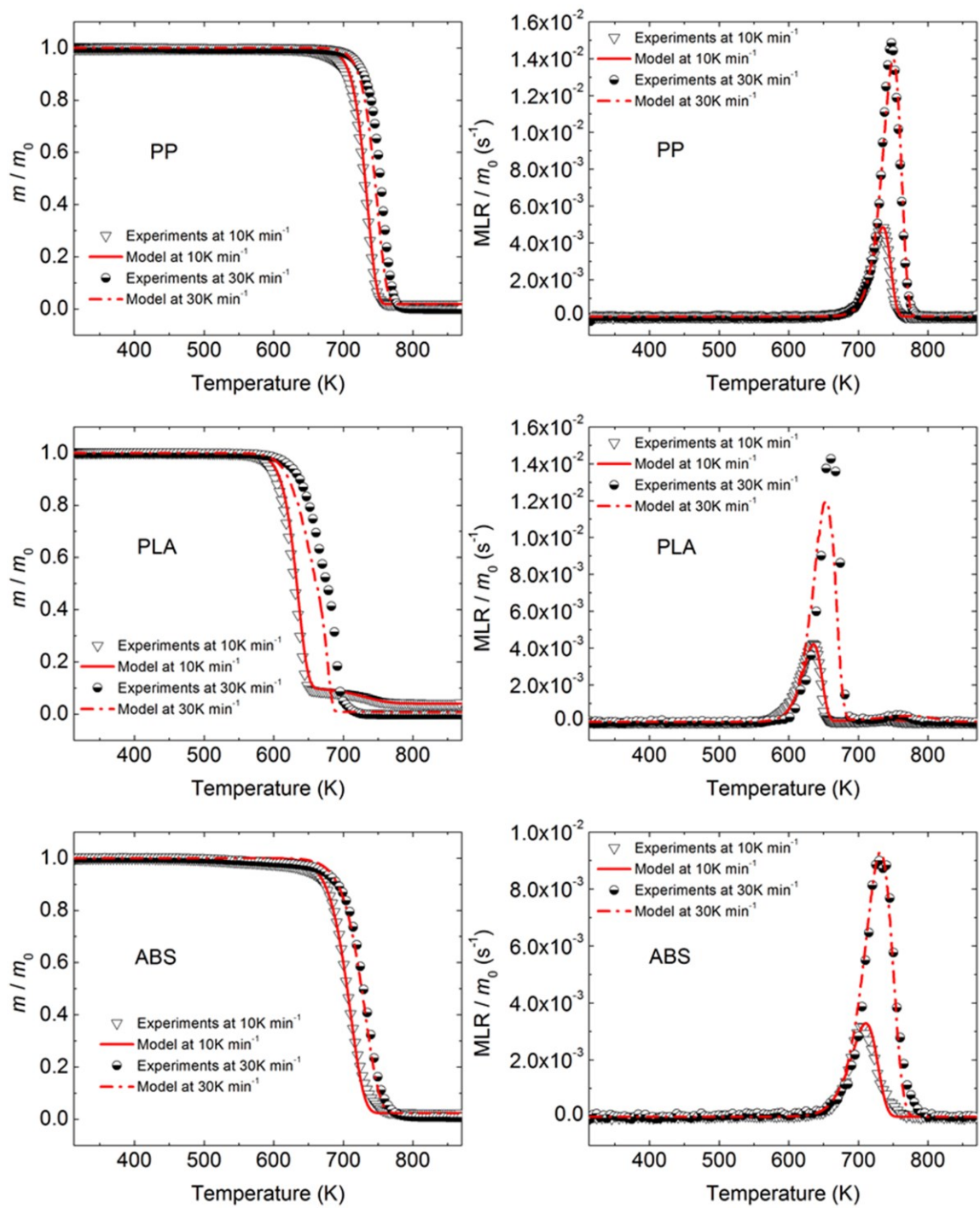


Figure 5.10 Experimental and simulated TGA of PP, PLA and ABS at 10 K min⁻¹ and 30 K min⁻¹.

Section 5.4 DSC of PMMA, HIPS, PA 66, PP, PLA and ABS

The experimental and simulated DSC results obtained for the rest of the studied materials are shown in Figure 5.11 and Figure 5.12. These data are presented as m_0 -normalized heat flow plotted with respect to time and temperature (left plot) and the heat flow integral plotted with respect to time (right plot). The thermodynamic model parameters were derived from the experiments by following the procedure described in the section 5.2. These parameters are listed in Table 5-5 and Table 5-6. Melting was observed for PA66, PP and PLA at about 535, 435 and 425 K, respectively. The kinetic parameters for all the non-charring polymers describing these processes are given in Table 5-4. Overall, the models fit experimental heat flow data well. The discrepancies observed in the low temperature region (313-450 K) are attributed to heating rate deviations detected in the experiments (and discussed above). The decomposition region (550-750 K) disagreements are most notable in the cases of ABS and PLA. These disagreements are speculated to be a result of a temporary loss of thermal contact between the sample and the pan due to bubble formation at the onset of decomposition. The modeled integral heat at the end of decomposition was found to be within 5% of the corresponding experimental values for all polymers.

Table 5-5 Heat capacities of material components for non-charring polymers.

Component	c (J g ⁻¹ K ⁻¹)	Component	c (J g ⁻¹ K ⁻¹)
POM	$(-1.86+0.0099T) \pm 14\%$	POM_melt	$(1.65+0.0012T) \pm 40\%$
PMMA	$(0.60+0.0036T) \pm 11\%$	N/A	N/A
HIPS	$(0.59+0.0034T) \pm 13\%$	N/A	N/A
PA 66	$(-1.18+0.0087T) \pm 20\%$	PA_melt	$(1.71+0.0023T) \pm 30\%$
PP	$(-2.05+0.0123T) \pm 10\%$	PP_melt	$(1.45+0.0033T) \pm 35\%$
PLA	$(1.09+0.0012T) \pm 25\%$	PLA_melt	$(1.93+0.0004T) \pm 45\%$
ABS	$(1.58+0.0013T) \pm 22\%$	N/A	N/A

Table 5-6 Heats of melting and decomposition for non-charring polymers.

Polymer	h_m (J g ⁻¹)	$h_1+\theta_1*h_2$ (J g ⁻¹)	h_1 (J g ⁻¹)	h_2 (J g ⁻¹)
POM	$192 \pm 6\%$	$1733 \pm 5\%$	$1192 \pm 5\%$	$1352 \pm 5\%$
PMMA	N/A	$846 \pm 5\%$	$846 \pm 5\%$	N/A
HIPS	N/A	$689 \pm 8\%$	$689 \pm 8\%$	N/A
PA 66	$65 \pm 24\%$	$625 \pm 11\%$	$625 \pm 11\%$	N/A
PP	$90 \pm 10\%$	$412 \pm 8\%$	$412 \pm 8\%$	N/A
PLA	$30 \pm 30\%$	$656 \pm 6\%$	$655 \pm 6\%$	$8 \pm 6\%$
ABS	N/A	$460 \pm 5\%$	$460 \pm 5\%$	N/A

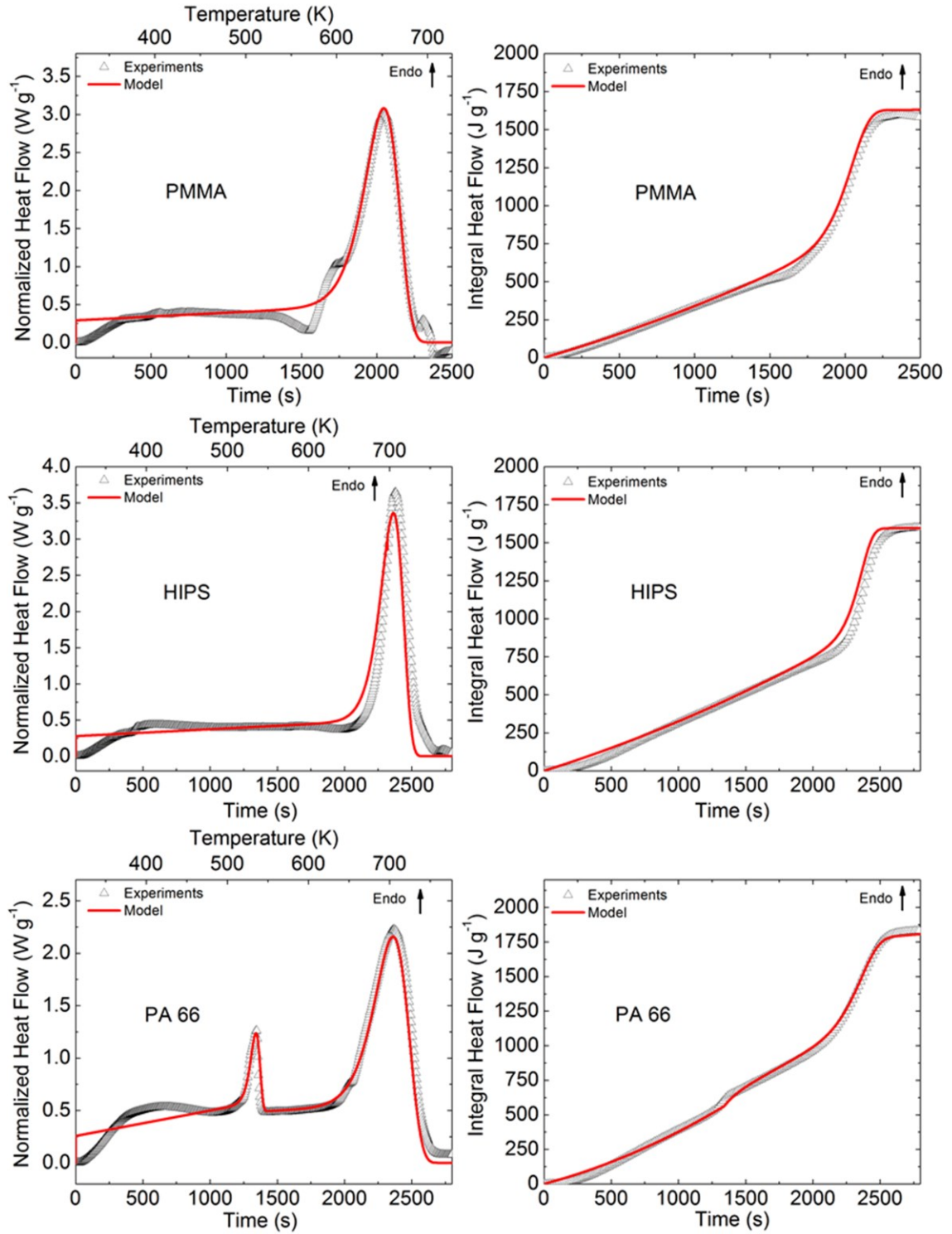


Figure 5.11 Experimental and simulated DSC of PMMA, HIPS and PA 66 at 10 K min⁻¹.

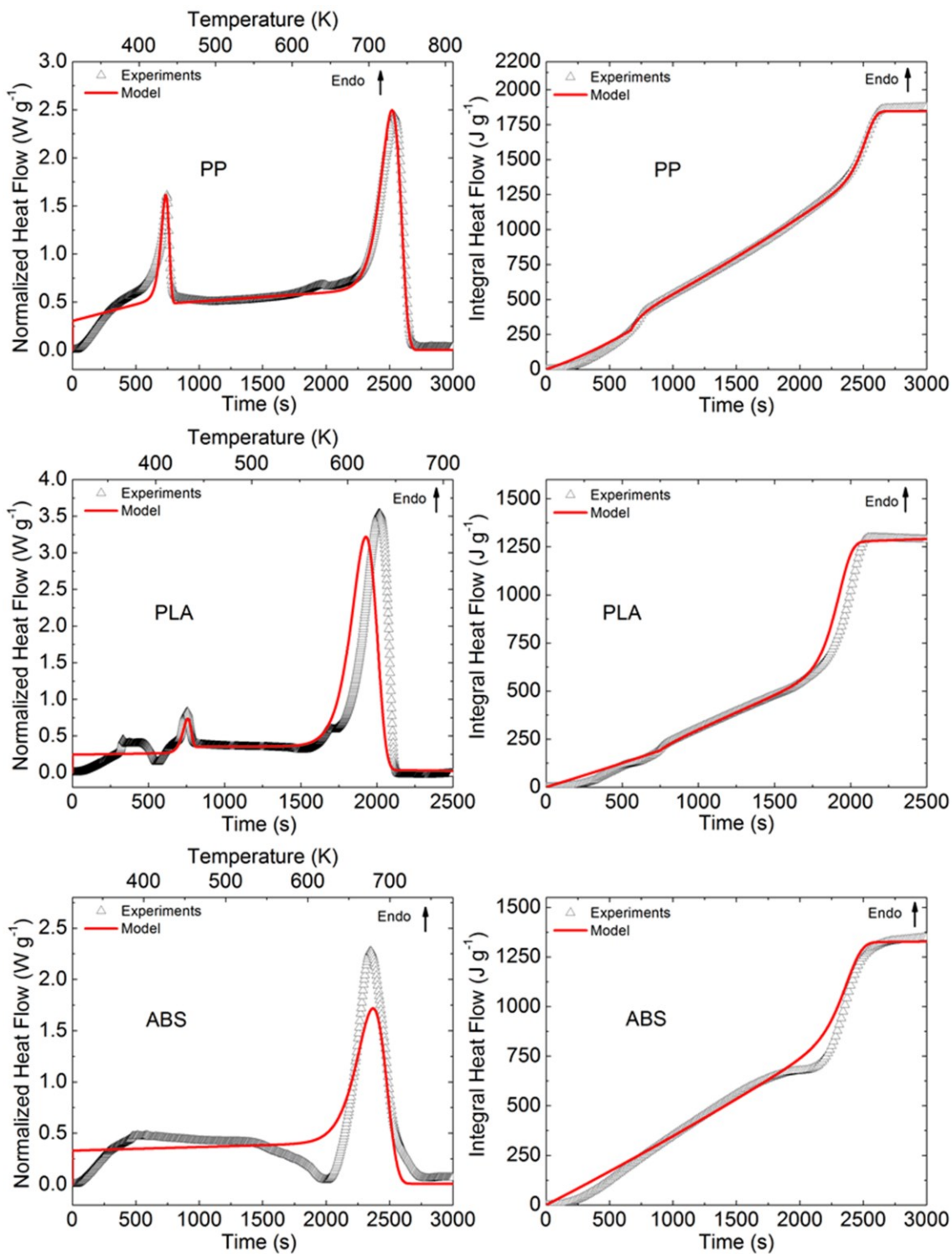


Figure 5.12 Experimental and simulated DSC of PP, PLA and ABS at 10K min⁻¹.

It is difficult to compare kinetic parameters obtained in this work with those determined in other studies of polymer degradation because of model-specific nature

of these parameters and their partial interdependence [149]. The thermodynamic parameters measured in this work are also model-specific. However, it should still be possible to compare the integral values of heat required to degrade a given material. This heat is frequently referred to as the heat of gasification (H_g). It can be defined as the amount of energy required to completely degrade and volatilize a unit mass of material that is initially at room temperature (298 K). In principle, this quantity depends on heating rate. This is the case because the temperature range at which the degradation takes place shifts to higher values with increasing rate of heating (see Figure 5.9 and Figure 5.10). As a consequence, the solid (or molten) polymer is heated to a higher temperature before it degrades (in this analysis, it is assumed that gaseous degradation products leave instantaneously and do not contribute to the heat capacity of the system). In addition, the heat of decomposition is a temperature dependent quantity. The former dependence is captured by the current material models. The latter dependence is considered to be minor and is ignored. Ignoring this dependence is equivalent to assuming that the integral of the difference in the heat capacities of the polymer and gaseous decomposition products over a decomposition temperature shift (induced by a change in the heating rate) is negligibly small with respect to the overall heat of gasification value [150].

The heats of gasification calculated by simulating material heating and decomposition at 10 and 100 K min⁻¹ are shown in Table 5-7. This table also gives the final simulation temperatures (T_e), which correspond to the earliest point at which the decomposition process is complete. For most polymers, the higher heating rate H_g values are within uncertainties of the lower heating rate H_g values. These

uncertainties were calculated by propagating errors [151] in the thermodynamic parameters. Table 5-7 also contains the heats of gasification measured by means of mass pyrolysis calorimetry (MPC) [152]. In MPC, a thermally thick sample is heated by a constant radiant heat flux. While the heating rate observed in these experiments is highly variable and depends on the set heat flux value, time and position inside the sample, it may still be appropriate to compare MPC heats of gasification with those calculated using constant heating rates because, as shown above, H_g dependence on heating rate is weak. For all polymers for which MPC values are available (POM, PMMA, HIPS, and PP), this comparison shows a very good agreement. The heats of gasification obtained by numerical integration the material models developed in this study converge within 1-11% of the MPC heats.

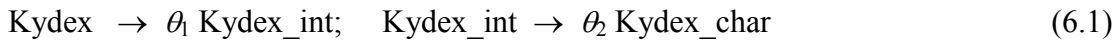
Table 5-7 Heats of gasification for non-charring polymers.

Polymer	$H_g^{298K-T_f}$, 10 K min ⁻¹ (J g ⁻¹)	T_e , 10 K min ⁻¹ (K)	$H_g^{298K-T_f}$, 100 K min ⁻¹ (J g ⁻¹)	T_e , 100 K min ⁻¹ (K)	H_g^{MPC} [152] (J g ⁻¹)
POM	2700 ± 7%	730	2700	760	2400
PMMA	1660 ± 5%	730	1780	760	1600
HIPS	1620 ± 7%	780	1710	800	1700
PA 66	1830 ± 11%	780	1980	800	N/A
PP	1870 ± 12%	815	2010	830	2000
PLA	1310 ± 12%	730	1370	740	N/A
ABS	1370 ± 12%	815	1450	815	N/A

Chapter 6 : Results- kinetics and thermodynamics for charring polymers

Section 6.1 TGA of Kydex

The results of 10 K min^{-1} TGA experiments performed on Kydex are shown in Figure 6.1. In this figure, sample mass (m) and mass loss rate (MLR) normalized by the initial mass (m_0) are plotted with respect to sample temperature. The MLR curve shows two well resolved peaks, which is probably a consequence of the fact that Kydex is an alloy of two chemically distinct polymers, poly(methyl methacrylate) and poly(vinyl chloride). These two peaks can be represented by two reactions:



where Kydex_int and Kydex_char denote condensed-phase decomposition products from the first and second reaction, respectively. Gas-phase products are not shown because, as stated in Chapter 4, they are assumed to leave the condensed phase and sample container instantaneously.

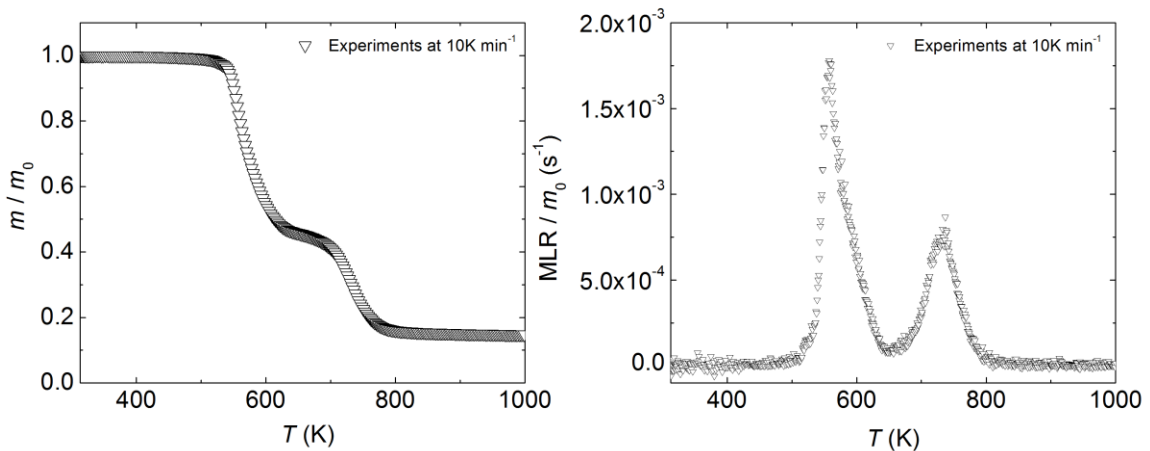


Figure 6.1 TGA of Kydex at 10 K min^{-1} .

The kinetic parameters describing these reactions were obtained by following the procedure that explained in the section 5.1. Compared to the procedure for analyzing the TGA data for non-charring polymers, there are two major differences to the kinetics analysis for charring polymers. Firstly, θ_2 was set to $m/(\theta_1*m_0)$ when $T \approx 1000$ K for charring polymers (750 K for non-charring polymers). Secondly, because of the complexity due to the char formation during thermal degradation, the iterations stop earlier when R^2 of the model for the experimental MLR reached 0.85.

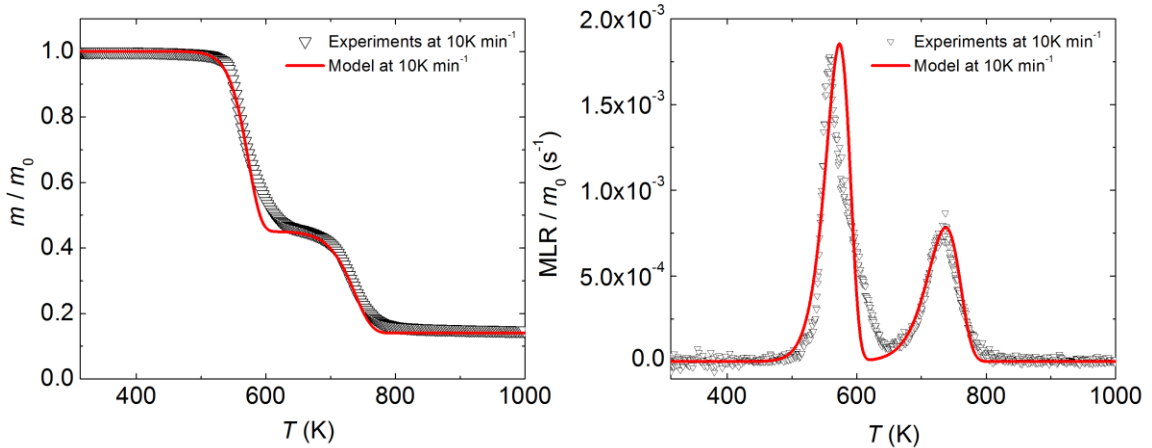


Figure 6.2 Experimental and simulated TGA of Kydex at 10 K min⁻¹.

The results of this fitting process are shown in Figure 6.2. The optimized kinetic parameters and the computed uncertainty values are given in Table 6-1. The model captures both Kydex mass and MLR behaviors with a reasonable accuracy ($R^2 = 0.86$).

Table 6-1 Kinetic parameters describing decomposition reactions for Kydex.

Polymer	A_1 (s ⁻¹)	E_1 (kJ mol ⁻¹)	θ_1	A_2 (s ⁻¹)	E_2 (kJ mol ⁻¹)	θ_2
Kydex	$6.03 \times 10^{10} \pm 50\%$	$141 \pm 3\%$	0.45	$1.36 \times 10^{10} \pm 40\%$	$174 \pm 5\%$	0.31

A comparison of 30 K min^{-1} experiments with a simulation (performed at the same heating rate) is shown in Figure 6.3 to examine the parameterized kinetic models' ability to reproduce experimental data at a higher heating rate. The quality of agreement indicates that the developed kinetic model is still valid at higher heating rates.

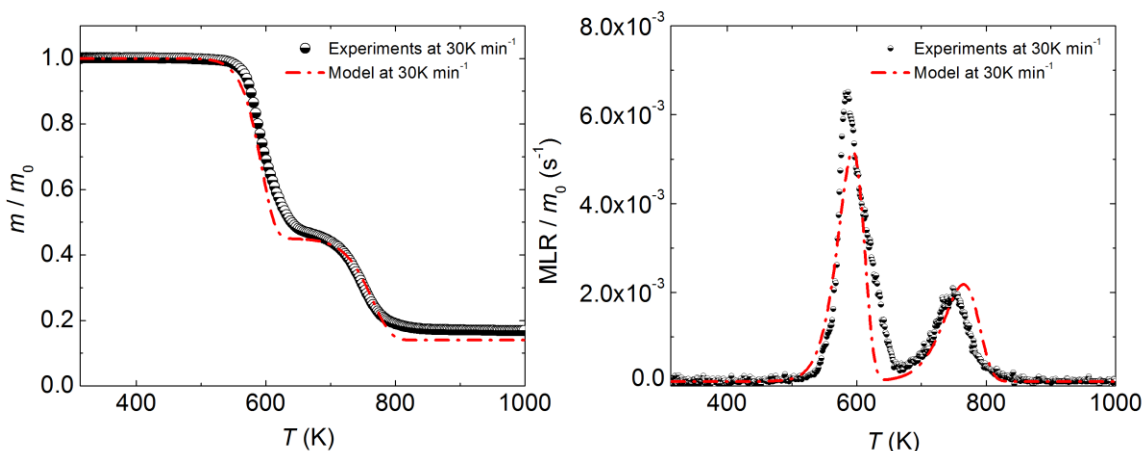


Figure 6.3 Experimental and simulated TGA of Kydex at 30 K min^{-1} .

Section 6.2 DSC of Kydex

Figure 6.4 shows the result of DSC experiments performed on Kydex. The heat flow normalized by the initial mass is plotted as a function of sample temperature. There are two distinct peaks in this heat flow curve, which approximately match the temperatures of Kydex decomposition reactions.

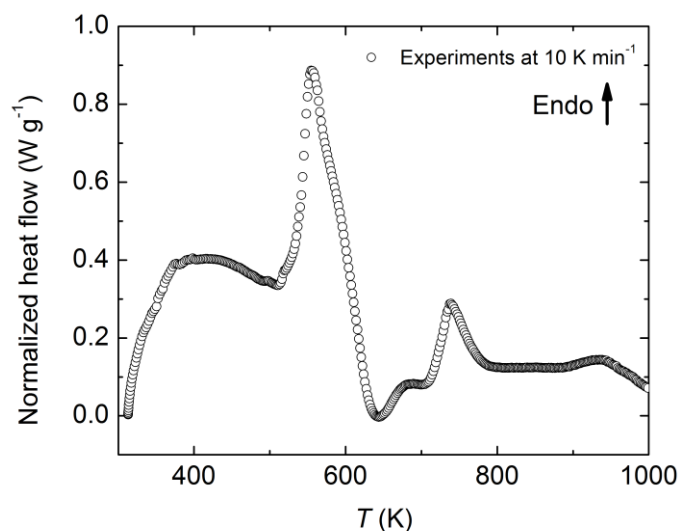


Figure 6.4 DSC of Kydex at 10 K min⁻¹.

Then DSC curve was normalized by instantaneous heating rate, as shown in the left graph of Figure 6.5. The pre-decomposition part of this curve was fit with a straight line. The parameters of this line describe temperature dependence of heat capacity of non-degraded Kydex and are reported in Table 6-2. In a similar manner, the post-decomposition part of this curve could theoretically be used to obtain heat capacity of the final char (represented by component *Kydex_char* in the reaction model). However, an in-depth analysis revealed that the post-decomposition heat flow was a subject to large random and systematic errors. The random errors were a consequence of a significant decrease in the sensitivity of the heat flow sensor with increasing temperature. The systematic errors were probably caused by heat transfer effects brought about by the formation of char, which had a porous structure.

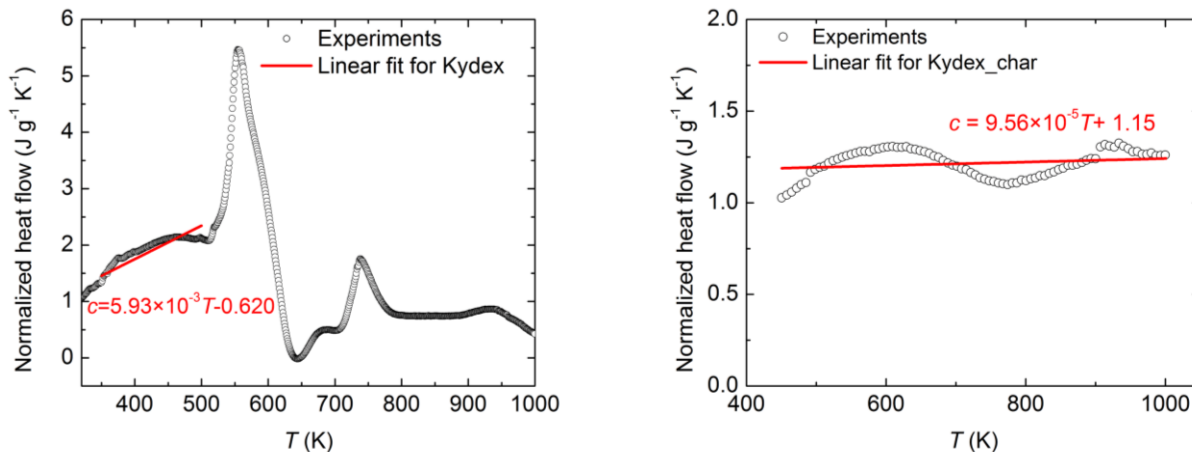


Figure 6.5 DSC of Kydex (left) and Kydex decomposition residue (right) normalized by instantaneous heating rate.

Table 6-2 Heat capacities of material components for Kydex.

Component	c ($\text{J g}^{-1} \text{K}^{-1}$)	Component	c ($\text{J g}^{-1} \text{K}^{-1}$)
Kydex	$(-0.624 + 5.93 \times 10^{-3} T) \pm 8\%$	N/A	N/A
Kydex_int	$(0.265 + 3.01 \times 10^{-3} T) \pm 12\%$	Kydex_char	$(1.15 + 9.56 \times 10^{-5} T) \pm 15\%$

To elucidate Kydex_char heat capacity, separate DSC experiments were performed on the polymer decomposition residue. As stated in the section 3.2.2, the residue, collected from several polymer tests, was compacted in a crucible to improve the thermal contact with the heat flow sensor. The results of these experiments are shown in the right graph of Figure 6.5. The normalized heat flow data collected between 450 to 1000 K were fitted with a straight line to obtain Kydex_char heat capacity. The heat capacity of the intermediate component, Kydex_int, could not be resolved because of the proximity of two reaction peaks. Therefore, the heat capacity of this component was assumed to be the mean of the heat capacity of Kydex and Kydex_char components. Heat capacity parameters for Kydex_int and Kydex_char are also listed in Table 6-2. The uncertainties in the heat capacities reported in this table were obtained from individual heat flow curves (only the average curves are

shown in Figure 6.4 and Figure 6.5) by calculating two standard deviations of the mean at several temperatures within the fitted temperature range and averaging these uncertainty values.

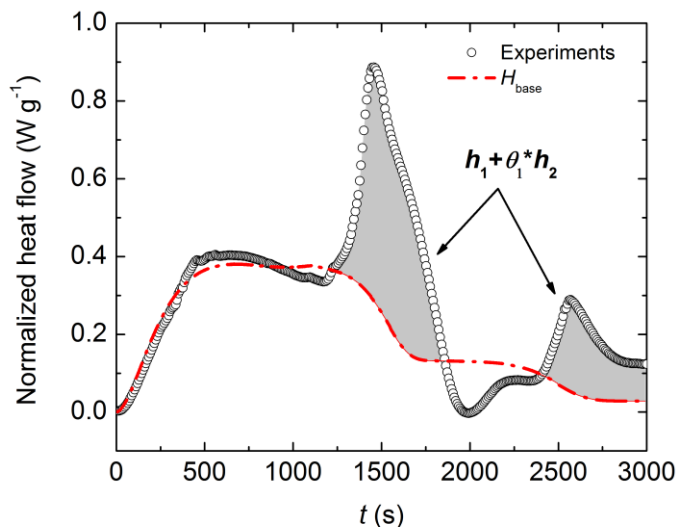


Figure 6.6 Determination of decomposition reaction contributions to the Kydex DSC signal.

The sensible heat flow baseline was calculated by following the procedure described in the section 5.2 and equation 5.4. This calculated baseline is plotted together with the total DSC heat flow as a function of time in Figure 6.6. Note that the deepening of the heat flow curve below the baseline between the reaction peaks is ignored during the integration because it is assumed to be associated with a temporary loss of thermal contact between the sample and crucible. The difference integration in the decomposition region produced the value of the total heat of decomposition, $h_1 + \theta_1 * h_2$. The after decomposition heat flow (at 2750-3000 s) is notably higher than what is predicted on the basis of the char heat capacity measurement. This discrepancy is a manifestation of the systematic errors mentioned above. To minimize

the impact of these errors on the results of the integration, this integration was bound by the point in time where the second decomposition reaction was 95% complete. Performing this integration procedure for individual experiments (using the same average baseline) produced a set of the heat of decomposition values that were used to compute uncertainties. The values of h_1 and h_2 were calculated to be $180 \pm 10\%$ and $125 \pm 12\% \text{ J g}^{-1}$ respectively.

The thermodynamics of the parameterized reaction model was verified by comparing ThermaKin calculated heat flow with that observed in the experiments. This comparison is presented using time resolved heat flow as well as heat flow integral, which are depicted in left and right graph of Figure 6.7, respectively. The experimental and simulated heat flow integrals match very well. The heat flow comparison is not as favorable. The most notable deviations occur in the pre-decomposition region. These deviations are primarily due to the fact that, as mentioned earlier in Chapter 5, the instant experimental heating rate deviates from its set value, while, in the simulations, no deviation takes place.

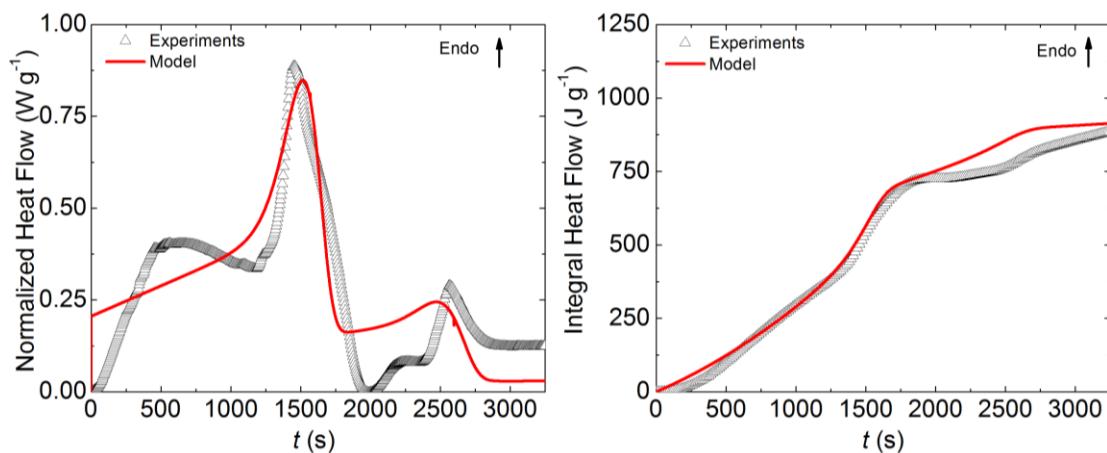


Figure 6.7 Experimental and simulated DSC heat flow (left) and heat flow integral (right) for Kydex at 10 K min^{-1} .

Section 6.3 TGA of DGEBA, PET, Kevlar, BACY, PPS, PEI and PEEK

The experimental and simulated TGA results obtained for the rest of the studied charring materials are shown in Figure 6.8, Figure 6.9 and Figure 6.10. Figure 6.8 shows the results for charring polymers with relatively low char yields, while Figure 6.9 contains results for highly charring polymers. PPS results are presented in a separate figure, Figure 6.10, because of the limited amount of data obtained for this material (see explanation in the section 3.2.2). For each charring polymer with the exception of PPS, the normalized mass (left plot) and MLR (right plot) measured at 10 and 30 K min⁻¹ are compared with the corresponding modeling outcomes. The PPS comparison contains only 10 K min⁻¹ data.

All charring polymer mass loss processes were represented in the model by two consecutive reactions. The parameters describing kinetics of these reactions were obtained from 10 K min⁻¹ experiments by following the procedure described in the sections 5.1 and 6.1. These parameters are summarized in Table 6-3. Note that the amount of PPS data was insufficient for uncertainty calculation. Therefore, these uncertainties were estimated as the mean of uncertainties calculated for the other materials.

All charring polymer models represent 10 K min⁻¹ TGA experiments with a good accuracy. However, notable discrepancies are observed for 30 K min⁻¹ heating rate. These discrepancies are the highest for PEI and PEEK and are hypothesized to be caused by deviations of the experimental conditions from spatial isothermality.

Table 6-3 Kinetic parameters describing decomposition reactions and melting for charring polymers.

Polymer	A_1 (s ⁻¹)	E_1 (kJ mol ⁻¹)	θ_1	A_2 (s ⁻¹)	E_2 (kJ mol ⁻¹)	θ_2	A_m (s ⁻¹)	E_m (kJ mol ⁻¹)
Kydex	$6.03 \times 10^{10} \pm 50\%$	$141 \pm 3\%$	0.45	$1.36 \times 10^{10} \pm 40\%$	$174 \pm 5\%$	0.31	N/A	N/A
DGEBA	$1.72 \times 10^7 \pm 50\%$	$111 \pm 8\%$	0.97	$9.86 \times 10^{16} \pm 40\%$	$259 \pm 6\%$	0.12	N/A	N/A
PET	$1.60 \times 10^{15} \pm 30\%$	$235 \pm 8\%$	0.18	$3.53 \times 10^4 \pm 30\%$	$96 \pm 10\%$	0.72	1.5×10^{36}	380
Kevlar	$6.68 \times 10^{30} \pm 30\%$	$536 \pm 4\%$	0.42	$2.73 \times 10^3 \pm 50\%$	$107 \pm 8\%$	0.86	N/A	N/A
BACY	$2.20 \times 10^{30} \pm 50\%$	$442 \pm 10\%$	0.64	$1.25 \times 10^3 \pm 50\%$	$85 \pm 5\%$	0.69	N/A	N/A
PPS	$1.06 \times 10^{11} \pm 40\%$	$205 \pm 7\%$	0.5	$3.70 \times 10^{-1} \pm 40\%$	$36 \pm 7\%$	0.88	1.5×10^{34}	380
PEI	$7.66 \times 10^{27} \pm 50\%$	$465 \pm 7\%$	0.65	$6.50 \times 10^2 \pm 50\%$	$88 \pm 10\%$	0.77	N/A	N/A
PEEK	$4.30 \times 10^{28} \pm 20\%$	$505 \pm 6\%$	0.64	$9.57 \times 10^{-1} \pm 20\%$	$50 \pm 8\%$	0.79	3.5×10^{33}	415

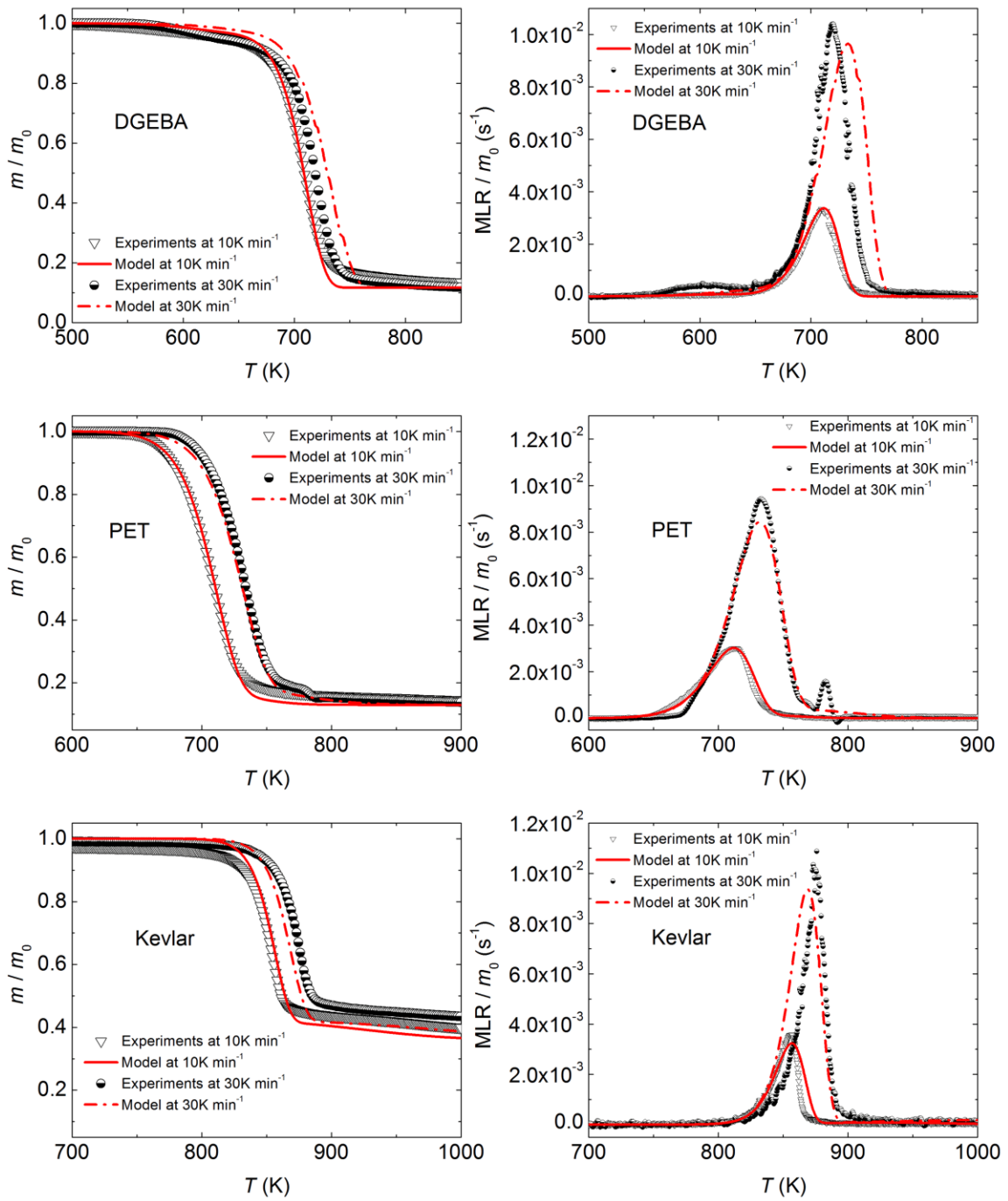


Figure 6.8 Experimental and simulated TGA of DGEBA, PET and Kevlar at 10 and 30 K min⁻¹.

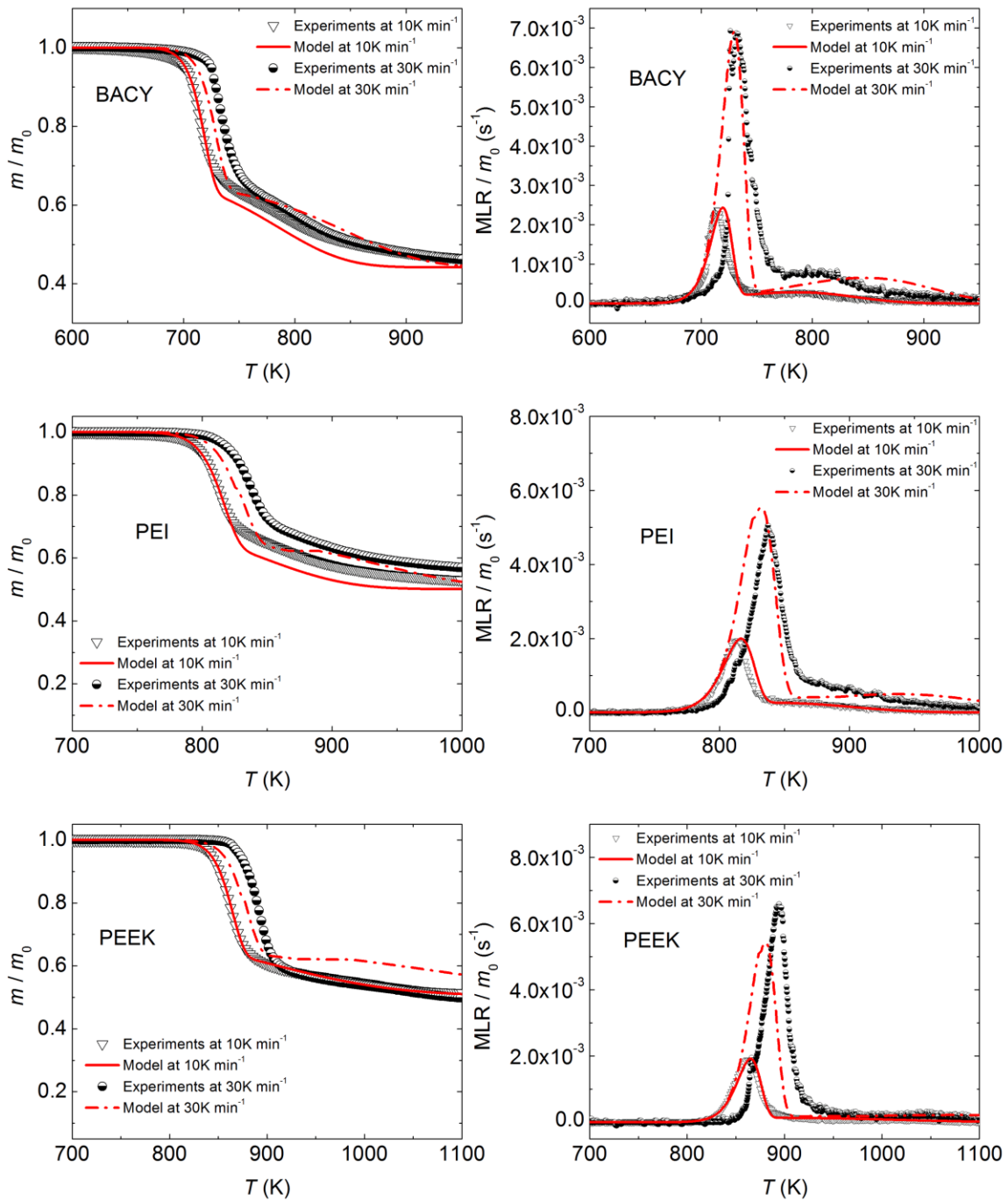


Figure 6.9 Experimental and simulated TGA of BACY, PEI and PEEK at 10 and 30 K min⁻¹.

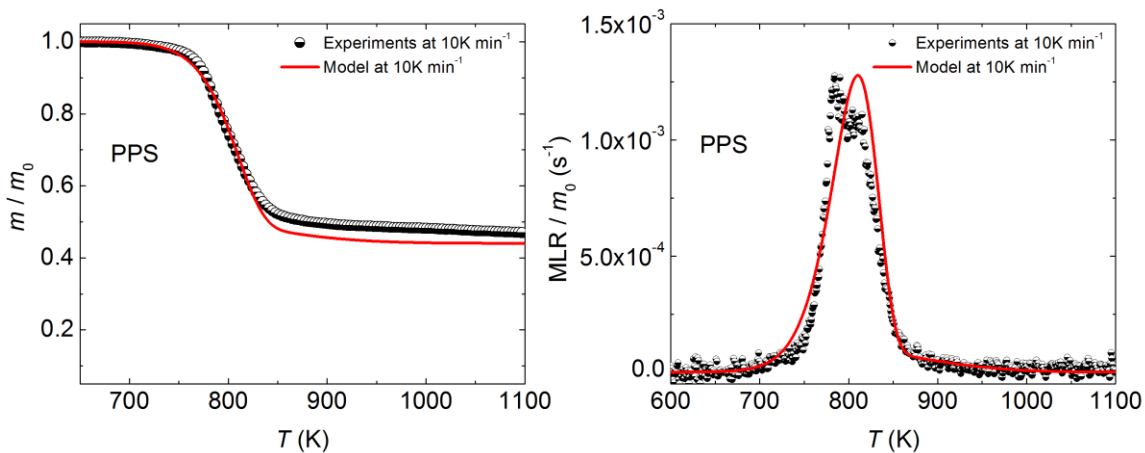


Figure 6.10 Experimental and simulated TGA of PPS at 10 K min⁻¹.

Section 6.4 DSC of DGEBA, PET, Kevlar, BACY, PPS, PEI and PEEK

The experimental and simulated DSC results obtained for the rest of the studied materials are shown in Figure 6.11, Figure 6.12 and Figure 6.13. These results are distributed among the figures in the same way as explained in the previous section. The DSC data are presented as m_0 -normalized heat flow plotted with respect to time and temperature (left plot) and the heat flow integral plotted with respect to time (right plot). The thermodynamic model parameters were derived from the experiments by following essentially the same procedure as described in the sections 5.2 and 6.2. These parameters are listed in Table 6-4 and Table 6-5.

Four of the seven charring polymers showed evidence of melting transition, which was not observed in Kydex. This transition was detected in PET, PEI, PEEK and PPS experiments at about 525, 500, 615 and 550 K, respectively. To take this transition into account during parameterization, additional components, PET_melt, PEI_melt, PEEK_melt and PPS_melt, were added to the corresponding material models. Then h_m , A_m and E_m were calculated and fitted to reproduce the shape of the

melting peak for each of the aforementioned charring polymer. The parameters describing melting kinetics are given in Table 6-3. The parameters describing melting thermodynamics are listed in Table 6-4 and Table 6-5.

Table 6-4 Heat capacities of material components for charring polymers.

Component	c ($\text{J g}^{-1} \text{K}^{-1}$)	Component	c ($\text{J g}^{-1} \text{K}^{-1}$)
Kydex	$(-0.624+5.93 \times 10^{-3}T) \pm 8\%$	N/A	N/A
Kydex_int	$(0.265+3.01 \times 10^{-3}T) \pm 12\%$	Kydex_char	$(1.15+9.56 \times 10^{-5}T) \pm 15\%$
DGEBA	$(3.89-5.08 \times 10^{-3}T) \pm 20\%$	N/A	N/A
DGEBA_int	$(2.04-8.05 \times 10^{-4}T) \pm 15\%$	DGEBA_char	$(0.185+3.29 \times 10^{-3}T) \pm 10\%$
PET	$(-0.269+4.64 \times 10^{-3}T) \pm 12\%$	PET_melt	$(2.050-2.08 \times 10^{-4}T) \pm 15\%$
PET_int	$(1.44-4.8 \times 10^{-5}T) \pm 13\%$	PET_char	$(0.820+1.12 \times 10^{-4}T) \pm 10\%$
Kevlar	$(1.71-1.49 \times 10^{-3}T) \pm 15\%$	N/A	N/A
Kevlar_int	$(1.15-3.43 \times 10^{-4}T) \pm 14\%$	Kevlar_char	$(0.585+8.04 \times 10^{-4}T) \pm 12\%$
BACY	$(-1.07+8.93 \times 10^{-3}T) \pm 18\%$	N/A	N/A
BACY_int	$(0.305+4.36 \times 10^{-3}T) \pm 19\%$	BACY_char	$(1.68-2.04 \times 10^{-4}T) \pm 20\%$
PPS	$(0.0687+2.73 \times 10^{-3}T) \pm 14\%$	PPS_melt	$(0.697+1.37 \times 10^{-3}T) \pm 18\%$
PPS_int	$(-1.04+3.36 \times 10^{-3}T) \pm 15\%$	PPS_char	$(-2.77+5.34 \times 10^{-3}T) \pm 14\%$
PEI	$(-0.0357+4.11 \times 10^{-3}T) \pm 16\%$	PEI_melt	$(1.88+5.75 \times 10^{-4}T) \pm 20\%$
PEI_int	$(1.59+3.08 \times 10^{-4}T) \pm 14\%$	PEI_char	$(1.30+4.08 \times 10^{-5}T) \pm 8\%$
PEEK	$(0.156+3.57 \times 10^{-3}T) \pm 10\%$	PEEK_melt	$(1.27+1.45 \times 10^{-3}T) \pm 20\%$
PEEK_int	$(0.859+1.36 \times 10^{-3}T) \pm 21\%$	PEEK_char	$(0.447+1.26 \times 10^{-3}T) \pm 22\%$

Table 6-5 Heats of decomposition reactions and melting (endo is positive) for charring polymers.

Polymer	$h_1 + \theta_1 \times h_2$ (J g ⁻¹)	h_1 (J g ⁻¹)	h_2 (J g ⁻¹)	h_m (J g ⁻¹)
Kydex	236 ± 10%	180 ± 10%	125 ± 12%	N/A
DGEBA	131 ± 17%	5 ± 200%	130 ± 10%	N/A
PET	265 ± 10%	220 ± 7%	250 ± 25%	30 ± 10%
Kevlar	382 ± 10%	300 ± 6%	195 ± 25%	N/A
BACY	-47 ± 3%	-226 ± 10%	280 ± 12%	N/A
PPS	-117 ± 38%	-102 ± 37%	-30 ± 40%	35 ± 9%
PEI	-83 ± 15%	-80 ± 15%	-5 ± 200%	1 ± 150%
PEEK	-768 ± 11%	-256 ± 10 %	-800 ± 12%	34 ± 8%

As evident from the right graphs of Figure 6.11, Figure 6.12 and Figure 6.13, the models reproduce experimental heat flow integral histories well. The modeled integral heat at the end of decomposition was found to be within 5% of the corresponding experimental values for the majority of the studied polymers (including Kydex). The exceptions were DGEBA and PEI, which models deviate from the experiments by 8 and 13%, respectively. As in the case of Kydex, discrepancies between the modeled and experimental heat flow (left graphs in Figure 6.11, Figure 6.12 and Figure 6.13) are more notable especially in the beginning of the experiments. These discrepancies can be explained by the fluctuation in the experimental heating rate.

Perhaps, the most significant outcome of the current heat flow analysis is an observation that all studied polymers with char yield exceeding 40 wt.%, which include BACY, PPS, PEI and PEEK, decompose exothermically, while the rest of the

polymers, including seven analyzed non-charring materials in Chapter 5 are characterized by an endothermic decomposition. Moreover, the most significant exothermicity is observed for PEEK, which also produces the highest char yield. The relationship between the char yield and decomposition exothermicity can be explained by noting that a polymer char, which molecular structure is likely to be similar to that of graphite or soot (i.e., multiple fused aromatic rings), is highly thermodynamically stable. When the char is produced in sufficient amount, its thermodynamic stability compensates an increase in enthalpy associated with the formation of small molecular mass volatiles.

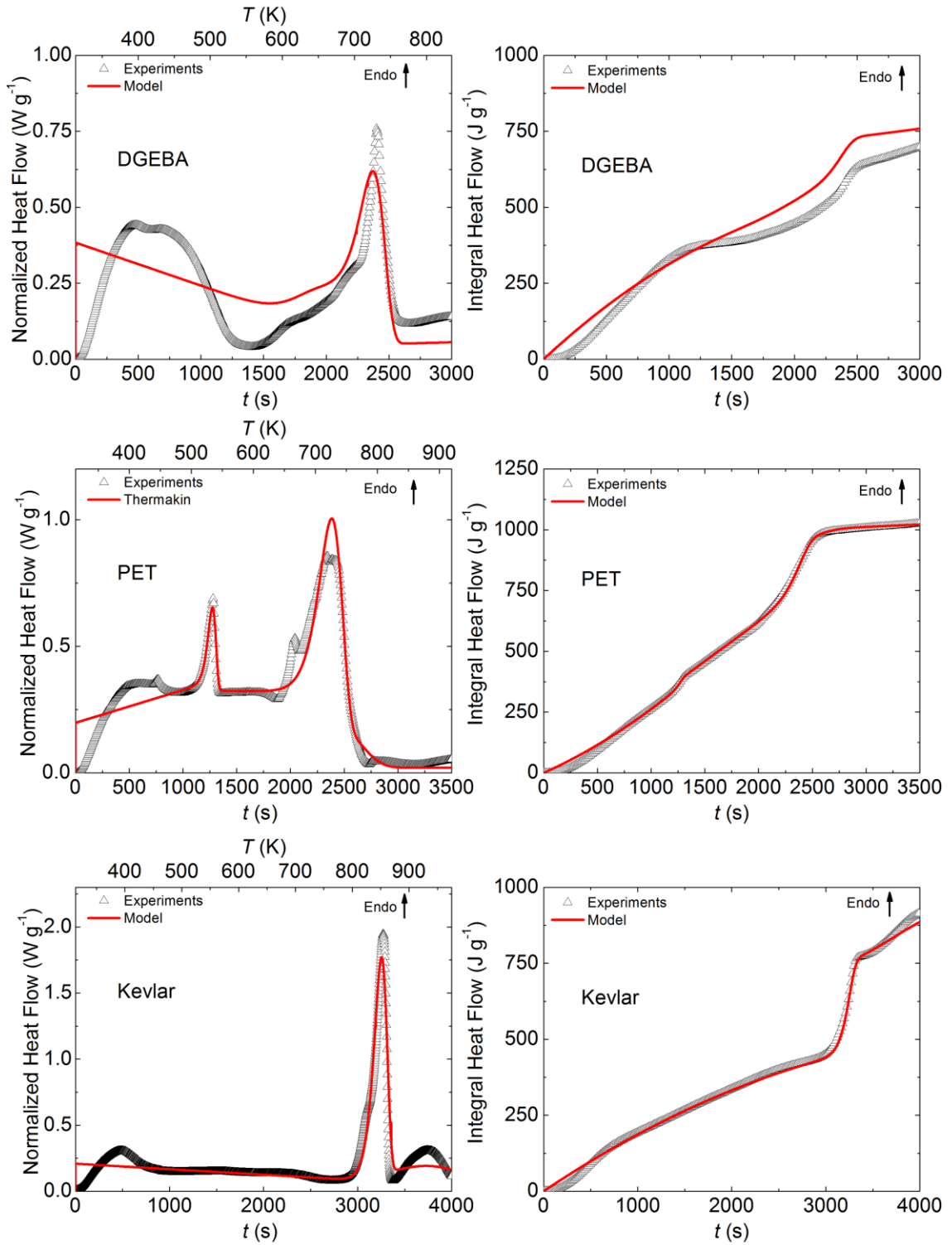


Figure 6.11 Experimental and simulated DSC of DGEBA, Kevlar and PET at 10 K min⁻¹.

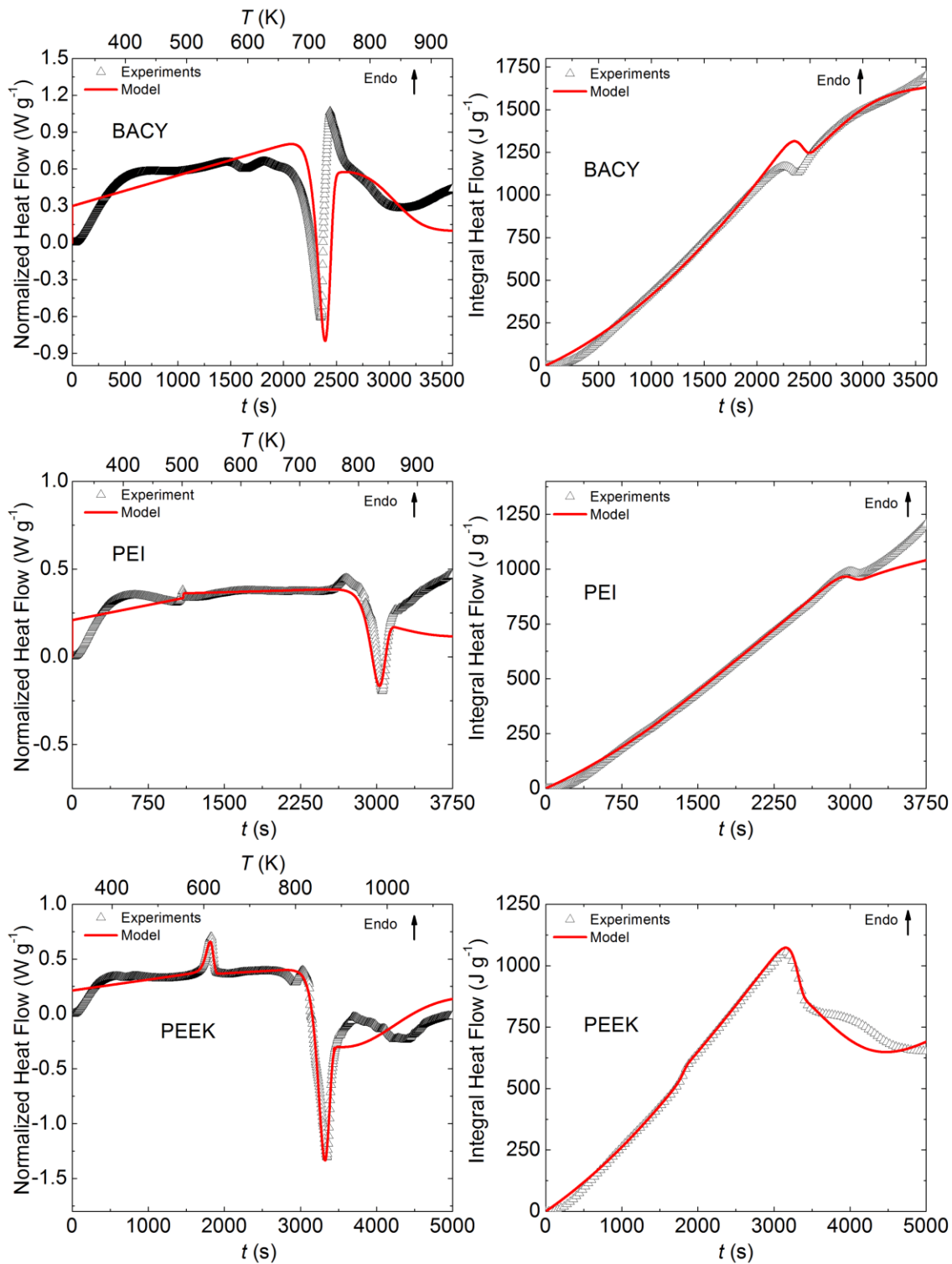


Figure 6.12 Experimental and simulated DSC of BACY, PEI and PEEK at 10 K min⁻¹.

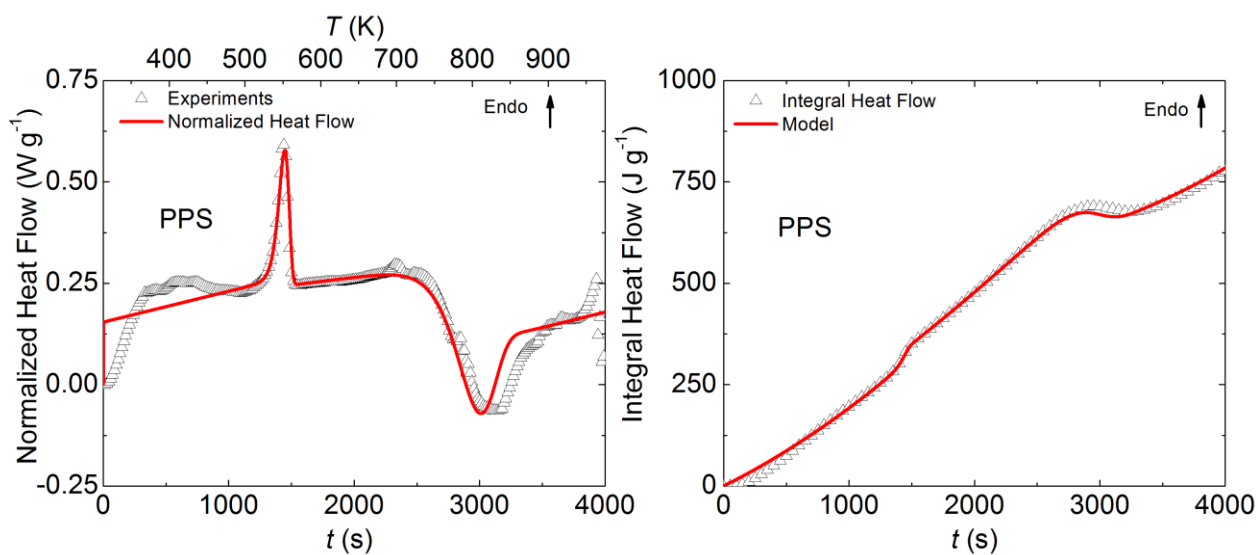


Figure 6.13 Experimental and simulated DSC of PPS at 10 K min^{-1} .

While the heat of decomposition of highly charring polymers is exothermic, it does not mean that the degradation of these polymers occurs spontaneously. It still takes a considerable amount of energy to degrade these materials. The H_g calculated for the charring materials are given in Table 6-6. H_g values listed in Table 6-6 are provided for specific heating rates (10 and 100 K min^{-1}) and specific T_e . The values obtained for low and high char yield polymers are similar in magnitude indicating that decomposition exothermicity has a minor impact on the overall thermodynamics of polymer degradation. The uncertainties provided for the low heating rate H_g values were calculated by propagating errors [151] in the thermodynamic parameters.

Table 6-6 Heats of gasification for charring polymers.

Polymer	$H_g^{298K-T_e}$, 10 K min ⁻¹ (J g ⁻¹)	T_e , 10 K min ⁻¹ (K)	$H_g^{298K-T_e}$, 100 K min ⁻¹ (J g ⁻¹)	T_e , 100 K min ⁻¹ (K)
Kydex	900 ± 9%	785	905	850
DGEBA	740 ± 18%	750	775	780
PET	1010 ± 8%	790	1095	910
Kevlar	905 ± 8%	1000	970	1175
BACY	1620 ± 12%	900	2070	1030
PPS	750 ± 10%	945	1050	1120
PEI	1060 ± 10%	970	1270	1105
PEEK	665 ± 21%	1100	1335	1540

Section 6.5 SEM of Chars

Figure 6.14 and Figure 6.15 show SEM images of the charring polymer decomposition residues generated in the thermal analysis experiments. One interesting feature of these residues is that, with the exception of one produced by PEI, the chars have a relatively homogeneous, solid-like structure at micrometer scale. This structure is fundamentally different from that of an intumescent coating char [153], which shows a fractal-like void pattern with an extremely wide range of pore sizes (from several millimeters to below 5 μm). PEI char is somewhat porous at the microscale with clear signs of exfoliation of the char layers.

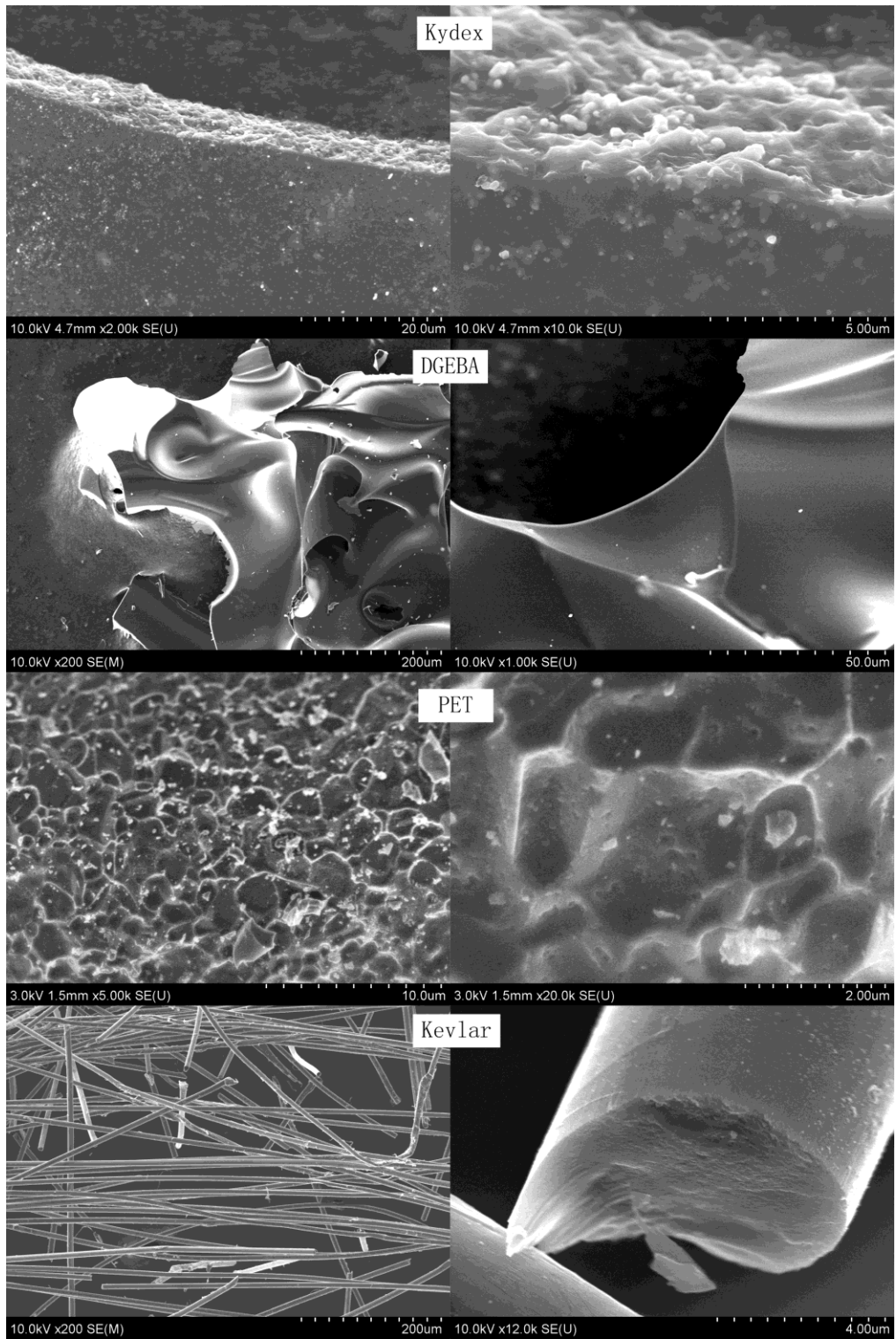


Figure 6.14 SEM images of chars produced as a result of anaerobic thermal degradation of Kydex, DGEBA, PET and Kevlar.

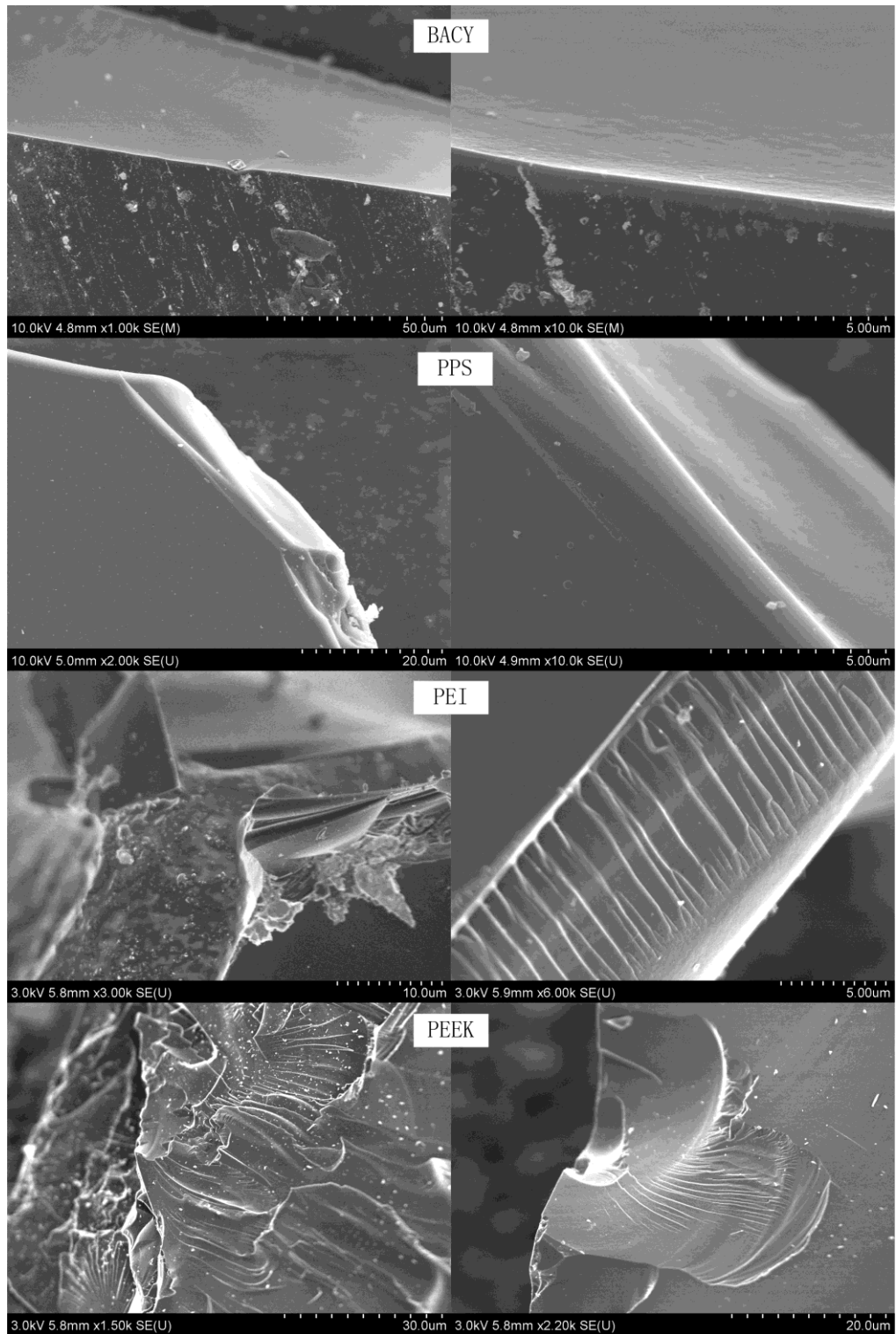


Figure 6.15 SEM images of chars produced as a result of anaerobic thermal degradation of BACY, PPS, PEI and PEEK.

Chapter 7 : Results-Heat transfer parameterization and pyrolysis model validation for non-charring polymers

Section 7.1 Absorption coefficients.

Table 7-1 summaries the absorption coefficients (in m^{-1}) obtained from this study for selective non-charring polymers that were used in the gasification experiments. The detail measurement procedure and calculation can be found in the section 3.3.1. The polymer broadband absorption coefficients used in the ThermaKin model were computed from the infrared transmission experiments and normalized by density. Thus the coefficient values were found to be 1.94, 2.12 and 2.14 $\text{m}^2 \text{kg}^{-1}$ for PMMA, HIPS and POM, respectively.

Table 7-1 Absorption coefficients for non-charring polymers

Polymers	Absorption coefficients (m^{-1})
PMMA	2240
HIPS	2250
POM	3040

Section 7.2 PMMA gasification experiment and validation part I.

Section 7.2.1 PMMA pyrolysis model parameterization

A one dimensional heat transfer scenario was produced where samples, insulated at their bottom surface, were subjected to a known radiative heat flux at their top. Bench scale gasification tests on PMMA provided requisite measurements needed to determine the material's temperature dependent thermal conductivity, k , by an inverse modeling analysis. This analysis is based on by the following assumptions: the only undefined parameters remained in the PMMA pyrolysis models were

condensed-phase thermal conductivities for all components (since kinetics and thermodynamics were measured in the Chapter 5; boundary conditions are described in Chapter 4; absorption coefficient was measured in the section 7.1; the density and thickness for PMMA samples used in bench-scale tests were measured as 1160 kg m^{-3} and 6.0 mm .) Then the thermal conductivities can be derived from average sample bottom temperatures measured in the gasification experiments. The thermal conductivity of most polymers shows a linear dependence on temperature with an abrupt change at the material's glass transition temperature, T_g [1]. Then the thermal conductivity was optimized against modeling PMMA bottom surface temperature by assuming a piecewise linear function of temperature with a discontinuity at the glass transition temperature $T_g \approx 378 \text{ K}$ [1]. Figure 7.1 shows the PMMA bottom surface temperature measurements using thermocouples at 20 and 60 kW m^{-2} . In Figure 7.1 for both heat fluxes, only average temperature (dot) from three experiments (each experiment includes 2 thermocouple measurements) are presented and the error bars indicate the uncertainties of these measurements, which are reported by calculating two standard deviations of the mean. Figure 7.1 also shows the optimization result for modeling PMMA bottom surface temperature under incident heat flux of 20 kW m^{-2} . Note that only sample bottom temperature measurements taken under incident heat flux of 20 kW m^{-2} were used in the optimization (fitting) process. Because these tests are significant longer than those at 60 kW m^{-2} thus provided larger usable data set, as demonstrated in Figure 7.1. The values of k , which were determined from the optimization process at 20 kW m^{-2} , were used to compute the PMMA bottom

surface temperature histories under incident heat flux 60 kW m^{-2} , which were not used as an optimization target. And this validation result is shown in Figure 7.1 also.

It was measured that the values of k for PMMA are: $(0.45-3.8 \times 10^{-4}T) \pm 10\%$ ($T < 378 \text{ K}$) and $(0.27-2.4 \times 10^{-4}T) \pm 13\%$ ($T \geq 378 \text{ K}$). The uncertainties are calculated as the following: k was varied, one at a time to assure its maximum variation that corresponded to a shift in the simulation results that was still within the scatter of the experimental data (which was not shown in this dissertation). The maximum variation was used to define this parameter's uncertainty.

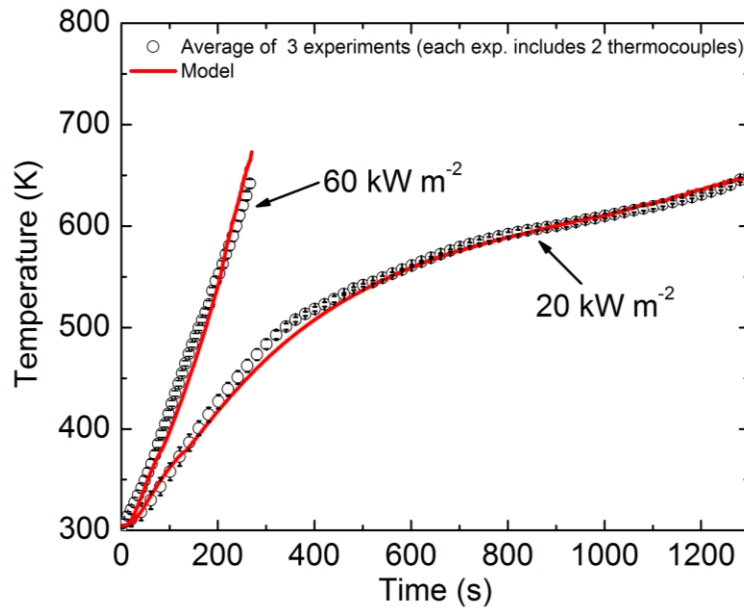


Figure 7.1 Back temperature measurement using thermocouple and model prediction of anaerobic pyrolysis for PMMA at 20 and 60 kW m^{-2} (the error bars for both heat fluxes are not significantly shown because the temperature measurement differences from two thermocouples are small).

Section 7.2.2 Prediction of burning rate for PMMA with insulation on bottom.

Until here, all the PMMA fundamental properties including kinetics, thermodynamics, heat transfer and boundary conditions are measured. The

parameterized model for PMMA gasification at this setup of experiment was validated against the experimental burning rate at various heat fluxes. Figure 7.2, Figure 7.3 and Figure 7.4 show experimentally measured (discrete points) and model predicted (solid lines) sample mass loss rate collected at three incident heat flux settings (20, 40, and 60 kW m⁻², respectively). The plots display data collected from the beginning of radiant exposure to the point of time when the PMMA sample was fully decomposed. Error bars in each figure indicate two standard deviations of the mean, calculated from three independent tests at each heat flux at each time step (1 s). The overall predictions at various heat fluxes are good with small discrepancies (< 6 % on average).

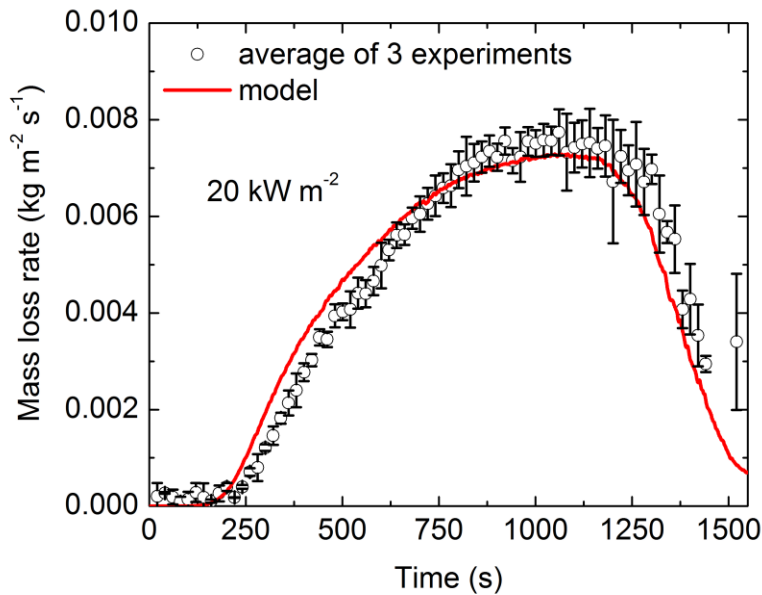


Figure 7.2 MLR measurements using CAPA and model prediction of PMMA anaerobic pyrolysis with insulation at 20 kW m⁻².

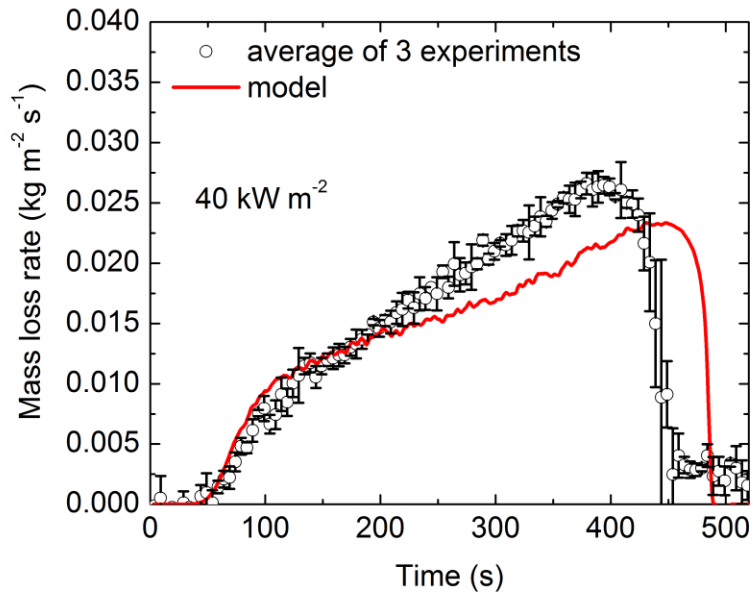


Figure 7.3 MLR measurements using CAPA and model prediction of PMMA anaerobic pyrolysis with insulation at 40 kW m^{-2} .

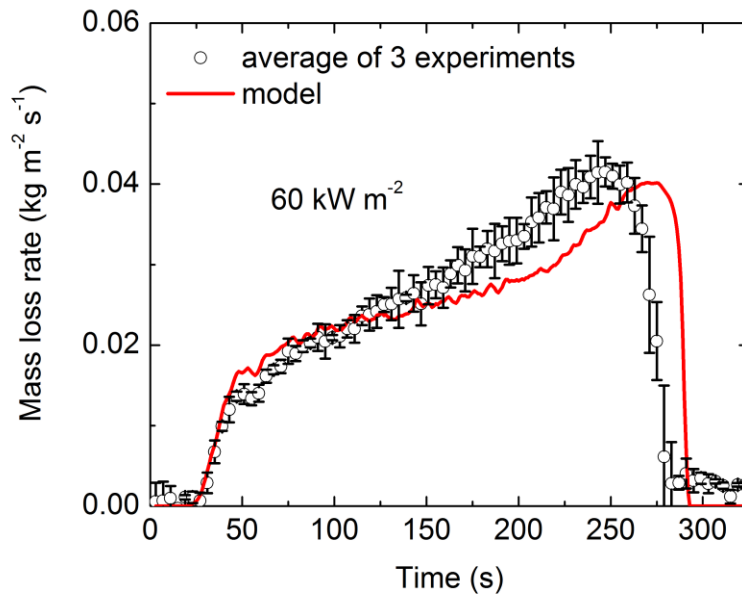


Figure 7.4 MLR measurements using CAPA and model prediction of PMMA anaerobic pyrolysis with insulation at 60 kW m^{-2} .

Section 7.3 Gasification experiment and validation part II for non-charring polymers

Section 7.3.1 Uniformity of thermometry for non-charring polymers

One of the major assumptions in the gasification work that performed under CAPA is one-dimensional pyrolysis. Thus it is important to check the bottom surface temperature uniformity, which is hard to obtain using limited number of thermocouples as described in the section 3.3.2.

An example of infrared images of the bottom sample surfaces at different stages of gasification for PMMA, POM and HIPS is shown in Figure 7.5. These images indicate that the surface temperature stays close to being spatially uniform with the largest difference (≈ 15 K) observed between the mesh and foil and attributed to the thermal resistance of the mesh-foil interface.

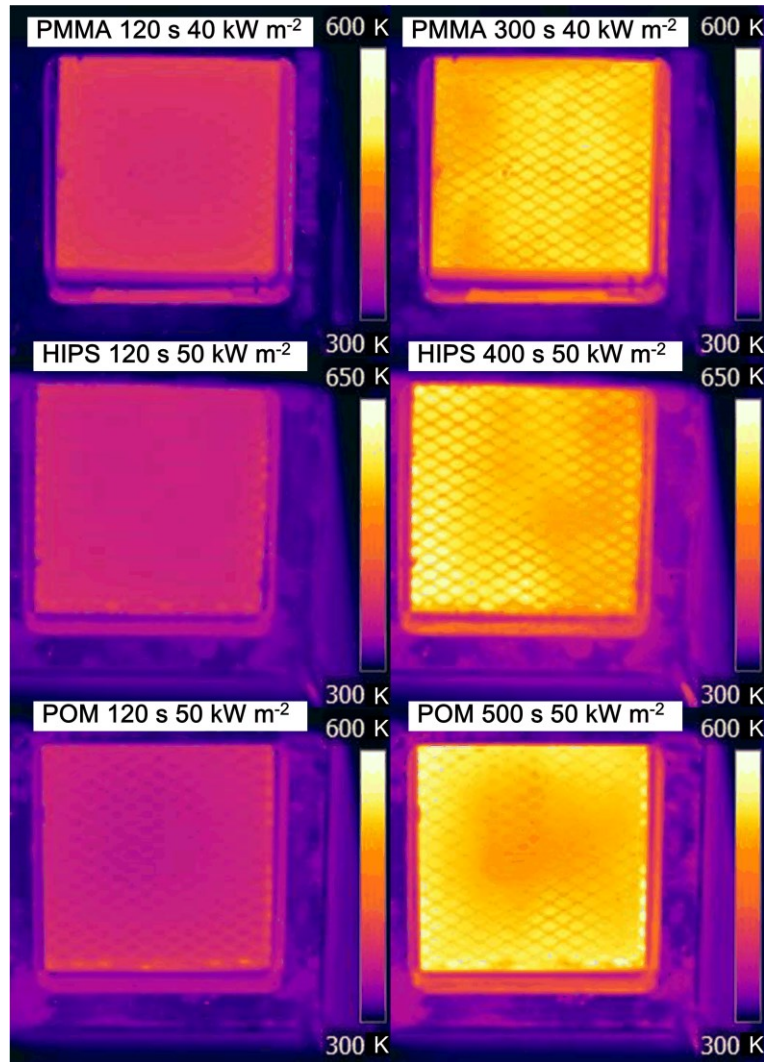


Figure 7.5 Infrared images of bottom surfaces of the non-charring samples undergoing gasification.

A quantitative comparison of the temperature histories sampled from different areas of the bottom surface of PMMA subjected to 40 kW m^{-2} of radiant heat flux is shown in Figure 7.6. The temperature histories obtained by randomly sampling pixels at the center (area 1) and middle (area 2) of the surface are well within each other uncertainties. These uncertainties were calculated as two standard deviations of the mean. The temperature of the peripheral area (area 3) deviates slightly from that of the central areas towards the end of the experiment. This deviation was attributed to a

partial obscuration of camera view by gaseous decomposition products, small amounts of which had a tendency to accumulate in the space below and near the outer edge of the sample holder.

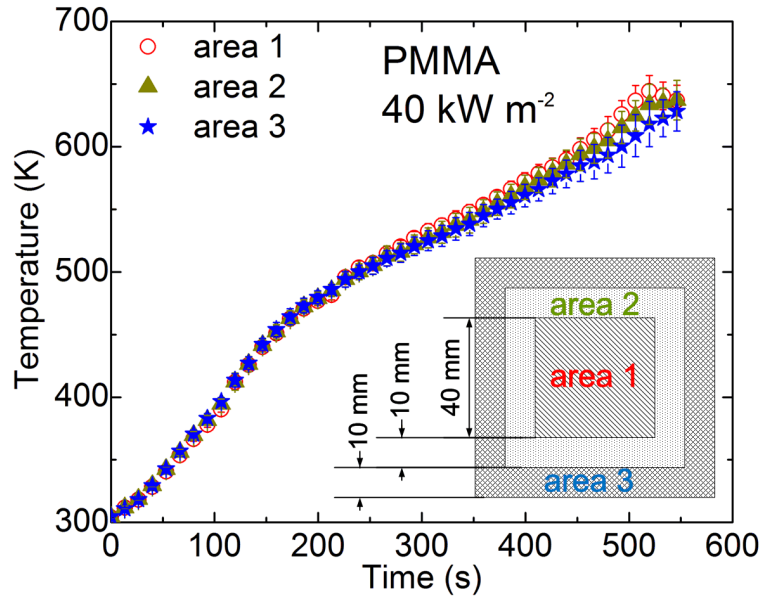


Figure 7.6 Spatial variation in bottom surface temperature histories.

Section 7.3.2 Thermal conductivity calibration and validation for non-charring polymers

The average sample bottom temperature history obtained from IR camera for PMMA gasified at 20 kW m^{-2} of radiant heat flux is shown in Figure 7.7 (circles). In this figure, each temperature point is the average of 90 pixels (36 from area 1, 36 from area 2, and 18 from area 3) which represents 10 randomly selected cursors (each cursor contains 9 pixels) further averaged over 3 gasification experiments. Error bars in Figure 7.7 show the uncertainties of the IR camera temperature measurements by computing the two times of standard deviation over the mean. The PMMA components thermal conductivities were calibrated from the section 7.2.1. The prediction of PMMA bottom surface temperature without insulation (using the

exactly same PMMA properties that used in the section 7.2.1) at 20 kW m^{-2} of radiant heat flux is also shown in Figure 7.7 (line). Besides, as it was demonstrated in Figure 7.8 , the derived thermal conductivity parameters also provide a good description of 40 and 60 kW m^{-2} bottom surface temperature histories. At all heat fluxes, the quality of agreement between the model and experiments tends to under predict somewhat to the IR measurements at different degrees. But the overall trends are close and the maximum discrepancy is found to be about 5%.

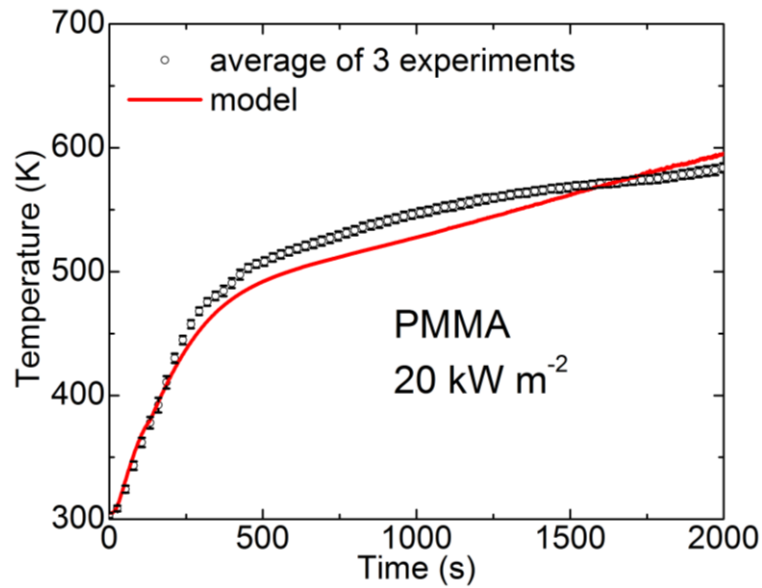


Figure 7.7 Experimental and simulated bottom surface temperature histories obtained for PMMA at 20 kW m^{-2} .

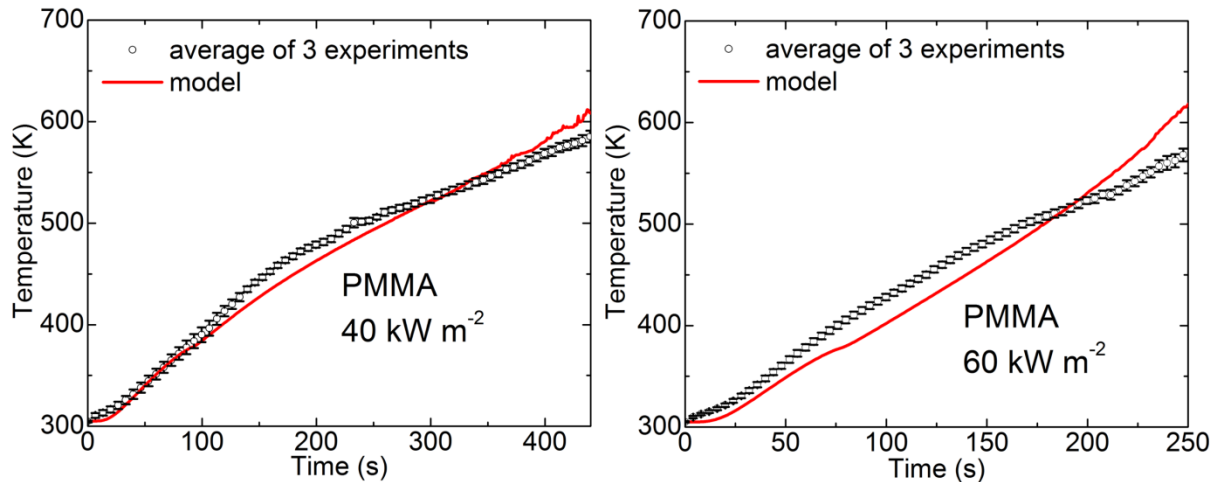


Figure 7.8 Experimental and simulated bottom surface temperature histories obtained for PMMA at 40 and 60 kW m⁻².

The HIPS and POM samples were 6.0 and 6.6 mm thick, respectively. Their densities were measured at room temperature and found to be 1060 and 1420 kg m⁻³, respectively. The thermal conductivities of the condensed-phase components representing HIPS and POM were determined using essentially the same approach. In all cases, the temperature data collected in the lowest heat flux gasification experiments were used as an optimization target because of the smallest uncertainties in the experimental conditions. Figure 7.9 (optimization target) and Figure 7.10 (validation results) show the experimental and simulation results of HIPS sample bottom surface temperature for 30 kW m⁻² and 50 and 70 kW m⁻² respectively. Experimental and simulated results for the POM sample bottom surface temperature at 30 kW m⁻² and 50 and 70 kW m⁻² are shown in Figure 7.11 (optimization target) and Figure 7.12 (validation results) respectively. For most of the comparisons, the quality of agreement between the model and experiments tends to deteriorate somewhat at later times and higher temperatures, where experimental data become less reliable due to decomposition of the high emissivity paint, camera view obscuration by pyrolyzates

and increasing uncertainties in the sample thickness and incident radiant heat flux. The resulting thermal conductivity expressions are summarized in Table 7-2. For POM, separate linear temperature dependencies were assigned to the original polymer, POM_mlt and POM_int.

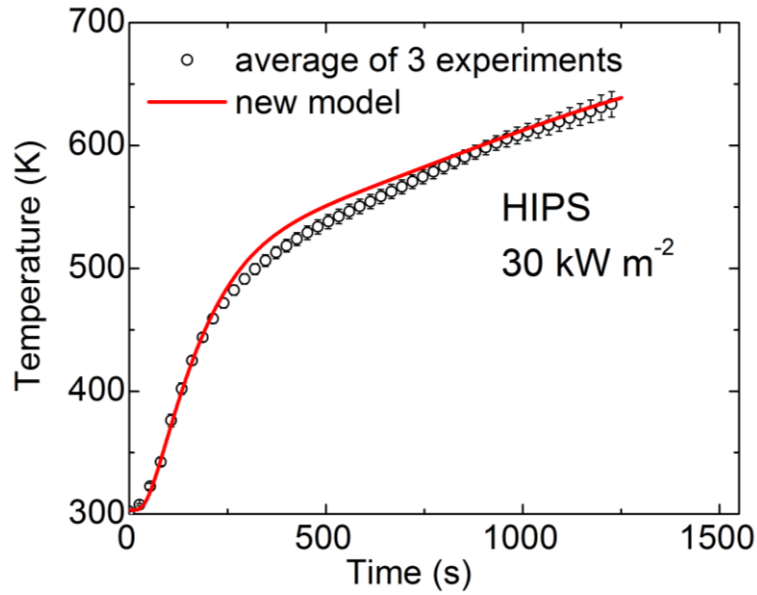


Figure 7.9 Experimental and simulated bottom surface temperature histories obtained for HIPS at 30 kW m^{-2} .

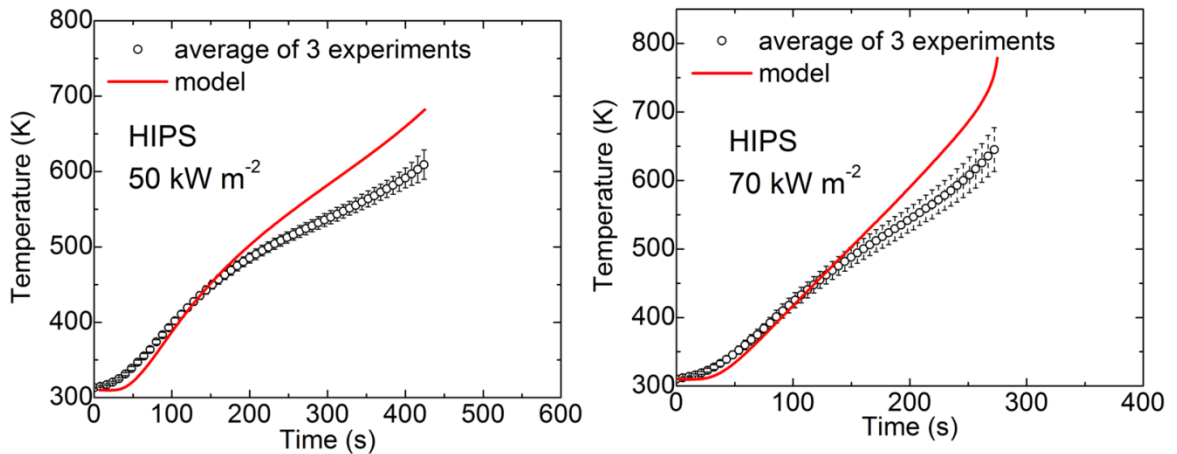


Figure 7.10 Experimental and simulated bottom surface temperature histories obtained for HIPS at 50 and 70 kW m^{-2} .

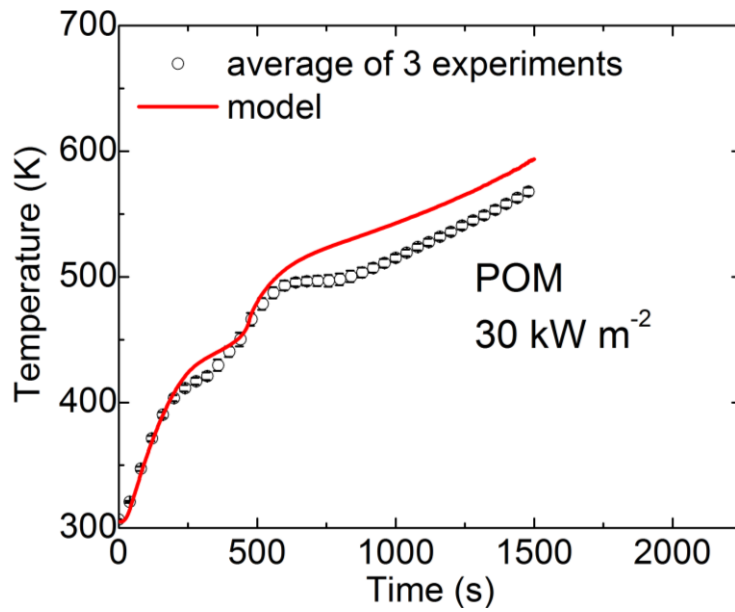


Figure 7.11 Experimental and simulated bottom surface temperature histories obtained for POM at 30 kW m^{-2} .

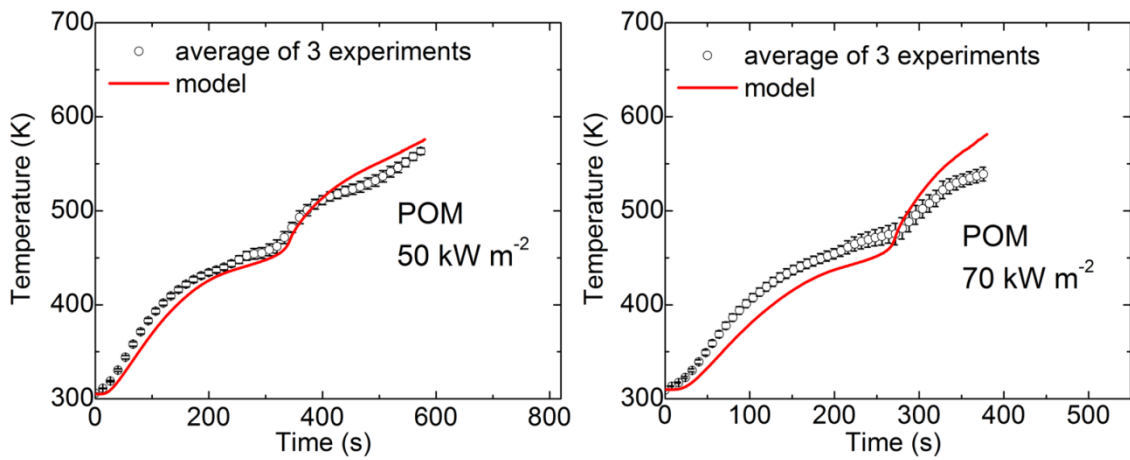


Figure 7.12 Experimental and simulated bottom surface temperature histories obtained for POM at 50 and 70 kW m^{-2} .

Table 7-2. Thermal conductivities for HIPS and POM.

Polymer	Thermal Conductivity ($\text{W m}^{-1} \text{K}^{-1}$)
---------	---

HIPS	$(0.10+1.0\times 10^{-4}T) \pm 5\%$
POM	POM: $(0.25+1.6\times 10^{-5}T) \pm 10\%$
	POM_mlt: $(0.21+8\times 10^{-6}T) \pm 15\%$
	POM_int: $(0.19-6\times 10^{-5}T) \pm 20\%$

To further investigate the k for PMMA that obtained in section 7.2.1, its value was compared to a list of literature values [71, 100-102, 154-156] that shown in Figure 7.13. As the results shown in this figure, between 378 and 600 K, the measured conductivity values lie roughly in between those previously measured by Assael *et al.* [154] and Stoliarov *et al.* [71]. Below 378 K, our current values are over 50% higher. This discrepancy is a consequence of the current presentation of the heat capacity as a linear temperature function, which ignores a discontinuity at the glass transition. While this presentation results in a significantly overestimated low temperature thermal conductivity, it has negligible impact on the overall heat transport and the heat of gasification [77].

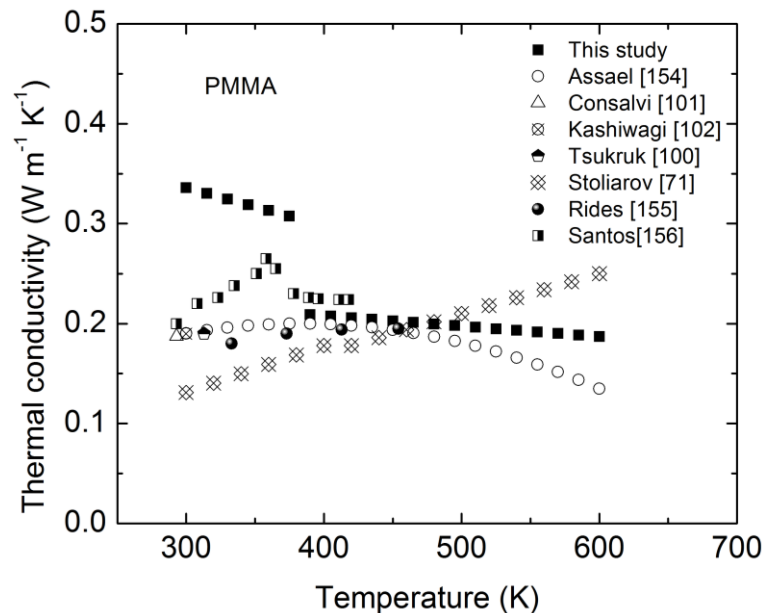


Figure 7.13 Thermal conductivity for PMMA.

As shown in Figure 7.14, the HIPS thermal conductivity is consistent with that reported by dos Santos [157]; however, it is about 25% lower than the values previously measured by Stoliarov *et al.* [71] in the same temperature range. The latter discrepancy is likely to be a consequence of the difference in the composition of HIPS, which is a manufacturer-specific copolymer/blend of polystyrene and polybutadiene.

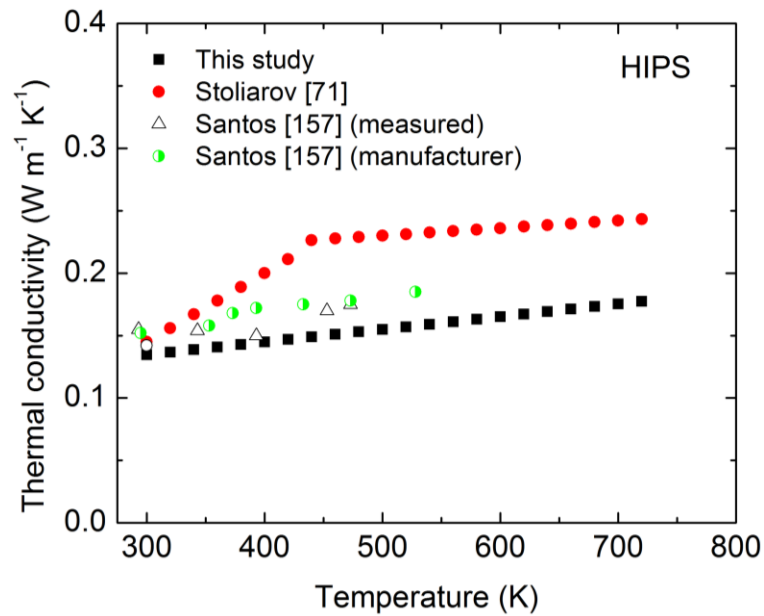


Figure 7.14 Thermal conductivity for HIPS.

The thermal conductivity of POM obtained in this work is similar to that recently measured by Linteris *et al.*[40] as shown in Figure 7.15. Other literature data [158, 159] are only available at room temperature and scattered in Figure 7.15.

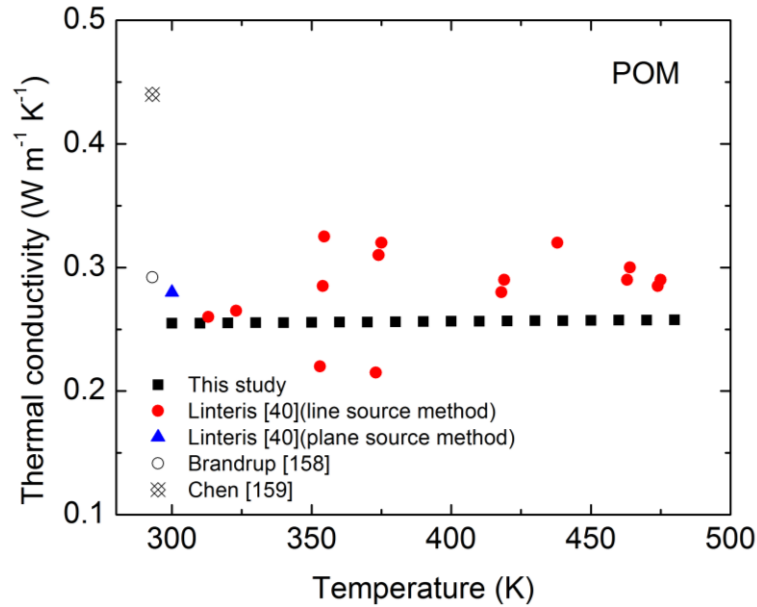


Figure 7.15 Thermal conductivity for POM.

Section 7.3.4 Prediction of burning rate for non-charring polymers

A comparison of the burning rates computed using the fully parameterized PMMA model with the results of the gasification experiments is shown in Figure 7.16. The model predicts the burning rates at a range of radiant heat fluxes with the accuracy comparable with the experimental repeatability.

The final comparison between the HIPS and POM models and the results of the corresponding gasification experiments is shown in Figure 7.17 and Figure 7.18. The model of HIPS demonstrates the quality of predictions similar to that observed for PMMA. POM burning rates are slightly (by average of about 13%) underpredicted by its model for all the heat fluxes, which suggests that the heats of POM decomposition are somewhat overestimated.

The total mass loss of experiment data is found to be approximately 4.3 %, 5.0 % and 1.4 % on average larger than the model predictions for PMMA, HIPS and

POM respectively because of the following reasons. The primary reason is due to two additional materials used in the experiments that were not mentioned in the model. They are glue which was used to stick Kaowool insulation layers and paper tape to prevent drippings during gasification experiment. When those two materials were placed together with the sample holder, they were partially or fully decomposed and the volatiles generated from those two material's decomposition were hardly separately from the total mass loss that from the experimental reading. The contributions of those two material's mass loss were estimated about 2.0 % and 0.5 % respectively. The other reason is probably caused by the errors of those materials' sizes (i.e size cutting error and thickness measurements error). It was found to be about 1-2 % on average.

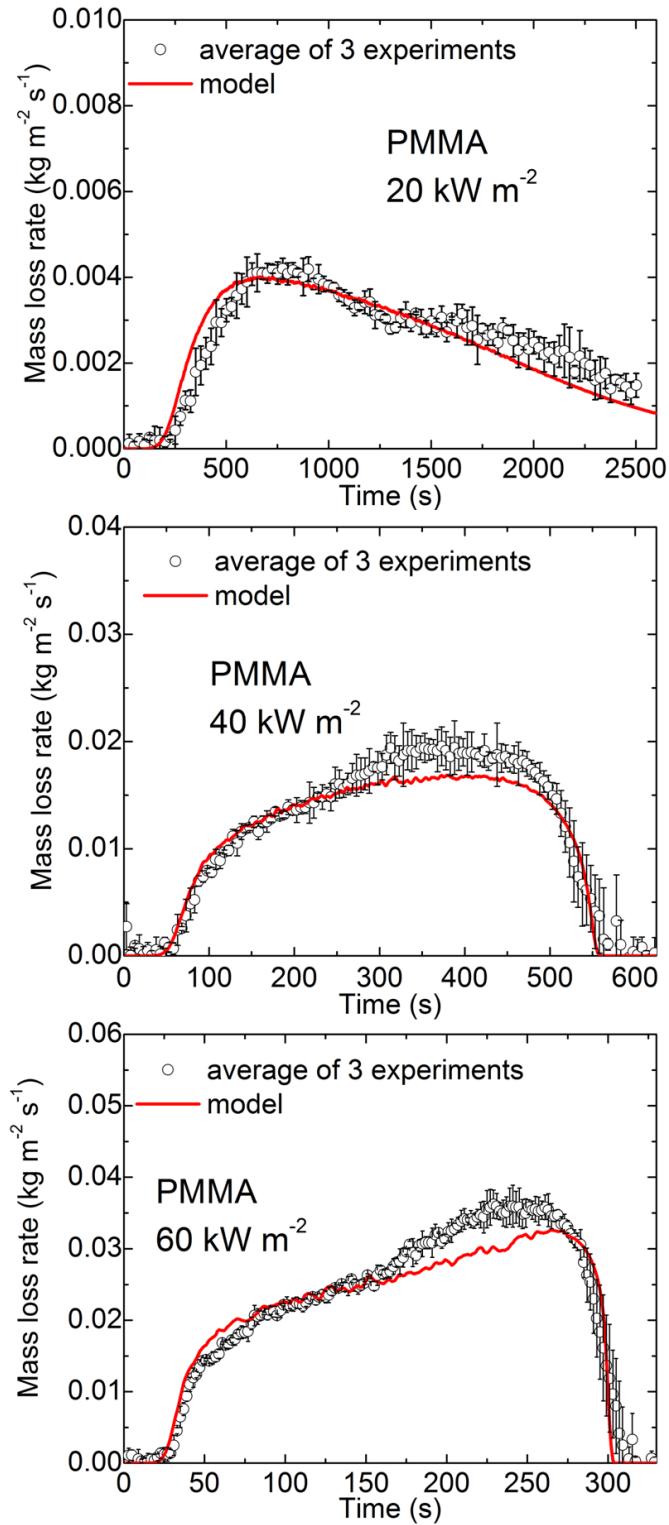


Figure 7.16 Experimental and simulated burning rate histories obtained for PMMA at 20-60 kW m⁻².

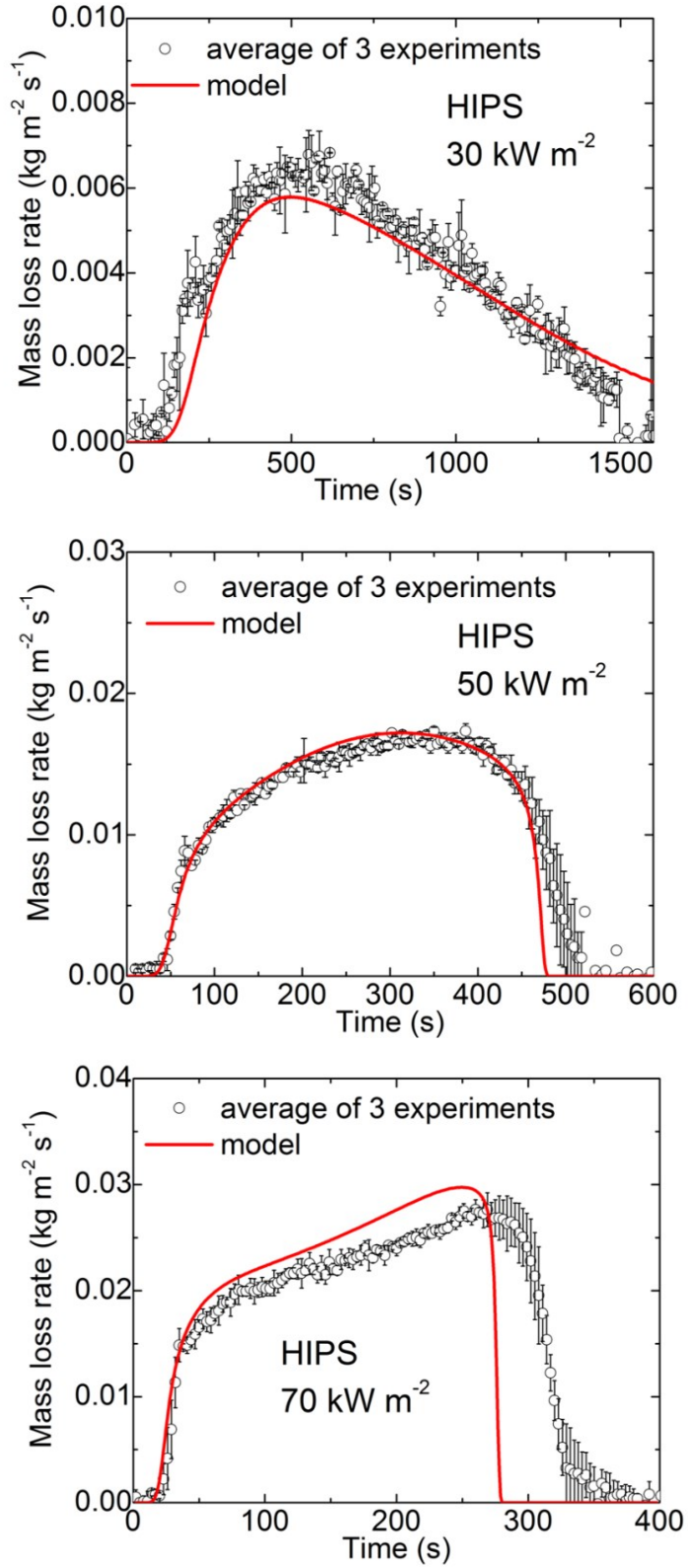


Figure 7.17 Experimental and simulated burning rate histories obtained for HIPS at 30-70 kW m⁻².

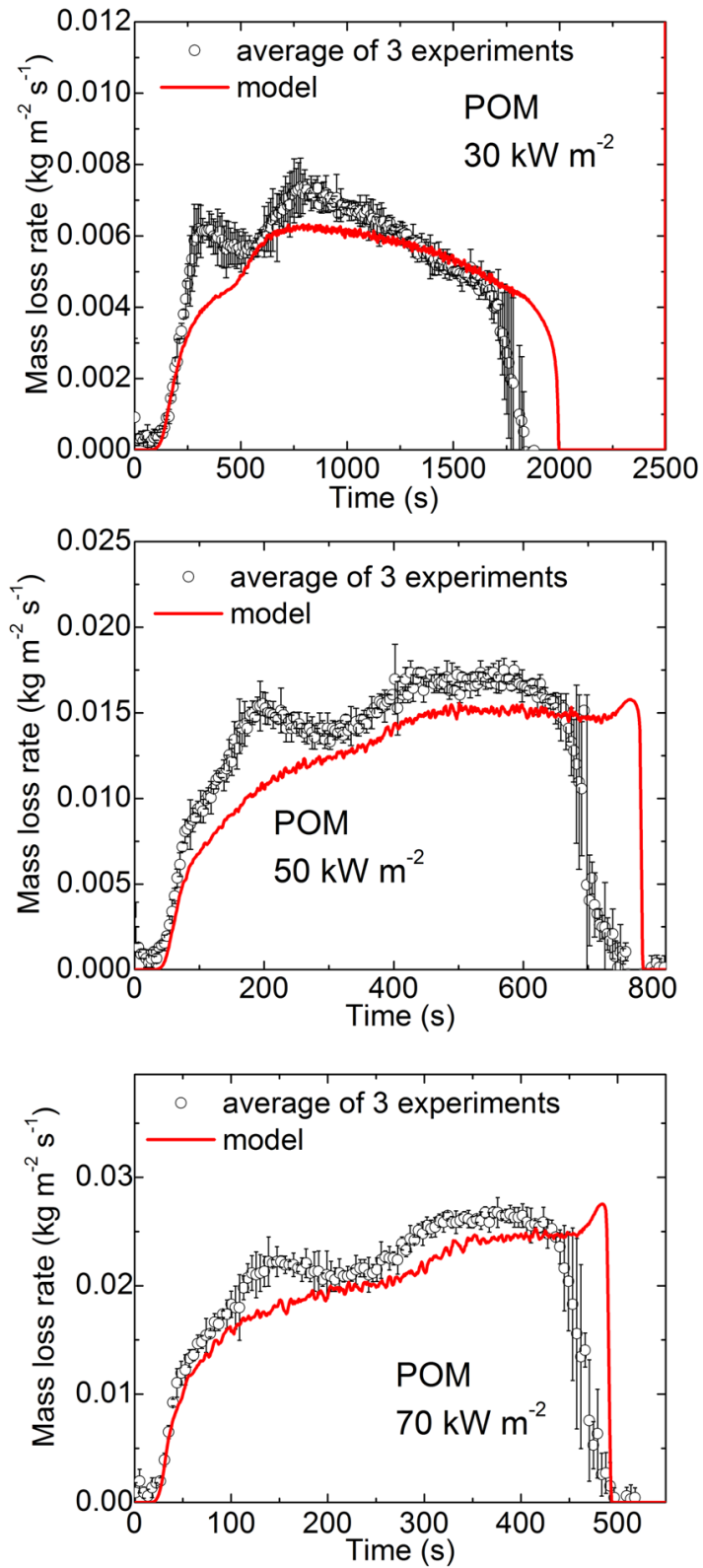


Figure 7.18 Experimental and simulated burning rate histories obtained for POM at 30-70 kW m⁻².

Chapter 8 : Results-Heat transfer parameterization and pyrolysis model validation for charring polymers

In this chapter, results of the bench-scale gasification results are presented including studying on ABS, PET, Kydex and PEI followed by the procedure described in the section 3.3.3. The reason why ABS is considered here is because, different from its TGA data, ABS produces different amount of char residue under various level of external heat fluxes, which has not been found in other non-charring polymers. For ABS at 30 kW m^{-2} , residue near the end of experiments remains about 35% (not decomposed completely) and this value is found to be about 4.5%, which is close to its TGA data (2.3%), under external radiative heat flux of 50 and 70 kW m^{-2} . Therefore, ABS was included in this chapter and treated as a charring polymer. Gasification experiments for PET were only conducted at 50 kW m^{-2} and 70 kW m^{-2} . Because PET melts during thermal decomposition and the molten PET, unlike other molten polymers, is low viscous fluid which drips from the edges of the sample holder and no good results can be obtained at the external heat flux of 30 kW m^{-2} . PEI gasification experiments were not conducted at 30 kW m^{-2} because no obvious mass generation was recorded at this heat flux level. Therefore, external heat fluxes from 50 to 90 kW m^{-2} were applied for PEI. ABS and PET results are presented together because the char yields are significant smaller and the char size changes were observed significant different than the other two polymers. Kydex and PEI, who were found to produce relative large amount of intumescent char during their gasification experiments are presented together in each section (sections 8.2 to 8.5).

Section 8.1 Absorption coefficients.

Table 8-1 summaries the absorption coefficients (in m^{-1}) obtained from this study for the polymers that were studied in this chapter. The data in this table are the mean values from two independent measurements for each material. The mean variance of these two measurements is about 3 % to the mean values.

Table 8-1 Absorption coefficients for ABS and charring polymers

Polymers	Absorption coefficients (m^{-1})
ABS	1800
PET	1935
Kydex	2145
PEI	1745

Section 8.2 Experimental observation

Section 8.2.1 ABS and PET

Figure 8.1 shows the char residues after gasification experiments for ABS at 50 kW m^{-2} . And Figure 8.2 displays the side video snapshots and bottom temperature for ABS under external heat flux of 50 kW m^{-2} at 0, 100, 200 and 400 s during gasification experiments. From the comparison at different stages of ABS pyrolysis at the heat flux of 50 kW m^{-2} , the temperature uniformity is quantified by calculating the maximum average temperature variations among the three area regions (see how the areas are divided in the section 3.3.3; data are available in the section 8.4) and termed as uniformity variation. And the value of this variation is found to be small (about 25 K) throughout the tests for ABS. The possible reason to cause this variation could be

the deformation of ABS sample to generate a possible gap between the sample and the aluminum foil.



Figure 8.1 Char residues after gasification experiments for ABS at 50 kW m^{-2} .

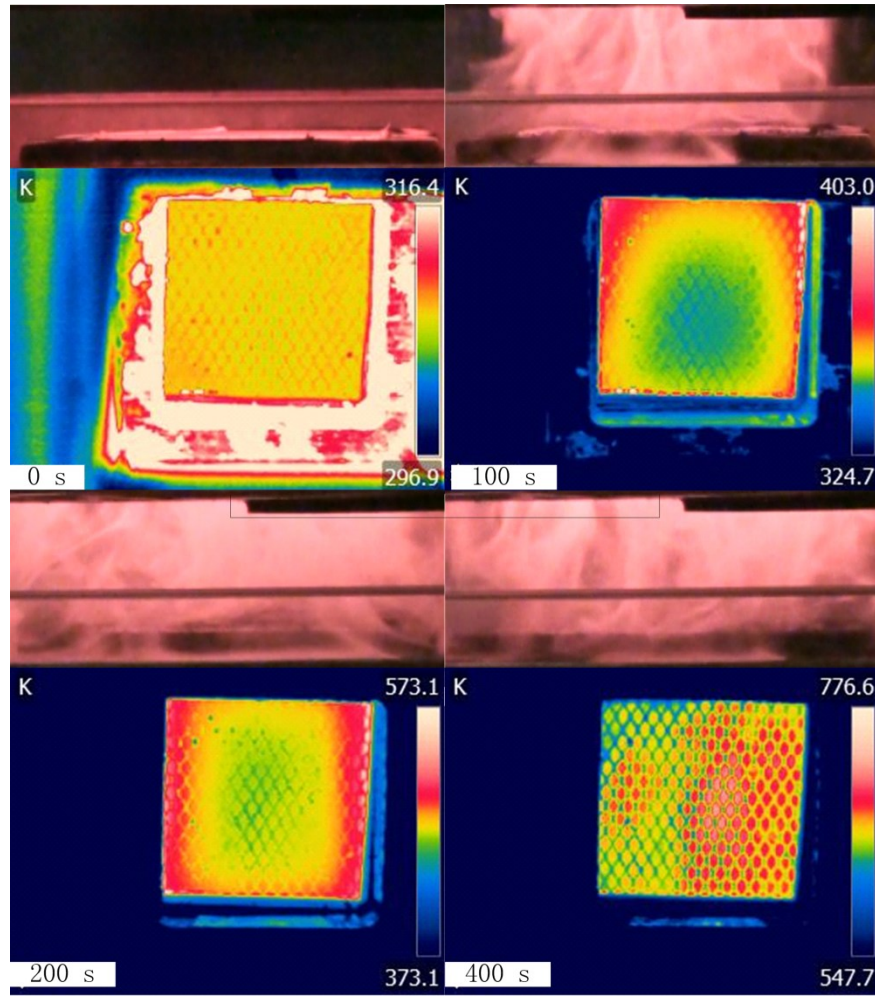


Figure 8.2 Infrared images of bottom surfaces of the ABS sample undergoing gasification at 50 kW m^{-2} .

The PEI char residue after gasification at 50 kW m^{-2} forms a brittle and porous hollow carbon-based object, as illustrated in Figure 8.3. In this figure, the bulk volume of the residue does not change significantly respect to the virgin PEI sample volume. It is observed from Figure 8.4 that the top surface of the testing sample during gasification experiments is nearly flat. Therefore, this is still a one-dimensional problem and the bottom surface temperature from the IR camera measurements indicates the temperature uniformity is not bad (the uncertainty variation is within 15 K). As it is presented in Figure 8.4, portion parts of the bottom

appear lower temperature nearby the edges of the testing sample near the end of the gasification, which is likely due to the dripping that discussed earlier in this Chapter. When dripping occurs, the dripping flow is accumulated near the edges of aluminum mesh and experiences natural cooling. The dripping is found significant severely at 30 kW m^{-2} when the burning rate is low, thus no data was recorded for this heat flux level.



Figure 8.3 Char residues after gasification experiments for PET at 50 kW m^{-2} .

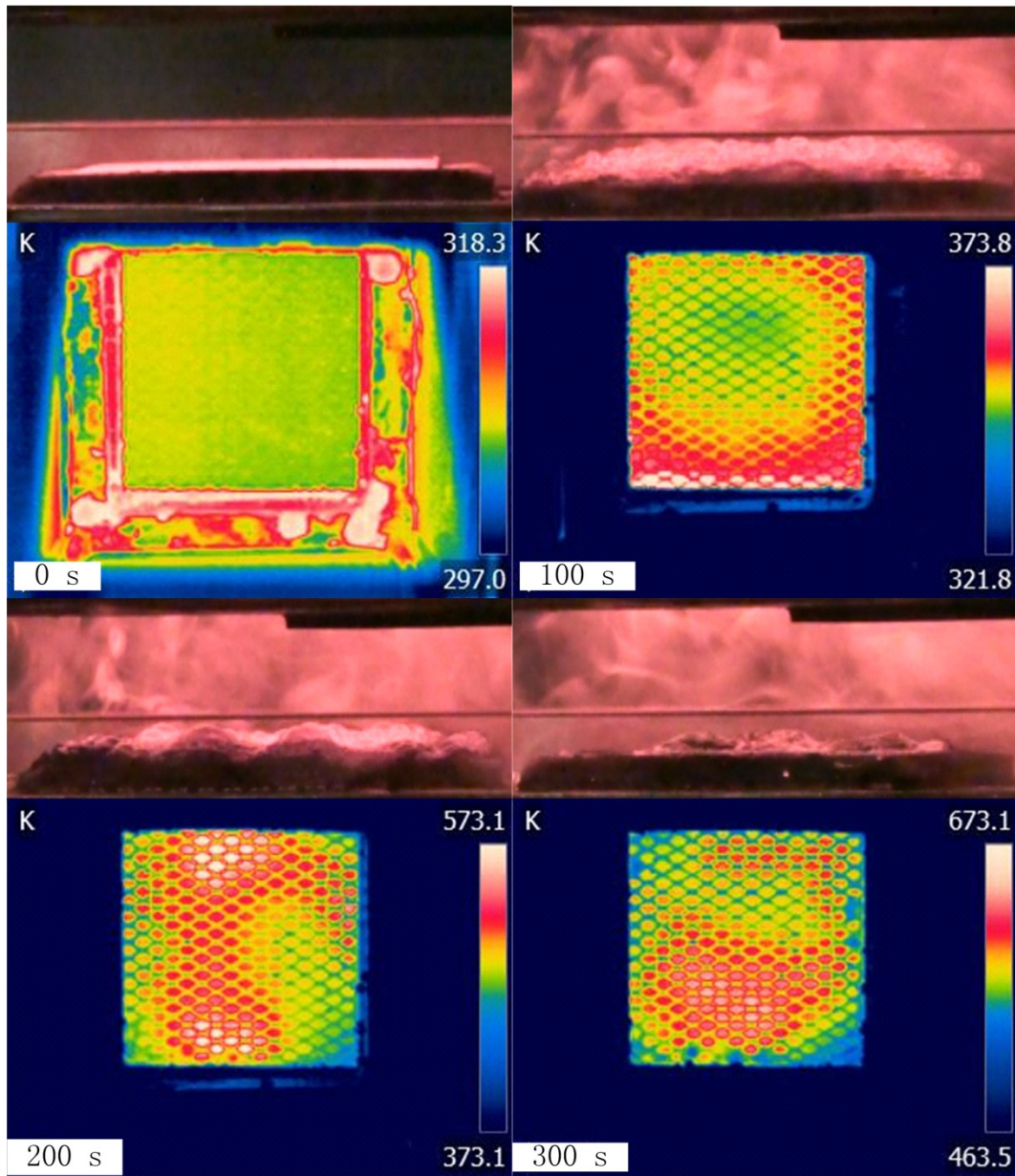


Figure 8.4 Infrared images of bottom surfaces of the PET sample undergoing gasification at 50 kW m^{-2} .

Section 8.2.2 Kydex and PEI

One of the interesting phenomenon observed during Kydex gasification experiments is the growth of char. As shown in Figure 8.5, the height of char residue after Kydex complete decomposition at 50 kW m^{-2} is about 6 cm (please note that the char was laid down and the top surface is facing up in this figure). The growth of the

char can be further witnessed by the snapshots from the side video camera, as shown in Figure 8.6. Please note that the black semi-circles shown on some of the images at latter period of tests are corresponding to the appearance of cone heater reflected from the gold coated mirror when the base of the testing sample shrinks gradually. In the meanwhile, the height of the testing sample rises and the whole object forms like a mushroom. Clearly from visual observation, the shape of Kydex char differs significant from ABS and PET. This observation threatens the one-dimensional assumption. However as it demonstrated from Figure 8.6, until 200 s, the testing sample is fairly under a one-dimensional heat transfer scenario because of the top surface is nearly flat and bottom surface temperature is crudely uniform (with maximum uniformity variance of 25 K).



Figure 8.5 Char residues after gasification experiments for Kydex at 50 kW m^{-2} .

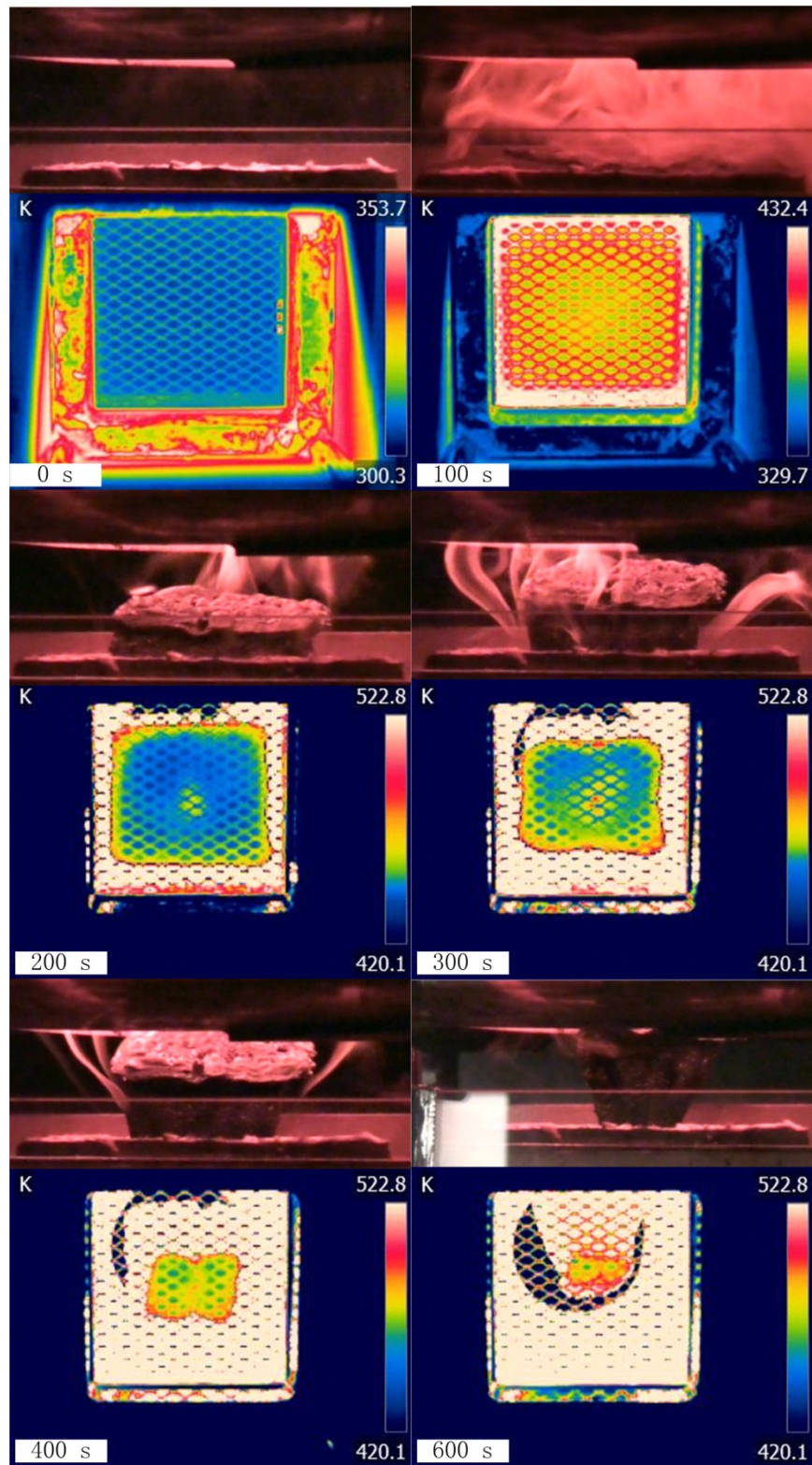


Figure 8.6 Side views and Infrared images of bottom surfaces of the Kydex sample undergoing gasification at 50 kW m^{-2} .

As mentioned earlier in this Chapter, PEI experiences similar features of char morphological changes as Kydex does during gasification experiments. However, PEI produces more char residues than Kydex does both in milligram TGA tests and bench-scale gasification tests. It was found that larger amount of char and pyrolyzing intermediacy formed in PEI gasification experiments generates heavier and bigger charring layers than in Kydex experiments, as shown in Figure 8.7. Please note that the top region part of the char residue shown in Figure 8.7 had to be removed to be taken out of the CAPA.

Figure 8.8 illustrates the PEI top surface morphological and bottom surface temperature changes during gasification at 50 kW m^{-2} . The temperature uniformity on the bottom surface is poor (about 35 K uniformity variations) and area 1 is clearly cooler than the area 2 and area 3 because of thicker char layer formed at the center. The aim of this work is developing a systemic methodology to measure the polymer including decomposition products properties that serves as inputs for CFD models at a modest experimental cost. However, to model some of the charring polymers like PEI need detail information about the progress changes of char structure and how it affects the heat transfer at the condensed phase which cannot be obtained from the current procedure.

When the PEI sample is swelling until its top surface reaching the cone heater, the anaerobic assumption also fails. Our measurement of oxygen concentration based on current experimental setup is found to be about 2.2 vol. % near the initial top surface. However, when a testing polymer expands and grows into the cone heater, the pyrolyzing polymer is expected to experience partial oxidation or even burning

because the oxygen concentration possibly reaches above 10 vol. %. Either from the side video or onsite experimental observation, visible flame was observed clearly at 70 and 90 kW m⁻² after the top surface reaching inside the cone heater. Therefore, the portion of the experimental data before the sample top surface reaches inside the cone heater at all conditions is considered valid for anaerobic assumption.



Figure 8.7 Char residues after gasification experiments for PEI at 50 kW m⁻².

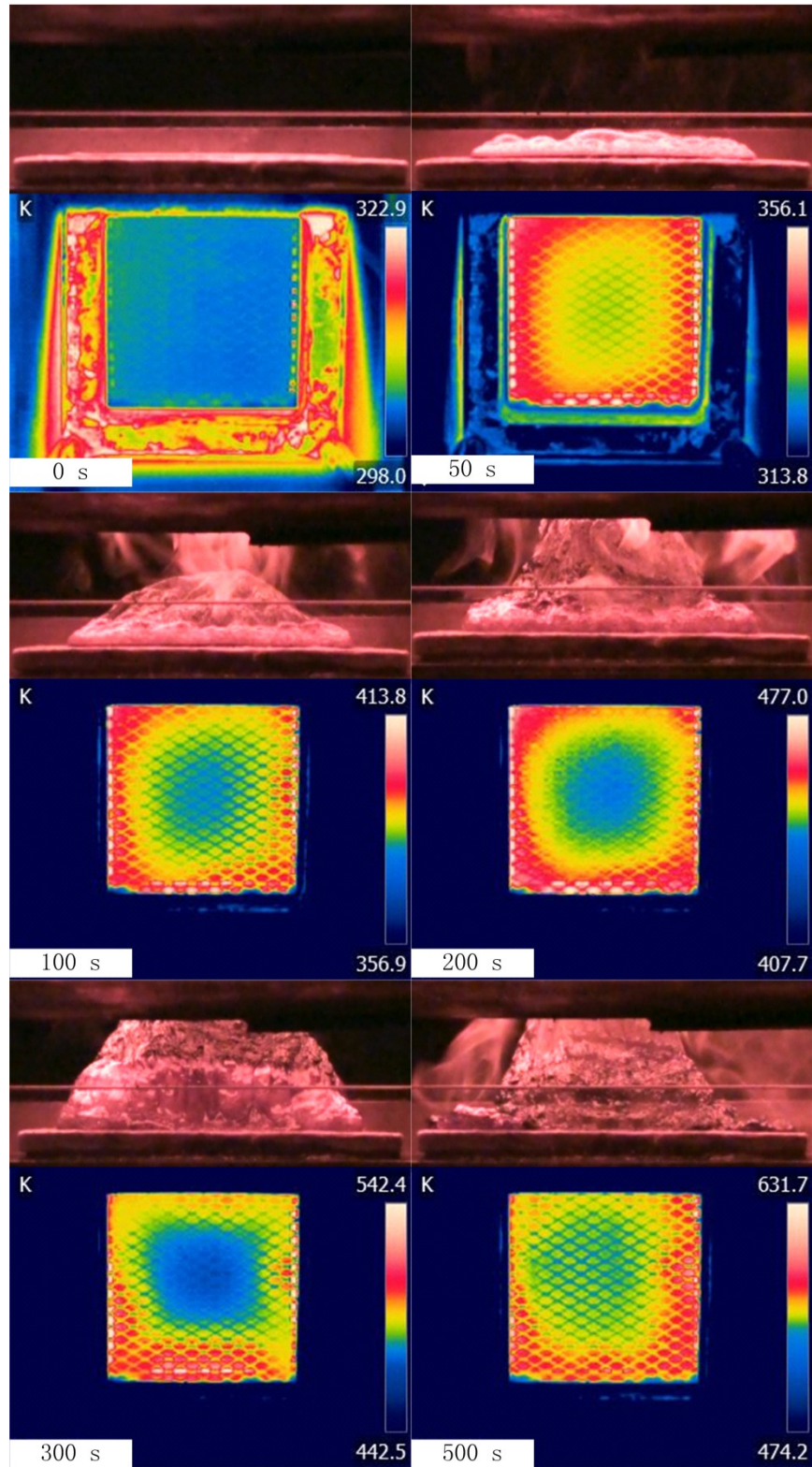


Figure 8.8 Side views and Infrared images of bottom surfaces of the PEI sample undergoing gasification at 50 kW m^{-2} .

Section 8.3 Modeling

Section 8.3.1 ABS and PET

ABS and PET virgin sample thicknesses were measured as 6.4 and 6.7 mm respectively at the room temperature. Then the density values for virgin ABS and PET are calculated as 1050 and 1385 kg m⁻³ respectively. The absorption coefficient values were found to be 1.71 and 1.40 m² kg⁻¹ for ABS and PET respectively. PET char was collected after completed decomposition at 50 kW m⁻² (experimental results show the sample is completely decomposed) and its bulk density was measured using a ruler and a balance at room temperature to measure its bulk volume and mass respectively. PET_melt density and absorption coefficient are assumed to be same as the values of PET. The PET char bulk density value is approximate to 80 kg m⁻³. As mentioned in the chapter 4, the density of PET_int is assumed to be the mean value of PET and PET_char. The absorption coefficient of PET_int is assumed same as the value of PET. The ABS char bulk density is assigned to be equal to the PET char bulk density value since the size of pure char produced at ABS gasification tests at 50 kW m⁻² is fairly small, as demonstrated from Figure 8.1, therefore it is hardly to measure ABS char bulk volume using a ruler. The heat capacity of char produced by ABS thermal decomposition (was not measured in the milligram scale work) is assumed to be same as the PET char heat capacity which was measured and reported in Chapter 6.

ABS and PET's kinetic and thermodynamic properties were obtained from the milligram-scale study in the Chapter 5 and the Chapter 6, respectively. The mass transport coefficient and heat transfer boundary conditions were defined in the section 4.3.

Section 8.3.2 Kydex and PEI

Kydex and PEI virgin sample thicknesses were measured as 6.1 and 6.6 mm respectively at the room temperature. Then the density values for virgin Kydex and PEI are calculated as 1350 and 1285 kg m⁻³ respectively. The absorption coefficient values were found to be 1.58 and 1.36 m² kg⁻¹ for Kydex and PEI respectively. The PEI_melt density is assumed same as PEI. The char residues for both polymers were collected after gasification experiments at 50 kW m⁻². This heat flux is chosen because it is considered as the most promising condition to obtain best char residue because of the following reasons. For Kydex, it was found that the char yield at this level of heat flux is close to the char yield value that obtained at TGA test, in which pyrolyzing sample is considered to be fully decomposed. In the case of PEI, 50 kW m⁻² (the lowest heat flux used in PEI gasification experiments) is chosen because it was found that visible flame appears on top of pyrolyzing sample surface when the pyrolyzing sample swells into the cone heater only at 70 and 90 kW m⁻². The flame is likely to destroy the PEI residue and brings less char yield compared to the non-flaming situation at 50 kW m⁻². The calculation of the residue density for Kydex and PEI was based on observation of the residue shape which is pyramid-like. The bulk volumes of the residue for both polymers were estimated carefully by measuring their lengths and heights with a ruler at room temperature. The entire mass of Kydex residue is considered to the mass of pure Kydex char and this char density is then calculated approximately to 100 kg m⁻³. Calculation on PEI char mass is somewhat different. At 50 kW m⁻², PEI residue mass was found about 88 wt. % compared to its initial mass. This means about 12 wt. % of volatiles were escaped from the condensed phase and in the meanwhile, 12 wt. % of char was produced at the condensed phase

because, from the TGA result, PEI samples produces about 50 % char during thermal decomposition. Here the density of PEI char can be estimated by excluding the unpyrolyzed mass and volume from the entire residue mass and bulk volume and its value is found to about 80 kg m^{-3} . As discussed in the chapter 4, the densities of intermediate component of those two polymers are assumed to be same as their char density.

Kydex and PEI 's kinetic and thermodynamic properties were obtained from the milligram-scale study in Chapter 6.

Differently from boundaries characterization of the ABS and PET, the top surface of the Kydex and PEI samples rise significantly during the experiments and therefore, the prescribed heat flux that acting on the sample top surface is also increasing. ThermaKin allows linear external heat flux function in its one-dimensional version. In addition to the bottom temperature and mass loss rate measurements for Kydex and PEI gasification experiments, the total heights from the sample top surface to its bottom were recorded by analyzing the video data obtained from the side camera. The Kydex pyrolyzing sample top surface is nearly flat during experiments (as demonstrated in Figure 8.6) and the top surface is considered as its maximum height. While PEI top surface experiences hill-like changes (as demonstrated in Figure 8.8), the value of the height for PEI (Figure 8.9 right part) is reported as 80% of its maximum height. The relation between the sample height and time for both polymers can be characterized at various heat fluxes by fitting them linearly, as illustrated in Figure 8.9.

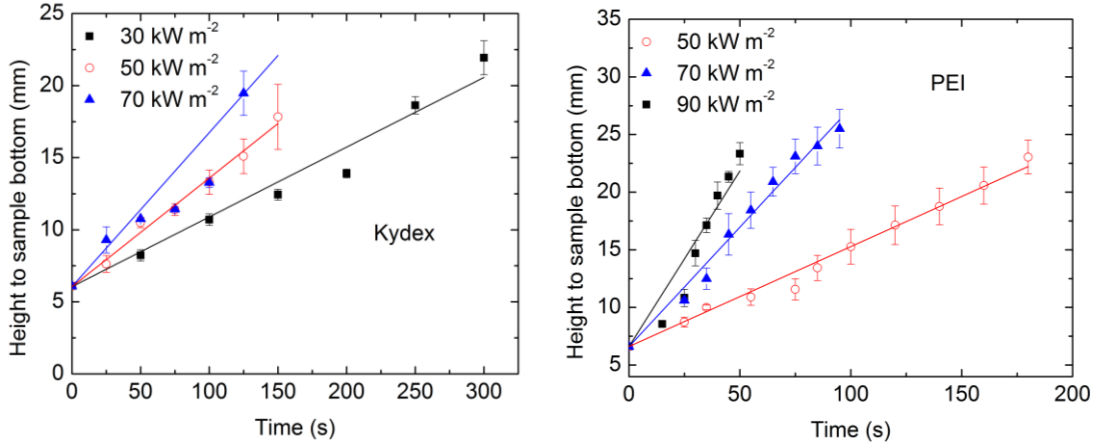


Figure 8.9 Experimental measurements and linear fits for the height to sample bottom vs time for Kydex and PEI at various heat fluxes.

Then these linear fits are used to calculate the relation of incident radiative heat flux on top surface and time, which are illustrated in Figure 8.10, since the heat flux at the elevated levels above sample initial surface level were already characterized in the section 4.3.3. In the ThermaKin model, the external heat flux for only these two polymers is set by a linear function and a constant value (dash line) from a transition point to the end of simulation as described in Figure 8.10. The transition point was chosen when the pyrolyzing sample top surface reaches nearly outside of the side camera visual field. After this point, the external radiative heat flux is assumed to be a constant value.

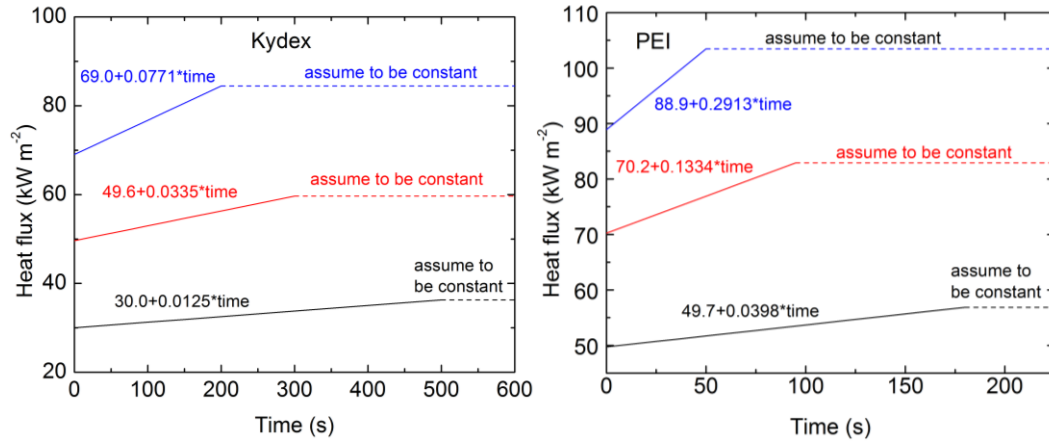


Figure 8.10 Relation of incident radiative heat flux on top surface and time.

Section 8.4 Thermal conductivity calibration

Section 8.4.1 ABS and PET

When a polymer sample produces significant amount of char during thermal degradation and the char may form an intumescent structure, the sample's temperature uniformity for this class of polymers fails. Therefore, instead of averaging 10 random selective cursors from three divided areas, the temperature profiles at the bottom part of charring samples are averaged by four random selective cursors which contain 36 pixels in individual area. In this way, the quality of its uniformity is displayed clearly by recognizing the differences among the three areas.

The temperature differences among the three areas of sample bottom surface can be investigated by displaying average temperature within each area for charring polymers in this chapter [Section 7.3.2 presents the method for averaging over 3 gasification experiments 90 pixels (36 from area 1, 36 from area 2, and 18 from area 3) for non-charring polymers]. Only in this chapter, each area's sample bottom surface temperature is displayed individually, as an example shown in Figure 8.11

(circles) for ABS bottom surface temperature histories at 30 kW m^{-2} . Each data point in Figure 8.11 for all the areas were calculated by averaging pixels over 3 gasification experiments and 36 pixels were randomly selected within corresponding area in each experiment.

The results of inverse modeling of this temperature are also presented in the Figure 8.11 (line). The thermal conductivities for ABS and ABS char and absorption coefficient for ABS char were adjusted (up to third order polynomial temperature-dependent function) to fit the bottom surface temperature. Please note that the densities of all the components for all the polymers in this dissertation were not adjusted in the fitting. The thermal transport properties for all the components at condensed phase and their estimated uncertainties are reported in Table 8-2. The uncertainties were computed by propagating variation in the temperature measurements.

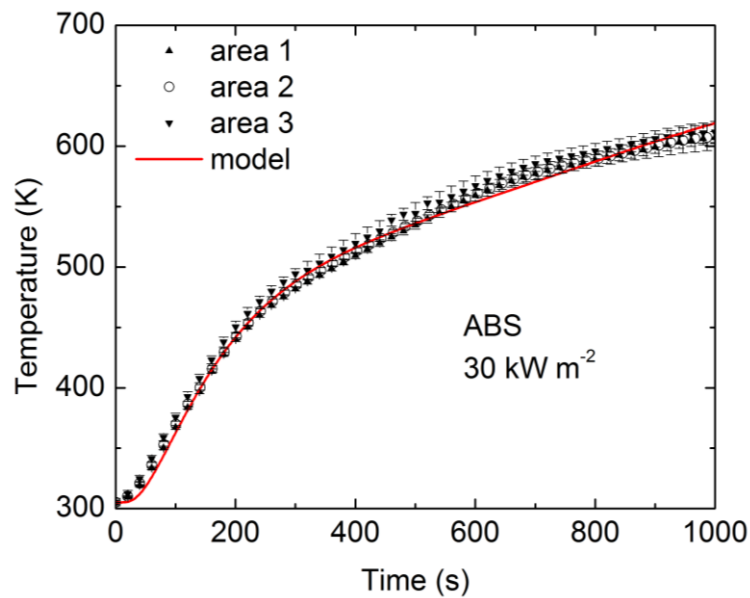


Figure 8.11 Experimental and simulated bottom surface temperature histories obtained for ABS at 30 kW m^{-2} .

Table 8-2 Thermal transport properties for ABS.

Properties	Density (kg m^{-3})	Emissivity	Absorption coefficient ($\text{m}^2 \text{kg}^{-1}$)	Thermal conductivity ($\text{W m}^{-1} \text{K}^{-1}$)
ABS	1050	0.95	1.71	$(0.30-2.8 \times 10^{-4} T) \pm 10\%$
ABS_char	80	0.86	31.25	$(0.13-5.4 \times 10^{-4} T + 4.8 \times 10^{-9} T^3) \pm 14\%$

As demonstrated in Figure 8.12 and Figure 8.13, the derived thermal conductivity parameters also provide a good description of 50 and 70 kW m^{-2} bottom surface temperature histories in a reasonable degree of accuracy, which were not used as optimization targets.

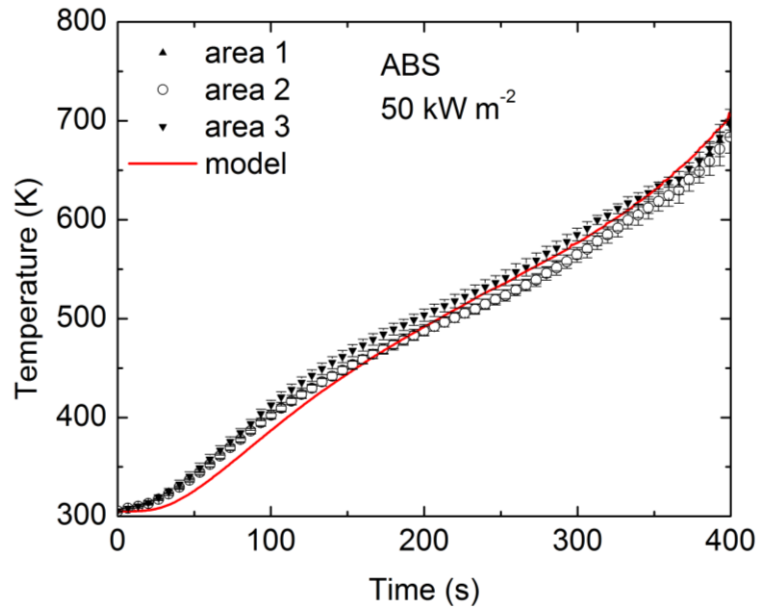


Figure 8.12 Experimental and simulated bottom surface temperature histories obtained for ABS at 50 kW m^{-2} .

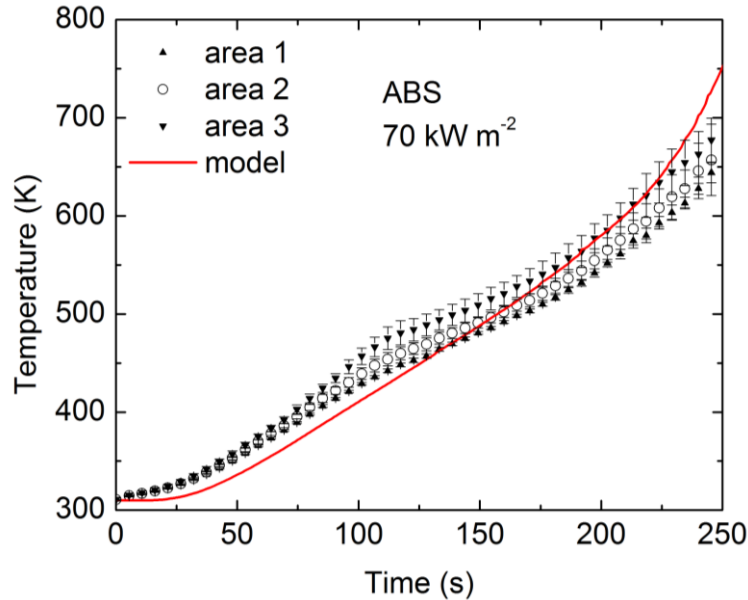


Figure 8.13 Experimental and simulated bottom surface temperature histories obtained for ABS at 70 kW m^{-2} .

For PET, back surface temperature measurements at 50 kW m^{-2} were considered as inverse modeling target. The thermal conductivities of all PET condensed phase components and PET char absorption coefficient were calibrated in the fitting process. The average sample bottom temperature history obtained for PET gasified at 50 kW m^{-2} of radiant heat flux is shown in Figure 8.14 (circles). This is the best fit obtained, although some discrepancies still exist. Table 8-3 lists all the heat transfer properties for PET. Then these properties are served as inputs for ThermaKin models to predict the sample bottom surface temperature at 70 kW m^{-2} , provided all the other material properties are well measured and qualified in the previous chapters. Bottom temperature profile under 70 kW m^{-2} , which is not served as the fitting target, is shown in Figure 8.15. From this figure, temperature differences among the three areas are clearly larger than the case at 50 kW m^{-2} , especially when bottom temperature is above 500K. This is probably caused by the fast heating acting on the

pours char structure. Even though the model does not account this, the prediction is still within the uncertainties of the IR measurement up till about 600 K in a reasonable good degree.

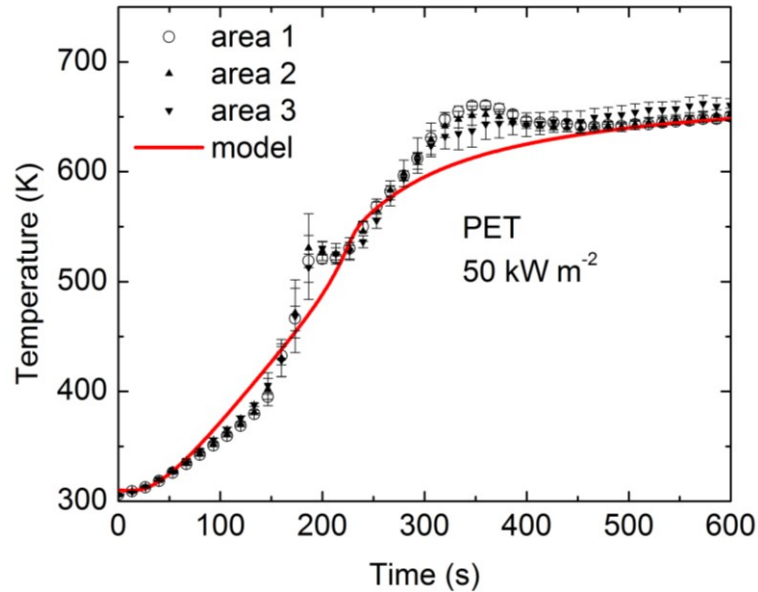


Figure 8.14 Experimental and simulated bottom surface temperature histories obtained for PET at 50 kW m^{-2} .

Table 8-3 Thermal transport properties for PET.

Properties	Density (kg m^{-3})	Emissivity	Absorption coefficient ($\text{m}^2 \text{ kg}^{-1}$)	Thermal conductivity ($\text{W m}^{-1} \text{ K}^{-1}$)
PET	1385	0.95	1.4	$(0.35-4.8 \times 10^{-4} T) \pm 8\%$
PET_melt	1385	0.95	1.4	$(0.33-2 \times 10^{-5} T) \pm 15\%$
PET_int	730	0.95	1.4	$(0.45+2 \times 10^{-4} T) \pm 20\%$
PET_char	80	0.86	100	$(0.45+3.8 \times 10^{-5} T + 5 \times 10^{-10} T^3) \pm 25\%$

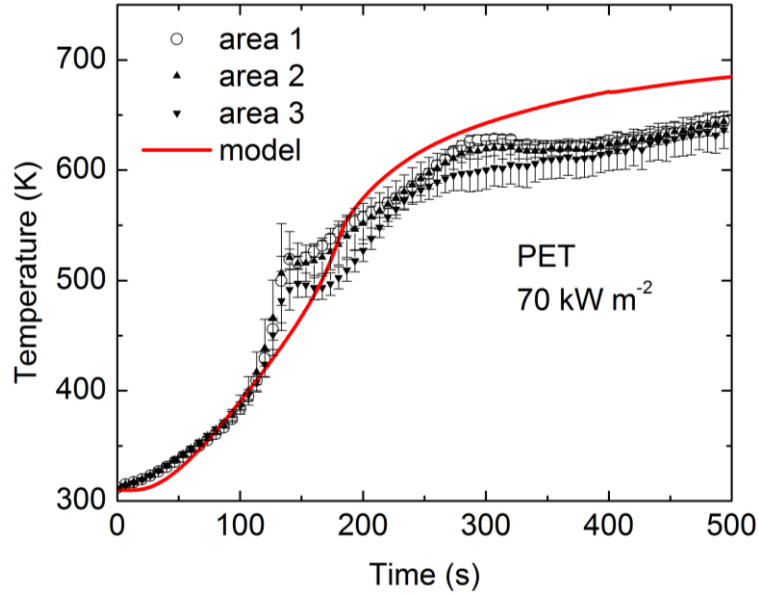


Figure 8.15 Experimental and simulated bottom surface temperature histories obtained for PET at 70 kW m^{-2} .

Section 8.4.2 Kydex and PEI

Kydex bottom surface temperatures for three different areas at 30 kW m^{-2} are plotted in Figure 8.16. As seen from this figure, the temperature uniformity appears good as least until 250 s which served as the thermal conductivity calibration optimization target (Figure 8.16). The thermal conductivities for condensed phase components are fitted and summarized in Table 8-4. Table 8-4 also provides $K_{\text{ydex_int}}$ and $K_{\text{ydex char}}$ absorption coefficients, which are also used in the optimization process. Cut-off time 250 s is chosen because, based on the observation from the side video camera, it is considered to be a critical point when Kydex sample is still under assumption of one-dimensional heat transfer. Beyond this point, the temperature data obtained from experiments is not used in the analysis. Figure 8.17 illustrates the extend range of temperature measurements for three areas and model prediction. This one-dimensional model does not predict the measurements well due

to the reason of incorrect description of sample geometry. Please note that because the bottom surface areas shrink during the gasification tests, area 3 and area 2 temperature measurements are only available partially.

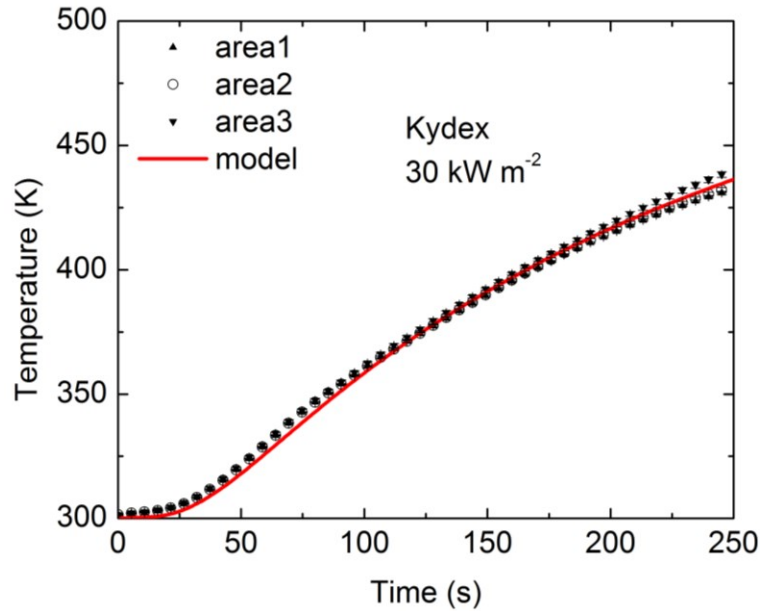


Figure 8.16 Experimental and simulated bottom surface temperature histories obtained for Kydex at 30 kW m^{-2} (fitted range).

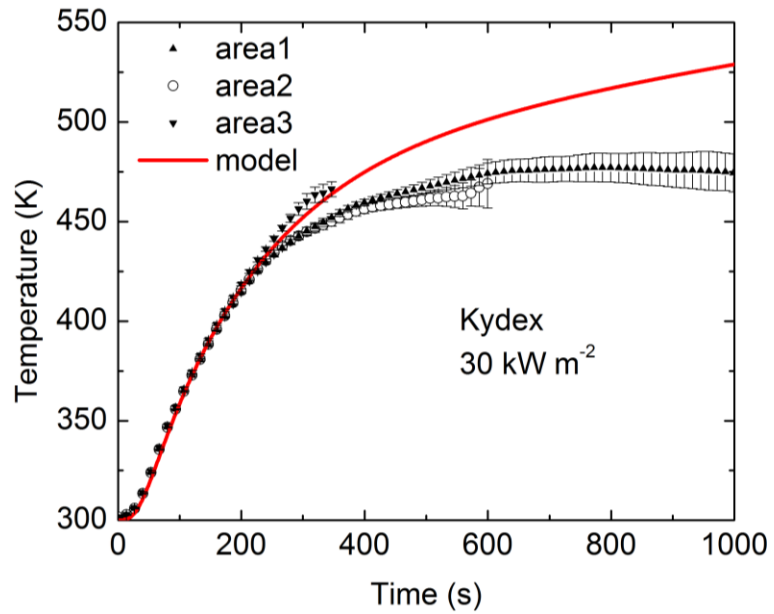


Figure 8.17 Experimental and simulated bottom surface temperature histories obtained for Kydex at 30 kW m^{-2} .

Bottom temperature profiles under 50 and 70 kW m⁻², which are not served as the fitting target, are shown in Figure 8.18 and Figure 8.19. Both of these predictions suggest the current model can predict the bottom in reasonable degree accuracy even though the entire Kydex pyrolysis is a complex non-one-dimensional problem.

Table 8-4 Thermal transport properties for Kydex.

Components	Density (kg m ⁻³)	Emissivity	Absorption coefficient (m ² kg ⁻¹)	Thermal conductivity (W m ⁻¹ K ⁻¹)
Kydex	1350	0.95	1.58	$(0.28-2.9 \times 10^{-4} T) \pm 20\%$
Kydex_int	100	0.95	30	$(0.55+3 \times 10^{-5} T) \pm 15\%$
Kydex_char	100	0.86	100	$(0.28+8.4 \times 10^{-5} T+3 \times 10^{-10} T^3) \pm 25\%$

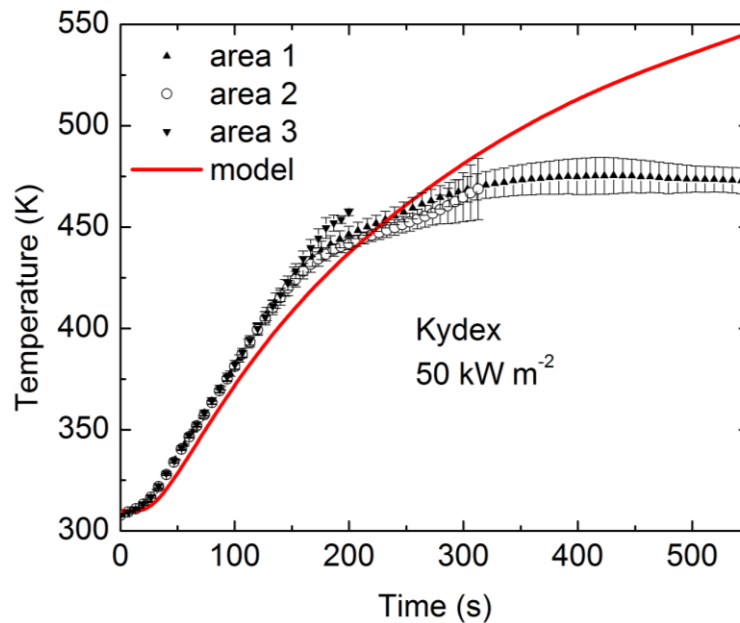


Figure 8.18 Experimental and simulated bottom surface temperature histories obtained for Kydex at 50 kW m⁻².

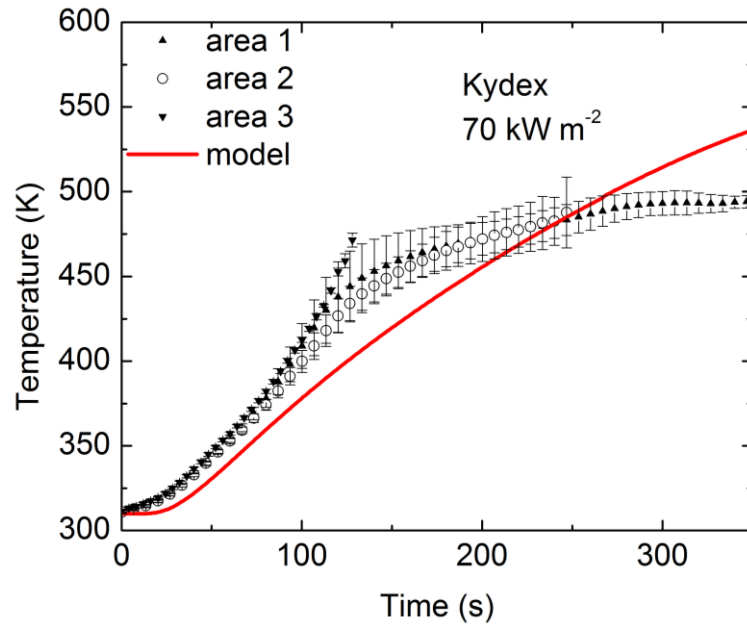


Figure 8.19 Experimental and simulated bottom surface temperature histories obtained for Kydex at 70 kW m^{-2} .

The thermal conductivities for all PEI condensed phase components were only optimized until 200 s when PEI sample is assumed to experience nearly one-dimensional heat transfer by fitting with experimental measurements at lowest heat flux, which is 50 kW m^{-2} . The absorption coefficients for the other condensed phase components were also optimized to improve the fit. And they are assumed to stay equal for simplicity. Table 8-5 summarizes the thermal transport properties that were measured and assumed for PEI. Figure 8.20 shows the experimental and fitted simulated data for PEI at this heat flux level for the fitted data range and Figure 8.21 illustrates the extend temperature measurements and simulation.

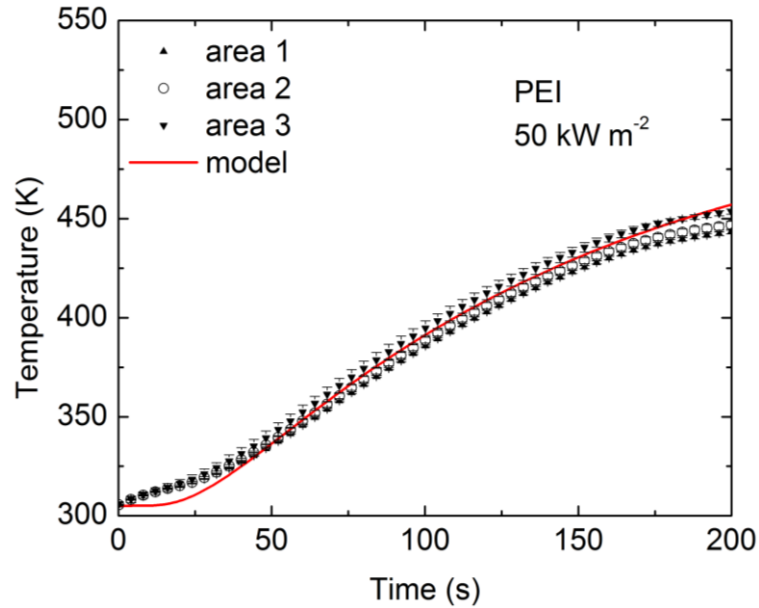


Figure 8.20 Experimental and simulated bottom surface temperature histories obtained for PEI at 50 kW m^{-2} (fitted range).

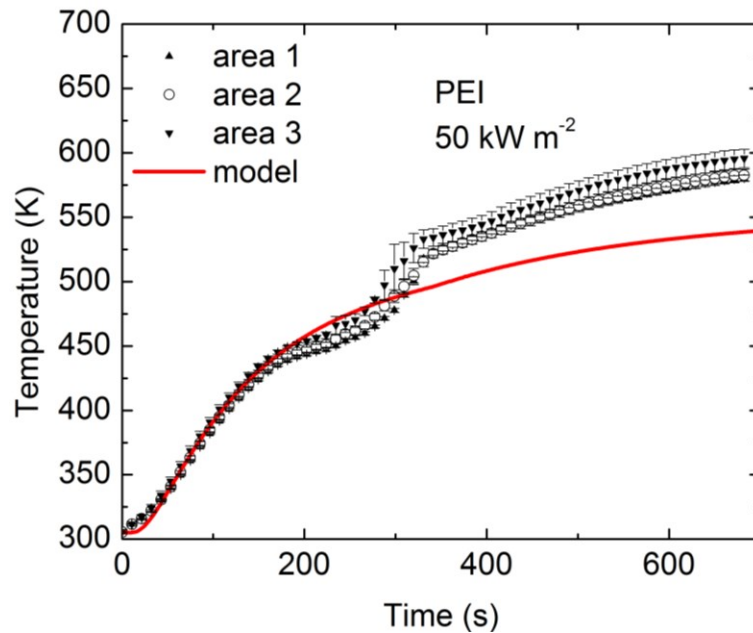


Figure 8.21 Experimental and simulated bottom surface temperature histories obtained for PEI at 50 kW m^{-2} .

The validations towards at higher external heat fluxes (70 and 90 kW m^{-2}) are shown at Figure 8.22 and Figure 8.23. Unlike other polymers in this study, the

predictions are not good because of multiple reasons. The first and most important one is the thick char layers formed during gasification test at first 100 s (as can be demonstrated from Figure 8.24), which makes the PEI pyrolysis problem highly non-one-dimensional. Secondly, one possible explanation is the inability to correct characterizes the top boundary condition in the model. As mentioned in the section 8.3.2, the top surface radiation is assumed to be constant after a critical point in the model; however, this is not true as it observed in the experiments. When PEI samples top surface swelling and expanding into the cone heater, it receives much higher heat flux than it was set in the model. Thus the model underestimates the heat transferred into the PEI sample. The last but not least, in both cases, visible flame was observed on top of the sample and it brings additional heat loading towards the sample, which is not described in the model.

Table 8-5 Thermal transport properties for PEI.

Properties	Density (kg m^{-3})	Emissivity	Absorption coefficient ($\text{m}^2 \text{kg}^{-1}$)	Thermal conductivity ($\text{kJ kg}^{-1} \text{K}^{-1}$)
PEI	1285	0.95	1.36	$(0.4-4 \times 10^{-4}T) \pm 10\%$
PEI_melt	1285	0.95	100	$(0.32-3.3 \times 10^{-4}T) \pm 14\%$
PEI_int	80	0.95	100	$(0.45+1.9 \times 10^{-4}T) \pm 14\%$
PEI_char	80	0.86	100	$(0.5-3.4 \times 10^{-5}T + 2 \times 10^{-10}T^3) \pm 25\%$

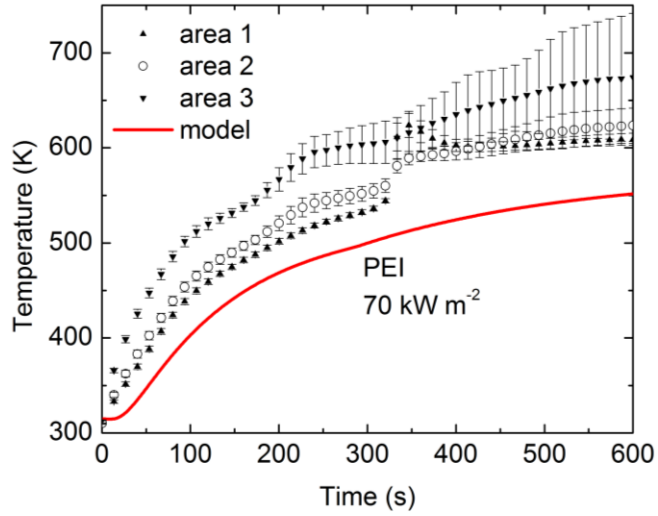


Figure 8.22 Experimental and simulated bottom surface temperature histories obtained for PEI at 70 kW m^{-2} .

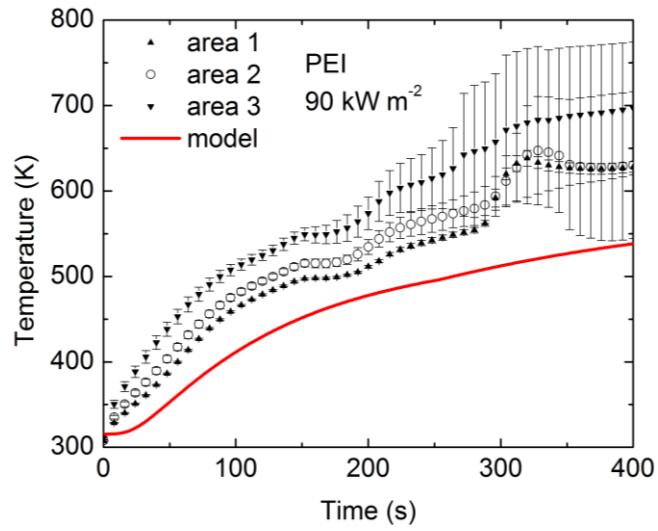


Figure 8.23 Experimental and simulated bottom surface temperature histories obtained for PEI at 90 kW m^{-2} .

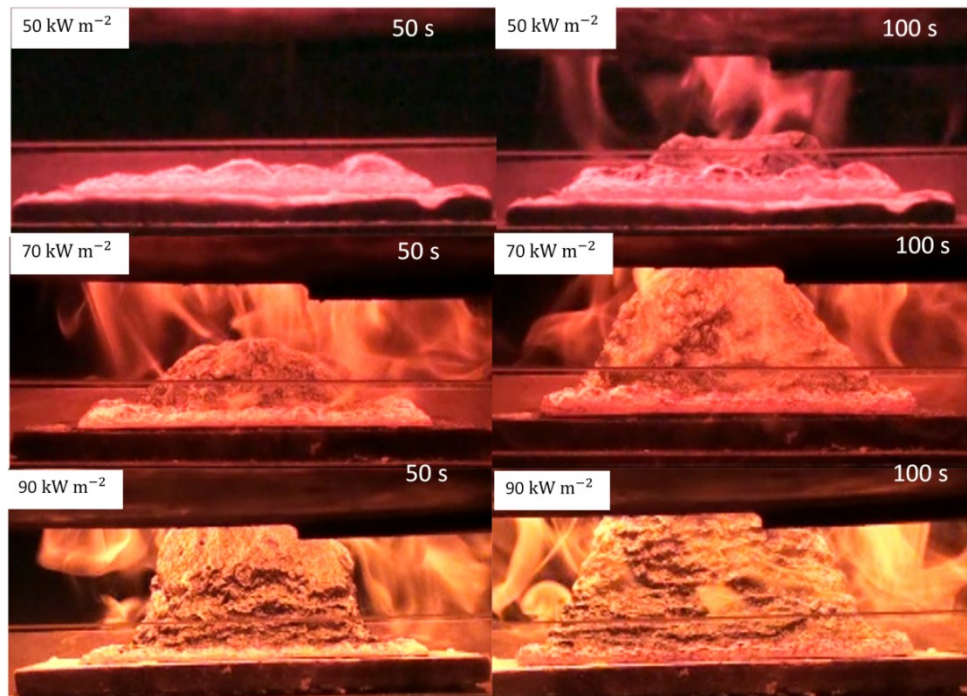


Figure 8.24 Side view snapshots of PET at 50-90 kW m⁻².

Section 8.5 Sample height and burning rate prediction

Section 8.5.1 ABS and PET

Figure 8.25 shows the experiment data (point) and model prediction (line) for the overall thickness of ABS at 50 kW m⁻² (single test). For ABS, since no significant swelling or expanding was observed, thus the data shown in this figure only represents the maximum visible thickness direct from video and so does for PET (Figure 8.27). The total thickness was not seen clearly from the video data and it was observed to continue decreasing.

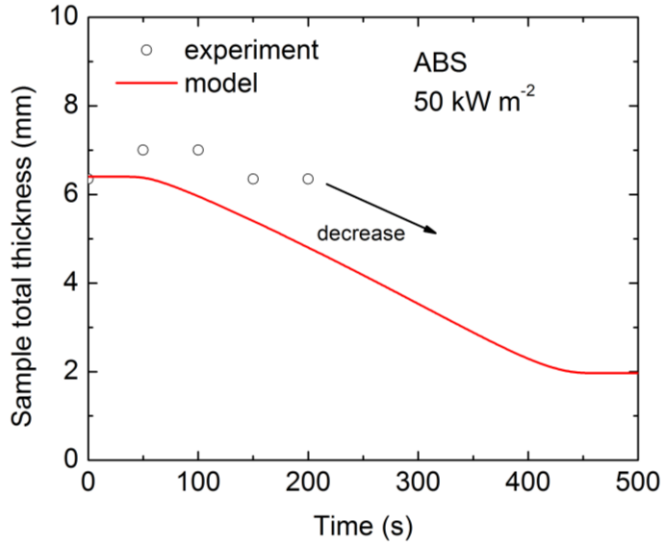


Figure 8.25 Experimental and simulated thickness histories obtained for ABS at 50 kW m^{-2} .

A comparison of the burning rates computed using the fully parameterized ABS model with the results of the gasification experiments is shown in Figure 8.26. The model predicts the burning rates with the accuracy comparable with the experimental repeatability except at 30 kW m^{-2} . At this heat flux level, as discussed earlier in this chapter, ABS produced extremely larger amount of residues at 30 kW m^{-2} , at which it was observed decomposed incompletely, than it did in 50 and 70 kW m^{-2} . And this larger amount of residue forms thicker insulation layer on top of the virgin polymer and further affects the heat transfer inside the condensed phase. However, the model does not fully reflect the same amount of char residue in the ABS experiment. The effect of the char can be further demonstrated in the cases of external heat fluxes of 50 and 70 kW m^{-2} , when ABS samples are nearly completed degradation. The largest discrepancy between experiment results and model prediction is found to be about 20 % on average at 30 kW m^{-2} from beginning up to

800 s. And these average values for 50 and 70 kW m⁻² are computed less than 10 % up to 400 s and 250 s respectively.

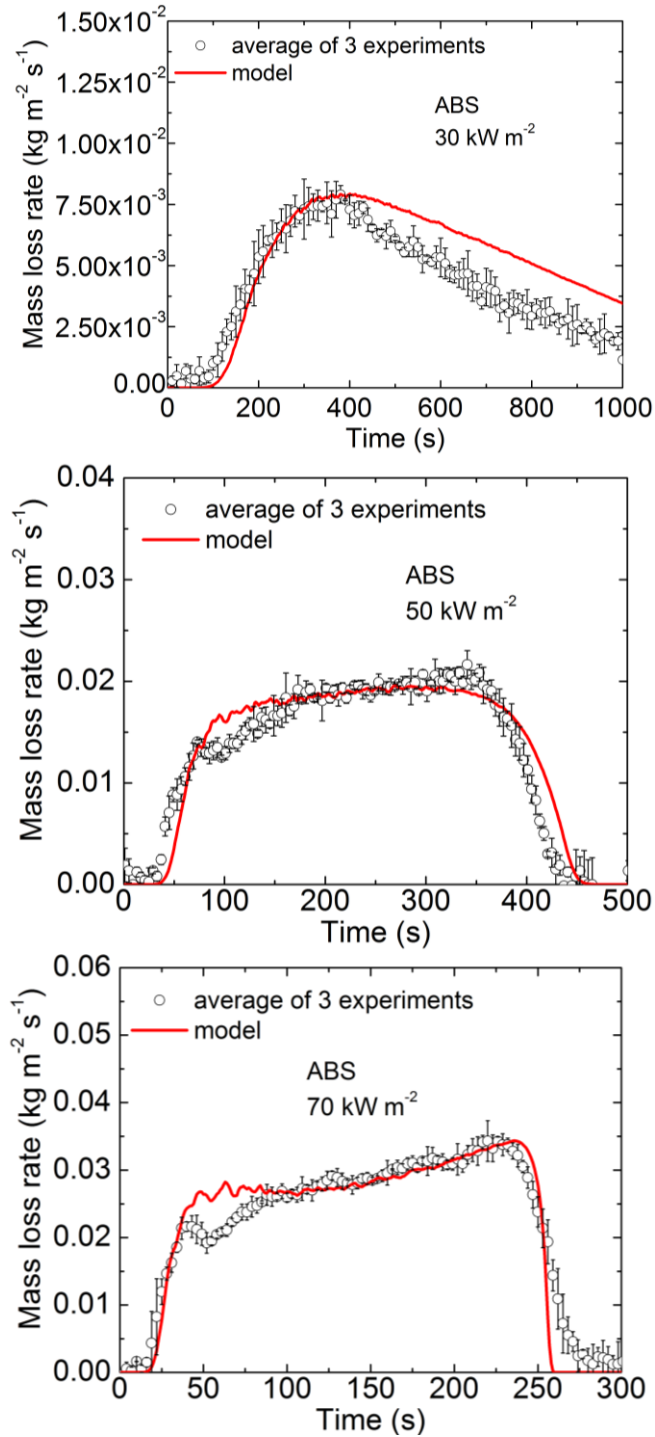


Figure 8.26 Experimental and simulated burning rate histories obtained for ABS at 30-70 kW m⁻².

The total thicknesses of PET for experiment (dot) and modeling (line) were shown in Figure 8.27. The dot data shows a single test data. The predication of model is good which demonstrates the volume consistency.

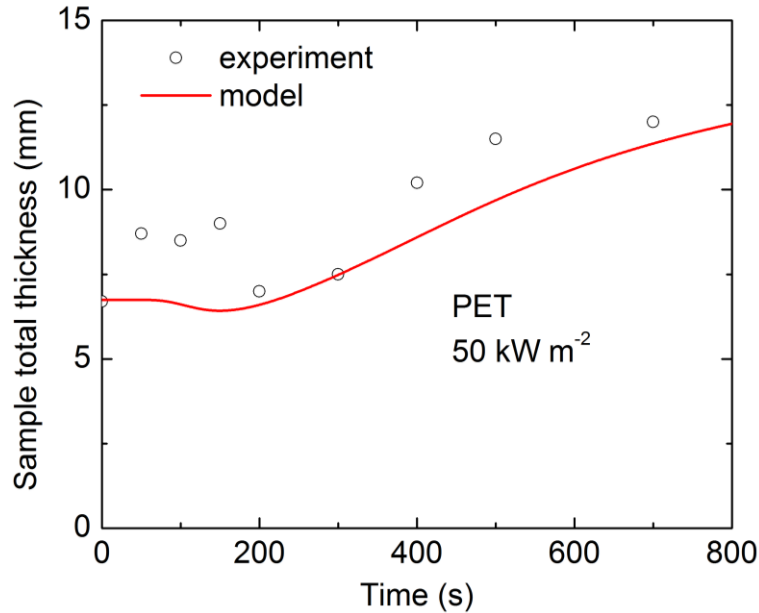


Figure 8.27 Experimental and simulated thickness histories obtained for PET at 50 kW m^{-2} .

A final comparison of the burning rates computed using the fully parameterized PET model with the results of the gasification experiments is shown in Figure 8.28. The model predicts the burning rates at two different stages of radiant heat fluxes with a notable improvement compared to an recent gasification experimental and modeling study on PET [40]. The mean discrepancies within experimental data and model prediction for 50 and 70 kW m^{-2} are calculated to be about 22 % (up to 400 s) and 17 % (up to 350 s) respectively.

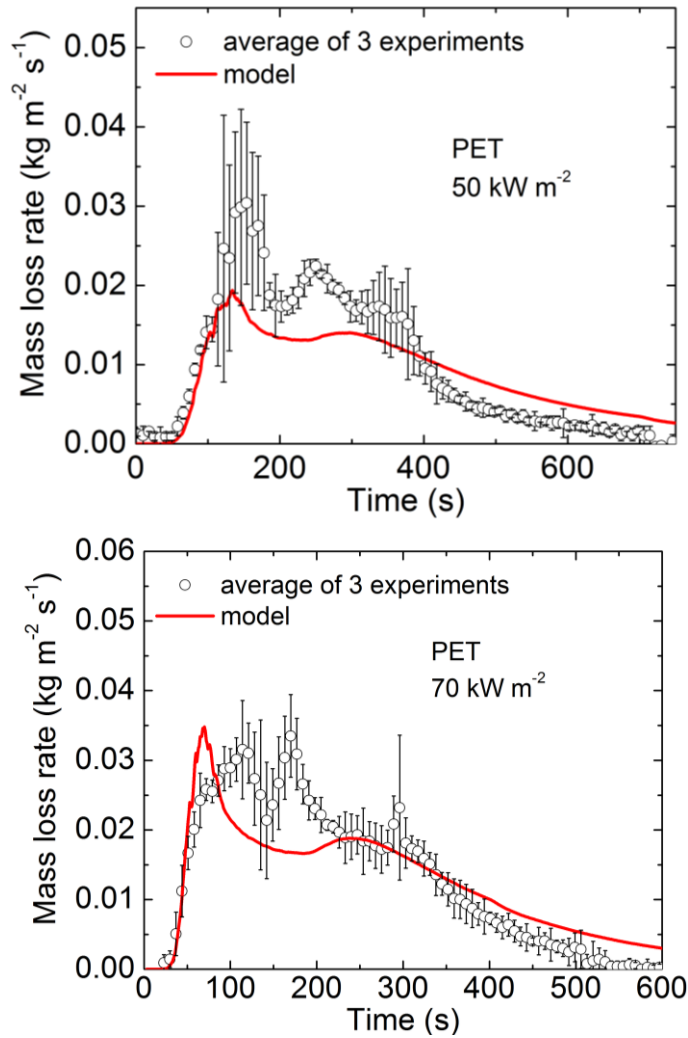


Figure 8.28 Experimental and simulated burning rate histories obtained for PET at 50 and 70 kW m⁻².

Section 8.5.2 Kydex and PEI

The heights of Kydex samples under thermal degradation of 50 kW m⁻² with areas 1 and 3 range are plotted in Figure 8.29. In this figure, the top and bottom boundaries of the bars indicate the maximum and minimum heights of the sample measured from its bottom surface and represent the data of three independent tests within area 1 and area 3. The results are cut when the top surface of the sample reaches outside of the side camera vision. As expected, the simulated results do not

match the experimental data well because of reduction of the sample cross-section area (the model does not include this behavior). However, they match each other until 100 s before the cross-section area changing significantly (as demonstrated in Figure 8.29).

A final comparison of the burning rates computed using the fully parameterized Kydex model with the results of the gasification experiments is shown in Figure 8.30. Although Kydex behaviors not purely one-dimensional pyrolysis, the model, which combines with previous knowledge on material kinetics and thermodynamics (Chapter 6), detail thermal transport properties and the enhanced top boundary characterization (this Chapter), predicts the burning rates with the mean discrepancies of experimental data and model prediction for 13 % (up to 950 s), 25% (up to 700 s) and 20 % (up to 600 s) for 30, 50 and 70 kW m⁻² respectively.

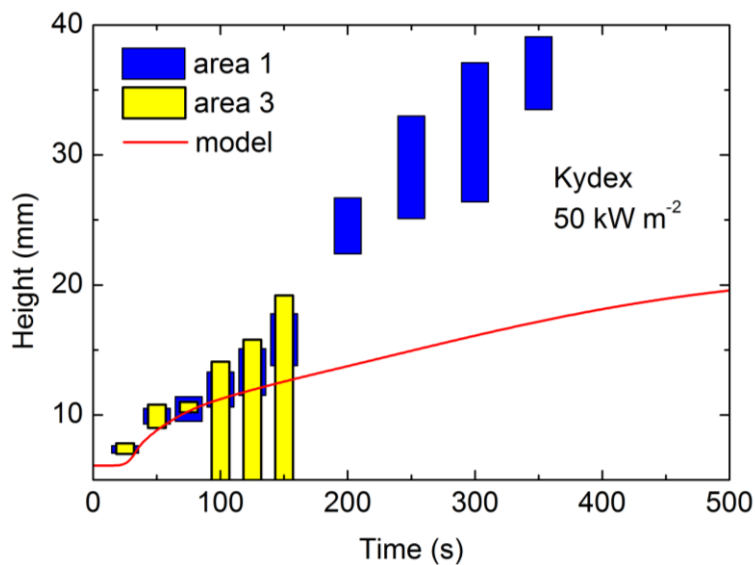


Figure 8.29 Experimental and simulated thickness histories obtained for Kydex at 50 kW m⁻².

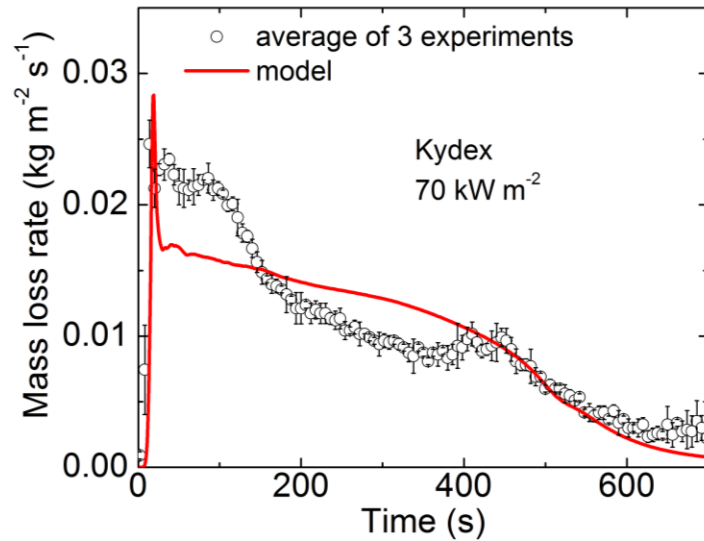
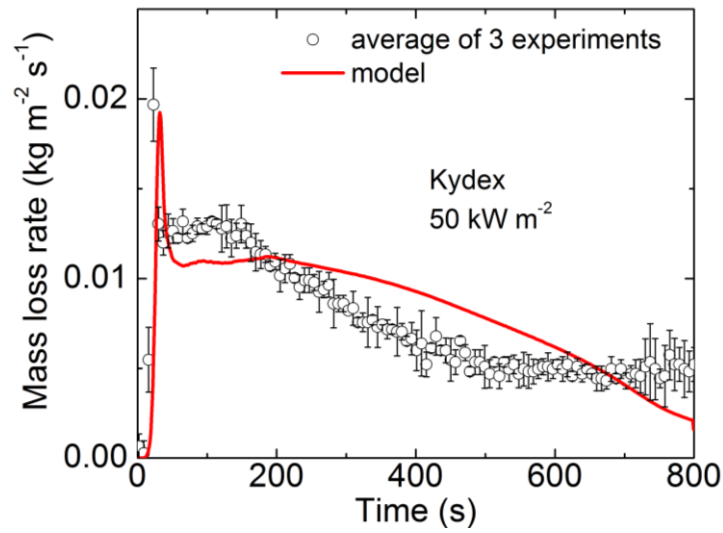
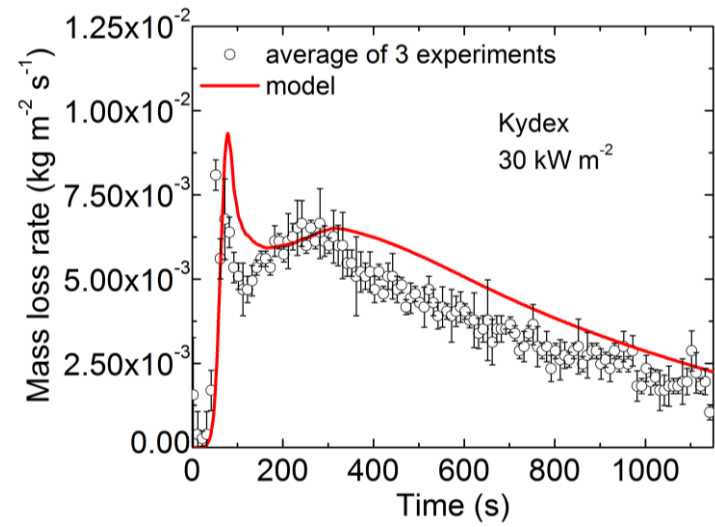


Figure 8.30 Experimental and simulated burning rate histories obtained for Kydex at 30 and 70 kW m⁻².

The heights of PEI sample within the area 1 and area 3 were examined similar to the study of Kydex and the results at 50 kW m^{-2} are shown in Figure 8.31. The prediction is not good because the thermal expansion induced by density change was not characterized with a temperature-dependent variable in the model, which is indicative of the density temperature dependence needs further investigation.

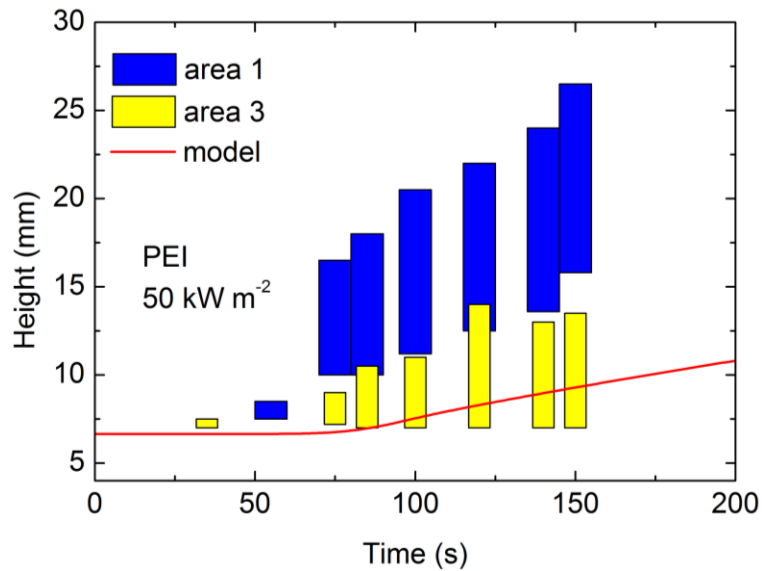


Figure 8.31 Experimental and simulated thickness histories obtained for PEI at 50 kW m^{-2} .

A final comparison of the burning rates computed using the fully parameterized PEI model with the results of the gasification experiments is shown in Figure 8.32. As one of the typical fire resistant polymers, the burning rate for PEI is extremely low, even at 90 kW m^{-2} .

From Figure 8.32, the predictions for all the conditions are relatively poor. The mean discrepancies of experimental data and model prediction for 27 % (up to 700 s), 34% (up to 600 s) and 44 % (up to 400 s) for 50, 70 and 90 kW m^{-2}

respectively. There are several reasons that cause these uncertainties. The first one is the model external heat flux characterization, which is discussed in the section 8.3.2. The top surface external heat flux used in the model is underestimated for all heat fluxes because estimation for a constant external heat flux was made after a transition point (see details in the section 8.3.2). Therefore after this transition time the external heat flux in the model does not represent the actual external radiation. Secondly, the density characterization needs improvement. All the densities for the char estimation are crude estimation and assumed temperature-independent. But the changes of density in the experiment affect the total volume and further affect the heat transfer at the condensed phase. The last but not the least, which may contribute majorly to this uncertainty, is considered to be the oxidation effects during char swelling. As discussed in the section 8.2.2 clear visible flame were observed at 70 and 90 kW m⁻² when PEI sample top surface reaches into the cone heater, where oxygen concentration is considered to be much higher than the initial state. The increases on mass loss rate due to the effect of oxidation are demonstrated in Figure 8.32 for 70 kW m⁻² at about 350 s and 90 kW m⁻² at about 300 s respectively, when visible flame appeared.

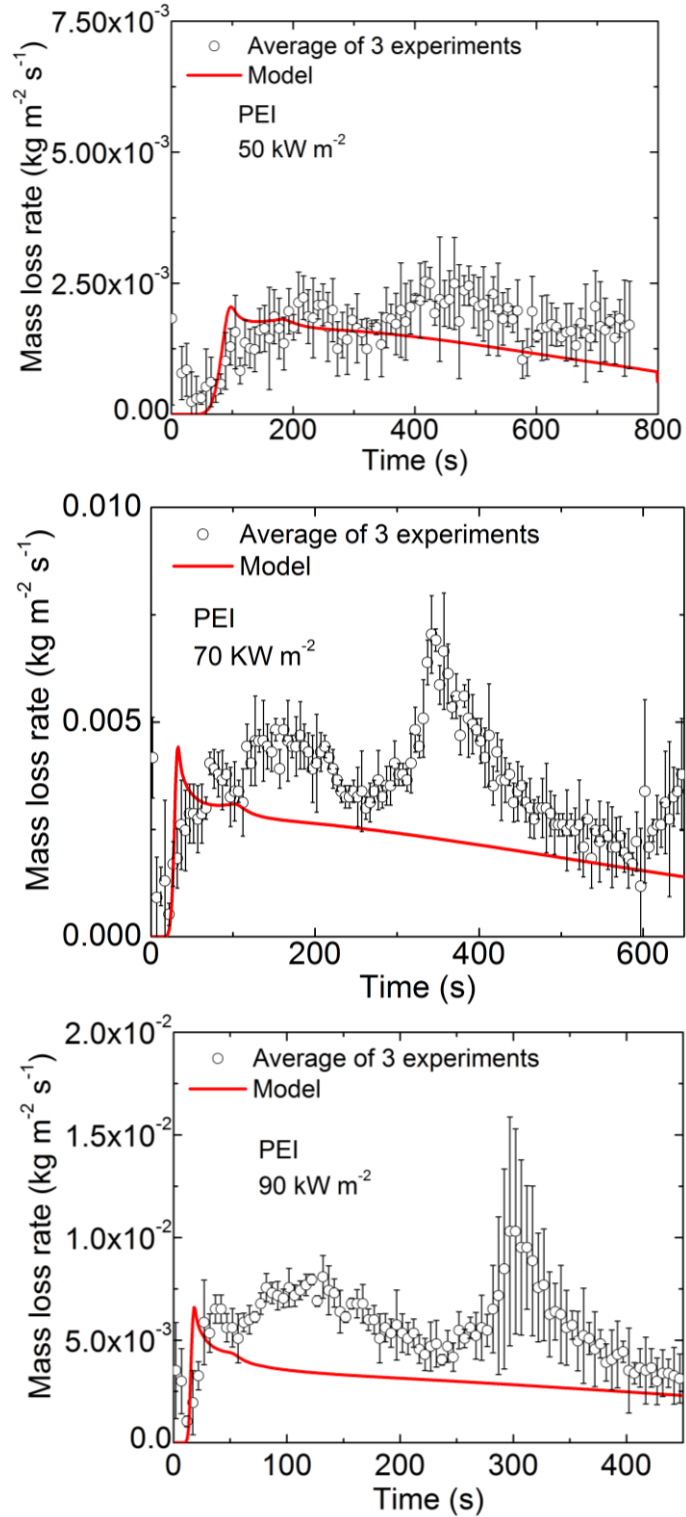


Figure 8.32 Experimental and simulated burning rate histories obtained for PEI at 50 and 90 kW m⁻².

Section 8.6 HRR calculation

Standard cone calorimeter tests were also performed followed by the procedures described in [128] additionally for 3 non-charring polymer studied in Chapter 7 and 4 polymers parameterized in this chapter to obtain the effective heats of combustion (HOC) for those polymers. These tests were performed two times for each polymer and the average effective heat of combustion values are summarized in Appendix A-B. Note that the HOC values reported in this dissertation were obtained by the total heat release over the burning mass loss. Figure 8.33 displays maximum heat release rate verse heat flux for those seven polymers. The maximum heat release rate was calculated by multiplying the maximum gasification experiment (no flame) mass loss rate (time-averaged for 10 s to avoid unusual fluctuations) obtained from this study to the values of effective heat of combustion acquired from above discussion for the corresponding polymer. As demonstrated in Figure 8.33, the maximum heat release rate shows a linear tendency to the external heat flux. The fact that this linear tendency is indicative that the maximum heat release rate or burning rate at the bench-scale is primary defined by the process of heat transfer (in the linear function to the external heat flux) at the condensed phase instead of the material kinetic decomposition, which is believed to highly non-linear to the external heat treatment.

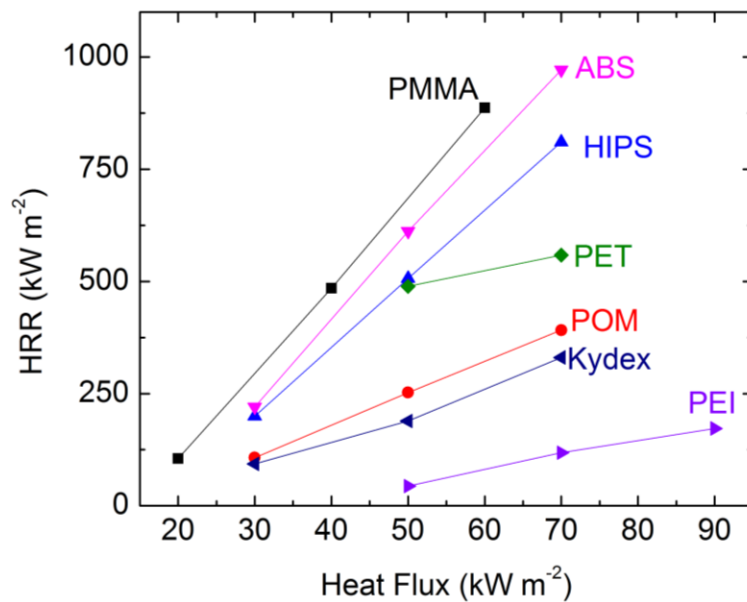


Figure 8.33 Maximum heat release rate verse heat flux for polymers (These maximum heat release rates were calculated by multiplying the maximum gasification experiment burning rate and effective HOC values obtained from this study).

Chapter 9 : Concluding remarks

This dissertation addressed the material flammability problem by developing and implementing a systematic methodology for parameterization and validation of continuum burning models over a number of representing polymeric materials including: widely used engineering plastics and promising high performance charring and intumescent polymers. The property values measured in this study form a foundation for a combustible material property database, which qualitatively improve the accuracy of fire growth simulations. The properties were measured and validated in the experiments performed at a wide range of scales and conditions. They are also validated against more than one numerical modeling solvers (see Appendix A), which further ensures that the property values reflect the fundamental aspects of material behavior and are neither test-specific nor model-specific. The modeling of this work helps reveal and close potential gaps in current understanding of polymer pyrolysis and clarify the roles and modes of heat and mass transport in the process of generation of gaseous fuels.

The model developed for each material was shown to capture both mass loss and heat flow data. To the best of my knowledge, this is the first example of a systematic approach that yields a global reaction model that simultaneously reproduces both TGA and DSC measurements. In addition, this methodology has also been recently proved to be applied more complex composite materials such as corrugated cardboard [160] and demonstrates that it can be applied to a wide variety of combustible solids. Exothermicity of thermal degradation for some highly charring

polymers, which was not found for polymers by previous researches, were observed and reported in this dissertation.

There are some novel methods in experimentally have been developed in this dissertation. In particular, temperature-dependent thermal conductivity of a solid material is extracted from material bottom surface temperature data in a computationally efficient way by an inverse modeling. Heat transfer through the solid was monitored by focusing an infrared camera on the bottom surface of a horizontally-mounted sample, which top surface faced the cone heater. The bottom surface of a testing material is designed expose to ambient air, which is significant differently from traditional experiments that are carried out in the cone calorimeter when the bottom surface is insulated. This new design allows possibility for the use of the non-contact nature of measurement. The use of an IR camera for the sample bottom surface thermometry with non-contact, spatially-resolved has been proved save time and effort in experiments and data analysis by at least factor of two prior to a previous design [137]. Spatial resolution of the temperature data (collected using the infrared camera) made it possible to assess the validity of the one-dimensional thermal transport assumption always invoked during analysis of this type of experiments. To the best of my knowledge, this is the first approach for monitoring both sample mass and temperature spatial data simultaneously applying an IR camera.

A new method for recording material morphological in time change during a solid material gasification experiment has also been adopted to potentially allow further analyzing some intumescent polymers which representing overwhelming majority of the new generation of flame resistant materials. This part of work

provides possibility to detail study the char formation at different stage of gasification for this type of materials.

The main distinguishing feature of our approach is that experimental burning rate histories, which serve as the main target for optimization-based methods, are not utilized in the property calculation. And this is completely different from many other material parameterization studies. Instead, they are employed to validate a fully parameterized model. This parameterization methodology minimizes possible compensation errors and extends the scope of the model validity. In essence, this combination of experiments and modeling represents a routine that generates complete property sets describing anaerobic pyrolysis of non-charring and charring polymers. The presented results clearly demonstrate that this routine produces consistent property values at a modest experimental cost.

Appendix A FDS simulation for non-charring polymers

A completed investigation to check whether the data set obtained from this study is model-specific or not has been done by modeling the same scenario using a FDS pyrolysis model [65]. FDS is a fire-driven fluid flow computational fluid dynamics (CFD) 3D model which solves the Navier-Stokes equations numerically at low-speed ($Ma < 0.3$) velocity. This model is written with an emphasis on smoke and heat transport from fires. Besides the gas phase simulation, FDS's pyrolysis model is also capable to predict the mass loss rate of a given material exposed to external heat flux at the condensed phase in a one-dimensional fashion, which is very similar to what ThermaKin does. The newest version is FDS 6.0.1 which was applied in this investigation. In this appendix results, all gas-phase reaction was essentially turned off by setting the mass fraction oxygen to 0.001 in the air to simulation the pyrolysis. Only a small domain was used in the simulation (($5 \times 5 \times 10$ rectangular cells, $0.05 \times 0.05 \times 0.1$ m). The time step is set to 0.01s and it was found that increase or decrease this value by a factor of 10 does not affect the results. The boundary conditions were set same as the conditions used in ThermaKin.

The difference between ThermaKin and FDS pyrolysis model is negligible at the condensed phase pyrolysis simulation [39, 107]. The major noticeable difference between those two models is the in-depth radiation absorption model selection. FDS treats the radiation transport within the condensed phase is a source term in the heat conservation equation while ThermaKin has two options: The element that absorbs radiation is determined at every time step using either a maximum absorption or a random absorption algorithm [110]. While the maximum absorption algorithm is

employed, the element absorbs most of the radiation is assumed to absorb all of it, which is similar to the way FDS does. The FDS also does not consider the convection loss induced by the escape of volatiles, which is found to be small and the main reason of the difference between those two model results. Since FDS and ThermaKin use comparable physical descriptions of the fundamental physical and chemical phenomena, the choice of the model between those two models is less significant. Tables A. 1-3 summarized the properties of PMMA, POM and HIPS used in the FDS simulations, which are as same as the properties used in the ThermaKin simulations. The gasification tests were conducted CAPA [137], as described in the section 3.3.3.

The reaction mechanism for PMMA is described as follows:

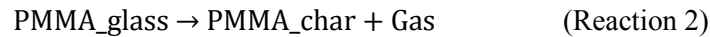


Table A. 1 FDS Input Parameters for PMMA.

Property	Units	Value	Method	Reference
PMMA Density	kg/m ³	1160	Directly Determined through Volume and Mass Measurement	[161]
PMMA Conductivity	W/m/K	$T < 378 \text{ K:}$ $0.45-3.8 \times 10^{-4} T$	Inverse Analysis of Material Temperature in Gasification Exp.	[161]
PMMA Specific Heat	kJ/kg/K	$0.60+0.0036T$	DSC	[77]
PMMA Emissivity		0.95	Literature	[134]
PMMA Absorption Coefficient	m ² kg ⁻¹ (m ⁻¹)	1.94 (2240)	Measured by Beer–Lambert law	[161]
PMMA_glass Density	kg/m ³	1160	Assumed same as PMMA	[161]
PMMA_glass Conductivity	W/m/K	$T \geq 378 \text{ K:}$ $0.27-2.4 \times 10^{-4} T$	Inverse Analysis of Material Temperature in Gasification Exp.	[161]
PMMA_glass Specific Heat	kJ/kg/K	$0.60+0.0036T$	DSC	[77]
PMMA_glass Emissivity		0.95	Assumed same as PMMA	[134]
PMMA_glass Absorption Coefficient	m ² kg ⁻¹ (m ⁻¹)	1.94 (2240)	Assumed same as PMMA	[161]
PMMA_char Density	kg/m ³	1160	Assumed same as PMMA	[161]
PMMA_char Conductivity	W/m/K	$0.27-2.4 \times 10^{-4} T$	Assumed same as PMMA_glass	[161]
PMMA_char Specific Heat	kJ/kg/K	$0.60+0.0036T$	Assumed same as PMMA_glass	[77]

PMMA_char Emissivity		0.95	Assumed same as PMMA_glass	[134]
PMMA_char Absorption Coefficient	$\text{m}^2 \text{kg}^{-1}$ (m^{-1})	1.94 (2240)	Assumed same as PMMA	[161]
Reaction 1 Pre-Exponential Factor	s^{-1}	1	Assumed occur at 378 K instantaneously	[77]
Reaction 1 Activation Energy	kJ/kmol	0	Assumed occur at 378 K instantaneously	[77]
Reaction 1 Heat of Reaction per mass of Reactant	kJ/kg	0	DSC	[77]
Reaction 1 Solid Residue		1	TGA	[77]
Reaction 2 Pre-Exponential Factor	s^{-1}	8.60E+12	TGA	[77]
Reaction 2 Activation Energy	kJ/kmol	1.88E+05	TGA	[77]
Reaction 2 Solid Residue		0.015	TGA	[77]
Reaction 2 Heat of Reaction per mass of Reactant	kJ/kg	846	DSC	[77]
Effective HOC of volatiles	kJ/kg	24450 (24800)*	Standard cone calorimeter tests	[162]
Thickness	mm	6.00	Directly measured	[161]
Top boundary temperature	K	323 at 20 kW m^{-2} 348 at 40 kW m^{-2} 370 at 60 kW m^{-2}	Directly measured	[161]
Top boundary convection coefficient	$\text{W/m}^2\text{K}$	5	Inverse Analysis of Material Temperature in Gasification Exp.	[161]
Bottom boundary temperature	K	310	Directly measured	[161]
Bottom boundary convection coefficient	$\text{W/m}^2\text{K}$	4	Inverse Analysis of Material Temperature in Gasification Exp.	[161]
PMMA initial temperature	K	305	Directly measured	[161]

* The value in the bracket is from literature and the value outside the bracket is from standard cone calorimeter measurement.

The mass loss rates predicted by the simulations were used to validate the model against mass loss rate data collected in gasification tests. The parameters of the model were determined through analysis of material temperature data collected in gasification tests and the mass loss rate data was used only for blind validation of the model. The data collected in tests conducted with the CAPA at heat fluxes of 20, 40, and 60 kW m^{-2} and the results of simulations are provided in Figure A. 1.

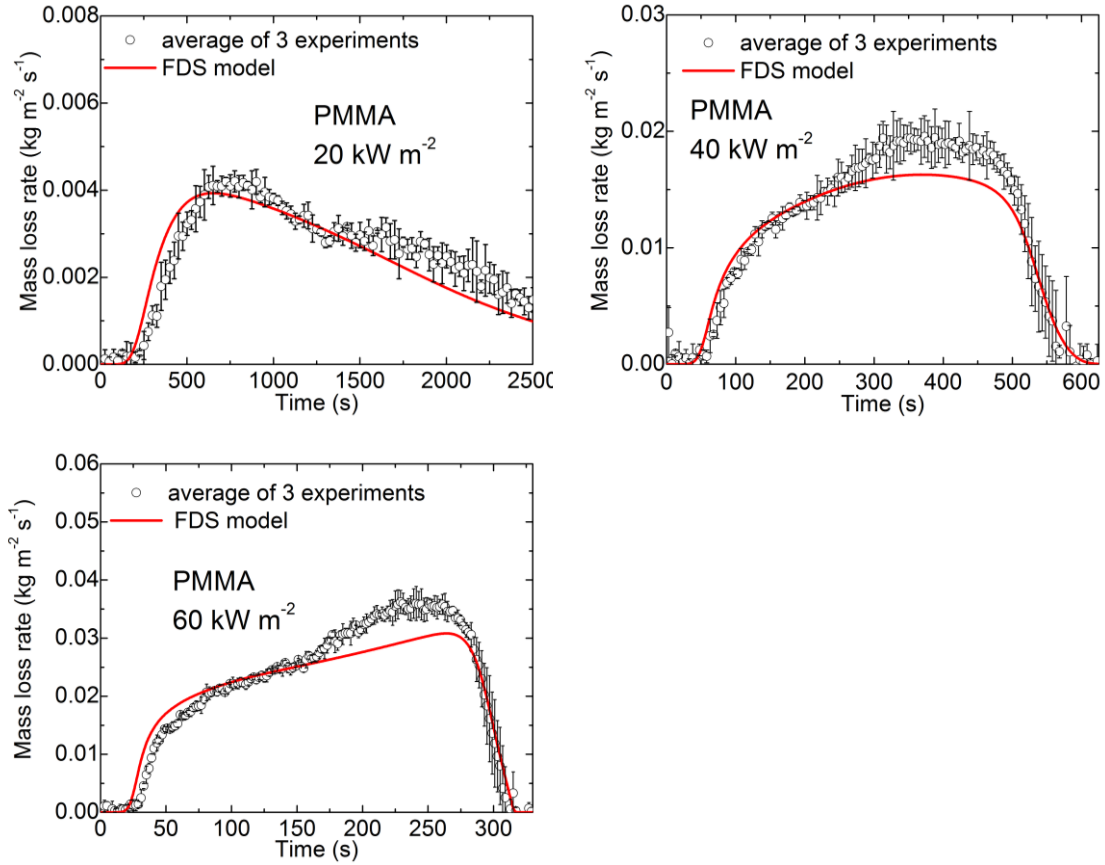


Figure A. 1 Comparison of predicted and measured mass loss rates for PMMA.

The reaction mechanism for POM is described as follows:

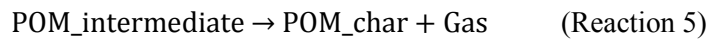


Table A. 2 FDS Input Parameters for POM.

Property	Units	Value	Method	Reference
POM Density	kg/m ³	1424	Directly Determined through Volume and Mass Measurement	[161]
POM Conductivity	W/m/K	$0.25+1.6 \times 10^{-5} T$	Inverse Analysis of Material Temperature in Gasification Exp.	[161]
POM Specific Heat	kJ/kg/K	$-1.86+0.0099 T$	DSC	[77]
POM Emissivity		0.95	Literature	[134]
POM Absorption Coefficient	m ² kg ⁻¹ (m ⁻¹)	2.12 (3050)	Measured by Beer–Lambert law	[161]
POM_melt Density	kg/m ³	1424	Assumed same as POM	[161]

POM_melt Conductivity	W/m/K	$0.21+8\times 10^{-6}T$	Inverse Analysis of Material Temperature in Gasification Exp.	[161]
POM_melt Specific Heat	kJ/kg/K	$1.65+0.0012T$	DSC	[77]
POM_melt Emissivity		0.95	Assumed same as POM	[161]
POM_melt Absorption Coefficient	$m^2 kg^{-1} (m^{-1})$	2.12 (3050)	Assumed same as POM	[161]
POM_intermediate Density	kg/m ³	1424	Assumed same as POM	[161]
POM_intermediate Conductivity	W/m/K	$0.19-6\times 10^{-5}T$	Inverse Analysis of Material Temperature in Gasification Exp.	[161]
POM_intermediate Specific Heat	kJ/kg/K	$1.65+0.0012T$	Assumed same as POM_melt	[77]
POM_intermediate Emissivity		0.95	Assumed same as POM	[134]
POM_intermediate Absorption Coefficient	$m^2 kg^{-1} (m^{-1})$	2.12 (3050)	Assumed same as POM	[161]
POM_char Density	kg/m ³	1424	Assumed same as POM_intermediate	[161]
POM_char Conductivity	W/m/K	$0.19-6\times 10^{-5}T$	Assumed same as POM_intermediate	[161]
POM_char Specific Heat	kJ/kg/K	$1.65+0.0012T$	Assumed same as POM_intermediate	[77]
POM_char Emissivity		0.95	Assumed same as POM_intermediate	[134]
POM_char Absorption Coefficient	$m^2 kg^{-1} (m^{-1})$	2.12 (3050)	Assumed same as POM	[161]
Reaction 3 Pre-Exponential Factor	s ⁻¹	2.69E+42	Fitted for melting process	[77]
Reaction 3 Activation Energy	kJ/kmol	3.82E+05	Fitted for melting process	[77]
Reaction 3 Heat of Reaction per mass of Reactant	kJ/kg	192.1	DSC	[77]
Reaction 3 Solid Residue		1	TGA	[77]
Reaction 4 Pre-Exponential Factor	s ⁻¹	3.84E+14	TGA	[77]
Reaction 4 Activation Energy	kJ/kmol	2.00E+05	TGA	[77]
Reaction 4 Solid Residue		0.4	TGA	[77]
Reaction 4 Heat of Reaction per mass of Reactant	kJ/kg	1192	DSC	[77]
Reaction 5 Pre-Exponential Factor	s ⁻¹	4.76E+44	TGA	[77]
Reaction 5 Activation Energy	kJ/kmol	5.90E+05	TGA	[77]
Reaction 5 Solid Residue		0.018	TGA	[77]
Reaction 5 Heat of Reaction per mass of Reactant	kJ/kg	1352	DSC	[77]
Effective HOC of volatiles	kJ/kg	14350 (14400)*	Standard cone calorimeter tests	[162]
Thickness	mm	6.60	Directly measured	[161]
Top boundary temperature	K	330 at 30 kW m ⁻² 360 at 50 kW m ⁻² 380 at 70 kW m ⁻²	Directly measured	[161]

Top boundary convection coefficient	W/m ² /K	5	Inverse Analysis of Material Temperature in Gasification Exp.	[161]
Bottom boundary temperature	K	310	Directly measured	[161]
Bottom boundary convection coefficient	W/m ² /K	4	Inverse Analysis of Material Temperature in Gasification Exp.	[161]
POM initial temperature	K	305 at 30 kW m ⁻² 305 at 50 kW m ⁻² 310 at 70 kW m ⁻²	Directly measured	[161]

* The value in the bracket is from literature and the value outside the bracket is from standard cone calorimeter measurement.

The data collected in POM gasification tests conducted with the CAPA at heat fluxes of 30, 50, and 70 kW m⁻² and the results of simulations are provided in Figure A. 2.

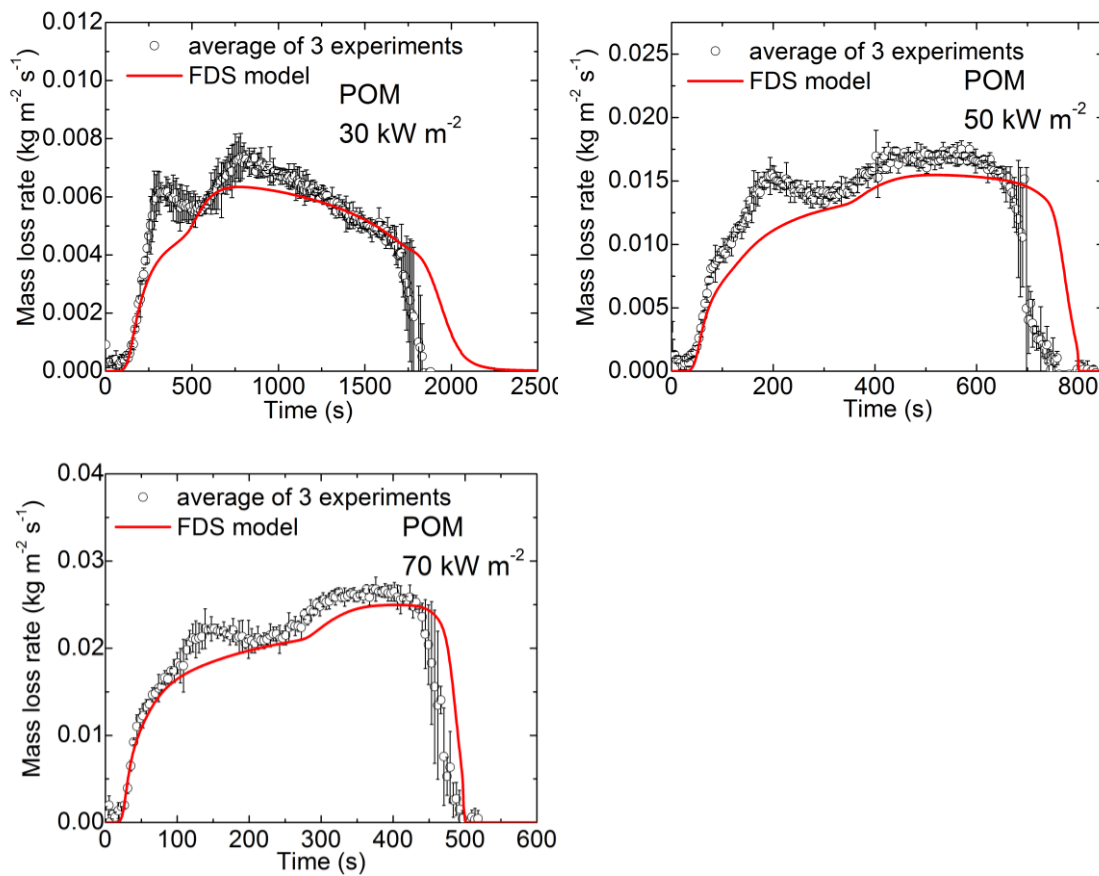


Figure A. 2 Comparison of predicted and measured mass loss rates for POM.

The reaction mechanism for HIPS is described as follows:



Table A. 3 FDS Input Parameters for HIPS.

Property	Units	Value	Method	Reference
HIPS Density	kg/m ³	1060	Directly Determined through Volume and Mass Measurement	[161]
HIPS Conductivity	W/m/K	$0.1+1.0 \times 10^{-4}T$	Inverse Analysis of Material Temperature in Gasification Exp.	[161]
HIPS Specific Heat	kJ/kg/K	$0.59+0.0034T$	DSC	[77]
HIPS Emissivity		0.95	Literature	[134]
HIPS Absorption Coefficient	m ² kg ⁻¹ (m ⁻¹)	2.14 (2250)	Measured by Beer–Lambert law	[161]
HIPS_char Density	kg/m ³	1424	Assumed same as HIPS	[161]
HIPS_char Conductivity	W/m/K	$0.21+8 \times 10^{-6}T$	Assumed same as HIPS	[161]
HIPS_char Specific Heat	kJ/kg/K	$1.65+0.0012T$	Assumed same as HIPS	[77]
HIPS_char Emissivity		0.95	Assumed same as HIPS	[134]
HIPS_char Absorption Coefficient	m ² kg ⁻¹ (m ⁻¹)	1000 (106000)	Assumed opaque	[161]
Reaction 6 Pre-Exponential Factor	s ⁻¹	1.70E+20	TGA	[77]
Reaction 6 Activation Energy	kJ/kmol	3.01E+05	TGA	[77]
Reaction 6 Heat of Reaction per mass of Reactant	kJ/kg	689	DSC	[77]
Reaction 6 Solid Residue		0.043	TGA	[77]
Effective HOC of volatiles	kJ/kg	29900 (29000)*	Standard cone calorimeter tests	[71]
Thickness	mm	6.00	Directly measured	[161]
Top boundary temperature	K	330 at 30 kW m ⁻² 360 at 50 kW m ⁻² 380 at 70 kW m ⁻²	Directly measured	[161]
Top boundary convection coefficient	W/m ² /K	5	Inverse Analysis of Material Temperature in Gasification Exp.	[161]
Bottom boundary temperature	K	310	Directly measured	[161]
Bottom boundary convection coefficient	W/m ² /K	4	Inverse Analysis of Material Temperature in Gasification Exp.	[161]
HIPS initial temperature	K	305 at 30 kW m ⁻² 310 at 50 kW m ⁻² 310 at 70 kW m ⁻²	Directly measured	[161]

* The value in the bracket is from literature and the value outside the bracket is from standard cone calorimeter measurement.

The data collected in HIPS gasification tests conducted with the CAPA at heat fluxes of 30, 50, and 70 kW m⁻² and the results of simulations are provided in Figure

A. 3.

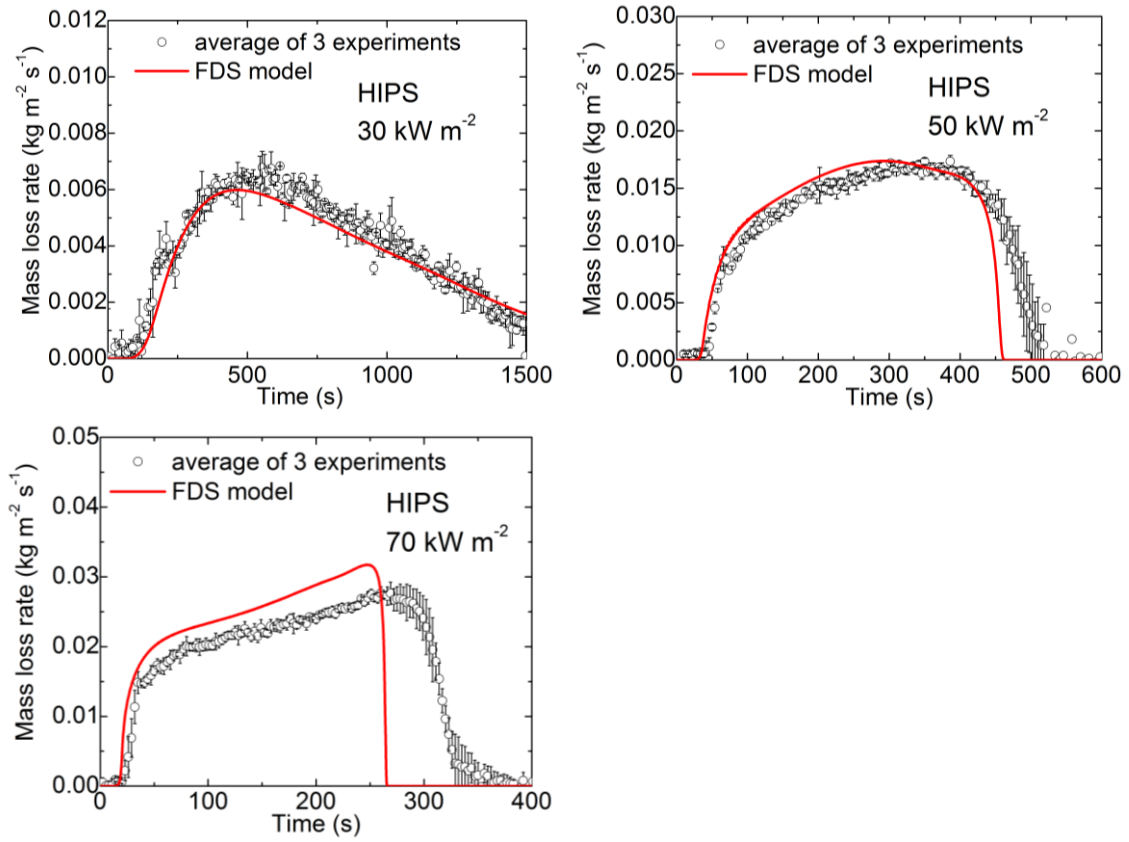


Figure A. 3 Comparison of predicted and measured mass loss rates for HIPS.

Appendix B Parameterized models for charring polymers

In this appendix, the properties of the four polymers that studied in the Chapter 8 and the fully parameterized models are summarized.

The reaction mechanism for ABS is described as follows:



Table B. 1 Parameters for ABS.

Property	Units	Value	Method	Reference
ABS Density	kg/m ³	1050	Directly Determined through Volume and Mass Measurement	
ABS Conductivity	W/m/K	$0.30-2.8 \times 10^{-4} T$	Inverse Analysis of Material Temperature in Gasification Exp.	
ABS Specific Heat	kJ/kg/K	$1.58+0.0013 T$	DSC	[77]
ABS Emissivity		0.95	Literature	[134]
ABS Absorption Coefficient	m ² kg ⁻¹ (m ⁻¹)	1.71 (1800)	Measured by Beer–Lambert law	
ABS_char Density	kg/m ³	80	Assumed same as PET_char	
ABS_char Conductivity	W/m/K	$0.13-5.4 \times 10^{-4} T + 4.8 \times 10^{-9} T^3$	Inverse Analysis of Material Temperature in Gasification Exp.	
ABS_char Specific Heat	kJ/kg/K	$0.82+1.12 \times 10^{-4} T$	Assumed same as PET_char	[79]
ABS_char Emissivity		0.86	Literature	[144]
ABS_char Absorption Coefficient	m ² kg ⁻¹ (m ⁻¹)	31.25 (2500)	Inverse Analysis of Material Temperature in Gasification Exp.	
Reaction 7 Pre-Exponential Factor	s ⁻¹	1.0E+14	Fitted for melting process	[77]
Reaction 7 Activation Energy	kJ/kmol	2.19E+05	Fitted for melting process	[77]
Reaction 7 Heat of Reaction per mass of Reactant	kJ/kg	460	DSC	[77]
Reaction 7 Solid Residue		0.023	TGA	[77]
Effective HOC of volatiles	kJ/kg	28750 (29000)*	Standard cone calorimeter tests	[162]
Thickness	mm	6.40	Directly measured	
Top boundary temperature	K	330 at 30 kW m ⁻² 360 at 50 kW m ⁻² 380 at 70 kW m ⁻²	Directly measured	[161]
Top boundary convection coefficient	W/m ² /K	5	Inverse Analysis of Material Temperature in Gasification Exp.	[161]
Bottom boundary temperature	K	310	Directly measured	[161]
Bottom boundary convection coefficient	W/m ² /K	4	Inverse Analysis of Material Temperature in Gasification Exp.	[161]
ABS initial temperature	K	305 at 30 kW m ⁻² 305 at 50 kW m ⁻² 310 at 70 kW m ⁻²	Directly measured	[161]

* The value in the bracket is from literature and the value outside the bracket is from standard cone calorimeter measurement.

The reaction mechanism for PET is described as follows:

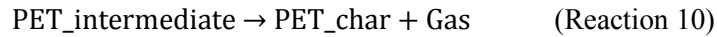


Table B. 2 Parameters for PET.

Property	Units	Value	Method	Reference
PET Density	kg/m ³	1385	Directly Determined through Volume and Mass Measurement	
PET Conductivity	W/m/K	$0.35-4.8 \times 10^{-4} T$	Inverse Analysis of Material Temperature in Gasification Exp.	
PET Specific Heat	kJ/kg/K	$-0.269+0.00464 T$	DSC	[79]
PET Emissivity		0.95	Literature	[134]
PET Absorption Coefficient	m ² kg ⁻¹ (m ⁻¹)	1.4 (1940)	Measured by Beer–Lambert law	
PET_melt Density	kg/m ³	1385	Assume same as PET	
PET_melt Conductivity	W/m/K	$0.33-2 \times 10^{-5} T$	Inverse Analysis of Material Temperature in Gasification Exp.	
PET_melt Specific Heat	kJ/kg/K	$2.05-2.08 \times 10^{-4} T$	DSC	[79]
PET_melt Emissivity		0.95	Assumed same as PET	
PET_melt Absorption Coefficient	m ² kg ⁻¹ (m ⁻¹)	1.4 (1940)	Assumed same as PET	
PET_intermediate Density	kg/m ³	730	Assumed to be average of PET and PET_char	
PET_intermediate Conductivity	W/m/K	$0.45+2 \times 10^{-4} T$	Inverse Analysis of Material Temperature in Gasification Exp.	
PET_intermediate Specific Heat	kJ/kg/K	$1.44-4.8 \times 10^{-5} T$	Assumed same as PET_melt	[79]
PET_intermediate Emissivity		0.95	Assumed same as PET	[134]
PET_intermediate Absorption Coefficient	m ² kg ⁻¹ (m ⁻¹)	1.4 (1025)	Assumed same as PET	
PET_char Density	kg/m ³	80	Directly measured	
PET_char Conductivity	W/m/K	$0.45+3.8 \times 10^{-5} T+5 \times 10^{-10} T^3$	Inverse Analysis of Material Temperature in Gasification Exp.	[161]
PET_char Specific Heat	kJ/kg/K	$0.82+1.12 \times 10^{-4} T$	DSC	[79]
PET_char Emissivity		0.86	Literature	[144]
PET_char Absorption Coefficient	m ² kg ⁻¹ (m ⁻¹)	100 (8000)	Inverse Analysis of Material Temperature in Gasification Exp.	
Reaction 8 Pre-Exponential Factor	s ⁻¹	1.5E+36	Fitted for melting process	[79]

Reaction 8 Activation Energy	kJ/kmol	3.80E+05	Fitted for melting process	[79]
Reaction 8 Heat of Reaction per mass of Reactant	kJ/kg	30	DSC	[79]
Reaction 8 Solid Residue		1	TGA	[79]
Reaction 9 Pre-Exponential Factor	s ⁻¹	1.60E+15	TGA	[79]
Reaction 9 Activation Energy	kJ/kmol	2.35E+05	TGA	[79]
Reaction 9 Solid Residue		0.18	TGA	[79]
Reaction 9 Heat of Reaction per mass of Reactant	kJ/kg	220	DSC	[79]
Reaction 10 Pre-Exponential Factor	s ⁻¹	3.53E+04	TGA	[79]
Reaction 10 Activation Energy	kJ/kmol	9.6E+04	TGA	[79]
Reaction 10 Solid Residue		0.72	TGA	[79]
Reaction 10 Heat of Reaction per mass of Reactant	kJ/kg	250	DSC	[79]
Effective HOC of volatiles	kJ/kg	15950 (18000)*	Standard cone calorimeter tests	[162]
Thickness	mm	6.70	Directly measured	
Top boundary temperature	K	360 at 50 kW m ⁻² 380 at 70 kW m ⁻²	Directly measured	[161]
Top boundary convection coefficient	W/m ² /K	5	Inverse Analysis of Material Temperature in Gasification Exp.	[161]
Bottom boundary temperature	K	310	Directly measured	[161]
Bottom boundary convection coefficient	W/m ² /K	4	Inverse Analysis of Material Temperature in Gasification Exp.	[161]
PET initial temperature	K	310 at 50 kW m ⁻² 310 at 70 kW m ⁻²	Directly measured	[161]

* The value in the bracket is from literature and the value outside the bracket is from standard cone calorimeter measurement.

The reaction mechanism for Kydex is described as follows:

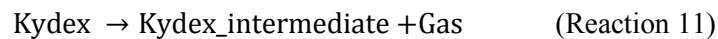


Table B. 3 Parameters for Kydex.

Property	Units	Value	Method	Reference
Kydex Density	kg/m ³	1350	Directly Determined through Volume and Mass Measurement	
Kydex Conductivity	W/m/K	$0.28-2.9 \times 10^{-4} T$	Inverse Analysis of Material Temperature in Gasification Exp.	

Kydex Specific Heat	kJ/kg/K	-0.624+0.00593T	DSC	[79]
Kydex Emissivity		0.95	Literature	[134]
Kydex Absorption Coefficient	m ² kg ⁻¹ (m ⁻¹)	1.58 (2135)	Measured by Beer–Lambert law	
Kydex_intermediate Density	kg/m ³	100	Assumed same as Kydex_char	
Kydex_intermediate Conductivity	W/m/K	0.55+3×10 ⁻⁵ T	Inverse Analysis of Material Temperature in Gasification Exp.	
Kydex_intermediate Specific Heat	kJ/kg/K	0.265+0.00301T	DSC	[79]
Kydex_intermediate Emissivity		0.95	Assumed same as Kydex	[134]
Kydex_intermediate Absorption Coefficient	m ² kg ⁻¹ (m ⁻¹)	30 (3000)	Inverse Analysis of Material Temperature in Gasification Exp.	[161]
Kydex_char Density	kg/m ³	100	Directly measured	[161]
Kydex_char Conductivity	W/m/K	0.28+8.4×10 ⁻⁵ T+3×10 ⁻¹⁰ T ³	Inverse Analysis of Material Temperature in Gasification Exp.	[161]
Kydex_char Specific Heat	kJ/kg/K	1.15+9.56×10 ⁻⁵ T	DSC	[79]
Kydex_char Emissivity		0.86	Literature	[144]
Kydex_char Absorption Coefficient	m ² kg ⁻¹ (m ⁻¹)	100 (10000)	Inverse Analysis of Material Temperature in Gasification Exp.	
Reaction 11 Pre-Exponential Factor	s ⁻¹	6.03E+10	TGA	[79]
Reaction 11 Activation Energy	kJ/kmol	1.41E+05	TGA	[79]
Reaction 11 Heat of Reaction per mass of Reactant	kJ/kg	180	DSC	[79]
Reaction 11 Solid Residue		0.45	TGA	[79]
Reaction 12 Pre-Exponential Factor	s ⁻¹	1.36E+10	TGA	[79]
Reaction 12 Activation Energy	kJ/kmol	1.74E+05	TGA	[79]
Reaction 12 Solid Residue		0.31	TGA	[79]
Reaction 12 Heat of Reaction per mass of Reactant	kJ/kg	125	DSC	[79]
Effective HOC of volatiles	kJ/kg	12650	Standard cone calorimeter tests	
Thickness	mm	6.10	Directly measured	
Top boundary temperature	K	330 at 30 kW m ⁻² 360 at 50 kW m ⁻² 380 at 70 kW m ⁻²	Directly measured	[161]
Top boundary convection coefficient	W/m ² /K	5	Inverse Analysis of Material Temperature in Gasification Exp.	[161]
Bottom boundary temperature	K	310	Directly measured	[161]
Bottom boundary convection coefficient	W/m ² /K	4	Inverse Analysis of Material Temperature in Gasification Exp.	[161]
Kydex initial temperature	K	300 at 30 kW m ⁻² 310 at 50 kW m ⁻² 310 at 70 kW m ⁻²	Directly measured	[161]

The reaction mechanism for PEI is described as follows:

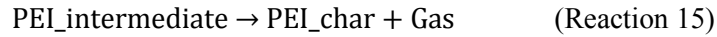


Table B. 4 Parameters for PEI.

Property	Units	Value	Method	Reference
PEI Density	kg/m ³	1285	Directly Determined through Volume and Mass Measurement	
PEI Conductivity	W/m/K	$0.4-4.0 \times 10^{-4} T$	Inverse Analysis of Material Temperature in Gasification Exp.	
PEI Specific Heat	kJ/kg/K	$-0.0357+0.0041 T$	DSC	[79]
PEI Emissivity		0.95	Literature	[134]
PEI Absorption Coefficient	m ² kg ⁻¹ (m ⁻¹)	1.36 (1745)	Measured by Beer–Lambert law	
PEI_melt Density	kg/m ³	1285	Assumed same as PEI	
PEI_melt Conductivity	W/m/K	$0.32-3.3 \times 10^{-4} T$	Inverse Analysis of Material Temperature in Gasification Exp.	
PEI_melt Specific Heat	kJ/kg/K	$1.88+5.75 \times 10^{-4} T$	DSC	[79]
PEI_melt Emissivity		0.95	Assumed same as PEI	
PEI_melt Absorption Coefficient	m ² kg ⁻¹ (m ⁻¹)	100 (128500)	Inverse Analysis of Material Temperature in Gasification Exp.	
PEI_intermediate Density	kg/m ³	80	Assumed same as PEI_char	
PEI_intermediate Conductivity	W/m/K	$0.45+1.9 \times 10^{-4} T$	Inverse Analysis of Material Temperature in Gasification Exp.	
PEI_intermediate Specific Heat	kJ/kg/K	$1.59+3.08 \times 10^{-4} T$	Assumed same as PEI_melt	[79]
PEI_intermediate Emissivity		0.95	Assumed same as PEI	[134]
PEI_intermediate Absorption Coefficient	m ² kg ⁻¹ (m ⁻¹)	100 (8000)	Assumed same as PEI_melt	
PEI_char Density	kg/m ³	80	Directly Determined through Volume and Mass Measurement	
PEI_char Conductivity	W/m/K	$0.5-3.4 \times 10^{-5} T+2 \times 10^{-10} T^3$	Inverse Analysis of Material Temperature in Gasification Exp.	[161]
PEI_char Specific Heat	kJ/kg/K	$1.30+4.08 \times 10^{-5} T$	DSC	[79]
PEI_char Emissivity		0.86	Literature	[144]
PEI_char Absorption Coefficient	m ² kg ⁻¹ (m ⁻¹)	100 (80000)	Assumed same as PEI_melt	
Reaction 13 Pre-Exponential Factor	s ⁻¹	1	Assumed occur at 496 K instantaneously	[79]
Reaction 13 Activation Energy	kJ/kmol	0	Assumed occur at 496 K instantaneously	[79]
Reaction 13 Heat of Reaction per mass of Reactant	kJ/kg	1	DSC	[79]

Reaction 13 Solid Residue		1	TGA	[79]
Reaction 14 Pre-Exponential Factor	s ⁻¹	7.66E+27	TGA	[79]
Reaction 14 Activation Energy	kJ/kmol	4.65E+05	TGA	[79]
Reaction 14 Solid Residue		0.65	TGA	[79]
Reaction 14 Heat of Reaction per mass of Reactant	kJ/kg	-80	DSC	[79]
Reaction 15 Pre-Exponential Factor	s ⁻¹	6.5E+02	TGA	[79]
Reaction 15 Activation Energy	kJ/kmol	8.8E+04	TGA	[79]
Reaction 15 Solid Residue		0.77	TGA	[79]
Reaction 15 Heat of Reaction per mass of Reactant	kJ/kg	-5	DSC	[79]
Effective HOC of volatiles	kJ/kg	18050 (16700)*	Standard cone calorimeter tests	[162]
Thickness	mm	6.60	Directly measured	
Top boundary temperature	K	360 at 50 kW m ⁻² 380 at 70 kW m ⁻² 400 at 90 kW m ⁻²	Directly measured	[161]
Top boundary convection coefficient	W/m ² /K	5	Inverse Analysis of Material Temperature in Gasification Exp.	[161]
Bottom boundary temperature	K	310	Directly measured	[161]
Bottom boundary convection coefficient	W/m ² /K	4	Inverse Analysis of Material Temperature in Gasification Exp.	[161]
PEI initial temperature	K	305 at 50 kW m ⁻² 315 at 70 kW m ⁻² 315 at 90 kW m ⁻²	Directly measured	[161]

* The value in the bracket is from literature and the value outside the bracket is from standard cone calorimeter measurement.

Bibliography

- [1] D. W. v. Krevelen and K. t. Nijenhuis, Properties of Polymers: Their Correlation with Chemical Structure; Their Numerical Estimation and Prediction from Additive Group Contributions, 4th Edition ed. Oxford, UK: Elsevier, 2009.
- [2] C. F. Cullis and M. M. Hirschler, The combustion of organic polymers. Oxford, New York: Clarendon Press, Oxford University Press, 1981.
- [3] T. Kashiwagi, "Polymer combustion and flammability—Role of the condensed phase" Symposium (International) on Combustion vol. 25, pp. 1423-1437, 1994.
- [4] T. Sell, S. Vyazovkin, and C. A. Wight, "Thermal decomposition kinetics of PBAN-binder and composite solid rocket propellants" Combustion and Flame vol. 119, pp. 174-181, 1999.
- [5] W. C. G. Jr., Ed., Gas-Phase Combustion Chemistry. New York: Springer, 1984 Pages.
- [6] (Retrieved March 30, 2014). CHEMKIN Overview- Sandia web site. Available: <http://public.ca.sandia.gov/chemkin/>
- [7] C. Diblasi, "Modeling and Simulation of Combustion Processes of Charring and Non-Charring Solid Fuels" Progress in Energy and Combustion Science vol. 19, pp. 71-104, 1993.
- [8] M. Delichatsios, B. Paroz, and A. Bhargava, "Flammability properties for charring materials" Fire Safety Journal vol. 38, pp. 219-228, 2003.

- [9] L. Yang, X. Chen, X. Zhou, and W. Fan, "The pyrolysis and ignition of charring materials under an external heat flux" *Combustion and Flame* vol. 133, pp. 407-413, 2003.
- [10] R. Lyon, R. Walters, and S. Stoliarov, "Thermal analysis of flammability" *Journal of Thermal Analysis and Calorimetry* vol. 89, pp. 441-448, 2007.
- [11] R. Carvel, T. Steinhaus, G. Rein, and J. L. Torero, "Determination of the flammability properties of polymeric materials: A novel method" *Polymer Degradation and Stability* vol. 96, pp. 314-319, 2011.
- [12] P. Patel, T. R. Hull, R. E. Lyon, S. I. Stoliarov, R. N. Walters, S. Crowley, and N. Safronava, "Investigation of the thermal decomposition and flammability of PEEK and its carbon and glass-fibre composites" *Polymer Degradation and Stability* vol. 96, pp. 12-22, 2011.
- [13] S. R. Wasan, P. Van Hees, and B. Merci, "Study of pyrolysis and upward flame spread on charring materials—Part I: Experimental study" *Fire and Materials* vol. 35, pp. 209-229, 2011.
- [14] M. R. Nyden, S. I. Stoliarov, P. R. Westmoreland, Z. X. Guo, and C. Jee, "Applications of reactive molecular dynamics to the study of the thermal decomposition of polymers and nanoscale structures" *Materials Science and Engineering: A* vol. 365, pp. 114-121, 2004.
- [15] A. Strachan, E. M. Kober, A. C. T. van Duin, J. Oxgaard, and W. A. Goddard, "Thermal decomposition of RDX from reactive molecular dynamics" *The Journal of Chemical Physics* vol. 122, pp. -, 2005.

- [16] S. I. Stoliarov, P. R. Westmoreland, M. R. Nyden, and G. P. Forney, "A reactive molecular dynamics model of thermal decomposition in polymers: I. Poly(methyl methacrylate)" *Polymer* vol. 44, pp. 883-894, 2003.
- [17] S. I. Stoliarov, R. E. Lyon, and M. R. Nyden, "A reactive molecular dynamics model of thermal decomposition in polymers. II. Polyisobutylene" *Polymer* vol. 45, pp. 8613-8621, 2004.
- [18] C. Lautenberger, "A Generalized Pyrolysis Model for Combustible Solids," Ph.D Dissertation, Department of Mechanical Engineering, University of California, Berkeley, Berkeley, CA, 2007.
- [19] B. Martel, "Charring processes in thermoplastic polymers: Effect of condensed phase oxidation on the formation of chars in pure polymers" *Journal of Applied Polymer Science* vol. 35, pp. 1213-1226, 1988.
- [20] A. I. Balabanovich and J. Engelmann, "Fire retardant and charring effect of poly(sulfonyldiphenylene phenylphosphonate) in poly(butylene terephthalate)" *Polymer Degradation and Stability* vol. 79, pp. 85-92, 2003.
- [21] S. V. Levchik, G. F. Levchik, A. I. Balabanovich, E. D. Weil, and M. Klatt, "Phosphorus oxynitride: A thermally stable fire retardant additive for polyamide 6 and poly(butylene terephthalate)" *Angewandte Makromolekulare Chemie* vol. 264, pp. 48-55, 1999.
- [22] C. H. Marvin, G. T. Tomy, J. M. Armitage, J. A. Arnot, L. McCarty, A. Covaci, and V. Palace, "Hexabromocyclododecane: Current Understanding of Chemistry, Environmental Fate and Toxicology and Implications for Global

Management" *Environmental Science & Technology* vol. 45, pp. 8613-8623, 2011/10/15 2011.

[23] S. Bourbigot and G. Fontaine, "Flame retardancy of polylactide: an overview" *Polymer Chemistry* vol. 1, pp. 1413-1422, 2010.

[24] J. W. Gilman, C. L. Jackson, A. B. Morgan, R. Harris, E. Manias, E. P. Giannelis, M. Wuthenow, D. Hilton, and S. H. Phillips, "Flammability Properties of Polymer-Layered-Silicate Nanocomposites. Polypropylene and Polystyrene Nanocomposites†" *Chemistry of Materials* vol. 12, pp. 1866-1873, 2000/07/01 2000.

[25] F. Samyn, S. Bourbigot, C. Jama, and S. Bellayer, "Fire retardancy of polymer clay nanocomposites: Is there an influence of the nanomorphology?" *Polymer Degradation and Stability* vol. 93, pp. 2019-2024, 2008.

[26] S. Bourbigot, G. Fontaine, S. Duquesne, and R. Delobel, "PLA nanocomposites: quantification of clay nanodispersion and reaction to fire" *International Journal of Nanotechnology* vol. 5, pp. 683-692, 2008.

[27] M. Zanetti, G. Camino, R. Thomann, and R. Mülhaupt, "Synthesis and thermal behaviour of layered silicate-EVA nanocomposites" *Polymer* vol. 42, pp. 4501-4507, 2001.

[28] S. D. Burnside and E. P. Giannelis, "Synthesis and properties of new poly(dimethylsiloxane) nanocomposites" *Chemistry of Materials* vol. 7, pp. 1597-1600, 1995.

- [29] T. Kashiwagi, F. Du, J. F. Douglas, K. I. Winey, R. H. Harris, and J. R. Shields, "Nanoparticle networks reduce the flammability of polymer nanocomposites" *Nat Mater* vol. 4, pp. 928-933, 2005.
- [30] S. Bourbigot, M. Le Bras, S. Duquesne, and M. Rochery, "Recent Advances for Intumescent Polymers" *Macromolecular Materials and Engineering* vol. 289, pp. 499-511, 2004.
- [31] C. Huggett, "Estimation of rate of heat release by means of oxygen consumption measurements" *Fire and Materials* vol. 4, pp. 61-65, 1980.
- [32] W. J. Parker, "Calculations of the Heat Release Rate by Oxygen Consumption for Various Applications," NIST1982.
- [33] G. Heskestad, Ed., *SFPE handbook, Third Edition*. Pages.
- [34] F. Jiang, J. L. de Ris, and M. M. Khan, "Absorption of thermal energy in PMMA by in-depth radiation" *Fire Safety Journal* vol. 44, pp. 106-112, 2009.
- [35] P. A. Beaulieu and N. A. Dembsey, "Flammability characteristics at applied heat flux levels up to 200 kW/m²" *Fire and Materials* vol. 32, pp. 61-86, 2008.
- [36] M. Chaos, "Spectral Aspects of Bench-Scale Flammability Testing: Application to Hardwood Pyrolysis " *Proceedings of the Eleventh International Symposium on Fire Safety Science (in press)* 2014.
- [37] P. J. Austin, R. R. Buch, and T. Kashiwagi, "Gasification of silicone fluids under external thermal radiation. Part I. Gasification rate and global heat of gasification" *Fire and Materials* vol. 22, pp. 221-237, 1998.

- [38] M. Liu, X. Zhang, M. Zammarano, J. W. Gilman, R. D. Davis, and T. Kashiwagi, "Effect of montmorillonite dispersion on flammability properties of poly(styrene-co-acrylonitrile) nanocomposites" *Polymer* vol. 52, pp. 3092-3103, 2011.
- [39] F. Kempel, B. Scharrel, G. T. Linteris, S. I. Stoliarov, R. E. Lyon, R. N. Walters, and A. Hofmann, "Prediction of the mass loss rate of polymer materials: Impact of residue formation" *Combustion and Flame* vol. 159, pp. 2974-2984, 2012.
- [40] G. T. Linteris, R. E. Lyon, and S. I. Stoliarov, "Prediction of the gasification rate of thermoplastic polymers in fire-like environments" *Fire Safety Journal* vol. 60, pp. 14-24, 2013.
- [41] M. Liu, X. Zhang, M. Zammarano, J. W. Gilman, and T. Kashiwagi, "Flame retardancy of poly(styrene-co-acrylonitrile) by the synergistic interaction between clay and phosphomolybdate hydrates" *Polymer Degradation and Stability* vol. 96, pp. 1000-1008, 2011.
- [42] S. S. Rahatekar, M. Zammarano, S. Matko, K. K. Koziol, A. H. Windle, M. Nyden, T. Kashiwagi, and J. W. Gilman, "Effect of carbon nanotubes and montmorillonite on the flammability of epoxy nanocomposites" *Polymer Degradation and Stability* vol. 95, pp. 870-879, 2010.
- [43] H. Yu, Z. Jiang, J. W. Gilman, T. Kashiwagi, J. Liu, R. Song, and T. Tang, "Promoting carbonization of polypropylene during combustion through synergistic catalysis of a trace of halogenated compounds and Ni₂O₃ for improving flame retardancy" *Polymer* vol. 50, pp. 6252-6258, 2009.

- [44] T. Kashiwagi, M. Mu, K. Winey, B. Cipriano, S. R. Raghavan, S. Pack, M. Rafailovich, Y. Yang, E. Grulke, J. Shields, R. Harris, and J. Douglas, "Relation between the viscoelastic and flammability properties of polymer nanocomposites" *Polymer* vol. 49, pp. 4358-4368, 2008.
- [45] T. Kashiwagi, R. H. Harris Jr, X. Zhang, R. M. Briber, B. H. Cipriano, S. R. Raghavan, W. H. Awad, and J. R. Shields, "Flame retardant mechanism of polyamide 6–clay nanocomposites" *Polymer* vol. 45, pp. 881-891, 2004.
- [46] T. Kashiwagi, A. B. Morgan, J. M. Antonucci, M. R. VanLandingham, R. H. Harris, W. H. Awad, and J. R. Shields, "Thermal and flammability properties of a silica–poly(methylmethacrylate) nanocomposite" *Journal of Applied Polymer Science* vol. 89, pp. 2072-2078, 2003.
- [47] R. E. Lyon, R. N. Walters, S. I. Stoliarov, and N. Safronava, "Principles and Practice of Microscale Combustion Calorimetry," Federal Aviation Administration, Atlantic City Airport, NJ 08405 2013.
- [48] X. Ding, "Design and Implementation of the Flaming Combustion Calorimeter," Master of Science, Department of Fire Protection Engineering, University of Maryland, College Park, 2013.
- [49] E. R. Tinney, "The combustion of wooden dowels in heated air" *Symposium (International) on Combustion* vol. 10, pp. 925-930, 1965.
- [50] C. D. Blasi, "Physico-chemical processes occurring inside a degrading two-dimensional anisotropic porous medium" *International Journal of Heat and Mass Transfer* vol. 41, pp. 4139-4150, 1998.

- [51] L. M. L. Helsen and E. V. M. Van Den Bulck, "Study of a new macro-particle model for the low-temperature pyrolysis of dried wood chips" *Heat and Mass Transfer/Waerme- und Stoffuebertragung* vol. 38, pp. 165-181, 2002.
- [52] C. Di Blasi and C. Branca, "Temperatures of wood particles in a hot sand bed fluidized by nitrogen" *Energy and Fuels* vol. 17, pp. 247-254, 2003.
- [53] M. L. Janssens, "Modeling of the thermal degradation of structural wood members exposed to fire" *Fire and Materials* vol. 28, pp. 199-207, 2004.
- [54] R. Gupta, "Pyrolysis modeling in a woodstove," pp. 73-85, 2009.
- [55] N. Prakash and T. Karunanithi, "Advances in modeling and simulation of biomass pyrolysis" *Asian Journal of Scientific Research* vol. 2, pp. 1-27, 2009.
- [56] Z. Zhang and S. W. Case, "Finite element modeling for composites exposed to fire," 2009.
- [57] H.-C. Kung, "A mathematical model of wood pyrolysis" *Combustion and Flame* vol. 18, pp. 185-195, 1972.
- [58] W.-C. R. Chan, M. Kelbon, and B. B. Krieger, "Modelling and experimental verification of physical and chemical processes during pyrolysis of a large biomass particle" *Fuel* vol. 64, pp. 1505-1513, 1985.
- [59] P. Carty and S. White, "Char formation in polymer blends" *Polymer* vol. 35, pp. 343-347, 1994.
- [60] R. E. Lyon, "Pyrolysis kinetics of char forming polymers" *Polymer Degradation and Stability* vol. 61, pp. 201-210, 1998.

- [61] S. J.E.J, "Heat and mass transport in developing chars" *Polymer Degradation and Stability* vol. 82, pp. 297-307, 2003.
- [62] R. H. White and E. L. Schaffer, "Application of CMA program to wood charring" *Fire Technology* vol. 14, pp. 279-290, 1978.
- [63] L. T. Fan, L.-S. Fan, K. Miyanami, T. Y. Chen, and W. P. Walawender, "MATHEMATICAL MODEL FOR PYROLYSIS OF A SOLID PARTICLE. EFFECTS OF THE LEWIS NUMBER" *Canadian Journal of Chemical Engineering* vol. 55, pp. 47-53, 1977.
- [64] S. I. Stoliarov and R. E. Lyon, "Thermo-Kinetic Model of Burning for Polymeric Materials," in *Proceedings of the Ninth International Symposium on Fire Safety Science (International Association for Fire Safety Science)*, Karlsruhe, German pp. 1141-1152, 2008.
- [65] K. McGrattan, S. Hostikka, J. Floyd, H. Baum, R. Rehm, W. Mell, and R. McDermott, "Fire Dynamics Simulator (Version 6) Technical Reference Guide " *National Institute of Standards and Technology Special Publication 1018-6, vol. 1: Mathematical Model*, 2013.
- [66] C. Di Blasi, "Modeling chemical and physical processes of wood and biomass pyrolysis" *Progress in Energy and Combustion Science* vol. 34, pp. 47-90, 2008.
- [67] A. Y. Snegirev, V. A. Talalov, V. V. Stepanov, and J. N. Harris, "A new model to predict pyrolysis, ignition and burning of flammable materials in fire tests" *Fire Safety Journal* vol. 59, pp. 132-150, 2013.

- [68] C. Lautenberger and C. Fernandez-Pello, "Generalized pyrolysis model for combustible solids" *Fire Safety Journal* vol. 44, pp. 819-839, 2009.
- [69] J. D. MENCZEL, *Thermal Analysis of Polymers, Fundamentals and Applications* by Joseph D. Menczel: Wiley & Sons, Inc., Hoboken, New Jersey, 2009.
- [70] N. A. Liu and W. C. Fan, "Modelling the Thermal Decompositions of Wood and Leaves under a Nitrogen Atmosphere" *Fire and Materials* vol. 22, pp. 103-108, 1998.
- [71] S. I. Stoliarov, S. Crowley, R. E. Lyon, and G. T. Linteris, "Prediction of the burning rates of non-charring polymers" *Combustion and Flame* vol. 156, pp. 1068-1083, 2009.
- [72] B.-S. Kang, S. G. Kim, and J.-S. Kim, "Thermal degradation of poly(methyl methacrylate) polymers: Kinetics and recovery of monomers using a fluidized bed reactor" *Journal of Analytical and Applied Pyrolysis* vol. 81, pp. 7-13, 2008.
- [73] Y. Liu, S. Guo, and J. Qian, "Study on the decomposition kinetics of polystyrene by using sequential pyrolysis gas chromatograph" *Petroleum Science and Technology* vol. 17, pp. 1089-1105, 1999.
- [74] R. W. J. Westerhout, J. Waanders, J. A. M. Kuipers, and W. P. M. Van Swaaij, "Kinetics of the low-temperature pyrolysis of polyethene, polypropene, and polystyrene modeling, experimental determination, and comparison with literature models and data" *Industrial and Engineering Chemistry Research* vol. 36, pp. 1955-1964, 1997.

- [75] P. Kannan, J. J. Biernacki, and D. P. Visco Jr, "A review of physical and kinetic models of thermal degradation of expanded polystyrene foam and their application to the lost foam casting process" *Journal of Analytical and Applied Pyrolysis* vol. 78, pp. 162-171, 2007.
- [76] P. Grammelis, P. Basinas, A. Malliopoulou, and G. Sakellariopoulos, "Pyrolysis kinetics and combustion characteristics of waste recovered fuels" *Fuel* vol. 88, pp. 195-205, 2009.
- [77] J. Li and S. I. Stoliarov, "Measurement of kinetics and thermodynamics of the thermal degradation for non-charring polymers" *Combustion and Flame* vol. 160, pp. 1287-1297, 2013.
- [78] S. Ciutacu, D. Fătu, and E. Segal, "On the thermal stability of some macromolecular compounds" *Thermochemica Acta* vol. 131, pp. 279-284, 1988.
- [79] J. Li and S. I. Stoliarov, "Measurement of kinetics and thermodynamics of the thermal degradation for charring polymers " *Polymer Degradation and Stability* vol. 106, pp. 2-15, 2014.
- [80] F. Thurner and U. Mann, "KINETIC INVESTIGATION OF WOOD PYROLYSIS" *Industrial & Engineering Chemistry, Process Design and Development* vol. 20, pp. 482-488, 1981.
- [81] H. Bockhorn, A. Hornung, U. Hornung, and S. Löchner, "Pyrolysis of polystyrene as the initial step in incineration, fires, or smoldering of plastics: Investigations of the liquid phase" *Symposium (International) on Combustion* vol. 28, pp. 2667-2673, 2000.

- [82] T. R. Nunn, J. B. Howard, J. P. Longwell, and W. A. Peters, "Product compositions and kinetics in the rapid pyrolysis of sweet gum hardwood" *Industrial & Engineering Chemistry Process Design and Development* vol. 24, pp. 836-844, 1985.
- [83] S. Ciutacu, D. Fătu, and E. Segal, "On the thermal stability of some macromolecular compounds" *Thermochimica Acta* vol. 131, pp. 279-284, 1988.
- [84] H. Bockhorn, A. Hornung, and U. Hornung, "Mechanisms and kinetics of thermal decomposition of plastics from isothermal and dynamic measurements" *Journal of Analytical and Applied Pyrolysis* vol. 50, pp. 77-101, 1999.
- [85] H. T. Borchardt, "The application of differential thermal analysis to the study of reaction kinetics" *Journal of the American Chemical Society* vol. 79, pp. 41-46, 1957.
- [86] A. W. Coats and J. P. Redfern, "Kinetic parameters from thermogravimetric data [12]" *Nature* vol. 201, pp. 68-69, 1964.
- [87] G. P. Ravanetti and M. Zini, "A study on the thermal degradation kinetics of syndiotactic polystyrene by thermogravimetric analysis" *Thermochimica Acta* vol. 207, pp. 53-64, 1992.
- [88] J. H. Flynn and L. A. Wall, *Polym. J. Polym. Sci.: Lett.* vol. 4, p. 323, 1966.
- [89] T. B. Ozawa, *Chem. Soc.* vol. 38, 1965.
- [90] R. K. Agrawal, "Kinetic analysis of complex reactions" *Journal of Thermal Analysis* vol. 31, pp. 1253-1262, 1986/11/01 1986.

- [91] S. Vyazovkin and C. A. Wight, "Isothermal and non-isothermal kinetics of thermally stimulated reactions of solids" *International Reviews in Physical Chemistry* vol. 17, pp. 407-433, 1998/07/01 1998.
- [92] H. A. Schneider, "Are kinetic parameters of non-isothermal thermogravimetric degradation of polymers unequivocal?" *Journal of Thermal Analysis* vol. 40, pp. 677-687, 1993/08/01 1993.
- [93] R. E. Lyon and M. L. Janssens, "Polymer Flammability," *Federal Aviation Administration* 2005.
- [94] C. A. Harper, *Handbook of Building Materials for Fire Protection*: McGraw-Hill, 2004.
- [95] U. Gaur, B. B. Wunderlich, and B. Wunderlich, "Heat Capacity and Other Thermodynamic Properties of Linear Macromolecules. VII. Other Carbon Backbone Polymers" *Journal of Physical and Chemical Reference Data* vol. 12, pp. 29-63, 1983.
- [96] U. Gaur, S. f. Lau, B. B. Wunderlich, and B. Wunderlich, "Heat Capacity and Other Thermodynamic Properties of Linear Macromolecules. VIII. Polyesters and Polyamides" *Journal of Physical and Chemical Reference Data* vol. 12, pp. 65-89, 1983.
- [97] U. Gaur, S. f. Lau, and B. Wunderlich, "Heat Capacity and Other Thermodynamic Properties of Linear Macromolecules. IX. Final Group of Aromatic and Inorganic Polymers" *Journal of Physical and Chemical Reference Data* vol. 12, pp. 91-108, 1983.

- [98] S. I. Stoliarov and R. N. Walters, "Determination of the heats of gasification of polymers using differential scanning calorimetry" *Polymer Degradation and Stability* vol. 93, pp. 422-427, 2008.
- [99] J. B. Henderson, J. A. Wiebelt, M. R. Tant, and G. R. Moore, "A method for the determination of the specific heat and heat of decomposition of composite materials" *Thermochimica Acta* vol. 57, pp. 161-171, 1982.
- [100] V. V. Tsukruk, V. V. Gorbunov, and N. Fuchigami, "Microthermal analysis of polymeric materials" *Thermochimica Acta* vol. 395, pp. 151-158, 2002.
- [101] J. L. Consalvi, Y. Pizzo, A. Kaiss, J. L. Torero, and B. Porterie, "A theoretical and numerical evaluation of the steady-state burning rate of vertically oriented PMMA slabs" *Combustion Theory and Modelling* vol. 12, pp. 451-475, 2008/05/20 2008.
- [102] T. Kashiwagi, "Effects of sample orientation on radiative ignition" *Combustion and Flame* vol. 44, pp. 223-245, 1982.
- [103] M. Assael, S. Botsios, K. Gialou, and I. Metaxa, "Thermal Conductivity of Polymethyl Methacrylate (PMMA) and Borosilicate Crown Glass BK7" *International Journal of Thermophysics* vol. 26, pp. 1595-1605, 2005.
- [104] X. Zhang and M. Fujii, "Measurements of the thermal conductivity and thermal diffusivity of polymers" *Polymer Engineering & Science* vol. 43, pp. 1755-1764, 2003.
- [105] X. Zhang, W. Hendro, M. Fujii, T. Tomimura, and N. Imaishi, "Measurements of the Thermal Conductivity and Thermal Diffusivity of Polymer Melts with the

Short-Hot-Wire Method" International Journal of Thermophysics vol. 23, pp. 1077-1090, 2002/07/01 2002.

[106] S. I. Stoliarov, N. Safronava, and R. E. Lyon, "The effect of variation in polymer properties on the rate of burning" Fire and Materials vol. 33, pp. 257-271, 2009.

[107] G. T. Linteris, "Numerical simulations of polymer pyrolysis rate: Effect of property variations" Fire and Materials vol. 35, pp. 463-480, 2011.

[108] N. BAL, "Uncertainty and complexity in pyrolysis modelling," DOCTOR of PHILOSOPHY, THE UNIVERSITY of EDINBURGH, 2012.

[109] A. Witkowski, "The use of Numerical Methods to Interpret Polymer Decomposition Data," Doctor of Philosophy, University of Central Lancashire, 2012.

[110] S. I. Stoliarov and R. E. Lyon, "Thermo-Kinetic Model of Burning," Federal Aviation Administration Technical Note DOT/FAA/AR-TN08/17, 2008. Available: <http://www.fire.tc.faa.gov/reports/reports.asp>

[111] S. I. Stoliarov, S. Crowley, R. N. Walters, and R. E. Lyon, "Prediction of the burning rates of charring polymers" Combustion and Flame vol. 157, pp. 2024-2034, 2010.

[112] C. Cain and B. Y. Lattimer, "Measuring properties for material decomposition modeling" Journal of ASTM International vol. 7, 2010.

[113] B. Y. Lattimer, J. Ouellette, and J. Trelles, "Measuring properties for material decomposition modeling" Fire and Materials vol. 35, pp. 1-17, 2011.

- [114] G. Agarwal and B. Lattimer, "Method for measuring the standard heat of decomposition of materials" *Thermochimica Acta* vol. 545, pp. 34-47, 2012.
- [115] C. Lautenberger, G. Rein, and C. Fernandez-Pello, "The application of a genetic algorithm to estimate material properties for fire modeling from bench-scale fire test data" *Fire Safety Journal* vol. 41, pp. 204-214, 2006.
- [116] M. Chaos, M. M. Khan, N. Krishnamoorthy, J. L. De Ris, and S. B. Dorofeev, "Evaluation of optimization schemes and determination of solid fuel properties for CFD fire models using bench-scale pyrolysis tests," in *Proc. Combust. Inst.*, pp. 2599-2606, 2011.
- [117] ASTM(E2058-09), "Standard Test Methods for Measurement of Synthetic Polymer Material Flammability Using a Fire Propagation Apparatus (FPA)," West Conshohocken, PA2009.
- [118] Z. Ghorbani, R. Webster, M. Lázaro, and A. Trouvé, "Limitations in the predictive capability of pyrolysis models based on a calibrated semi-empirical approach" *Fire Safety Journal* vol. 61, pp. 274-288, 2013.
- [119] N. Bal and G. Rein, "Relevant model complexity for non-charring polymer pyrolysis" *Fire Safety Journal* vol. 61, pp. 36-44, 2013.
- [120] V. Christian, D. Jean-Louis, R. Marcelline, B. Jacques, and L. Najib, "Experimental and Numerical Study of the Thermal Degradation of PMMA" *Combustion Science and Technology* vol. 53, pp. 187-201, 1987/06/01 1987.

- [121] K. D. Steckler, Kashiwagi, T., Baum, H.R. and Kanemaru, K., "Analytical Model For Transient Gasification Of Noncharring Thermoplastic Materials" *Fire Safety Science* vol. 3, pp. 895-904, 1991.
- [122] J. E. J. Staggs and R. H. Whiteley, "Modelling the combustion of solid-phase fuels in cone calorimeter experiments" *Fire and Materials* vol. 23, pp. 63-69, 1999.
- [123] E. K. Nicolette VV, Vembe BE., "Numerical simulation of decomposition and combustion of organic materials," in *Proceedings of Interflam 10th International Conference on Fire Science and Engineering.*, 2004.
- [124] F.-P. A. Lautenberger C, "Approximate Analytical Solutions for the Transient Mass Loss Rate and Piloted Ignition Time of a Radiatively Heated Solid in the High Heat Flux Limit" *Fire Safety Science—Proceedings of the Eighth International Symposium, International Association for Fire Safety Science* pp. 445-456, 2005.
- [125] J. D. Menczel and R. B. Prime, *Thermal Analysis of Polymers - Fundamentals and Applications*. Hoboken, New Jersey: John Wiley & Sons, Inc., 2009.
- [126] S. Vyazovkin and C. A. Wight, "Kinetics in solids" *Annual Review of Physical Chemistry* vol. 48, pp. 125-149, 1997.
- [127] W. J. Frederick and C. C. Mentzer, "Determination of heats of volatilization for polymers by differential scanning calorimetry" *Journal of Applied Polymer Science* vol. 19, pp. 1799-1804, 1975.
- [128] ASTM(E1354), "Standard Test Method for Heat and Visible Smoke Release Rates for Materials and Products Using an Oxygen Consumption Calorimeter," West Conshohoken, PA 2007. Available: www.astm.org

- [129] NETZSCH. (2012). STA 449 F3 Jupiter® brochure Available: http://www.netzsch-thermal-analysis.com/uploads/tx_nxnetzschmedia/files/STA_449_F3_E_0912.pdf
- [130] R. E. Lyon, N. Safronava, J. Senese, and S. I. Stoliarov, "Thermokinetic model of sample response in nonisothermal analysis" *Thermochimica Acta* vol. 545, pp. 82-89, 2012.
- [131] NETZSCH, "Temperature Calibration Version 5.2.0," NETZSCH Gerätebau GmbH, Wittelsbacherstrasse 42, D-95100 Selb/Bayern 2010.
- [132] NETZSCH, "Sensitibity Calibration Version 5.2.0," NETZSCH Gerätebau GmbH, Wittelsbacherstrasse 42, D-95100 Selb/Bayern 2010.
- [133] D. A. Ditmars, S. Ishihara, S. S. Chang, and G. Bernstein, "Enthalpy and Heat-Capacity Standard Reference Material: Synthetic Sapphire (a-A1203) from 10 to 2250 K" *Journal of Research of the National Bureau of Standards* vol. 87, pp. 159-163, 1982.
- [134] G. Linteris, M. Zammarano, B. Wilthan, and L. Hanssen, "Absorption and reflection of infrared radiation by polymers in fire-like environments" *Fire and Materials* vol. 36, pp. 537-553, 2011.
- [135] P. T. Tsilingiris, "Comparative evaluation of the infrared transmission of polymer films" *Energy Conversion and Management* vol. 44, pp. 2839-2856, 2003.
- [136] ASTM, " Standard Test Method for Heat and Visible Smoke Release Rates for Materials and Products Using an Oxygen Consumption Calorimeter," vol. Standard E1354 - 11b, ed. West Conshohocken, PA: ASTM International, 2011.

- [137] M. Semmes, X. Liu, M. B. McKinnon, S. I. Stoliarov, and A. Witkowski, "A Model for Oxidative Pyrolysis for Corrugated Cardboard," in Proceedings of the Eleventh International Symposium on Fire Safety Science (accepted for publication), University of Canterbury, New Zealand, 2014.
- [138] M. B. McKinnon, "Development of a model for flaming combustion of double-wall corrugated cardboard," College Park, Masters Thesis 2012.
- [139] X. Liu, "DESIGN AND ANALYSIS OF NEW GASIFICATION APPARATUS BASED ON THE STANDARD CONE CALORIMETER," Master thesis, Fire Protection Engineering, University of Maryland, College Park, 2012.
- [140] P. Patel, T. R. Hull, R. W. McCabe, D. Flath, J. Grasmeder, and M. Percy, "Mechanism of thermal decomposition of poly(ether ether ketone) (PEEK) from a review of decomposition studies" *Polymer Degradation and Stability* vol. 95, pp. 709-718, 2010.
- [141] R. Lyon, Safronava N. and Oztekin E., "A Simple Method for Determining Kinetic Parameters for Materials in Fire Models" *Fire Safety Science* 2011.
- [142] W. J. Massman, "A review of the molecular diffusivities of H₂O, CO₂, CH₄, CO, O₃, SO₂, NH₃, N₂O, NO, and NO₂ in air, O₂ and N₂ near STP" *Atmospheric Environment* vol. 32, pp. 1111-1127, 1998.
- [143] J. E. Mark, *Physical Properties of Polymers Handbook*: AIP Press, 1996.
- [144] T. Matsumoto and A. Ono, "Specific heat capacity and emissivity measurements of ribbon-shaped graphite using pulse current heating" *International Journal of Thermophysics* vol. 16, pp. 267-275, 1995/01/01 1995.

- [145] NIST_Chemistry_WebBook. The National Institute of Standards and Technology (NIST) Chemistry WebBook. Available: <http://webbook.nist.gov/chemistry/name-ser.html>
- [146] (07.16. 2013). Organic RCF Vacuum Formed Products. Available: <<http://www.morganthermalceramics.com/files/datasheets/kaowoolpmvacuumformed514-700.pdf>
- [147] Engineeringtoolbox. (07.17.2013). Resources, Tools and Basic Information for Engineering and Design of Technical Applications. Available: <http://www.engineeringtoolbox.com/index.html>
- [148] R. E. Lyon, R. N. Walters, and S. I. Stoliarov, "A Thermal Analysis Method for Measuring Polymer Flammability" *Journal of ASTM International* vol. 3, p. 18, 2006.
- [149] A. V. Nikolaev, V. A. Logvinenko, and V. M. Gorbachev, "Special features of the compensation effect in non-isothermal kinetics of solid-phase reactions" *Journal of Thermal Analysis and Calorimetry* vol. 6, pp. 473-477, 1974.
- [150] S. M. Blinder, *Advanced Physical Chemistry: A Survey of Modern Theoretical Principles*. London, UK, : The Macmillan Company, 1969.
- [151] P. R. Bevington and D. K. Robinson, *Data reduction and error analysis for the physical sciences*, 2 ed. Boston: WCB/McGraw-Hill, 1992.
- [152] A. Tewarson, "Heat release rate in diffusion flames" *Thermochimica Acta* vol. 278, pp. 19-37, 1996.

- [153] J. E. J. Staggs, "Thermal conductivity estimates of intumescent chars by direct numerical simulation" *Fire Safety Journal* vol. 45, pp. 228-237, 2010.
- [154] M. J. Assael, S. Botsios, K. Gialou, and I. N. Metaxa, "Thermal Conductivity of Polymethyl Methacrylate (PMMA) and Borosilicate Crown Glass BK7" *International Journal of Thermophysics* vol. 26, pp. 1595-1605, 2005/09/01 2005.
- [155] M. Rides, J. Morikawa, L. Halldahl, B. Hay, H. Lobo, A. Dawson, and C. Allen, "Intercomparison of thermal conductivity and thermal diffusivity methods for plastics" *Polymer Testing* vol. 28, pp. 480-489, 2009.
- [156] W. N. dos Santos, J. A. de Sousa, and R. Gregorio Jr, "Thermal conductivity behaviour of polymers around glass transition and crystalline melting temperatures" *Polymer Testing* vol. 32, pp. 987-994, 2013.
- [157] W. N. dos Santos, "Thermal properties of polymers by non-steady-state techniques" *Polymer Testing* vol. 26, pp. 556-566, 2007.
- [158] J. Brandrup and E. H. Immergut, Eds., *Polymer Handbook*. New York: Wiley-Interscience, 1989 Pages.
- [159] F. C. Chen, Y. M. Poon, and C. L. Choy, "Thermal diffusivity of polymers by the flash method" *Polymer* vol. 18, pp. 129-136, 1977.
- [160] M. B. McKinnon, S. I. Stoliarov, and A. Witkowski, "Development of a pyrolysis model for corrugated cardboard" *Combustion and Flame* vol. 160, pp. 2595-2607, 2013.

[161] J. Li, J. Gong, and S. I. Stoliarov, "Gasification Experiments for Pyrolysis Model Parameterization and Validation" *International Journal of Heat and Mass Transfer* vol. 77, pp. 738-744, 2014.

[162] R. E. Lyon and M. L. Janssens, "Polymer Flammability," U.S. Department of Transportation Federal Aviation Administration, Washington, DC 205912005.